CRANFIELD UNIVERSITY

SCHOOL OF APPLIED SCIENCES

PhD THESIS

Academic Year 2002 – 2005

M. Fouinneteau

Damage and failure modelling of carbon and glass 2D braided composites

Supervisor: A K Pickett

April 2006

This thesis is submitted in partial fulfilment of the requirements
for the degree of Doctor of Philosophy

Abstract

Composite materials have been increasingly used in the past two decades since they offer significant potential weight reduction, part design flexibility and improved specific mechanical performance compared to traditional metals. For specific applications, braid reinforced composites offer better near net shape part and manufacturing flexibility than conventional unidirectional laminates, albeit at the expense of slightly lower in-plane stiffness and strength. Furthermore, for impact and crash applications, which is the emphasis of this thesis, their tow waviness and interlocking can offer excellent damage tolerance and energy absorption.

In this work, heavy tow (24k) biaxial carbon and glass braided preforms were used to manufacture coupons and beam structures to undertake an extensive testing campaign to characterise different damage and failure mechanisms occurring in braided composites. Due to large shear deformation and surface degradation, non conventional measurement techniques based on marker tracking and Digital Image Correlation were successfully used to measure strains in the damaging material.

The modelling of braided composites was conducted using the meso-scale damage approach first proposed by P. Ladevèze for unidirectional composites. The calibration of an equivalent braid unidirectional ply was achieved using the experimental results obtained for different braided coupons. Furthermore, failure mechanisms observed experimentally, such as tow stretching and fibre re-orientation occurring during loading history, were integrated into the model. A new unidirectional ply formulation was subsequently implemented into the explicit finite element code PAM-CRASH^{TM}. Validation of the new model using single element, coupons and beams were conducted that provided a satisfying correlation between experimental tests and numerical predictions.

To my grand-father

Acknowledgements

I wish to thank my supervisor, Professor Anthony Pickett, for his valuable help and consistent support during my PhD.

I am greatly indebted to all my colleagues from the Cranfield Composites Department for their advice along these past three years.

I would like to thank Ralf Lichtenberger from LIMESS GmbH for his availability and technical advice.

I also wish best of luck to my friends Gavin and Harry for their future career.

I express my special thanks to my beloved parents, Patrick and Joëlle, and grand father, Gaston, who gave me the chance to study and be where I am now.

Finally, I want to thank particularly Cristina for her patience and support during this experience.

List of contents

Chapter 4- Damage model theoretical developments 106

List of tables

List of figures

Abbreviations and symbols

Abbreviations.	Meaning
CLT	Classical Laminate Theory
CPU	Central Processing Unit
DIC	Digital Image Correlation
FE	Finite Element
FGM	Fabric Geometry Model
ROI	Region Of Interest
RTM	Resin Transfer Moulding
RUC	Repetitive Unit Cell
STS	Standard Tensile Strength
UCCM	Unit Cell Continuum Mode
UD	Unidirectional
VARTM	Vacuum Assisted Resin Infusion
WF	Woven Fabric
WWFE	World Wide Failure Exercise

Symbol	Meaning	Units
θ	Braid Angle	Degrees
S	Compliance Matrix	-
C	Stiffness Matrix	-
E_{11}^{t}	Tensile Young’s modulus in the 1-direction	GPa
E_{11}^{c}	Compressive Young’s modulus in the 1-direction	GPa
E_{22}^{c}	Tensile Young’s modulus in the 2-direction	GPa
G_{12}	Shear modulus in the 1,2 plane	GPa
ν_{12}^{0}	Poisson’s ratio in 1,2-plane	-
ε_{11l}^{t}	Tensile fibre initial strain	-
ε_{11u}^{t}	Tensile fibre ultimate strain	-

d_{11u}^{t}	Tensile fibre ultimate damage	-
γ	Compressive factor for non-linear fibre compressive behaviour	-
ε_{11l}^{c}	Compressive fibre initial strain	-
ε_{11u}^{c}	Compressive fibre ultimate strain	-
d_{11u}^{c}	Compressive fibre ultimate damage	-
Y_{12C}	Critical shear damage limit	√GPa
Y_{120}	Initial shear damage limit	√GPa
Y_{12R}	Elementary shear damage fracture limit	√GPa
$d_{\max}$	Maximum shear damage	-
β	Hardening law multiplier	GPa
α	Hardening law exponent	-
R_0	Initial yield stress	GPa
Y_{22C}	Critical transverse damage limit	√GPa
Y_{220}	Initial transverse damage limit	√GPa
Y_{22R}	Brittle transverse damage limit of fibre–matrix interface	√GPa
b	Coupling factor between shear and transverse damage	-
a^2	Coupling factor between shear and transverse plastic strains	-

Chapter 1- Introduction and objectives

In recent decades, the aerospace and automotive industries have preferred to use metals in the design of structural parts due to their low cost and well established mechanical properties. However, in the past 10 years, a general effort has been conducted to reduce vehicle fuel consumption by reducing vehicle weight. Accordingly, novel non-metallic materials have been investigated and, particularly, fibre polymer composites materials. This alternative material offers numerous advantages such as weight reduction, high mechanical properties per unit mass [99], design flexibility, corrosion resistance and reduced noise transmission. Also, in certain applications, they can offer reduced manufacturing costs compared to conventional metals, despite raw material costs being higher [122].

1.1 Frame of research

In material science, most of the phenomenological models predicting material behaviour are generally based on experimental observations. The main challenge is in understanding and elaborating laws which predict material response for different loading scenarios. In the last century extensive research on isotropic materials such as steel, or aluminium, has provided reliable elastic, elasto-plastic and failure models which are nowadays used routinely by engineers. However, novel fibre polymer composites materials, developed over the last 30 years, still demonstrate complexity and challenge in terms of mechanical modelling.

Composite research is still challenged by fully understanding and reproducing phenomenon, even for fairly standard composites such as pre-impregnated unidirectional laminates, and this is attributed to the complex nature of the composite itself. Composites can be tailored to various and specific applications; for instance, stiffness can be increased by adding fibres in the loading direction, or large deformations and ductile failure can be produced by using a resin with large strain to failure and extensible fibres or “open” fabric architectures that may readily shear. Furthermore, manufacturing processes often employed are not as consistent as those used for metals manufacturing, often leading to poor reproducibility of material mechanical properties. Their inherent manufacturing defects may be caused by numerous factors, such as resin air entrapment causing voids formation, or fibre misalignment creating variable mechanical properties.

Classical laminate theory and simple failure criteria are commonly used as the first methods to estimate composites stiffness and approximate failure loads. Nevertheless, this approach presents limitations by ignoring damage progression and distinction between the different failure modes. Hence, more recently, advanced methods have been proposed to improve prediction of damage evolution, failure and post failure mechanisms. However, recent publications resulting from the World Wide Failure Exercise, conducted by Hinton et al [60] [74], have demonstrated that many of these models used were not accurate enough to predict failure of simple unidirectional composites which have been in common use for the last 40 years.

1.2 Potential of braided composite materials

An increasing and general interest has been shown by industry towards braided composites, since they offer near net shape part and manufacturing flexibility, even though they exhibit lower in-plane stiffness and strength than unidirectional plies laminates. A further advantage is that their tow waviness acts as reinforcement through thickness offering higher damage tolerance and energy absorption. Paradoxically, the open literature provides only a few publications considering their failure mechanisms characterisation or modelling.

The main existing models for braids characterisation are generic to fabrics and offer to predict elastic properties using micro model representation of a Repetitive Unit Cell (RUC). Most of them are based on the Classical Laminate Theory (CLT), or assume an ideal geometry of the fibre architecture using the assumption of isostrain or isostress conditions [26]. More complex models based on finite element analysis simulate tows and resin pockets, which require increased computation time and calculation power. Nevertheless, most of these models predict only material initial stiffness and only a few consider failure prediction [107].

Braided composites can exhibit large deformations through shearing mechanism, or, so called ‘scissoring effect’, which leads to progressive damage at the fibre/matrix interface. Models based on damage mechanics are therefore more appropriate than the previous models in this particular case. The damage model based on an elementary unidirectional ply, proposed by Ladevèze [87], and developed initially for unidirectional composites, was chosen to model braided composites and the different failure mechanisms that can occur.

1.3 Research objectives

This thesis contributes new scientific work on the modelling of braided composites. The existing Ladevèze damage model is used and adapted for the 2D biaxial braided composites. The main objective was to enable the use of finite element modelling to predict damage and failure of braided structures such as flat panels and beams.

The main goals of this work can be summarised as follows,

- manufacture of 2D carbon and glass braided composite panels and beams,
- characterisation of their mechanical characteristics and failure modes,
- adaptation of the damage model proposed by Ladevèze for 2D braided composites,
- implementation of this adapted model in the explicit code PAM-CRASH^{TM},
- validation of the new predictive model through comparisons between FE simulations and experimental results on braided coupons and beams.

1.4 Thesis structure

This section presents a brief overview of the different chapters appearing in this thesis.

Chapter 2- *Literature review*

A general review on properties and manufacture of carbon and glass fibre preforms used in this work is presented. General consideration on the resin infusion routes used for braided composites manufacture and inherent quality issues are introduced.

General mechanical characteristics for braided composites and the state-of-the-art of their mechanical modelling are presented. The original damage model proposed by Ladevèze used to represent progressive damage in unidirectional composites is presented in detail together with the explicit finite element code PAM-CRASH^{TM} in which it is implemented.

Chapter 3- *Experimental work: Manufacturing and mechanical characterisation of glass and carbon braided composites*

This chapter investigates the different problems relative to quality control encountered during the manufacturing of coupon and beams. The limitations of conventional measurement techniques when monitoring large deformations and surface degradation observed for braided composites are also discussed. New methods based on image analysis are introduced and presented.

A preliminary testing study on fibre continuity and over-braiding and the main characteristics found in braided composites are presented. Furthermore, in order to characterise the different failure mechanisms, an extensive test campaign on coupon and beams is conducted; a detailed description of these test results is presented.

Chapter 4- *Damage model theoretical developments*

The current implementation in PAM-CRASH^{TM} of the Ladevèze damage model is briefly reviewed. A new damage model formulation based on the calibration of an 'equivalent braid unidirectional ply' is proposed and comprehensively detailed. A method to calibrate the elastic properties based on CLT is first presented and then integration of the fibre rotation, throughout loading history, in damage and plasticity laws is achieved.

<u>Chapter 5</u>- *Damage model validation*

The new damage model introduced in the previous chapter is validated using the explicit FE code PAM-CRASH^{TM} in which model modifications have been implemented. Simulation results on different braided coupons and beams are compared with experimental results and discussed.

<u>Chapter 6</u>- *Overall discussion*

The different limitations relative to braided composites mechanical characterisation and modelling are presented and discussed. Solutions to improve material damage and failure prediction are also proposed.

<u>Chapter 7</u>- *Conclusion and future work*

Conclusions on the achievements of the thesis and contribution to knowledge of this work are summarised. Finally different directions of possible future research concluded from this work are proposed.

Chapter 2- Literature review

Continuous fibre reinforced composites have long been used in preference to metals in aerospace and other high performance applications where high specific properties are required for secondary and primary structures such as the fuselage or wings. In recent years, the automotive industry has also started to develop fibre reinforced components capable of matching the performance of equivalent metal parts for high stress applications such as leaf springs and drive shafts. This alternative material has numerous advantages such as weight reduction, high mechanical properties per unit mass [99], design flexibility, corrosion resistance and reduced noise transmission. Also, in certain applications, continuous fibre composites can offer reduced manufacturing costs compared with conventional materials despite raw material costs being higher than sheet metals [122].

Table 2.1 presents the two main classes of fibrous composites, glass and carbon epoxy; a comparison is made with two structural metals, aluminium and steel.

Properties	**E-Glass/Epoxy**	**Carbon/Epoxy (AS4/3501-6)**	**Aluminium (Standard alloy)**	**Steel (Mild strength)**
Density ρ [g/cm^3]	2.1	1.58	2.8	7.8
Young's modulus E^t_{11} [GPa]	39	142	73	207
In-plane shear modulus G_{12} [GPa]	3.8	7.2	26.6	79
Poisson's ratio υ_{12}	0.28	0.27	0.33	0.3
Longitudinal tensile strength [MPa]	1080	2280	414	394

Table 2.1: Properties of typical fibrous composites and metals [28]

Glass and carbon fibre composites exhibit low densities compared to metals, also their general mechanical properties with respect to density are significantly higher. In particular, carbon fibre composites exhibit the highest specific stiffness E/ρ and strength σ_{ult}/ρ [80]. A good choice of the reinforcement directions in the component design can lead to superior mechanical properties compared to equivalent metal components. This possibility of tailoring the material to suit mechanical requirements makes composites particularly interesting in engineering.

Until recently most fibre reinforced composites were manufactured by hand laying laminated unidirectional plies. This process is expensive and time consuming and is only used in high technology applications such as aerospace or motorsport. However, in the last 15 years, textile composites have been increasingly developed and studied due to their higher through-thickness elastic and strength properties, impact/fracture resistance and damage tolerance [106]. Also, their manufacturability compared to unidirectional composite is more efficient due to near-net shape processing.

One of the most attractive techniques is 2D and 3D braiding, which has been one of the main focuses of research for textile processing in the last 10 years. For instance, through the ATCAS program Boeing demonstrated the cost-effective potential of braided composites for fuselage structural elements by manufacturing a 0.9m fuselage circumferential hoop frame [36].

Braided composites present advantages compared to standard unidirectional or woven composites since they offer fibre continuity leading to larger strains to failure. They also offer the possibility for near net shape preforms and greater manufacturing flexibility compared to conventional unidirectional and woven laminate composites. Generally preforms are manufactured using rotary braiding machines which can provide a wide range of yarn architectures and shapes and are particularly suited to preforms for closed form sectional members. Furthermore, the availability of new low cost carbon and glass fibres and the use of automated resin injection processes are helping to encourage industrial interest, particularly for low volume niche applications.

Generally braided composites exhibit lower in-plane stiffness and strength than unidirectional laminates; however, due to the through thickness tows and tow interlocking they are more suited for applications requiring high through-thickness elastic/strength properties, good impact and fracture resistance and high levels of energy absorption under crash loading. For axial crushing properly designed composite braided sectional members can significantly outperform metals in terms of specific energy absorption. For instance, braided tubes are used in automotive crashworthiness to absorb energy in frontal impacts, as shown in figure 2.1 for the SLR McLaren Mercedes.

Figure 2.1: SLR crash cones used in frontal impact [37].

Under crash loading, the composite cones absorb the impact energy through plasticity, material fragmentation and internal friction. At present, these crash absorbers are expensive and can only be justified in high performance automotive structures; however, car manufacturers are also showing an interest in replacing metal energy absorbing structures, such as bumper beams, by composite alternatives in mass produced vehicles.

Braided composites are generally based on epoxy resin systems due to its high toughness, high strength, low viscosity, good flow rates and low shrinkage [80]. The most common routes for manufacture of braided composites use liquid moulding methods, such as Resin Transfer Moulding (RTM), as described briefly in figure 2.2. The full manufacture first involves, tows made from fibres that are braided into, for instance, a 3D preform. The fabric is then laid up into the mould of the required shape using, possibly, stitching to create an integral preform. Finally, the dry preform is infused with resin and then cured to give the final part which is extracted from the mould.

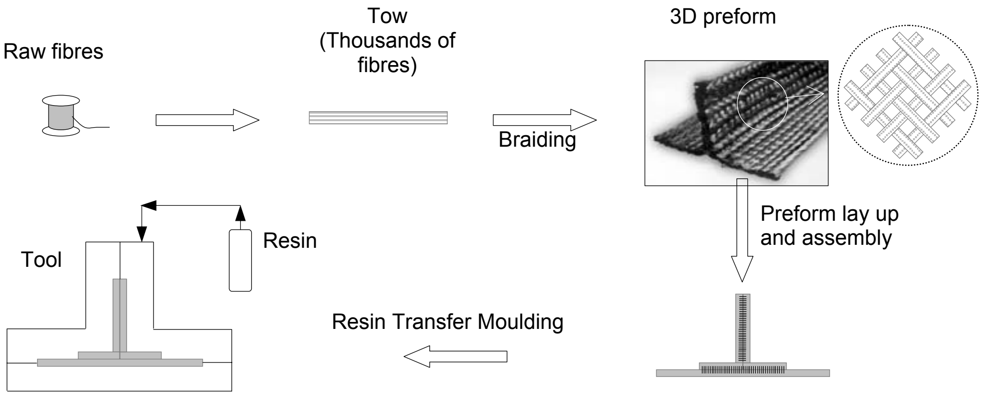

Figure 2.2: Manufacture of braided textile composites (reproduction from [26]).

Recent work has been conducted for modelling the mechanical behaviour of braided composites; however, even if elastic properties can be accurately predicted, failure and post-failure are areas where reliable predictive failure models are still needed. Nevertheless, it should be noted that these difficulties of modelling failure and post-failure are not only encountered in braided composites, but also for the majority of composites.

A recent study, the World Wide Failure Exercise (WWFE) [60] [74] [125], proposed and conducted by Hinton et al., provides an assessment of the status of the current failure models for fibre reinforced polymer composites. Comparison of the models with experiment indicates that failure prediction, even on simple laminates extensively studied for the last 40 years, differs with experimental failure observations [29] [30]. This shows that research on the failure mechanisms of composites is still a challenging area.

In this chapter a brief review on the main fibre types, especially glass and carbon fibres used in this work is presented along with a short section dedicated to the different common fabric types. In addition, a detailed description of braided preform manufacture by the use of a maypole braider is given.

Braid reinforced coupons and beams manufactured for this work used the resin infusion route; therefore, this technique is briefly introduced and described. Also, the epoxy resin system characteristics and general comments on composites manufacture quality issues are mentioned. Also, as discussed earlier, braided composites can offer certain superior mechanical properties to unidirectional composites such as high damage tolerance, high strain to failure and post failure and high specific energy absorption. These characteristics will be presented and discussed in detail.

Finally, a section dedicated to the state-of-the-art of mechanical modelling of braid reinforced composites is presented and special attention is brought to the Ladevèze damage model and the explicit FE code PAM-CRASH^{TM} in which it is implemented.

2.1 Fibres and braided textiles

The following section intends to present, firstly, the manufacturing and mechanical characteristics of glass and carbon fibres. Secondly, the different fabric types are briefly mentioned to introduce 2D biaxial and triaxial braided fabric architecture. Finally, the manufacture of 2D and 3D braided preforms using conventional and non-conventional maypole braider will be described.

2.2.1 Fibre types

In composites materials, fibres are used to reinforce the matrix. A large variety of types exist offering a wide range of mechanical characteristics, such as high strength, high stiffness and relatively low density. In this work, E-glass and STS carbon fibres were investigated; table 2.2 presents their main mechanical and physical properties.

Properties	**E-Glass**		**Carbon STS**	
	[122] [80]	[100]	[92] [80]	[100]
Density [g/c^3]	2.60	2.55-2.60	1.75	1.75
Young's modulus E_{11} [GPa]	82	85	237	240
Transverse modulus E_{22} [GPa]	72	-	22	-
Poisson's ratio ν_{12}	0.22	-	0.3	-
Longitudinal tensile strength [GPa]	2.6	3.44	3.93	4.0
Elongation to failure [%]	3-4	4.8	1.7	1.67
Coefficient of thermal expansion [K^{-1}x10^{-6}]	4.8	-	-0.4	-0.5

Table 2.2: Typical properties of E-glass and STS carbon fibres [92] [100] [122].

2.2.1.1 Carbon fibre

Carbon fibres are generally chosen for high performance applications, such as in the aerospace industry, where high mechanical properties are required. They offer a wide range of stiffness and strength depending upon their processing temperature. However, where low costs are necessary, such as in the automotive industry, low cost carbon fibres, such as STS, will be preferred.

Carbon fibres consist of carbon atoms arranged in hexagonal arrays aligned to the fibre axis. This atomic configuration offers high longitudinal stiffness and strength, but low transverse properties. Manufactured through different heating operations, they are the results of the degradation of an organic precursor such as polyacrylonitrile. The filament diameters are typically in the range of 4µm to 10µm. Thousands of filaments are then combined to form a continuous tow which is used to form textiles and braids. Different tow sizes are available, usually from 1,000 to 24,000 fibres. A surface coating can also be added to improve the fibre to matrix interface, but also to protect and lubricate the fibres during handling and manufacturing.

2.2.1.2 Glass fibre

Glass fibres are obtained from a compound of silica (SiO2) to which metal oxides are added. As shown in figure 2.3, these two constituents are melted together at a temperature of 1500°C. The molten raw materials are then fed into bushings of several hundred holes, from which filaments are drawn and cooled with water before finally being combined as strands and wound on a forming package.

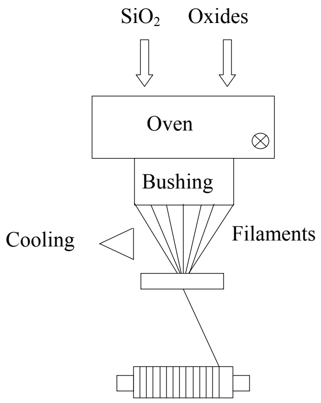

Figure 2.3: Manufacture of glass fibres (reproduction of [122]).

Usually, glass filaments are wider than carbon filaments; their diameters are in the range of 5µm to 24µm. Also, as for carbon fibres, a surface treatment such as an aqueous solution can be applied. Glass fibres are preferably used for low cost applications requiring relatively high tensile strength properties. However, their use is limited due to low stiffness, low fatigue, and poor resistance to environmental conditions. For these reasons, they will be used in low and medium performance composite applications.

2.2.2 Fabric types

2.2.2.1 Generalities and classification

Fabric reinforced composites belong to the class of advanced composites using preforms produced by textile forming techniques. Compared to usual unidirectional laminates, they exhibit higher intra- and inter-laminar strength and damage tolerance, particularly for thick section composites. Also, they offer better shapeability for near net shape manufacturing and can be tailored to match optimum mechanical performances [21].

Prior to preform manufacture yarns, or tows, are manufactured through a linear assemblage of fibres formed into continuous strands. They can be made with single, multiple, or short fibres and also twisted together to form ‘ply tows’ which affect the density of fibre packing and influence stiffness [21].

Fabrics are classified into two main categories; namely, two and three dimensional textile preforms. The division of 2D and 3D is determined by the presence of reinforcing fibres lying in the through thickness direction [26]. Figure 2.4 shows a brief overview and examples of the main fabric categories.

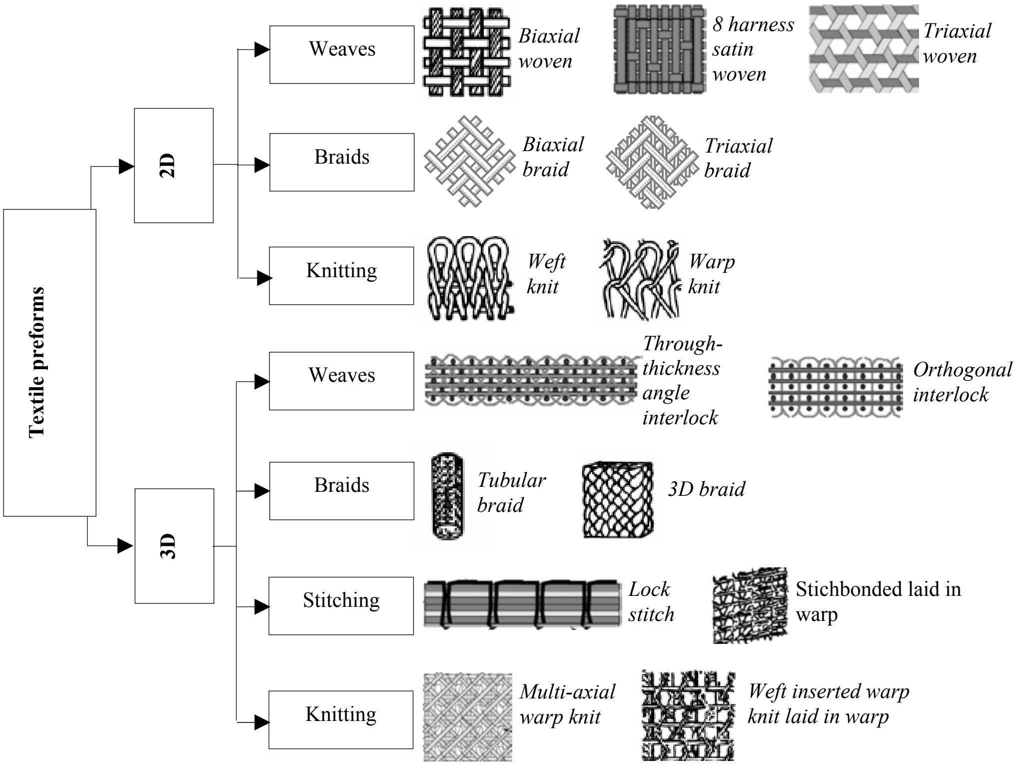

Figure 2.4: Main categories of textiles preforms (adapted from [26] [83]).

2.2.2.2 Braided fabric – Repetitive Unit Cell (RUC) concept and notations

Generally, the architecture of any fabric is defined in term of a Repetitive Unit Cell (RUC) from which the entire textile can be constructed by simple spatial translation. Figure 2.5 (a) presents an example of a so called ‘twill’ weave having intertwined tows at ±θ° fibre angle. The braider tows follow the +θ° and –θ° directions and are braided in a 2x2 pattern, meaning each +θ° tow passes over two –θ° tows and then under two –θ° tows [15]. Axial tows can be introduced to reinforce the fabric and create a triaxial braid as shown in figure 2.5 (b). These axial tows are locked by the braider tows at each cross-over point, thus, remaining straight, so that they can retain much of their unidirectional properties.

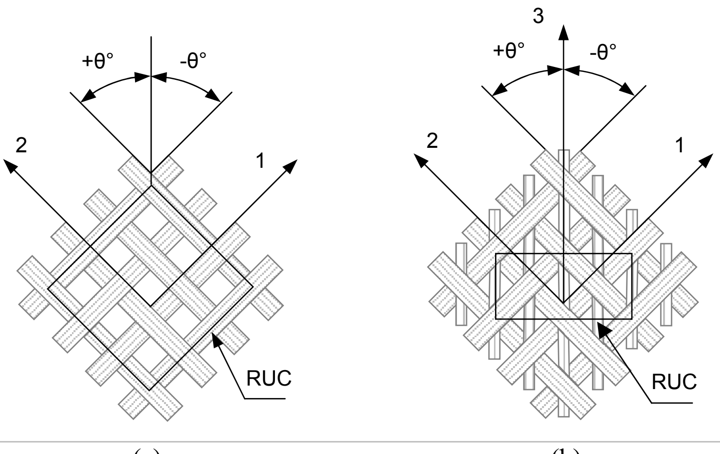

(a) (b)

Figure 2.5: (a) Architecture of a 2D biaxial braided fabric, (b) Architecture of a 2D triaxial braided fabric.

A notation similar to unidirectional can be used to characterise the braided fabric properties such as [0nK/±θ°mK]Y% *Axial*, where n is the axial tow size in K thousands of fibres, m is the braider tow size and Y the percentage of axial tows. For a biaxial braid this notation is simplified to become [±θ°mK] and, in the case of overbraiding where layers are superimposed, the notation can be rewritten such as $[\pm\theta°mK]_{ls}$, where l stands for the number layers and s for symmetry.

This general notation is not appropriate for this work since the damage model used has to be considered at the single ply scale. Hence, a ±θ° single layer of braid corresponds to two distinct unidirectional plies orientated at +θ° and -θ°. For instance, a two layer braid coupon with 45° braid angle is written as $[\pm 45°]_{2S}$.

2.2.2.3 Braided fabric manufacture

In 1964, Douglass proposed the operation of different braiding processes [21] in which a series of tow (or yarn) carriers follow intersecting circular paths in order to intertwine the tows over a mandrel and construct a tubular fabric, figure 2.6 (a) and (b). The braiding technique is highly versatile and offers a wide range of geometric patterns. For instance, varying the transverse speed of the mandrel relative to the tow carrier's rotational speed will affect the orientation of the yarns.

Recently, 3D-Rotary braiding was developed as a new manufacturing process offering the potential for cheap production of continuous three dimensional textile reinforcement in a near net shape, figure 2.6 (c) and (d). Specific advantages include the possibility of producing members which have arbitrary and varying cross-sections and an optimal design of the yarn architecture to meet loading and other design criteria.

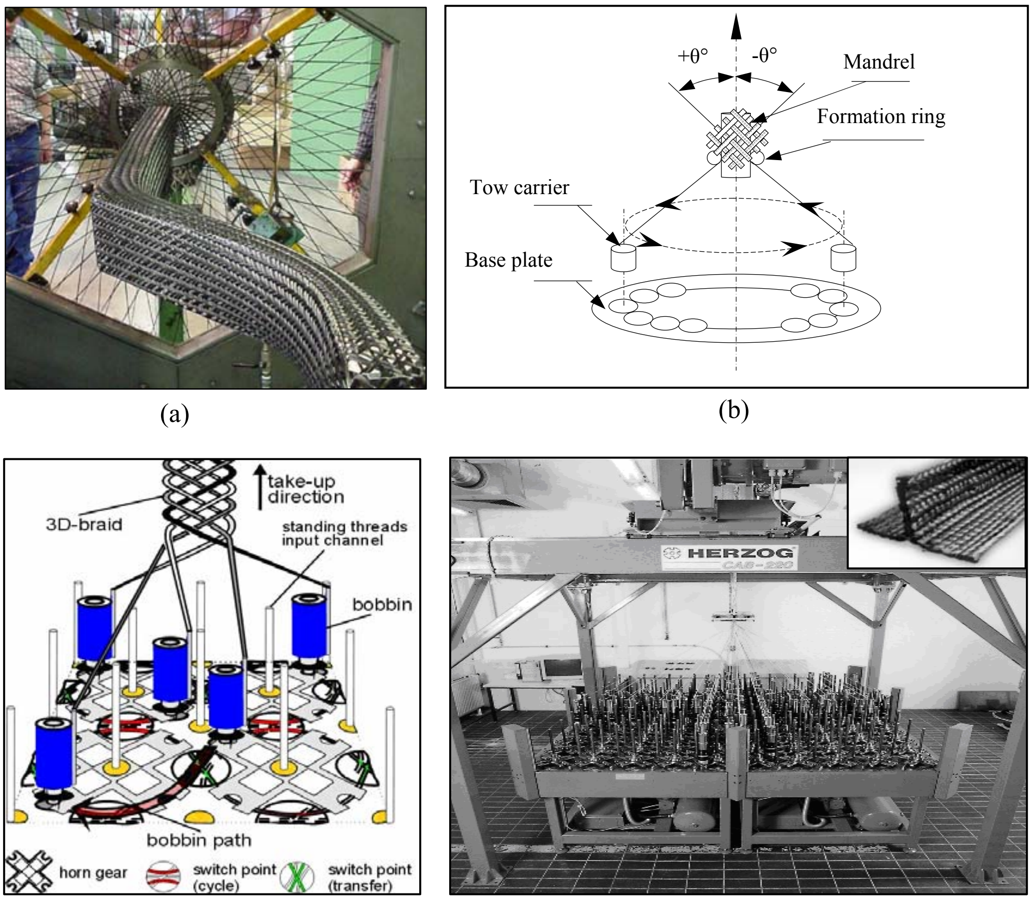

(a) (b)

(c) (d)

Figure 2.6: **(a) Standard automatic braiding system (courtesy of Eurocarbon), (b) Principle for 2D tubular braid manufacturing [26], (c) and (d) Principles and view of the prototype 3D-rotary braiding machine [117].**

In the braiding process fibres are inevitably bent and twisted through their path into guides and pulleys before being placed onto the mandrel. These frictions and tensions create stresses and strains leading to fibre damage degrading their mechanical properties. Tension tests on fibre tows reveals a 20% decrease in tension strength resulting from damage through the braiding process [34].

2.2 Manufacturing of braided composites

A wide range of manufacturing processes is available for braid reinforced composites. The most commonly used is Resin Transfer Moulding (RTM) which allows the manufacturing of net shape parts in closed tooling. The main feature is the injection of the liquid polymer through a dry preform laid in a closed mould. The impregnation quality depends on the combination of pressure at which the resin is injected, temperature, resin viscosity, mould cavity shape and preform properties.

Many others techniques are derived from this manufacturing route, such as the resin infusion process in which the resin flows through the mould and impregnates the fibres due to vacuum applied at the outlet. This particular route will be discussed in more detail in the following section and special attention will be paid to the characteristics of the epoxy resin system used in this work. Also, since mechanical properties are highly dependent on manufacturing, a section dedicated to manufacture quality issues will be presented.

2.2.1 Resin infusion

2.2.1.1 Manufacturing advantages and limitations

Resin infusion is derived from resin transfer moulding and is distinguishable by the way that the pressure gradient is applied to force resin flow through the mould. Indeed, the pressure gradient, in this case, is created by applying vacuum to the outlet port, leaving the inlet port, in which resin is injected, at ambient pressure. The main advantage of this process, compared to RTM, is the absence of large forces when resin is injected under high pressure.

The use of lower pressure also considerably simplifies the mould design allowing the use of a light and low cost mould. This technique reduces the emission of volatile components into the workspace by wetting out and curing the laminate in a closed system. Compared to hand lay-up resin infusion decreases human contact with liquid resin and emissions to the environment [1]. However, the process reveals a strong sensitivity to leakage, leading to air flows into the mould, giving poor preform impregnation or parts with high void content.

2.2.1.2 Basic principles

In this work simple parts, such as flat panels and square cross-section beams have been manufactured using the resin infusion route. In this section the main steps usually followed in this process are described. The first step consists of mould preparation by cleaning it to remove any impurities which could be mixed with the resin. Then a release agent is applied in order to enable better demoulding.

The dry reinforcement can then be positioned into the mould cavity where clamps can be used to hold it in position. A flow medium layer is applied on the top of the reinforcement with a peel ply in between to enable flow medium layer removal after infusion. The flow medium layer allows guiding the resin and helps to prevent partial impregnation.

The resin inlet/outlet pipes are integrated into the mould by using sealant tape on the flanges of the mould. Their positioning and number depends entirely on the mould design and the complexity of the part to be impregnated. When the mould is sealed using a vacuum bag, a vacuum is applied at the outlet as shown in figure 2.7.

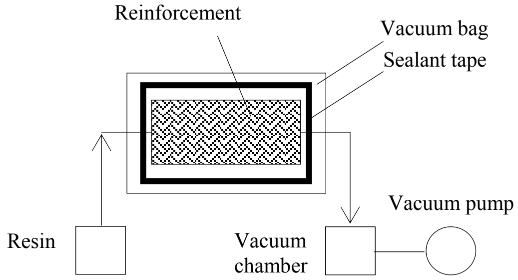

Figure 2.7: Schematic description of the resin infusion process.

To prevent leakage, vacuum and leak rate are measured. A vacuum of 5mbar to 10mbar and a leak rate of 5mbar per minute are usually considered acceptable [7]. After achieving the desired infusion pressure, resin components can be mixed carefully to avoid air entrapment in the mix. Prior to infusion, the resin is degassed in a vacuum chamber to remove air bubbles dragged in the resin during mixing. At this stage resin is infused just by connecting inlet pipe to the resin bucket as shown in figure 2.7. When infusion is finished the inlet is closed in order to expel excess resin in the mould cavity. Finally, after complete excess resin is removed, the outlet is closed and curing at the required temperature can start.

2.2.2 Epoxy resin system characteristics

2.2.2.1 Resin choice upon component performance

The most important parameters determining the choice of matrix is the temperature at which the composite will be used in service, but also the mechanical properties required. Composites exposed to temperatures between 100°C and 200°C usually have a polymer matrix. Thermoset polymer matrices are often preferred for their higher heat resistance, compared to thermoplastics, due to a rigid network of bonded polymers chains [21].

The thermoset epoxy resin is the most developed group and widely used in composites. Broadly, there are two types of epoxies, those curing at low temperature (120°C) which are used in components exposed to low or moderate temperature variations and those cured at higher temperature (175°C) which are used in high performance components exposed to high temperature and moisture variation [28].

2.2.2.2 Epoxy resin general properties

Epoxy resins are a high strength polymer with low viscosity which allows good wetting of the fibres. The ability to infuse under low pressure helps to prevent fibre misalignment during processing. Also, these resins exhibit low shrink rate reducing the tendency of internal stresses and especially large shear stresses of the bond between epoxy and fibres after curing [80]. They offer good adhesion to the substrate which leads to high resistance at the fibre/matrix interface and, consequently, high mechanical properties. However, their main drawback is slow processing, compared to other resin types such as polyester, due to their comparatively higher viscosity and longer gel times [122].

2.2.2.3 Resin/Hardener systems

Resin systems are usually composed of two parts; namely resin and hardener, or cross-link agent, which initiates the curing reaction. The choice of resin/hardener system depends on the application, the process selected and the properties required. For difficult large parts, a slow hardener will be preferred in order to allow the resin to fully impregnate the reinforcement before gel initiation. For a short processing time medium, or fast hardeners, are preferable to reduce gel and cure time.

2.2.3 Composites manufacture quality issues

2.2.3.1 Voids effect on composites mechanical performance

The resin infusion process route is able to fabricate high performance composite structures in low to medium series production. Improved resin curing process and control of relevant processing parameters, such as temperature and resin flow, are key issues to enhance product quality and process repeatability. If these parameters are not fully controlled void formation can occur leading to a dramatic reduction in mechanical properties, especially strength, but also to poor surface finish.

For instance, Judd and Wright [72] demonstrated that inter-laminar shear strength decreases by 7% for each 1% of void content up to a total of 4%. Also, Ghoirse [47] reported flexural and inter-laminar strengths are reduced by 10% for each 1% of voids. Harper et al. [54] showed that matrix dominated moduli E_{22} and G_{12} are also significantly dependant on void contents, contrary to longitudinal modulus E_{11} and Poisson ratio ν_{12} which are not affected. Tang et al. [130] found that above a certain void content threshold, compressive and shear strength and moduli all decrease.

2.2.3.2 Voids main formation mechanisms

The main driving forces for void formation in the resin infusion process are related to:

(a) Partial evaporation of mould release agent into the preform, volatilisation of dissolved gases in the resin and initial air bubble content in the resin.

Evaporation of mould release agent results in the formation of bubbles in the preform surface leading to macro-voids. In order to limit this, the mould release agent needs to be applied to the mould surface avoiding unnecessary layers.

Voids can also form from the gaseous components coming out of the resin during the vacuum injection process. Consequently, the resin has to be degassed to reduce the risk of resin outgassing. Wood [140] measured the equilibrium gas concentration of nitrogen, entrapped in the resin, at atmospheric pressure to be approximately 1.7% by volume, which expands 50 times if brought out of solution under a pressure of 20 mbar; this corresponds to the infusion pressure. Furthermore, degassing increases the capability to dissolve bubbles in the resin formed during flow.

(b) Differential resin flow velocity leading to mechanical air entrapment.

Resin infiltration through the fibres is controlled by the preform permeability which includes the characteristics of fibre network (fibre dimensions and arrangement). Therefore, permeability is one of the most critical parameters in resin infusion allowing control of fibre impregnation, complete fibre wetting and thereby ensuring high quality production [6].

Mechanical entrapment arises from the presence of alternative flow paths caused by heterogeneous preform permeability. This leads either to viscous flow through the opening between fibre bundles, or capillary flow where resin penetrates into fibre bundles [53], as illustrated in figure 2.8. Differences in permeability result in either long cylindrical bubbles inside fibre bundles, or large spherical bubbles in the space between fibre bundles [19].

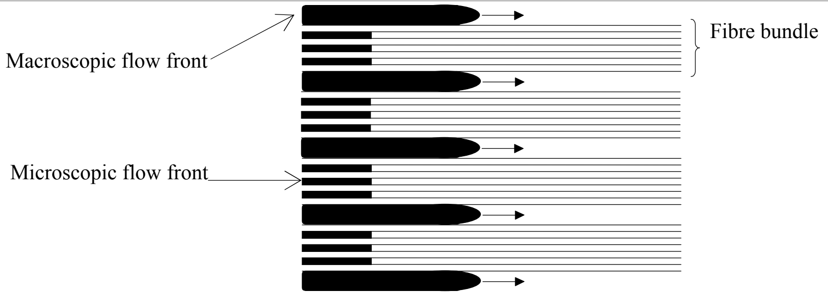

Figure 2.8: Macroscopic and microscopic flows front [124].

Also, void locations depend upon resin velocity; for instance, in the case of a high resin velocity voids will form within tows because the flow in the channel is faster than in the tow, figure 2.9 (a). However, for a low resin velocity, the capillary flow will dominate within tows and hence voids may form in the channels between tows, figure 2.9 (b).

(a) high resin velocity (b) low resin velocity

Figure 2.9: Voids formation relative to resin flow velocity [76].

(c) Race tracking and mechanical air entrapment during mould filling.

Race tracking can occur in high permeability flow channels formed at the edges of two sections of a preform, the edges of mould guides, or the preform mould interfaces within the mould. Figure 2.10 shows the principal resin flow, in an air gap, between preform and guide, representing a region of high permeability; even if the secondary flow impregnates the preform, impregnation is partial and will lead to large dry areas.

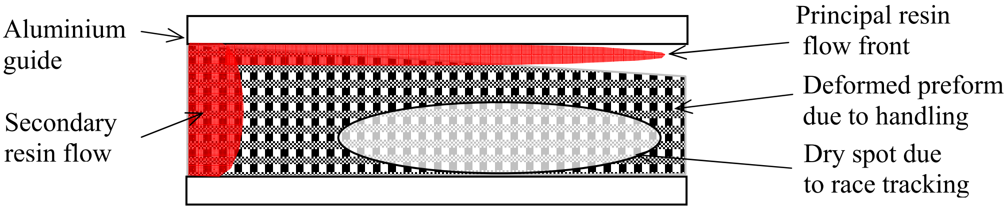

Figure 2.10: Race tracking leading to voids or poor impregnation.

Race tracking is difficult to avoid as it requires a perfect set up. However, it can be minimised by using a high viscosity resin achieved with a low temperature; a slow resin flow is then obtained and the discrepancy between principal and secondary flows is reduced. Low temperature is not only used to obtain low macroscopic flow, but also to limit air bubble expansion. From experience and referring to the work of Lundström [97], the optimal temperature for infusion used for this work was around 35°C.

Finally, air can be mechanically entrapped within the mould due to leakage, for instance, a punctured vacuum bag or at the pipe connections.

The different sources of void creation can be classified and summarised as a diagram, presented in figure 2.11.

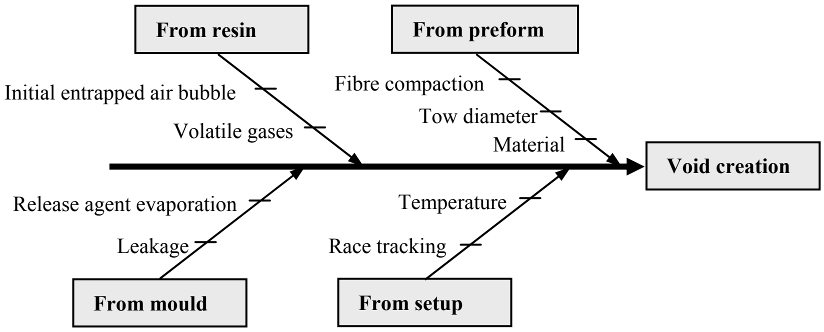

Figure 2.11: Main causes leading to void formation.

2.3 Mechanical characteristics of braid reinforced composites

2.3.1 General characteristics

2.3.1.1 Braided composites advantages over conventional tape laminates

The ease and cost of manufacturing are generally the main factors for which textiles are chosen instead of conventional tape laminates. Their cost effectiveness directly depends on the best choice of technology (2D/3D braiding) used for the particular application; indeed, parts can be automatically manufactured to near net shape reducing intermediate steps.

Braid reinforced composites exhibit a reduction in in-plane stiffness and strength properties compared to equivalent unidirectional laminates due to undulation of the fibre paths [127]. However, they exhibit an improved damage resistance and also have better through-the-thickness and inter-laminar (for 2-D braided composites) strength [142] [143].

Unidirectional composites are sensitive to delamination due to a lack of through thickness reinforcement. For textile, and in particular braided composites, this superior inter-laminar strength is the product of tow waviness in the thickness direction and nesting of the braided layers that occurs during manufacture. Both of which also contribute to excellent energy absorbing characteristics [55].

2.3.1.2 Mechanical properties consistency

Braided composites mechanical properties are highly dependent on the manufacturing quality; indeed, a poorly manufactured preform will present a significant variation in tow spacing which will subsequently influence volume fraction and mechanical properties. Furthermore, poor handling of the preform when inserted into the mould can aggravate the fibre architecture and mechanical properties; for instance, laying over a curved surface can spread and distort fibres. Therefore, maintaining accurate positioning of fibre tows during manufacture is the key to good structural and mechanical consistency.

2.3.2 Mechanical characteristics

2.3.2.1 Stiffness and in-plane strength

In braids, tows passing under and over one another create a waviness which can be eventually reduced but not eliminated by using a satin weave. Comparison with an equivalent tape laminate shows that a braid in-plane stiffness is generally lower and this reduction can be determined using a corrective factor [26],

$$\eta = \left\{ 1 + 2\left(\frac{\pi d}{\lambda} \right)^2 \left[\frac{E_x}{G_{xy}} - 2\left(1 + \upsilon_{xy}\right) \right] \right\}^{-1}, \qquad (2\text{-}1)$$

where λ, d, E_x, G_{xy} and ν_{xy} are wavelength, amplitude, axial modulus, shear modulus and Poisson's ratio respectively.

Tensile and compressive strength are also generally lower for braided composites than tape laminates. This is explained by the tow waviness generating an off-axis local stress and also by fibre damage created during the braiding operation. Therefore, strength for a 2D braid can be related to its architecture parameters such as degree of waviness; tow size, tow spacing and RUC size [26].

2.3.2.2 Impact resistant and high energy absorption

Traditionally metals are used in many applications for their good energy absorption; however, the design often tends to be heavy. Linked to a demand for lightweight and fuel efficiency in vehicles there is a move toward the use of composite components. Properly designed composites can absorb a significantly greater amount of energy per unit mass than metals [16] [35] [64] [123]. Metals tend to absorb energy by local plastic deformation; whereas composites exhibit more complex mechanisms.

Most composite materials are brittle and absorb energy via a combination of fracture mechanisms such as matrix cracking, delamination and fibre breakage [15]. Extensive research has been conducted on the energy absorption of tubular composite material structures loaded under axial compression, figure 2.12.

Figure 2.12: A braided tube having a ±45° braid angle after axial compression.

A trigger can be used to initiate progressive crushing in the tube in order to maintain a constant load and energy absorption. The amount of energy absorbed depends upon different parameters such as the fibre and matrix types, fibre angle and percentage distribution of hoop and axial reinforcements.

As mentioned previously, due to tow waviness and interlocking, braid reinforced composites have higher damage tolerance compared to laminated 2D composites. Many possible designs can be realised with braided composites; the choice on the braid parameters, such as fibre architecture, influences greatly component mechanical properties or failure mode. For this reason modelling their crushing behaviour is extremely complex.

Usually used as shock absorbers under axial loading, only little work has been done on the transverse loading [56] [57]. Due to their capability for high deformation, they also have the potential to be used as side impact absorbers such as for car bumper beam, figure 2.13.

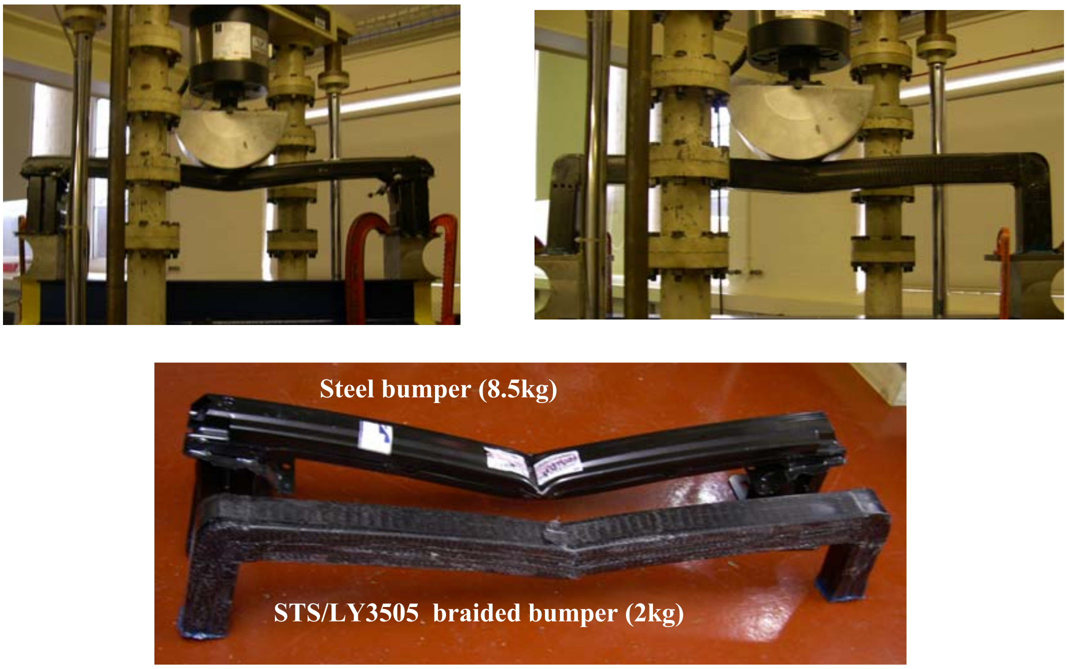

Figure 2.13: Braid reinforced composites car bumper beam.

Recent work sponsored by EPSRC at Cranfield University has shown that a braid reinforced composite could outperform usual steel car front bumper beam in terms of specific strength. Results obtained in preliminary study on a STS carbon braid bumper gave 25% lower strength; however, the weight was substantially reduced. This would offer a considerable weight saving and energy absorption advantage by using an appropriate lay-up and resin system.

Braid reinforced composites can absorb significant specific energy under tensile loading [118]; for instance, figure 2.14 compares a $[\pm 45^\circ]_{2S}$ biaxial braid reinforced composite (67.2x1.6mm) and an automotive grade Aluminium 6014/T6 coupon (65.0x1.7mm) loaded to failure. Despite the lower ultimate strength of the composite the ability of the fabric architecture to reorientate enables large strains and high energy levels to be absorbed over a much greater ‘non-local’ necking zone; figure 2.14. In terms of specific energy absorption the 220 mm long braided composite achieves 9.16J/g compared to 4.16J/g for the Aluminium coupon. This superior performance could be advantageous in applications such as automotive side intrusion where large amounts of energy must be absorbed.

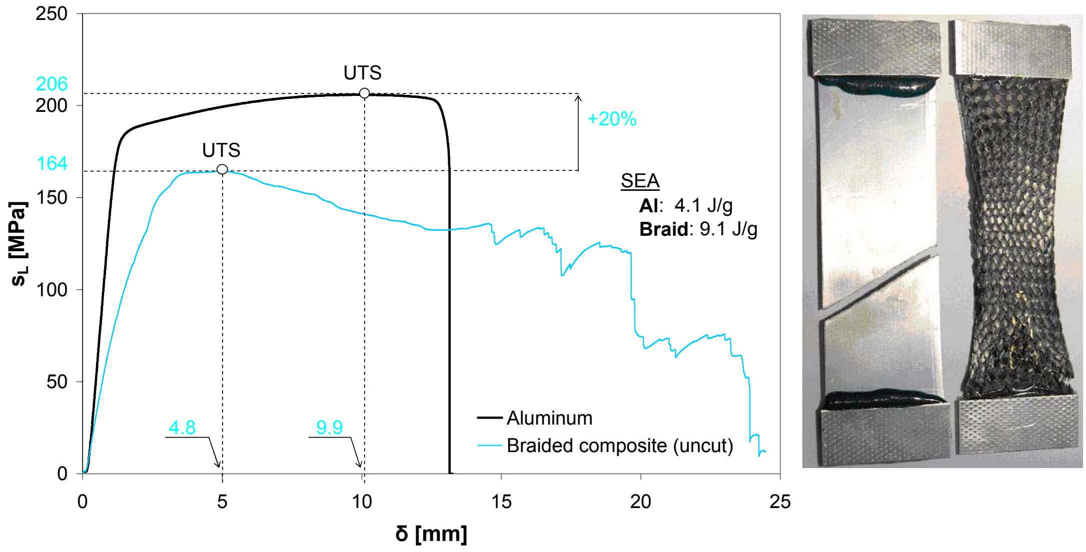

Figure 2.14: Engineering stress versus displacement for a bi-axial braided composite and aluminium tensile coupon (details on materials can be found in [118]).

2.3.2.3 High strain material

Mechanical behaviour of 2D biaxial braid reinforced composites can be compared, in terms of kinematics, to a dry braided fabric. Indeed, when a dry braid is pulled axially the individual tows of the braid scissor and the width of the coupon decreases [57].

Figure 2.15 (a) illustrates clearly that the dry fabric carries minimal load until the tow locking angle. When this threshold is reached, tows can no longer scissor and are packed and aligned in the axial direction. The energy absorbed (work of deformation) by the dry fabric is negligible compared to the one with matrix. However tow scissoring can be kinematically modelled in the same way. This extensive deformation exhibited by braided composite is directly the result of tow scissoring.

Post failure microscopic analysis of braids has revealed that microcracking between tow is also linked with microcracking in between tow's fibres [57]. This means that tow scissoring describes the relative motion of the fibres. The kinematics relationship is based on a simple 'trellis' where each side corresponds to a single inextensible fibre as depicted in figure 2.15 (b).

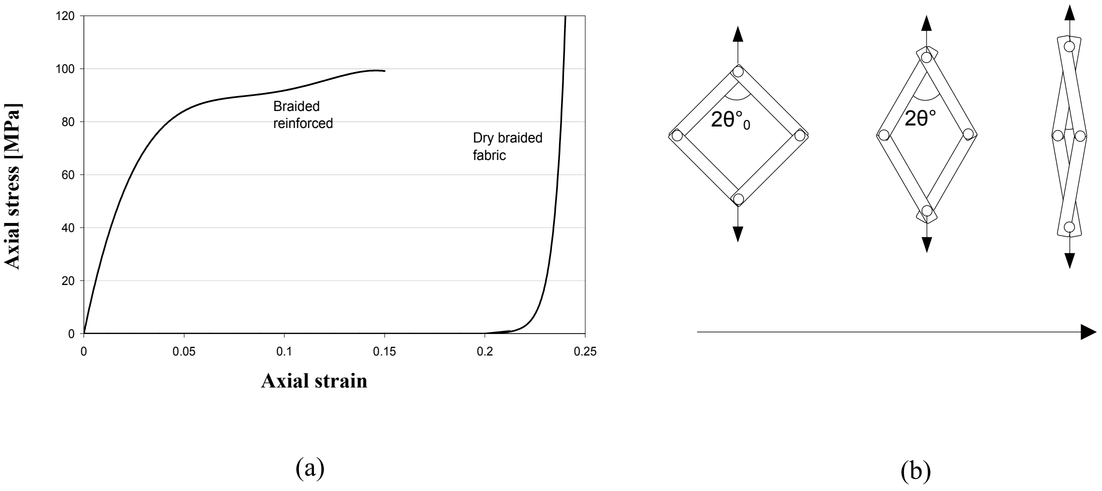

(a)

(b)

Figure 2.15: Braid kinematics, (a) Matrix effect on tensile behaviour of a braided tube (reproduction from [56]), (b) braid tow scissoring schematic.

As illustrated above, the fibre orientation will start from an initial braid angle to reach the lock up angle which is dependent on the braid maximum fibre compaction rate. The fibre angle variation Δθ can be determined using longitudinal and transverse strains as follows [58],

$$\Delta\theta = ArcTan\left[\left(\frac{1+\varepsilon_y}{1+\varepsilon_x}\right)\tan\theta_0\right] \tag{2-2}$$

where ε_x, ε_y , θ are longitudinal strain, transverse strain and braid angle respectively.

2.3.3 Failure mechanisms

2D composite laminates generally have three main intra-laminar failure modes; namely, fibre failure, matrix micro-cracking and fibre/matrix debonding; and an additional inter-laminar (inter-ply) delamination mode. These failure modes for a single unidirectional ply and a stack of plies are detailed and illustrated in figure 2.16.

Intra-laminar failure

Fibre failure	**Matrix failure**		
Tension/compression	Transverse tension/compression	In-plane shear	Out-of plane shear
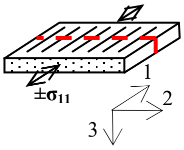	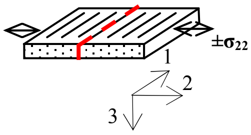	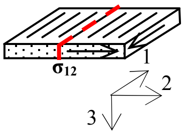	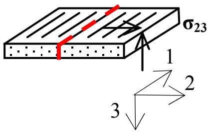
Examples			
Fibre tensile failure	Fibre compressive failure – kink band	Matrix micro-cracking under transverse tension	Fibre/matrix debonding under shearing
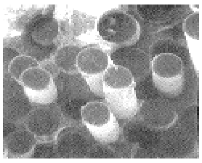	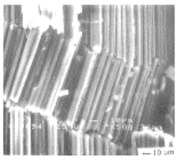	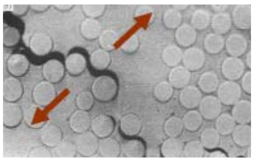	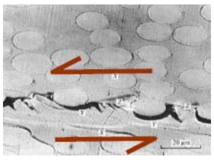

Inter-laminar failure

Delamination Mode I	**Delamination Mode II**	**Delamination Mode III**
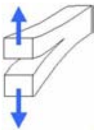	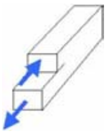	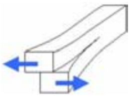
Examples		
Delamination Mode I	*Mixed mode bending*	*Ends notched flexural*
		

Figure 2.16: Failure modes for a single unidirectional ply [28] [65]

It is proposed in the following to describe the main failure mechanisms relative to 2D braided composites, such as tensile, compressive and shear mechanism. Inter-ply delamination is not presented since it was not considered in this work.

2.3.3.1 Tensile mechanism

Usually for a unidirectional laminate under tensile loading in the fibre direction, most of the load is carried by the fibres which results in a linear elastic failure mode. For fabrics, tow waviness creates fluctuations in the stiffness of tows which results in uneven load distribution and a knock down in strength [26]. Failure usually comprises first of tows straightening inducing matrix plasticity, which propagates along the tow. Tow straightening ceases when the tow is either perfectly straight and reaches a critical strain, or when the loading cannot be sustained.

Cox et al. [26] measured that tow failure under tensile loading in a braid is usually 30-50% lower than would be expected from the pristine fibres, or comparable unidirectional tape laminates. This strength reduction can be due to:

- tow damage during textile processing,
- tow waviness which creates stiffness fluctuations within a tow resulting in uneven load distribution,
- misaligned tows,
- additional lateral loads imposed by the transverse interlaced tows.

2.3.3.2 Compression mechanism

Under compression loading fabric composites, such as braided composites, generally fail by kink band formation and delamination followed by Euler buckling [26]. The kink band, figure 2.17, is the result of local shear instabilities where fibres can rotate and break leading to complete loss in axial strength.

In plain weave braided composites of high tow waviness the load bearing axial tows undergo large misalignments with respect of the applied loading axis. In order to improve braids compressive strength, fibre misalignment with respect to the loading axis has to be minimised by reducing tow waviness. Also, in contrast to tensile strength, fibre defects due to braid manufacture has a negligible effect on compressive strength [26].

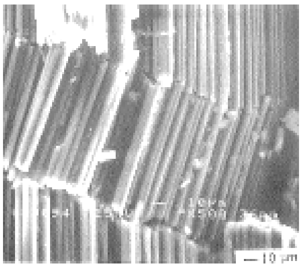

Figure 2.17: Kink band formation in a laminate [28].

2.3.3.3 Shear failure mechanism

Shear failure in fibre composite materials starts with the occurrence of arrays of elliptic microcracks aligned between pairs of fibres. These cracks grow and can coalesce to form a macro-crack amidst considerable plasticity which probably involves crazing and fibril tearing [26], figure 2.18 (a).

In a 2D biaxial braided composite, micro-cracks coalescence is combined with fibre scissoring which change crack shape in respect of the braid angle. For instance, figure 2.18 (b) presents three scanning electron microscope (SEM) images of the state of the matrix within the necking region of a braided tube under tensile loading.

The matrix between the fibres breaks up into arrays of parallel micro-cracks. Arrays of tensile micro-cracks form approximately perpendicular to the loading direction. Under loading, the fibres scissor and the beam-like micro-cracks rotate until eventually they align perpendicular to the fibres [56]. At high strains, the damaged matrix divides into fragments. This microscopic behaviour can be measured using a ±45° specimen under uniaxial tensile loading.

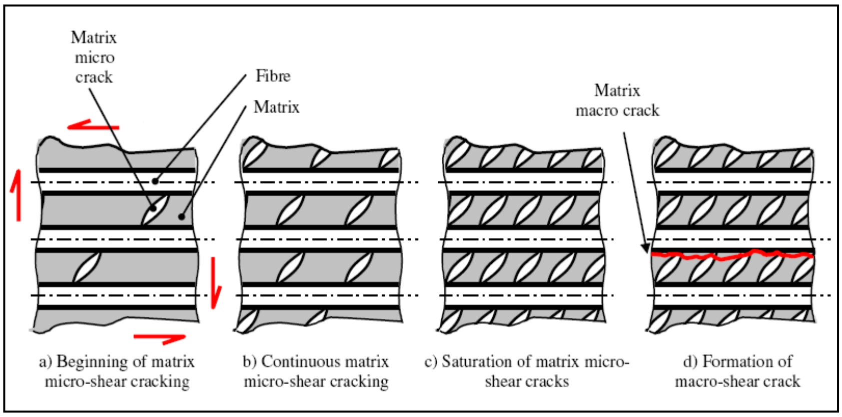

(a)

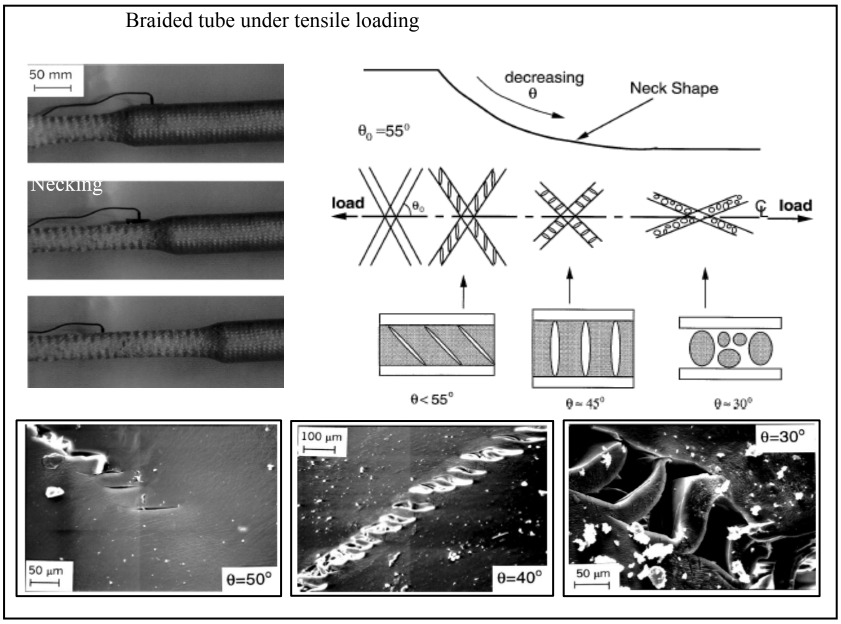

(b)

Figure 2.18: Shear failure mechanism, (a) intra-laminar micro-cracking and macro-cracking development under shear loading [50], (b) SEM images of the crack state within the necking of a braided tube [56].

2.4 State-of-the-art of mechanical modelling of braid reinforced composites

As mentioned in section 2.3.3, braid reinforced composites exhibit different types of failure mechanism, such as fibre/matrix interface debonding, matrix micro-cracking, fibre breakage and delamination. Even though stiffness (before damage initiation) can be readily represented using existing models, it is much a more challenging task to predict failure and post-failure behaviour.

The following presents the different models used to predict elastic and non-linear elastic behaviour of braid reinforced composites. For failure prediction, two well known macromechanical models are presented and discussed. Finally, an alternative failure model proposed by P. Ladevèze based on damage mechanics is introduced and explained. This model has been implemented in an explicit FE code which is also presented in this section.

2.4.1 Elastic and non-linear elastic behaviour modelling of braid reinforced composites

Numerous models for structural analysis of woven/braided composites are available in literature. They can be broadly classified into two main categories: numerical and analytical methods.

2.4.1.1 Numerical methods based on finite element analysis

In the first category, the general FE analysis method is used for structural analysis of the fabric and enables the modelling of elastic and inelastic properties of fabric composites. The material properties are assumed to be constant within each material (fabric and resin). This is valid for most materials having a micro-structural scale much smaller than the element size. However, this becomes invalid for fabrics which exhibit a very coarse ‘micro-structure’.

In order to use the finite element method to solve this problem, finite elements have to be defined such that the material properties vary smoothly in each finite element, figure 2.19. This approach leads to large numbers of elements and the modelling of large structures rapidly becomes impractical.

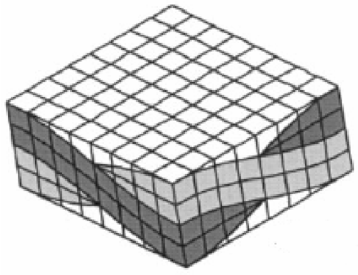

Figure 2.19: Modelling of the fibre tows and matrix using 384 20-node hexahedron elements [137].

From this problem emerged a different approach based on material homogenisation to treat heterogeneous fabric materials. In the following, state-of-the-art fabric failure models using FE analysis are presented. For conciseness, only the main modelling methods are presented.

(a) Sub-cells discretisation approach

Foye [40] studied material properties of fabric reinforced composites using sub-cell analysis. In this method, the fibre and matrix are each considered as a homogeneous sub-structuring volume of the material. This analysis is based on a RUC approach in which one unit cell is surrounded by identical unit cells as shown in figure 2.20 (a). Each unit cell is subdivided into similar small sub-cells which are hexahedra brick elements.

The main drawback of this Unit Cell Continuum Mode (UCCM) is a mathematical instability in the main global stiffness matrix due to the existence of extremely different stiffness values of each constitutive element (fibre and matrix) [48]. This leads to inaccurate predictions of elastic properties.

In order to overcome this problem, Gowayed et al. coupled to the UCCM method an analytical model of the Fabric Geometry Model (FGM), defined later in this section, as shown in figure 2.20 (b). The FGM is invoked in the UCCM to predict sub-element mechanical properties and formulate a homogeneous global stiffness matrix.

This combination of models was used to predict the elastic properties of complex textile composite structures. Also, it has been demonstrated that treatment of material non-elastic behaviour and development of cracks and failure may be foreseen using this model [27].

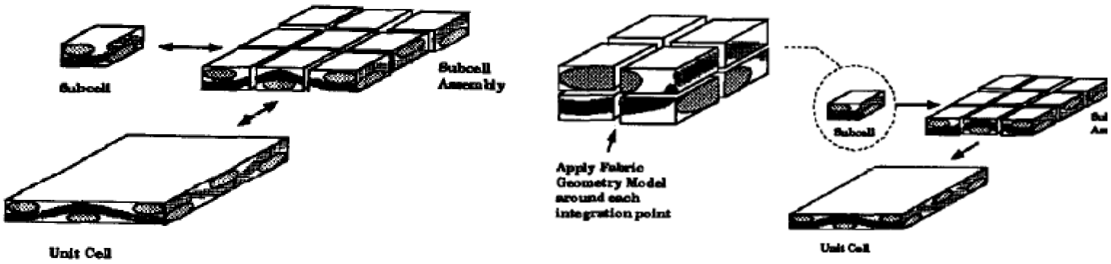

(a) (b)

Figure 2.20: Sub-cell approach, (a) finite element divisions for a unit cell, (b) micro-level homogenisation for hexahedra brick elements [48].

(b) Macro-element discretisation

This modelling approach, proposed by Woo and Whitcomb [138], defines a 'macro' finite element which accounts for details of the microstructure within an element. This macro-element is characterised by several sub-domains as shown in figure 2.21. Discontinuities can be present inside the macro-element; however, mechanical properties of the sub-domains are homogeneous.

The macro-element takes into account the composite micro-geometry, fibre and matrix mechanical properties; however, there is no accurate correspondence with the spatial position of the fabric. Nevertheless, the model gives a good prediction of fabric global stiffness and deformation using a lower number of elements for material discretisation.

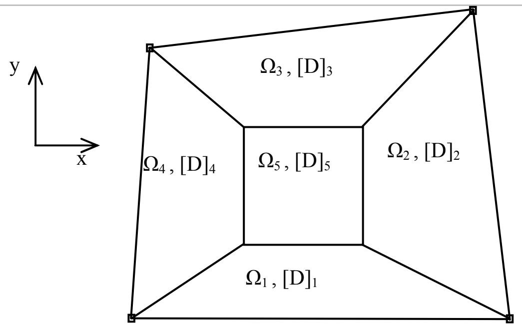

Figure 2.21: Classical 4-node macro-element [138].

(c) Global/Local analysis

Woo and Whitcomb [133] used the previous approach to develop an iterative global/local finite element analysis. It was originally used to study stress distribution in a small portion of the structure in great details. In this method a coarse mesh is used to obtain overall response of the structure and refined local meshes are then used in the region of interest where rapid stress gradients may occur.

For a fabric, a crude global mesh with homogenised material properties is defined, figure 2.22 (a). A typical finite element mesh is used to create a four node macro element, figure 2.22 (b), which is introduced in the global mesh. After obtaining the global response, the global/local boundary displacements are applied to the local mesh as boundary conditions and the local problem is solved.

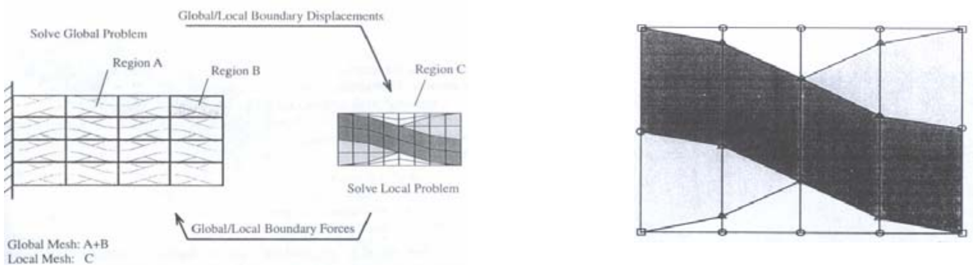

(a) (b)

Figure 2.22: Global/local analysis, (a) schematic of iterative global/local analysis [136], (b) a typical sub-mesh for a macro element [136].

To avoid equilibrium violation at the global/local boundary, caused by mesh refinement in the local region, a force criterion is introduced which is validated by an iterative method until convergence [134] [135] [136] [137] [139]. The reliability of this method depends on careful choice of mesh discretisation at the different levels [27].

(d) Semi-microscopic approach

This approach is based on an analytical model using the numerical analysis [41] [42]. As shown in figure 2.23 (a) fibre bundles and resin in a braided flat coupon are expressed by beam elements. The fibre has a rectangular shape and the resin at the surface and between crossing fibres is differentiated. This model is then integrated into a finite element mesh where thick lines express the fibre and fine lines the resin, figure

2.23 (b). This approach is used to analyse the evolution of cracks inside the material and calculate ultimate strength [27].

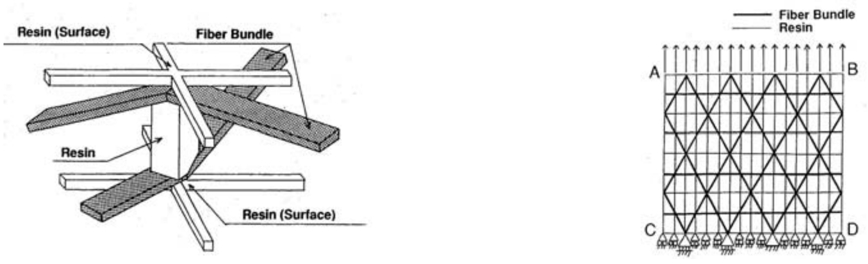

(a) (b)

Figure 2.23: Semi-microscopic approach (a) analytical model at cross over point between fibres [42], (b) finite element mesh of triaxial braided flat coupon [42].

Detailed 3D finite element analysis of textile composites is highly CPU demanding even for a single unit cell. In engineering applications the mechanical properties obtained from finite element analysis of a single unit cell are used as input data for the modelling of a more complex part. When the part is in the plastic region, the input data is updated and the overall stress distribution re-calculated.

This approach using a unit cell sub-model leads to tremendous run-time and memory requirements for simulation of large structures [63]. In order to overcome the excessive CPU requirement of FE methods, several authors have proposed analytical approaches.

2.4.1.2 Analytical methods based on micromechanics

Analytical micromechanics analysis is based on the closed form solution of mathematical models, applied to very simplified single cells which allow a good global analysis to be performed [27]. Mainly based on Classical Laminate Theory (CLT), these models tend to simplify, or represent in detail, the fabric architecture. Popular models include the mosaic model, fibre undulation and bridging models introduced by Yshikawa and Chou as depicted in figure 2.24 [21] [67] [68].

In the mosaic model, figure 2.24 (a), tow undulations are neglected and the RUC comprises an assemblage of cross-ply laminates. For the fibre undulation model, figure 2.24 (b), the undulation of the yarn is represented for the fill yarn direction but neglected for the warp yarn. The bridging model, figure 2.24 (c), extends the undulation model to a satin weave composite by separately modelling the straight portions of the yarns only [107]. Initially the model was developed to predict thermoelastic behaviour of woven composites but, more recently the approach has been improved to represent also their inelastic behaviour [69].

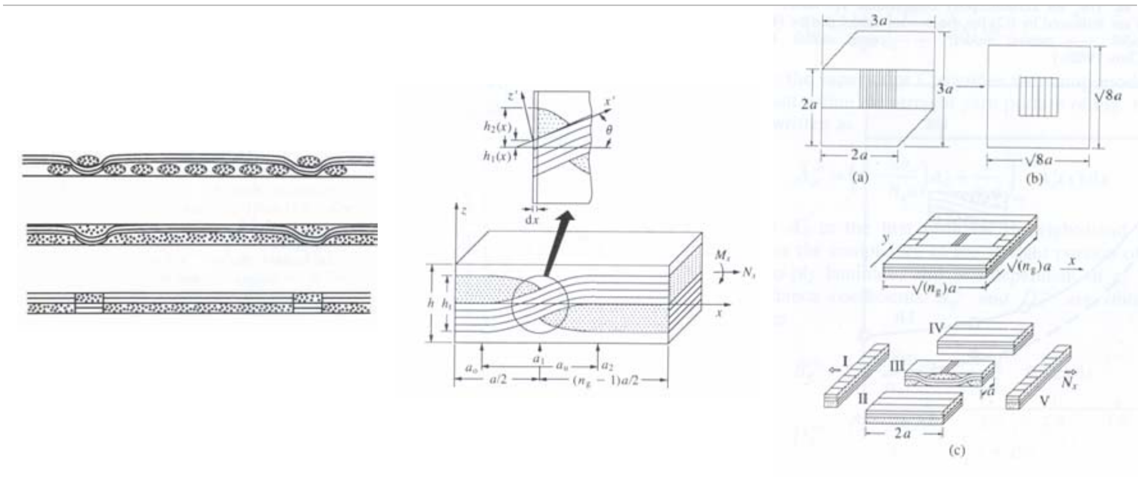

(a) (b) (c)

Figure 2.24: Classical analytical models for fabric composites based on CLT [21].

(a) Naik's model

Naik proposed a micromechanics model analysis that discretely modelled the tow architecture within a RUC of the braid [106] [107] [108] [109]. It has been developed for predicting overall, three dimensional, thermal and mechanical properties based on an iso-strain assumption [22]. The braid tows and matrix are divided into slices using parallel planes perpendicular to the fabric plane and along the fibre-tow direction, as shown in figure 2.25.

The slice stiffnesses are defined in a local coordinate system using micromechanical formulae for unidirectional laminate. These are then transformed to the global system (X, Y) and summated to obtain the overall stiffness of the RUC.

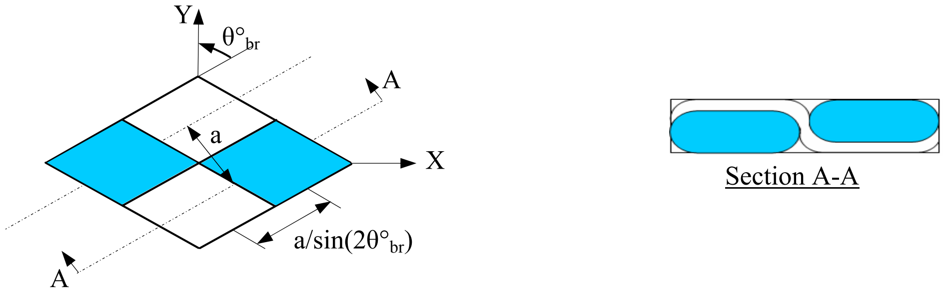

Figure 2.25: The RUC geometry for a 2-D braided composite (reproduction of [107]).

This technique gives a good approximation for the overall mechanical behaviour of the RUC and allowed accurate analysis of the influence of undulation and orientation of the tow to give the overall three dimensional effective properties. Also, further improvements have been done to determine material non-linearity due to shear.

(b) The fabric geometry model

The fabric geometry model (FGM) [75] is another analytical model widely used to predict fabric characteristics. This model considers the fibres and matrix as a group of rectilinear bars with various spatial orientations, figure 2.26.

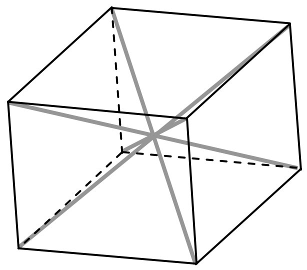

Figure 2.26: Representative volume element for a 3D braided composite [75].

Once the whole group of bars is characterised, the composite global stiffness matrix is obtained by adding the contributions of single bars having transverse isotropy. However, this simplified model of the representative volume element neglects crimp of the yarn.

2.4.2 Failure prediction based on macromechanical strength theories

Both numerical and analytical approaches can enable characterisation of the braid architecture and used to determine stiffness and non-linear behaviour. However, ultimate strength and post failure are characteristics that micromechanics approaches have difficulty to predict.

Most of the failure criteria used today for unidirectional and fabric reinforced composites are based on macro-mechanical strength theories. For conciseness, only two well known failure criteria are presented in the following. The reader is referred to the 'World Wide Failure Exercise (WWFE)' conducted by Hinton et al. [60] [74] for an exhaustive list of failure models and their comparison for unidirectional laminate lay-ups composites

2.4.2.1 Maximum stress and maximum strain

The maximum stress and maximum strain criteria are related to the Maximum Normal stress theory proposed by Rankine and the Maximum Shearing stress theory proposed by Tresca, both of which were applied for isotropic materials [80]. In this theory, failure is expected to occur when any state of stress in the local reference (σ_1, σ_2, τ_{12}) system exceeds the corresponding allowable limits (σ_{1u}, σ_{2u}, τ_{12u}) determined from a test program.

This criterion is written as follows,

$$f = \max\left(\left|\frac{\sigma_1}{X_\sigma}\right|, \left|\frac{\sigma_2}{X_\sigma}\right|, \left|\frac{\tau_{21}}{S_\sigma}\right|\right) \tag{2-3}$$

$$\begin{cases} if\ f < 1, & no\ failure \\ if\ f \geq 1, & failure \end{cases}$$

Where,

$$\begin{cases} X_\sigma = \sigma_{1u}^t & if \quad \sigma_1 \geq 0 \\ X_\sigma = \sigma_{1u}^c & if \quad \sigma_1 < 0 \end{cases} \qquad \begin{cases} X_\sigma = \sigma_{2u}^t & if \quad \sigma_2 \geq 0 \\ X_\sigma = \sigma_{2u}^c & if \quad \sigma_2 < 0 \end{cases} \tag{2-4}$$

$$S_\sigma = \tau_{12u}$$

The indices t and c refer respectively to tension and compression. The maximum strain criterion is identical, except that the criterion is expressed in terms of strains. Naik used this failure criterion for the ultimate strength prediction of woven braided fabric composites [108].

2.4.2.2 The Tsai-Wu quadratic failure criterion

This failure theory is based on the total strain energy failure theory of Beltrami. This criterion states a general quadratic failure equation expressed in stress space. A lamina is considered to be failed if,

$$f^2 = \sum_{i=1}^{6} F_i \sigma_i + \sum_{i,j=1}^{6} F_i \sigma_i \sigma_{ji} < 1 \tag{2-5}$$

is violated [80].

The F_{ij} terms denote the interaction of stress components on failure. Also, distinction between tensile and compression is introduced in the F coefficients denoted below. In terms of plane stress, equation 2.5 becomes,

$$f^2 = F_1\sigma_1 + F_2\sigma_2 + F_{11}\sigma_1^2 + F_{22}\sigma_2^2 + F_{66}\tau_{12}^2 + 2F_{12}\sigma_1\sigma_{12}\,, \tag{2-6}$$

where

$$F_1 = \frac{1}{\sigma_{1u}^t} - \frac{1}{\sigma_{1u}^c}; \qquad F_{11} = \frac{1}{\sigma_{1u}^t \sigma_{1u}^c} \tag{2-7}$$

$$F_2 = \frac{1}{\sigma_{2u}^t} - \frac{1}{\sigma_{2u}^c}; \qquad F_{22} = \frac{1}{\sigma_{2u}^t \sigma_{2u}^c}$$

$$F_{66} = \frac{1}{\tau_{12u}^p \tau_{1u}^n}; \qquad F_{12} = \frac{1}{2}\sqrt{F_{11}F_{22}}$$

From the WWFE study, it appears that even failure criteria applied to simple laminates predict failure loads significantly different to experimental observations [29] [30]. Generally, macro-mechanical strength theories are unable to indicate which constituent materials, fibre or matrix, initiate failure of the composite, which is important information for composite design [63]. Also, these models do not predict the material damage initiation and progression; therefore, other more accurate approaches for failure determination have been proposed.

For example, NASA has recently proposed, in the LaRC04 software, six physically based failure criteria for different failure modes. Well established models, such as Puck and Hashin’s, are enhanced with fracture mechanics to predict the main failure modes in a laminate; including, delamination, matrix compression failure, fibre compression failure, matrix tensile failure and fibre tensile failure [119].

2.4.3 Damage and failure prediction based on damage mechanics – Ladevèze damage model

2.4.3.1 ‘Meso-scale’ damage model - Generalities

Generally, textile composites offer a multitude of failure modes which make their failure analysis appreciably more difficult than metals. For braided composites, possible failure modes include tensile fibre failure, compressive fibre failure, matrix micro-cracking and fibre/matrix interface debonding. Also, delamination between adjacent layers may occur; however, this work will focus specifically on intra-ply failure.

Damage mechanics aims to develop a framework that describes the material response caused by the evolving damage state. The greatest difficulty is to analyse material micro-structural changes and relate them to the material response. Kachanov [73] and Rabotnov [120] first introduced continuous damage as a variable to perform creep failure of metals; this concept was then generalised within the framework of irreversible thermodynamics for isotropic materials under multiaxial loading [91].

Evolution of damage in composites has been studied both at the micro- (fibre and matrix) and meso-scale (individual layer) levels. Amongst numerous damage theories applied to composites, the meso-scale damage model proposed by Ladevèze [87] has demonstrated success for damage and failure prediction applied to carbon/epoxy composites, ceramic matrix composites [46], 4D carbon/carbon composites [12] [13], delamination growth [2] [3] and applications involving elevated temperature [96].

Damage assessment in composites depends on the scale at which analysis is undertaken; indeed, while macro-cracks in concrete, resulting from the curing process, do not constitute significant damage, cracks of this magnitude in composite structures are considered to be significant damage [58]. Therefore, in order to eliminate such difference of scale, Ladevèze proposed the meso-scale modelling as intermediate between micro-mechanics (analysis at the individual fibre/matrix scale) and macro-mechanics (laminate scale). The scale of interest corresponds to the individual ply of a laminate called the fundamental representative volume element, where the ply has continuous thickness and only one fibre orientation. In order to simplify the damage theory, damage is assumed to be uniform through the thickness of each individual ply and it can vary from ply to ply.

Specific damage mechanisms at the microscopic level, such as fibre/matrix debonding, or matrix cracking, are not individually identified; indeed, in the model definition, damage is considered more generally as the accumulation of fibre breaks and microcracks resulting in stiffness loss and plastic strain accumulation.

The model provides a damage history law in which stiffness degradation is governed by associated thermodynamic forces. In addition, a distinction between damage growth under tension and compression, inelastic strain development and coupling between different damage mechanisms are accounted for in the model.

The fundamental inter-relationships between these quantities are determined by measurement of carefully selected laminates subjected to different loading types. Interlaminar damage between layers can also be included considering an interfacial layer [2]; however, this will not be considered in this work.

2.4.3.2 Theoretical modelling of the elementary unidirectional ply

The elementary ply exhibits continuous thickness and has fibres orientated in one direction as shown in figure 2.27. Subscripts 1 and 2 respectively designate the fibre and transverse directions. Also, it is assumed a state of plane stress.

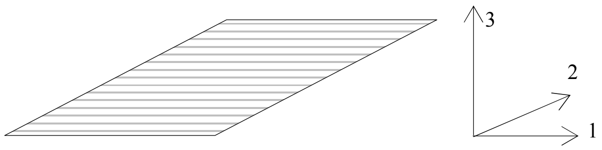

Figure 2.27: Elementary ply and fibre orientation definition [87].

The damaged-material strain energy is derived from thermodynamics and is written as follows [87],

$$\begin{aligned} E_D &= \frac{1}{2}\underline{\underline{\sigma}} : \underline{\underline{\varepsilon}}^e \\ &= \frac{1}{2}\left[\frac{\sigma_{11}^2}{E_{11}^0} - \frac{2\nu_{12}^0}{E_{11}^0}\sigma_{11}\sigma_{22} + \frac{\langle\sigma_{22}\rangle_+^2}{E_{22}^0(1-d_{22})} + \frac{\langle\sigma_{22}\rangle_-^2}{E_{22}^0} + \frac{\sigma_{12}^2}{G_{12}^0(1-d_{12})}\right] \end{aligned} \tag{2-8}$$

where ε^e correspond to the elastic strain, superscript ^{0} indicates original undamaged values and bracketed quantities < > are defined as follows,

$$\begin{aligned} \langle x\rangle_+ &= x \quad if \;\; x > 0, \quad and \; \langle x\rangle_- = 0 \\ \langle x\rangle_- &= x \quad if \;\; x < 0, \quad and \; \langle x\rangle_+ = 0. \end{aligned} \tag{2-9}$$

The model distinguishes tensile from compressive transverse behaviour; indeed, when σ_{22} is compressive no degradation is assumed to occur with closure of micro-cracks. Also, scalar damage variables d_{22} and d_{12} have been introduced as a measure of the loss in stiffness of transverse and shear moduli respectively. Therefore, the current damaged value for E_{22} and G_{12} can be calculated at any time in the loading history using,

$$\begin{aligned} E_{22}^D &= E_{22}^0(1-d_{22}) \\ G_{12}^D &= G_{12}^0(1-d_{12}). \end{aligned} \tag{2-10}$$

In addition, it is assumed that fibres do not exhibit any stiffness loss prior to failure; that is E_{11} is not degraded.

From the damaged-material strain energy, two conjugate quantities Y_{22} and Y_{12} are derived and are thermodynamic forces associated with damage variables d_{22} and d_{12},

$$\begin{aligned} Y_{22} &= \left.\frac{\partial E_D}{\partial d_{22}}\right|_\sigma = \frac{1}{2}\frac{\langle\sigma_{22}\rangle_+^2}{E_{22}^0(1-d_{22})^2} \\ Y_{12} &= \left.\frac{\partial E_D}{\partial d_{12}}\right|_\sigma = \frac{1}{2}\frac{\sigma_{12}^2}{G_{12}^0(1-d_{12})^2}, \end{aligned} \tag{2-11}$$

where Y_{22} and Y_{12} are analogous to strain energy release rates governing crack propagation but, in this case, they govern damage evolution.

Two distinct ply degradation mechanisms contributing to damage development are included in the model; namely, matrix micro-cracking and fibre/matrix debonding. Two variables of the thermodynamic forces, Y and Y', are then introduced in order to describe, at any time t, the damage development in each individual layer. They are defined as maximum value attained at any time τ during the interval $0< \tau<t$,

$$Y(t) = \max\big|_{\tau<t} \left[Y_{12}(\tau) + bY_{22}(\tau)\right]$$
$$Y'(t) = \max\big|_{\tau<t} Y_{22}(\tau)\ . \tag{2-12}$$

The variable Y is a linear combination of the two thermodynamic forces, with b being a material dependent coupling parameter and Y' corresponds to brittle failure of a single ply under transverse tension.

The two damage variables d_{22} and d_{12} for intra-ply transverse tension and shear are then identified from experimental results. These two functions are related to the type of material are generally written in the form,

$$d_{22} = h(Y)\ \ if\ d_{22} < 1,\ \ otherwise\ d_{22} = 1 \tag{2-13}$$
$$d_{12} = g(Y)\ \ if\ d_{12} < 1,\ \ otherwise\ d_{12} = 1\ ,$$

where h and g are linear functions.

In order to model the inelastic strains due to damage and matrix plasticity, effective stress and effective inelastic strains are introduced as follows,

$$\tilde{\sigma}_{ij} = \begin{bmatrix} \tilde{\sigma}_{11} \\ \tilde{\sigma}_{22} \\ \tilde{\sigma}_{12} \end{bmatrix} = \begin{bmatrix} \sigma_{11} \\ \left[\langle\sigma_{22}\rangle_+ /(1-d_{22})\right] + \langle\sigma_{22}\rangle_- \\ \sigma_{12}/(1-d_{12}) \end{bmatrix} \tag{2-14}$$

$$\dot{\tilde{\varepsilon}}_{ij}^{p} = \begin{bmatrix} \dot{\tilde{\varepsilon}}_{11}^{p} \\ \dot{\tilde{\varepsilon}}_{22}^{p} \\ \dot{\tilde{\varepsilon}}_{12}^{p} \end{bmatrix} = \begin{bmatrix} 0 \\ \left(\dot{\varepsilon}_{22}^{p}/\sigma_{22}\right)\left[\langle\sigma_{22}\rangle_+ (1-d_{22}) + \langle\sigma_{22}\rangle_-\right] \\ \dot{\varepsilon}_{12}^{p}(1-d_{12}) \end{bmatrix}.$$

Assuming isotropic hardening and that inelastic strains are independent of σ_{11}, the elasticity domain is given by the yielding function f as,

$$f(\tilde{\sigma}, R) = \sqrt{\tilde{\sigma}_{12}^2 + a^2\tilde{\sigma}_{22}^2} - R(\tilde{p}) - R_0\ , \tag{2-15}$$

where a is a material inelastic coupling constant, R_0 the initial threshold of the function for inelastic strain accumulation and $R(\tilde{p})$ is a material dependent hardening function of the accumulated inelastic strain $\tilde{p}$.

2.5 The explicit code PAM-CRASH^{TM}

The PAM-CRASH^{TM} code has been designed and developed by the French company ESI, founded in1973, and is mainly focused on non-linear and dynamic problems.

2.5.1 Implicit/Explicit methods

Two classes of Finite Element methods are generally available, either the Implicit or Explicit method. The Implicit method is generally used in static stress analysis problems; whereas the Explicit method is particularly suited to dynamic and highly non-linear, contact dominated problems, such as car crash or metal stamping simulations.

Both techniques use conventional finite elements to discretise and represent the structure. The Implicit method is superior for static, mildly non-linear problems; whereas the Explicit method is advantageous for medium to high velocity dynamic problems involving large scale deformation and material non-linearity. Although unconditionally stable, Implicit method needs many time steps to correctly trace the physical phenomena and converge, the explicit analysis requires smaller time steps for stability, leading lower CPU time.

2.5.1.1 Implicit method

The Implicit method assembles the global stiffness matrix [K] which is used to determine resulting nodal displacements {u} from applied nodal forces {P},

$$\{P\} = [K]\{u\} \ or \ \{u\} = [K]^{-1}\{P\} \tag{2-16}$$

From nodal displacements the element stresses and strains are computed for each element. Problems involving contact, buckling and material non-linearity yield a non-linear stiffness matrix [K] which requires a CPU intensive iterative solution. In this case load increments must be small to follow the physical phenomena.

2.5.1.2 Explicit method

The alternative explicit algorithm uses a different solution strategy and poses the problem as a dynamic one, using the linearised equations of motion,

$$[M]\{\ddot{u}\}_n + [K]\{u\}_n = \{P\}_n \tag{2-17}$$

where {u} and {ü} are vectors of nodal displacement and acceleration, n is the cycle number at time T_n (after nΔT time steps); [M] and [K] are the Mass and Stiffness matrices respectively. A central finite difference solution is used to update nodal displacements from which element stresses and strains at each time step are computed.

The method is 'conditionally stable' through use of an integration time step ΔT that must be below a critical value which depends on the size of the smallest element and material properties of the element.

For instance, considering the following system where a simple spring links a mass m to a fixed point as shown in Figure 2.28.

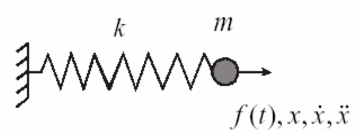

Figure 2.28: Spring system mass.

From equation (2.17), the applied force f(t) at a time t gives the following dynamic equation of motion for the system,

$$m\ddot{u} + ku = f(t) \tag{2-18}$$

where u and ü are the displacement and acceleration of the mass m. This equation can be expressed at any arbitrary time t after n time steps giving,

$$m\ddot{u} + ku_n = f_n(t) \tag{2-19}$$

The acceleration can be successively determined from central finite differences as shown in figure 2.29.

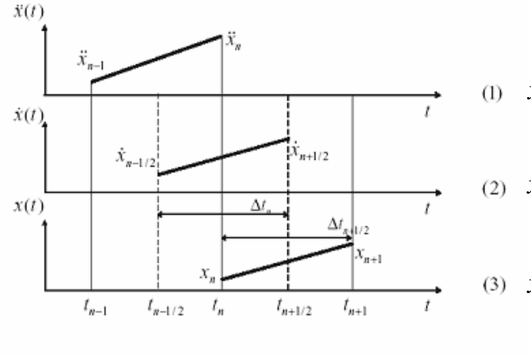

(1) $\ddot{x} = m^{-1}(f_n - kx_n)$

(2) $\dot{x}_{n+1/2} = \dot{x}_{n-1/2} + \Delta t_n \ddot{x}_n$

(3) $x_{n+1} = x_n + \Delta t_{n+1/2} \dot{x}_{n+1/2}$

Figure 2.29: Explicit method integration scheme [115].

For which Δt is a stable time step which must be used in the ‘conditionally stable’ solution scheme. For instance, in this method, a bar of length L, cross-section A, density ρ and elastic modulus E will be modelled as a spring, as shown in figure 2.30.

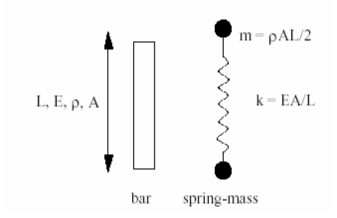

Figure 2.30: Representation of a stable time step [115].

The time step Δt will then be expressed through the following form,

$$\Delta t = \sqrt{\frac{2m}{k}} = L\sqrt{\frac{\rho}{E}} = \frac{L}{\sqrt{E/\rho}} = \frac{L}{c} \tag{2-20}$$

where $c=\sqrt{E/\rho}$ is the speed of sound.

2.5.2 Composites modelling in PAM-CRASH^{TM}

2.5.2.1 Multilayered shell Element – Material 131

The multilayered shell element is used in this work to simulate each individual braid layer within a coupon. A shell element comprises of plies numbered from z=-t/2 to z=+t/2 where t corresponds to the element thickness, figure 2.31.

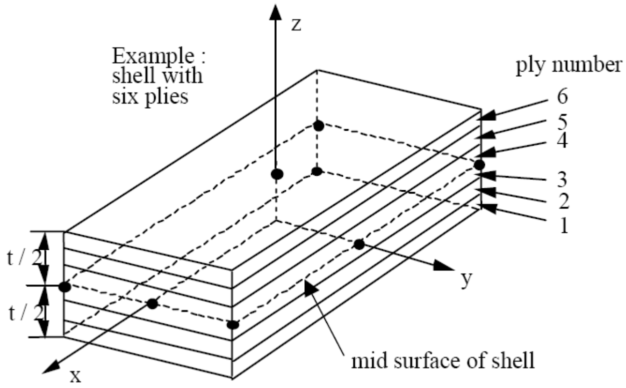

Figure 2.31: Example of a 6 plies layered shell element [115].

The elementary ply properties are then selected from the unidirectional composite ply card (ITYP=1). Each specified ply corresponds to one integration point across the thickness of the multilayered shell element.

2.5.2.2 Unidirectional composite global ply model – ITYP=1

The Ladevèze model described earlier has been implemented in the code as a unidirectional composite global ply model. As previously described, the model enables to predict fibre failure and also other damage mechanisms that relate to experimentally observed phenomena, such as matrix microcracking and fibre/matrix interface debonding as pictured in figure 2.32.

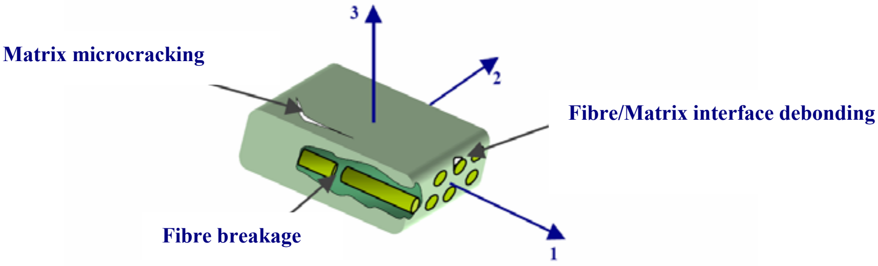

Figure 2.32: Global composite ply damage mechanisms [121].

The ply coordinate system implemented is orthotropic in which the first axis of orthotropy coincides with the fibre direction (1), the second axis is perpendicular to the first in the plane of the element (2) and the third axis is normal to the plane defined by the two previous axes. In order to retrieve materials constants for the elementary ply calibration, an experimental campaign comprising monotonic/cyclic tension and compression on diverse laminates is conducted. Table 2.3 presents the different parameters obtained for each test for the ply calibration under static loading. These parameters are used as input in the material and ply data cards for characterisation of the composite shell element.

	Tension on	**Cyclic tension on**			**Compression on**
Test/Parameters	**$[0^\circ]_8$**	**$[\pm 67.5^\circ]_S$**	**$[\pm 45^\circ]_S$**	**$[+45^\circ]_8$**	**$[0^\circ]_8$**
Elastic properties	E_{11}^{t0} ν_{12}^{0}		G_{12}^{0}	E_{22}^{0}	E_{11}^{0c}
Matrix and fibre tensile damage-related constants	ε_{11l}^{t} ε_{11u}^{t} d_{11u}^{t}	Y_{22R} Y_{22C} Y_{220} b	Y_{12C} Y_{120} Y_{12R} $d_{\max}$	Y_{22C} Y_{220} b	γ ε_{11l}^{c} ε_{11u}^{c} d_{11u}^{c}
Plastics constants			R_0 β α	a^2	

Table 2.3: Testing campaign for ply calibration [121] [115].

This work uses this model as a basis for braided composites modelling; however, necessary model improvements for this different class of composite will be presented and validated.

2.6 Overview

Braided composites are attractive for industrial applications since they offer multiple combinations between fibre types, architectures and manufacturing routes. For instance, the choice on the fibre directions (bi- or triaxial) and angle can be tuned to fulfil the components mechanical requirements. Also, the braiding process allows near net shape preforms to be manufactured, which can be subsequently impregnated with an adapted resin system.

Manufacturing is generally based on Liquid Composite Moulding (LCM) techniques in which resin flows through the preform and is progressively cured. Quality issues are frequent in such technique compared to pre-impregnated composites. Voids and poor impregnation are often the results of a poor manufacturing protocol and inappropriate equipment. Such defects affect significantly the composite mechanical properties, and also influence part reproducibility.

In comparison to unidirectional composites, braided composites can exhibit better damage/impact tolerances, and larger deformation to failure; however, due fibre waviness they suffer from lower in-plane stiffness and different failure mechanisms under tension and compression loading.

Different numerical and analytical methods, based on FE or micromechanics analysis respectively, are now available to determine accurately elastic braided composite properties; however, very few models can predict failure and damage evolution. The damage model investigated in this work was initially developed for unidirectional and it is attempted here to adapt it for braided composites. However this necessitates to fully characterising failure mechanisms under different loadings. This is presented in the next chapter.

Chapter 3- Experimental work: Manufacturing and mechanical characterisation of glass and carbon braided composites

The main failure mechanisms for braided composites were briefly presented in the previous chapter. Accordingly, a comprehensive material characterisation of the carbon and glass braids investigated in this work was conducted via an extensive test programme. The fabric types, architectures and resin system properties used are presented in this chapter together with the quality assessment method conducted on panels.

Due to large deformations of the braid through scissoring, strain measurement using conventional techniques, such as strain gauges or extensometers, was not possible and full material characterisation could not be achieved. An alternative technique, based on 'marker tracking', was therefore specifically developed for this material. This technique is introduced and discussed further in this chapter. Furthermore, from successful results found with the in-house measurement method, a more sophisticated non-contact technique based on Digital Image Correlation (DIC) was acquired and applied. This technique will also be presented in detail in this chapter.

Preliminary material characterisation was first conducted to assess how various characteristics of braided composites affect their mechanical behaviour. It was necessary to study the impact of preform continuity on the failure mode; therefore tensile testing on cut and uncut specimens were conducted. In addition, due to the overbraiding characteristic found in braided composites, the effect of number of layers also had to be quantified.

The initial test campaign, introduced in section 2.5.2.2 (table 2.3), for damage model calibration had to be adapted to match braided composite characteristics. Tensile and compressive loading in the fibre direction and shear cyclic loading was undertaken for fibre and matrix damage and plasticity laws identification. Tests were conducted on both carbon and glass braided composites.

In order to validate the damage model for a structural part, 4 point bending tests were conducted on square cross-section beams manufactured from carbon and glass fibre braided composites. Their manufacturing and testing is also presented.

3.1 Coupons manufacturing

3.1.1 Fabrics and matrix

3.1.1.1 STS carbon and E-glass braided fabrics

Tubular preforms were manufactured using a maypole type braider in which the preform diameter and fibre architecture could be tailored according to the mandrel's diameter, rotation speed and feed rate. In this work, 24k tows made of STS carbon and E-glass fibres, respectively, were used to manufacture a plain weave preform having 100mm diameter and made of 84 ends as shown in figure 3.1. The manufacturing of these two preforms was conducted by Eurocarbon [33].

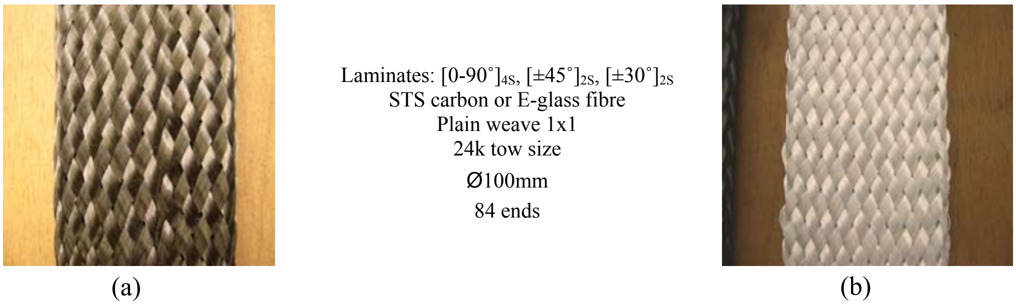

Figure 3.1: Braided preforms investigated (a) STS carbon fibre preform, (b) E-glass fibre preform.

3.1.1.2 Resin system - Epoxy resin LY3505/Hardener XB3403

Epoxy resin LY3505 with hardener XB3403, manufactured by Huntsman Advanced Materials [66], were used for the coupon manufacture. The reaction between these two components, classified as an amine/epoxy reaction, enables the resin system formulation to be adjusted to give a wide range of properties. The properties of this system are presented in table 3.1 using a slow (XB3403), medium (XB3404) and fast hardener (XB3405) types.

The choice of hardener determines the final mechanical properties of the mix as shown in table 3.1. As it was not a requirement to optimise the mechanical properties of the parts, a slow hardener has been chosen due to its greater manufacturing flexibility.

Matrix systems	**LY3505 /XB3403**	**LY3505 /XB3404**	**LY3505 /XB3405**
Mix ratio	100:35	100:35	100:35
Initial viscosity @25°C [mPas]	300-400	550-800	1000-1200
Gel time [min] @60°C	105-125	60-70	18-26
Cure cycle	4h@60°C+6h@80°C	4h@60°C+6h@80°C	4h@60°C+6h@80°C
Tg (glass transition temperature) [°C]	78-83	76-81	87-92
Tensile modulus [GPa]	3.18-3.28	3.4-3.7	3.5-3.9
Poisson's ratio	0.35	0.35	0.35
Tensile strength [MPa]	70-74	82-86	85-90
Ultimate elongation [%]	10-13	5.2-5.8	5.0-6.2

Table 3.1: Properties for LY3505 epoxy with hardener [66].

3.1.2 Resin Infusion process

3.1.2.1 Standard manufacturing procedure

The main goal of the manufacturing process was to achieve high and consistent coupon quality. For this, a basic tool consisting of two aluminium sheets were used for the mould surfaces; preliminary cleaning with acetone, and subsequent coatings with release agent was used to obtain practical demoulding. Sealant tape was then used to create the vacuum chamber between bag and bottom plate. Finally, inlet and outlet pipes were connected to the resin pot and vacuum pump respectively, as shown in figure 3.2 (a). Experience has shown that a better impregnation was obtained by using two different peel plies located at the preform/sheet interface as shown in figure 3.2 (b).

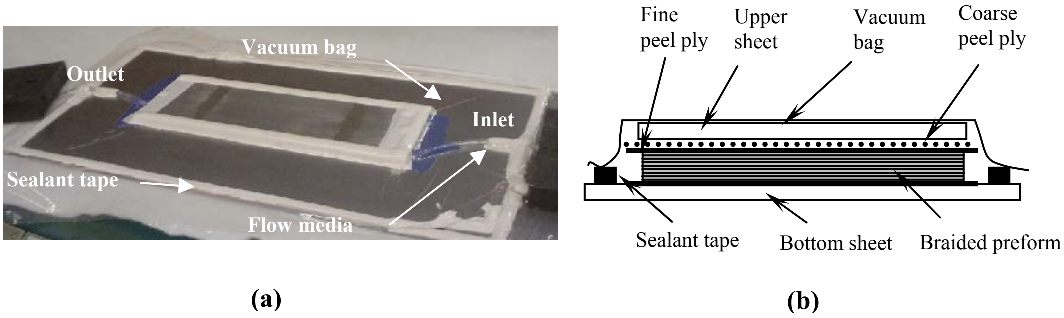

Figure 3.2: Infusion process used (a) manufacturing set-up, (b) set-up cross-sectional view.

3.1.2.2 Resin degassing – Air entrapment removal

The resin and hardener were mixed together, according to the mix ratio defined in table 3.1, and degassed for 40 minutes at 5-10mbar absolute pressure to remove air, figure 3.3.

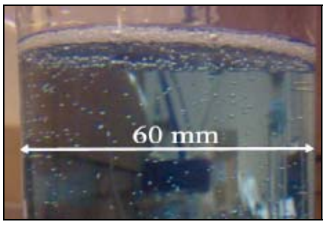

Figure 3.3: Micro-bubbles removal during degassing [1].

This step was performed to remove any gaseous components entrapped in the resin, which could lead to void formation within the specimen affecting its mechanical properties. Afendi et al. [1] have recommended 15 min degassing, followed by 1 hour at atmospheric pressure, in order to let the bubbles diffuse to the surface.

In the current work, the degassing process was monitored visually and stopped when bubbles were fully collapsed at the resin surface. The degassing time was dependant on the resin quantity; for instance, 300g of mix took approximatively 40-45min at room temperature to be completely degassed.

3.1.2.3 Curing and post curing

Simultaneous to resin degassing, another vacuum pump was connected to the outlet to expel air in the system and check for any leakage. Pressure within the chamber was monitored to obtain 5-10mbar absolute pressure. System temperature was then raised to 35°-40°C prior to the start of infusion. Initially, the resin mix was relatively viscous, 400mPa.s; however, when contact occurred with the heated aluminium sheets the mix viscosity dropped and the resin impregnation speed increased.

After a gel time of 150-200min, the temperature was elevated to 60°C in order to localise the bubbles, and prevent their dispersion between fibres due to shrinkage [1]. After 4 hours curing at 60°C, the braided panel was then post-cured for 6 hours at 80°C according to the manufacturer's specifications, presented in table 3.1, and finally carefully demoulded.

3.1.3 Manufacturing control and quality issues

3.1.3.1 Voids formation and effect on composites mechanical performance

As stated in section 2.2.3, controlled manufacturing is essential for achieving repeatable mechanical properties. During the manufacture of a composite using the resin infusion technique the potential for voids formation is generally greater than in competing manufacturing process based on pre-impregnated materials. Voids are generally caused by three main sources [122],

- Macroscopic voids due to race tracking, or flow front coalescence,
- Moisture or volatiles within the raw materials,
- Entrapment of air in the fibre bundles.

Void content can be limited, for instance, by resin degassing to eliminate air bubbles entrapped in the resin. Void creation can cause detrimental effects on the mechanical properties such as lower shear stiffness, shear strength, compressive strength, transverse tensile strength, fatigue, and moisture resistance [80]. If the manufactured parts appear to have high void content, the material becomes highly heterogeneous and does not exhibit consistent mechanical properties. Consequently, the manufacture of resin infused parts requires careful control and minimisation of void contents.

For these reasons, the manufacturing technique had to be perfectly controlled to minimise void formation. Figure 3.4 shows two manufactured specimens with either high, or low, void content; it has been found that any voids that occurred were mainly localised at the tow intersections.

(a) (b)

Figure 3.4: Void content in braided composites, (a) high void content, (b) low void content.

3.1.3.2 Macroscopic and microscopic voids characterisation in braided specimens

A visual inspection was conducted to check if tows were misaligned, impregnation incomplete or a high void content was present. For instance, figure 3.5 (a) shows a combination of tow misalignment and voids observed on a $[0, 90^\circ]_{4S}$ panel. Also, preliminary problems to achieve complete impregnation were encountered, for example, in the beam manufacture as shown in figure 3.5 (b).

(a) (b)

Figure 3.5: Visual quality inspection for specimen selection, (a) tow misalignment and macro-voids, (b) incomplete impregnation.

Generally, only macro-voids can be detected using visual inspection and complementary tests using non-destructive techniques, such as C-scan, should have been carried out to fully assess panel integrity. However, such techniques were not used for this work for due time scale considerations; therefore a microscopic visual analysis was conducted in order to determine defects at the micro-scale.

Figure 3.6 shows a sample extracted from a [±30°]$_{2S}$ specimen mounted with epoxy resin and analysed using a digital optical microscope. The micrograph analysis presents a part of the specimen cross-section where tows from upper and lower layers are interlaced and embedded in matrix. Using a microscope with x20 magnification no micro-defects were detected within the tows or inter-tows areas.

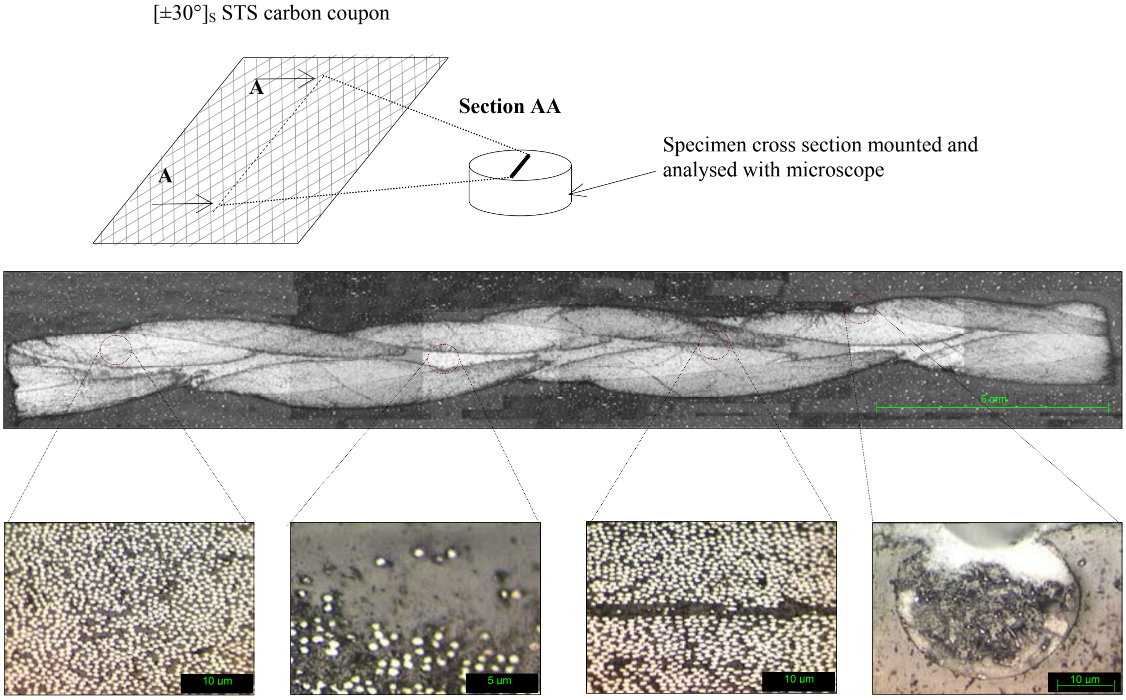

Fibres within a tow Area between two layers Area between tows Defect at tow intersection

Figure 3.6: Microscopic analysis on a [±30°]$_{2S}$ STS carbon fibre specimen: sample extraction and analysis with general view and areas of interest.

This study also revealed large resin rich areas between layers with low fibre content, reflecting a poor compaction between the two single layers. However, fibre volume fraction reaches its maximum within tows and between tows indicating a better compaction within a single layer. Finally, small surface defects at tows intersection could be seen, figure 3.6, which were not obvious just by visual inspection.

This analysis was repeated for two other samples extracted at random locations from two different infused panels. Even if this microscopic study showed no apparent micro-defects within panels; samples reflects only local and not global panel quality and caution must be taken when extrapolating the results to draw conclusions about the overall quality of the full panel.

3.1.3.3 Volume fraction measurement

From these microscopic images, local volume fractions were readily determined using Labview NI vision post-processing tool [110], where fibre surface area could be automatically calculated. For instance, the overall surface fibre determined for the $[\pm 30°]_{2S}$ specimen presented previously was approximatively 55% which was the highest fibre volume fraction area achieved within the specimen.


(a) **(b)**

Figure 3.7: Fibre volume fraction determination within a tow from a [±30°] coupon.

In order to obtain average values of the panel volume fraction (V_f), an approximation based on masses and densities of the preform and resin was used. For all samples manufactured and reported in this work, fibre volume fraction mean values of 40% and 50% have been consistently found for the [±45°] and [±30°] braided panels respectively. This confirms a good quality control and repeatability of the manufacturing process and confidence in consistency of the material mechanical properties.

3.1.4 Beam manufacturing

3.1.4.1 Experimental set-up

As for coupons, resin infusion was used to manufacture carbon and glass braided beams. Four layers of preform were over-braided and introduced into a PVC closed mould previously cleaned and coated with release agent. In order to ensure a complete impregnation of the preform, strips of peel ply and coarse flow medium were added inside the mould. A tubular vacuum bag was subsequently fitted inside the preform then folded and sealed on each mould end as shown in figure 3.8.

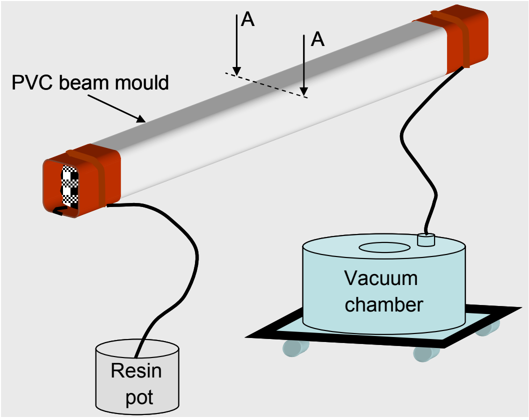

Figure 3.8: **Braided beams manufacturing set-up.**

Inlet and outlet pipes were placed at each end of the mould and connected to the resin pot and vacuum pump respectively. As the vacuum progressively settled in the system, the braided preform was pressurised by the vacuum bag against the mould cavity as shown in figure 3.9.

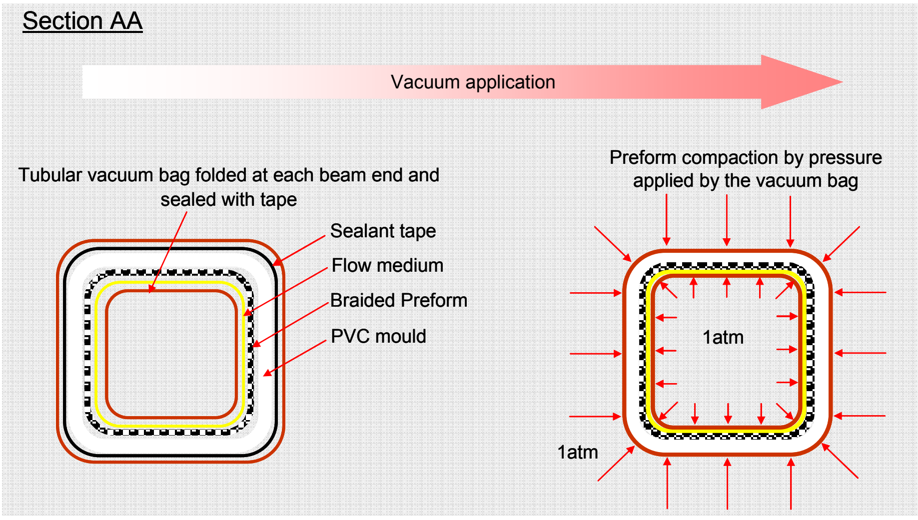

Figure 3.9: **Cross-section of the mould used for beam manufacture.**

Good vacuum and leak rates were obtained and the resin was infused into the preform for 60 to 80min at a temperature between 30°C to 35°C. In order to obtain a proper and homogenous impregnation, the mould was vertically positioned so that gravity helped reduce the resin flow velocity. Pipes were immediately clamped once resin appeared in the outlet pipe, and the temperature was immediately increased to 50°C for 4 hours for curing. The post curing was conducted at a higher temperature of 75°C. Due to the PVC mould's low stiffness, an external reinforcement box was used during the infusion, cure and post-cure to stiffen the assembly.

3.1.4.2 Beams properties

The infused beams were successfully impregnated giving a low void content and good surface finish; however, an inconsistent cross-sectional area was found along the beam due to the mode of manufacturing. The pressure applied by the vacuum bag onto the preform could not be controlled affecting fibre placement, and particularly poor fibre compaction was found in the mould corners. Figure 3.10 presents a cross-section of the carbon beam taken at the centre of the span. Since the preform was not compacted in the mould corners, this created spaces for resin race-tracking.

Due to low resin infusion velocity this balanced the race-tracking and produced good impregnation. However, the final part exhibited high resin content, especially in the corners, affecting the volume fraction. Indeed, only 40 to 45% volume fraction was determined for the carbon and glass beams. In addition, it was found that the glass beam also exhibited side wall deformation during curing and post curing. This was attributed to a higher coefficient of thermal expansion than carbon (table 2.2); indeed, glass fibre expands and contracts with temperature, which has caused problems to obtain near net shape geometry.

Cross-section (middle beam – after test)

Figure 3.10: Resin rich areas at the beam corners.

3.2 Measurement techniques used for the material properties characterisation – Limitation and developments

Conventional measurement techniques such as surface-bonded resistive strain gauges and laser extensometer have been used in this testing campaign. They typically provided single measurements of strains and displacements at selected locations and gauge lengths. These techniques generally suffer from various limitations, which can lead to measurement errors; for instance, bad bonding, or strain gauge misalignment are common sources of significant scatter.

In this work the braided composite investigated used a 2D fabric reinforcement with relatively heavy tows, which results in surface waviness and non-uniform strain fields at the tow scale. In the [±45°] configuration the specimen is subjected to fibre scissoring in which fibres undergo large rotation and re-alignment in the loading direction. During this process the fibre/matrix interface debonds allowing fibre movement leading to internal/external macro-cracking and component surface damage. This becomes highly problematic when deformation has to be measured using techniques requiring contact with the specimen surface, such as strain gauges or extensometers.

In order to overcome these limitations an in-house non-contact technique was first developed to determine longitudinal and transverse strain. Successful results obtained using this approach led to the acquisition of a full field non-contact 3D Digital Image Correlation (DIC) system. In the following section, all these measurement techniques are presented and described.

3.2.1 Conventional measurement techniques

3.2.1.1 Wire strain gauges

Usually strain gauges, or resistance wires, are used in strain recording due to their high level of accuracy. This technique is mainly used for determining elastic properties due to a 3% strain limit of the gauge (manufacturer recommendation). In addition, the measurement is local and assumes uniform deformation over the gauge length, which may be valid for isotropic materials but is questionable for heterogeneous materials such as textile fibre composites. A further limitation of this technique is related to component surface degradation where the strain gauge is easily destroyed as shown in figure 3.11. In this work, wire strain gauges have been used to determine accurate values for elastic properties and also to validate other measurement techniques.

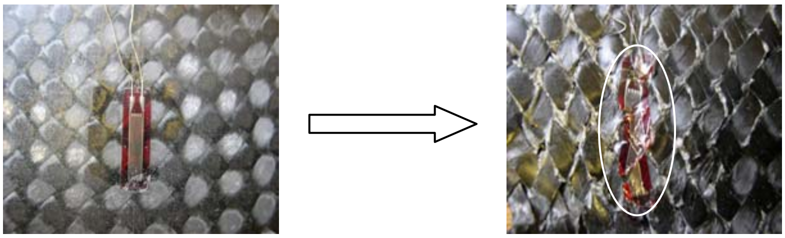

Figure 3.11: Strain gauge failure resulting from braided composites shear failure mechanism.

3.2.1.2 Uni-axial laser extensometer

The laser extensometer is a standard technique for measuring uni-axial strain in a homogenous strain field. Two reflective markers are glued onto the specimen surface at a chosen distance apart. A laser beam is then projected towards the specimen surface and the change in marker positions are recorded during loading history, figure 3.12.

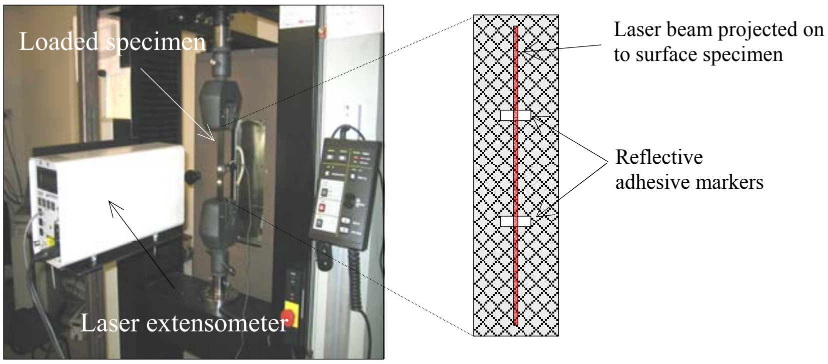

Figure 3.12: Laser extensometer experimental set-up.

The recorded value is expressed as the relative displacement of the two markers in the loading direction. Equation (3.1) gives the expression for longitudinal strain,

$$\varepsilon_{xx} = \frac{l - l_0}{l_0} \tag{3-1}$$

where l_0 is the initial length and l is the length at each displacement increment. In the elastic domain where strain was uniform, results were satisfactory; however, in the plastic-damage domain, once strain localisation occurred the average strain was no longer representative. In addition, this method was impractical due to the adhesive markers debonding with large fibre rotation and degradation of the damaged surfaces.

3.2.2 Non-conventional measurement techniques used for large and non-uniform deformation

3.2.2.1 Marker tracking technique- an 'in-house' method

Due to the difficulties outlined above in measuring large deformations a new technique using marker tracking was developed in collaboration with Dr Vivien Beyer. In order to calibrate the model, longitudinal strain, ε_{xx}, and transverse strain, ε_{yy}, were required. These were obtained through optically measuring the relative displacement of 4 markers painted at the specimen surface. The measurement was performed by direct visual means using a standard video camera placed in front of the specimen. From the generated movie, images were extracted at constant frequency, usually 1Hz, and used to obtain the marker displacements. These pictures were then analysed by extracting markers using NI Vision Assistant [110] as shown in figure 3.13.

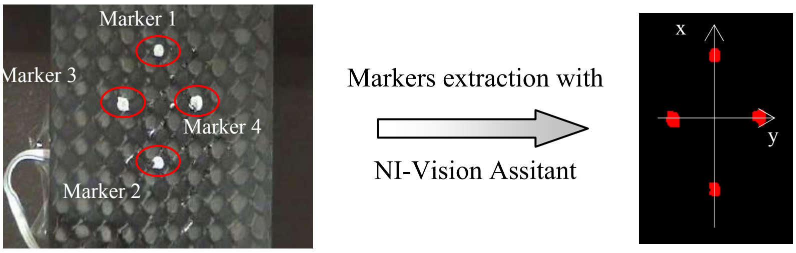

Figure 3.13: Marker tracking technique used to determine principal strains.

An in-house algorithm, developed in Labview [111], determined displacement of each dot centre of gravity. Relative displacement between markers 1&2 and markers 3&4 gave the specimen longitudinal and transverse displacements respectively. For strain calculations, it was assumed that each pair of dots was aligned in the x and y directions and strain could then be derived using equation (3.1).

This method overcame problems encountered with premature failure of strain gauges and enabled to fully measure material longitudinal and transverse strains up to complete failure. Figure 3.14 shows a typical cyclic loading on a $[\pm 45°]_{2S}$ carbon braided specimen; it can be noticed that a noisy signal in the stress-strain curve was found; this was attributed to an insufficient digital pixel resolution.

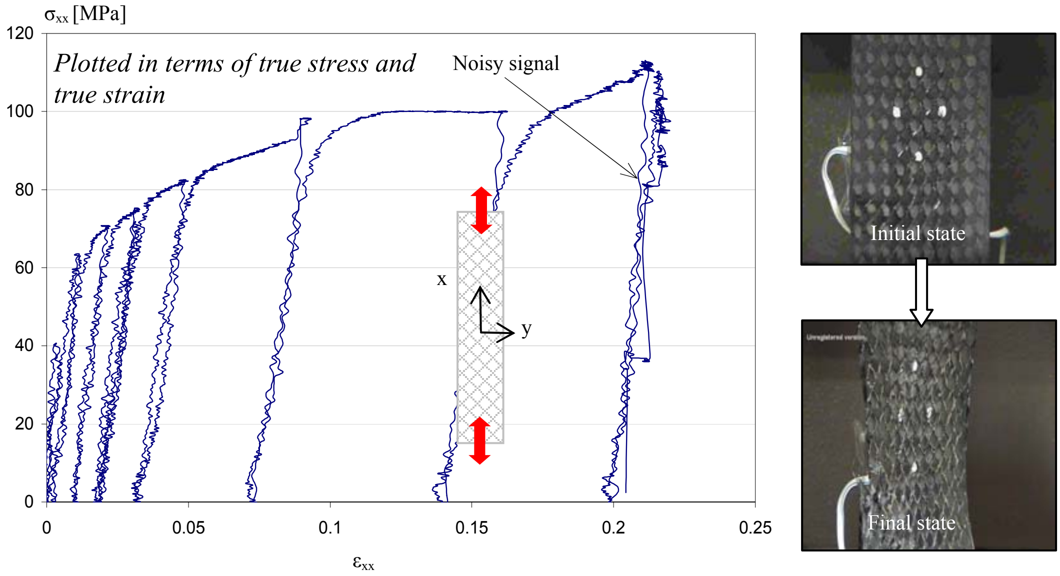

Figure 3.14: Example results from the markers tracking technique developed [118].

The noise was observed to increase in the failure region where markers underwent large deformations, figure 3.14. At this stage, marker recognition was difficult and the algorithm could not extract accurately the marker surface. Another limitation of this technique was that out-of-plane displacements were ignored. Indeed, it was assumed that the camera lens was parallel to the specimen surface, and that the specimens were only deforming in the *xoy* plane, figure 3.14.

3.2.2.2 Digital Image Correlation technique - DIC

In the light of results obtained by the marker tracking technique it appeared that a non-contact measurement technique was the most appropriate method to measure large strains on a damaging surface. Due to the limitations of the marker tracking technique it was decided to use a Digital Image Correlation (DIC) system, provided by LIMESS GmbH [94], in order to obtain a complete strain field of the tested specimen.

The digital image correlation method allows monitoring of the displacement of random dots painted on the surface of a specimen. By comparison of successive images acquired during a test, image correlation algorithms cross correlate the evolution of dot displacements and accurately calculate strain maps. The system consists of one, or two, 1.4 Mega Pixels cameras allowing 2D, or 3D, measurements respectively. The measurement has a strain range accuracy of between 0.02% and 100%.

Prior to testing the specimen surface was spray painted uniformly with a white background. A random speckle pattern of black dots was then sprayed onto this surface, as shown in figure 3.15.

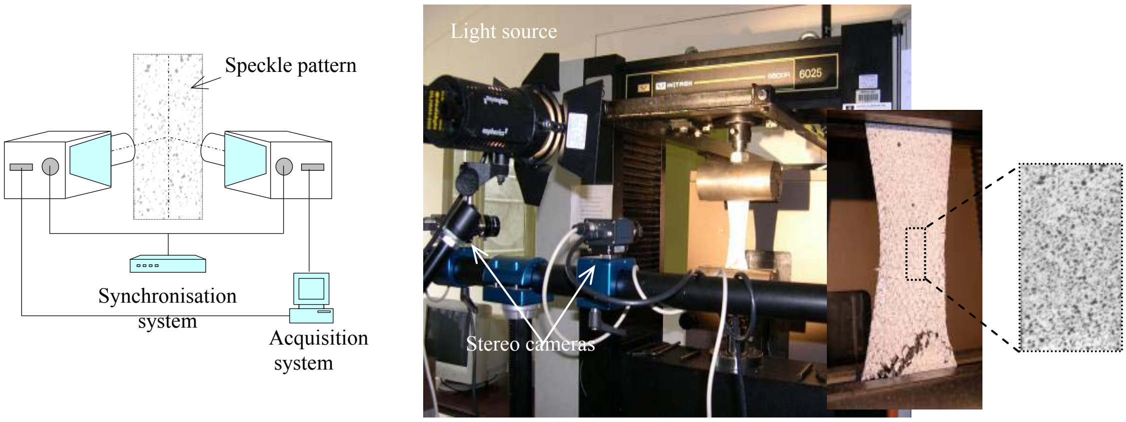

Figure 3.15: Digital Image correlation principle.

An image correlation algorithm enabled calculation of global and local strain maps, such as ε_{xx}. ε_{yy}, ε_{xy}, ε_{11}, ε_{22} and ε_{12} from the video recording. For instance, in figure 3.16, the plot of ε_{12} for a $[\pm45°]_{2S}$ carbon braid specimen is presented; for which a shear band along a tow could be observed and monitored throughout the loading history.

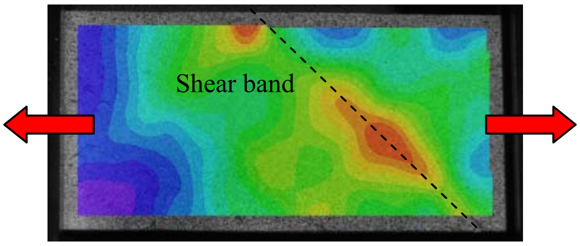

Figure 3.16: Shear strain map for a $[\pm45°]_{2S}$ carbon braided composite.

This technique comprises two main parts; firstly, calibration of the camera system and, secondly, a digital image correlation procedure to determine the full 2D (or 3D) surface displacement fields.

In the calibration step, the Vic3D program [94] was used to determine the relative positions and operating characteristics of the two cameras. An image series of a white dot grid, with known line spacing was acquired by each camera as shown in figure 3.17. This calibration grid has a pattern of white dots on a black background that are equally spaced and have the same diameter. Different plate sizes can be used according to the size of the Region of Interest (ROI). During the stereo calibration procedure the plate, located close to the specimen surface, was rotated at different angles and, for each angle, an image was taken, figure 3.17. From these images a cubic volume containing the ROI was computed.

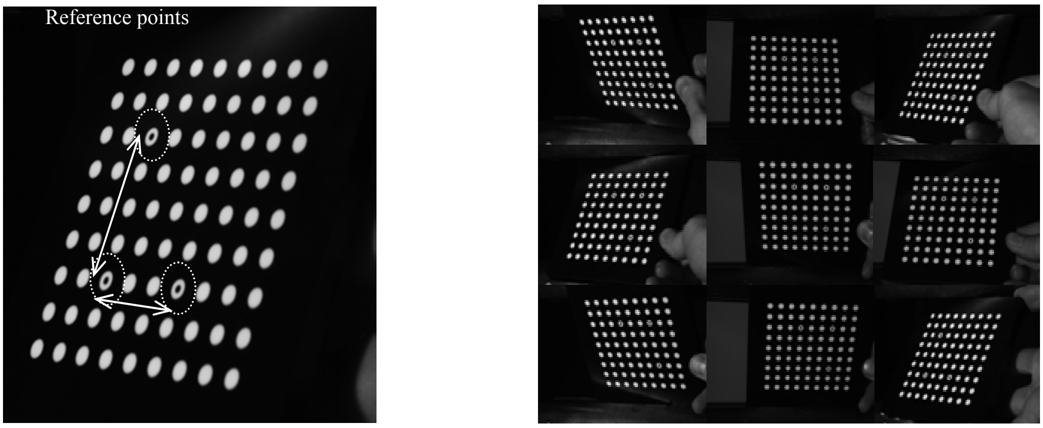

Figure 3.17: Target plate used in stereo calibration.

The specimen was installed in the grips and two Charge Coupled Device (CCD) cameras were placed in front of the specimen. Appropriate lighting, as shown in figure 3.15, was necessary to avoid reflections and post-processing difficulties. Once the calibration was complete the test could proceed and images were taken at a given frequency, usually 1Hz. A compromise had to be found between the testing time and the number of images to avoid excessive data storage.

The post-processing of images was realised in Vic3D using an image correlation algorithm. First, a reference picture was chosen and the zone of interest defined, as shown in figure 3.18 (a). The seed point was used to refer to the point in the reference image where the correlation was started. The correlation algorithms used this seed point to obtain an initial guess for the second point to be analyzed; this sequence is continued until all points in the region of interest are analysed. Generally, the placement of the seed point can greatly influence the amount of work required to select an initial guess. Ideally, the seed point should be placed in the area of the image that undergoes the least motion during the test; for instance, close to the fixed grips as shown in figure 3.18 (a). Subsequently, each image was analysed for which grey value patterns in small regions, called subsets, were tracked during deformation, as shown in figure 3.18 (b).

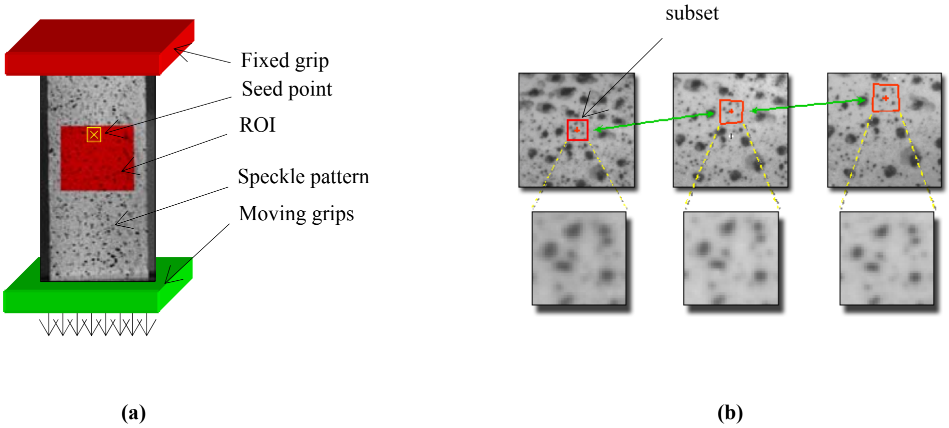

Figure 3.18: DIC post-processing, (a) coupon under tensile loading, (b) analysis of grey patterns deformation [24].

Generally the analysis input parameters in Vic3D for image correlation allow covering a wide range of materials. However, in the cyclic shear test where large deformation and surface degradation were observed, the speckle pattern was changing significantly and default parameters were no longer appropriate to determine deformation. Subset size, subset step and strain window size, three main analysis input parameters, were then tuned to optimise the correlation.

The subset size controls the area of the image used to track the displacement between images. It has to be large enough to ensure a sufficiently distinctive pattern contained in the area used for correlation. For instance, a subset size of 9x9 pixels, figure 3.19 (a), was used for low deformations (0.5-1%) encountered in the compression test on the $[0\text{-}90]_{4S}$ laminates. Instead a much larger subset, 45x45 pixels, was used for $[\pm 45°]_{2S}$ laminates which had the effect of improving point recognition without affecting the sensitivity in local strain variation. Lecompte et al. [90] recently showed that the size of the speckles combined with the size of the used pixel clearly influences the accuracy of the measured displacements.

The step size controls the spacing between subset analyzed during correlation as shown in figure 3.19 (b). For instance, if a step size of 1 is chosen, a correlation analysis is performed at every pixel inside the area of interest. The strain field will be continuous; however, if a large step size is chosen this will result in a discontinuous strain field.

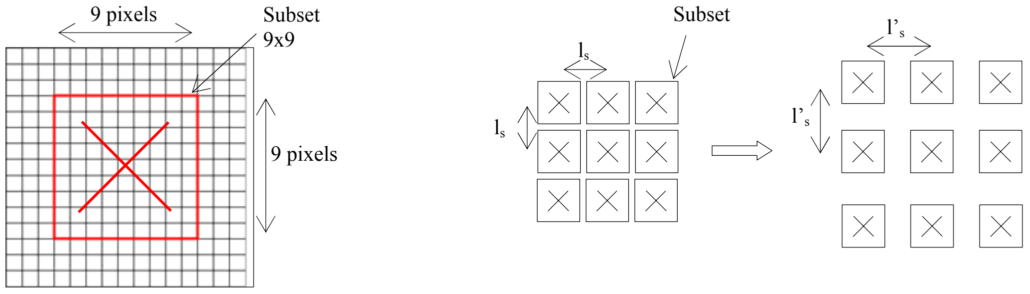

(a) (b)

Figure 3.19: Subset size and step size definition, (a) definition of 9x9 subset size, (b) small and large subset step.

The strain window size can be used to adjust the size of the subset in which the derivatives of the displacement field are calculated. The value indicates the number of neighbouring points. The size of the window used for derivative computations controls the amount of smoothing applied to the data. Larger values correspond to a higher degree of smoothing.

As mentioned above, strains are derived from the displacement fields. Due to planar displacements in the x and y directions the displacement field needs to be differentiated to obtain gradients. For this a local polynomial fit is used to calculate derivatives,

$$\begin{aligned} u(x,y) &= u_0 + u_x x + u_y y \\ v(x,y) &= v_0 + v_x x + v_y y\,. \end{aligned} \tag{3-2}$$

The general Green-Lagrange strain tensor is then used to calculate strains from displacement derivatives,

$$\varepsilon_{ij} = \frac{1}{2}\left(\frac{\partial u_i}{\partial x_j} + \frac{\partial u_j}{\partial x_i} + \frac{\partial u_k}{\partial x_i}\frac{\partial u_k}{\partial x_j}\right), \tag{3-3}$$

with $u_i=u(x,y)$, $u_j=v(x,y)$, $x_i=x$ and $x_j=y$.

The strains can be written as follows,

$$\varepsilon_{xx} = \frac{1}{2}\left(\frac{\partial u(x,y)}{\partial x} + \frac{\partial u(x,y)}{\partial x} + \frac{\partial u(x,y)}{\partial x}\frac{\partial u(x,y)}{\partial x} + \frac{\partial v(x,y)}{\partial x}\frac{\partial v(x,y)}{\partial x}\right), \tag{3-4}$$

$$\varepsilon_{yy} = \frac{1}{2}\left(\frac{\partial v(x,y)}{\partial y} + \frac{\partial v(x,y)}{\partial y} + \frac{\partial u(x,y)}{\partial y}\frac{\partial u(x,y)}{\partial y} + \frac{\partial v(x,y)}{\partial y}\frac{\partial v(x,y)}{\partial y}\right),$$

$$\varepsilon_{xy} = \frac{1}{2}\left(\frac{\partial u(x,y)}{\partial y} + \frac{\partial v(x,y)}{\partial x} + \frac{\partial u(x,y)}{\partial x}\frac{\partial u(x,y)}{\partial y} + \frac{\partial v(x,y)}{\partial x}\frac{\partial v(x,y)}{\partial y}\right).$$

Combining equation (3-2) and (3.4), the strain tensor can be written such as,

$$\begin{pmatrix} \varepsilon_{xx} \\ \varepsilon_{yy} \\ \varepsilon_{xy} \end{pmatrix} = \begin{pmatrix} u_x + \frac{1}{2}\left(u_x^2 + v_x^2\right) \\ v_y + \frac{1}{2}\left(u_y^2 + v_y^2\right) \\ \frac{1}{2}\left(u_y + v_x\right) \end{pmatrix}^{\dagger} . \qquad (3\text{-}5)$$

This technique has increasingly been used in the last 5 years to obtain complete strain field measurement and has advantages over traditional techniques. In composites, for example, it can yield deformations that are non-uniform and the method enables a strain field over a large area of measurement to be obtained. For instance, Ambur et al. [4] have used the DIC technique to determine and model through FE analysis progressive failure of stiffened composite panels, as shown in figure 3.20 (a). Also, Lomov et al. [95] showed another application of this technique by studying NCF in a picture frame test to measure the true fabric variation angle as shown in figure 3.20 (b).

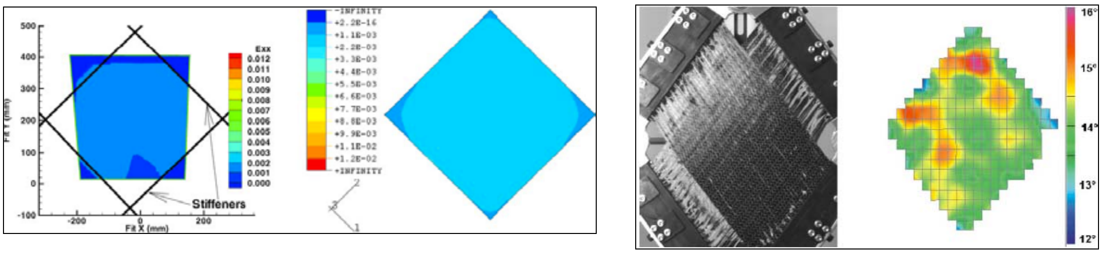

(a) (b)

Figure 3.20: DIC applications, (a) Strain (ε_{11}) field comparison between VIC-3D and ABAQUS, (b) Image of the deformed fabric and shear angle measurement.

In this work, this technique has allowed characterising not only braided composites, but also woven fabric, pre-impregnated unidirectional composites and aluminium which have exhibited larger deformations than were able to be measured using strain gauges. As mentioned previously, strain gauges were mainly used for measuring accurately

---

† The quadratic term in the ε_{xy} calculation is neglected due to the assumption of small displacements.

elastic mechanical properties, such as elastic modulus and Poisson's ratio, due to their limited 3% extension.

A comparison between strain gauges and DIC was conducted in order to validate this relatively new measuring method for textile composites. Comparative results between strain gauges and DIC indicate an excellent correlation. For instance, figure 3.21 presents longitudinal and transverse strains recorded both with strain gauges and DIC for a $[\pm 45°]_{8S}$ T300/913 unidirectional specimen under tensile cyclic loading. The strain curves were identical between the two methods up to a total measured strain of 3%. The DIC technique covered the complete specimen loading history whereas, in this case, strain gauges covered only the part in which specimen undergoes small deformation. For conciseness, only DIC results are shown in the following experimental work as they enable to monitor accurately the complete specimen deformation to failure.

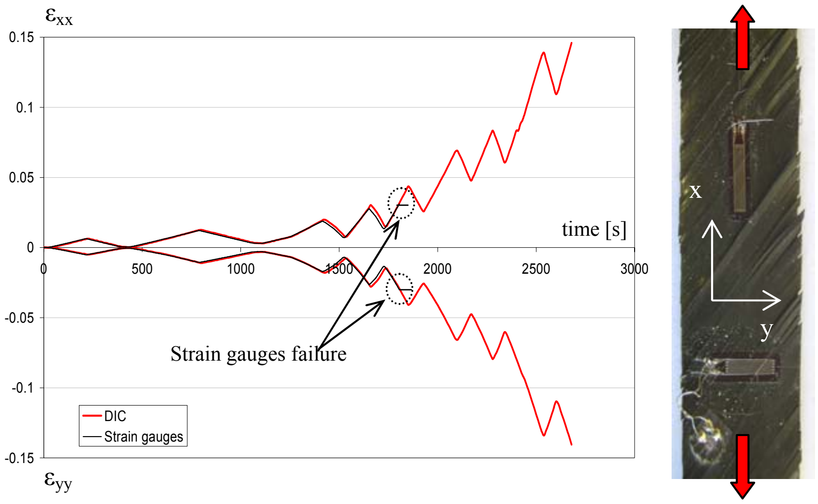

Figure 3.21: DIC versus strain gauge for a tensile cyclic test on a $[\pm 45°]_{8S}$ T300/913 unidirectional laminate.

3.3 2D braided composites failure mechanisms

Braided 2D composites exhibit just two main intra-laminar failure modes; firstly, fibre failure occurring under tensile or compressive loading in fibre direction and, secondly, fibre/matrix interface debonding under shear loading, as pictured in figure 3.22. Inter-laminar failure mode can also occur in multilayered braided composites; indeed, delamination is closely linked to intra-laminar failure especially tow straightening and fibre re-orientation.

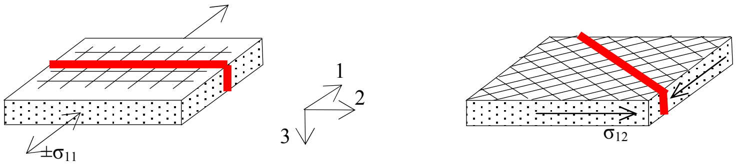

Figure 3.22: Fibre failure and fibre/matrix interface debonding.

Matrix microcracking caused by transverse loading is unlikely since a 2D braided laminate has sufficient transverse reinforcement. However, this failure mode can take place when the braid angle exceeds ±45°, in which case transverse damage is combined with shear damage. However, for this work, this case was not considered since only braid angle lower than ±45° were investigated.

An extensive test campaign was conducted in order to characterise the different modes of failure of carbon and glass braided composites. Usually appropriate regulatory tests, such as the ASTM test standards, are available for generic uni-directional laminates; however, their direct application to braided composites is inappropriate. For instance, braided composites do have some particular features such as continuous architecture, whereas coupon testing is usually performed on specimens cut from flat panels. Therefore, this section proposes an appropriate testing method for braided composites in order to account for their particular mechanical and failure characteristics.

First, preliminary test results on edge and layer effect were conducted on carbon and glass braids. Tensile, compressive and cyclic tests on specific laminates were also conducted in order to characterise elastic properties, damage and plasticity laws required for model calibration. Results obtained from these tests are also presented and discussed. Finally, four point bending on the square cross-section beams is conducted in order to validate the damage model for a ‘complex’ braided component. Testing results obtained for carbon and glass are presented.

Table 3.2 presents the detailed test campaign undertaken for carbon and glass braid characterisation. For each test, laminate, objectives and mechanical properties are defined in detail.

Specimen type	Number of specimens	Fibre orientation/ ply number	Data extracted from test	Test objectives
Monotonic tensile test				
Section 3.3.2 The edge effect: cut and uncut coupons				
C-B	3 cut+3uncut	[±30°]$_{2S}$	E_{xx}, ν_{xy}, σ_{UTS}, ε_{UTS}	– Study to determine difference between mechanical properties and failure mechanisms for coupon having cut and uncut edges for two different braid angles. – Used for model validation.
G-B	3 cut+3uncut	[±30°]$_{2S}$		
C-B	3 cut+3uncut	[±45°]$_{2S}$		
G-B	3 cut+3uncut	[±45°]$_{2S}$		
Section 3.3.3 Influence of the number of braided layers on braided composites				
C-B	3	[±45°]$_{2}$ 1 layer	G^0_{12}, ν_{12}, damage and plasticity laws equations	– Influence number of layers on composites strength, damage and plasticity for braids
	3	[±45°]$_{2S}$ 2 layers		
	3	[±45°]$_{4S}$ 4 layers		
	3	[±45°]$_{6S}$ 6 layers		
Section 3.3.4 Tensile loading in the fibre direction				
C-B	10	[0-90°]$_{4S}$	E_{xx}, ν_{xy}, σ_{UTS}, ε_{UTS}	– Mechanical characterisation of carbon and glass specimens loaded under tension in the fibre direction. – Used for model validation
G-B	10	[0-90°]$_{4S}$		
C-WF	1	[0-90°]$_{8S}$	E_{xx}, ν_{xy}, σ_{UTS}, ε_{UTS}	– Used for comparison purposes between braid and woven fibre failure modes.
Monotonic compression test				
Section 3.3.5 Compressive loading in the fibre direction				
C-B	6	[0-90°]$_{4S}$	E_{xx}, σ_{UTS}, ε_{UTS}	– Mechanical characterisation of carbon and glass specimens loaded under compression in the fibre direction. – Used for model validation
G-B	7	[0-90°]$_{4S}$		
Cyclic tensile test				
Section 3.3.6 Tensile shear cyclic loading				
C-B	5	[±45°]$_{2S}$	G^0_{12}, ν_{12}, damage and plasticity laws equations	– Determination of the damage and plasticity laws – Used for model validation
G-B	5	[±45°]$_{2S}$		
C-UD	1	[±45°]$_{8S}$		– Used to demonstrate that fibre rotation should be considered even for uni-directional and WF laminates
C-WF	1	[±45°]$_{8S}$		
Al	2	-	-	– Use for comparison in hysteresis loop explanation
Four point bending				
Section 3.3.7 Carbon and glass beams under 4 point bend loading				
C-B	2	[±30°]$_{2S}$	Stiffness Force/displacement at failure + quantitative information on strain field	– Used for model validation
G-B	2	[±30°]$_{2S}$		

C-B: Carbon braid, STS/{LY3505/XB3403}, 24k, Ø100mm, 84 ends, 1x1, 40% and 50% Vf for 45° and 30° braid angle respect.
G-B: Glass braid, E-glass/{LY3505/XB3403}, 24k, Ø100mm, 84 ends, 1x1, 40% and 50% Vf for 45° and 30° braid angle respect.
C-WF: Carbon woven fabric, IM9/2035, 6k, 2x2, prepreg, 62% Vf
C-UD: Carbon uni-directional, T300/913, prepreg, 68% Vf
Al: Aluminium 6014/T6

Table 3.2: Test programme undertaken for braids mechanical characterisation.

3.3.1 Determination of the region of interest for strain calculation

3.3.1.1 Region of Interest (ROI) and Repetitive Unit Cell (RUC)

ASTM standards [8] [9] are available for determining elastic and failure properties of carbon fibre reinforced composites, either by using strain gauges, or extensometers located at the mid-length of the specimen where deformation is assumed uniform. In this case, the ROI is limited corresponding either to the strain gauge or extensometer gauge length. However, larger zones of interest, even equal to the specimen size, can be selected with the DIC technique.

The representative strain measurement is related to the type of composite tested; for instance unidirectional laminates require relatively small measurement regions (5-10mm length) to reflect the specimen global behaviour; however, for fabrics this region can be larger and depends on the Repetitive Unit Cell (RUC) size. Braided composites, in particular, have a significantly high degree of inhomogeneity resulting in non-uniform strain distribution within a given unit cell and it has been recommended by Minguet et al. that test coupons have a width covering at least 3 unit cells [104].

These local effects due to braid heterogeneity are not influential in the elastic region; indeed, Falzon et al. [34] proved that scatter in Young’s modulus measured with 12.7x4.5, 7.6x6.4 and 12.7x12.7mm strain gauges at various positions produce only 3% standard deviation, which confirms the validity of using strain gauges in the elastic region. Nevertheless, beyond elasticity, as local damaging occurs in the specimen, the strain distribution becomes increasingly non-uniform; for instance, figure 3.23 shows the strain concentration that were recorded at tow cross-over points on a $[0\text{-}90°]_{4S}$ carbon braided specimen. Therefore, through this technique the limitations of conventional (non-optical) measurement techniques are shown.

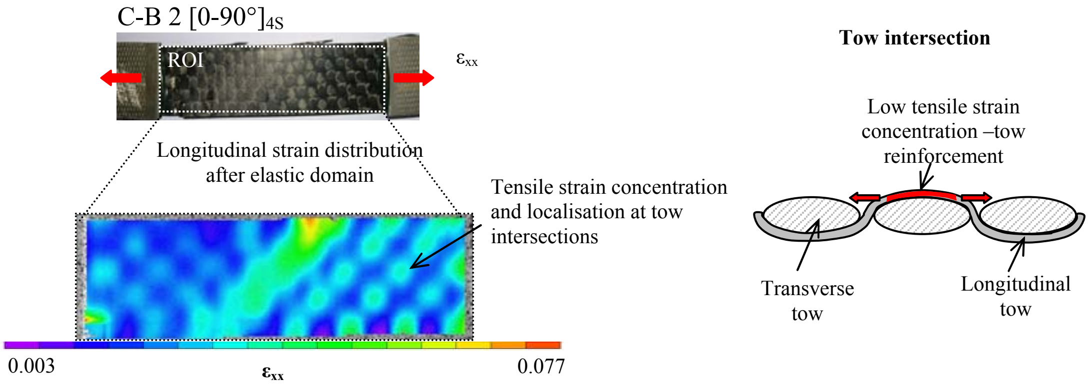

Figure 3.23: Strain concentration localisation for a [0-90°]$_{4S}$ carbon braided specimen.

3.3.1.2 Region of Interest (ROI) and stress concentration due to clamping conditions

Strain concentrations from the loading application points were also found to be an issue. A coupon under tensile loading with both ends clamped will exhibit strain concentrations in the neighbourhood of the clamping regions. For instance, figure 24 (a) shows rectangular strain concentration areas close to the grips for a [0-90°]$_{4S}$ carbon braid; also, for a different fibre orientation, such as [±30°]$_{2S}$, the shape of the strain concentration area changes to a triangular shape, figure 3.24 (b).

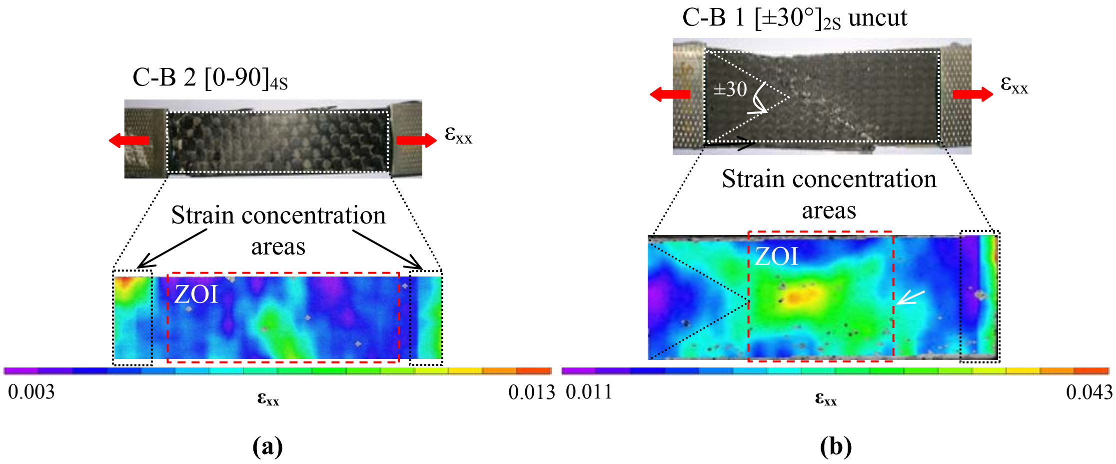

Figure 3.24: Strain concentrations at grips, (a) for a [0-90°]$_{2S}$ carbon braided specimen, (b) [±30°]$_{2S}$ carbon braided specimen.

The shape and size of the strain concentration have been found to be influenced by the coupon fibre orientation. The zone of interest was subsequently modified with respect of specimen size, and lay-up. Generally, the ROI was chosen to be centred relative to the specimen surface and removed from the clamping regions of a distance equal to the specimen width; this follows the Saint-Venant principle [59].

All regions of interest chosen in this work covered more than three unit cells and results obtained were found to be consistent. However, difficulties were encountered for compression tests where only a small ROI was possible due to geometric constraints of the test. This will be further discussed in the section dedicated to compression testing.

3.3.2 The edge effect: cut and uncut coupons

In comparison with woven fabrics braided composites exhibit fibre continuity which allows them to undergo larger deformation through tow scissoring as mentioned earlier in section 2.3.2.3. This feature will affect the damage and plasticity laws and must be integrated in the model calibration for correct representation of the material. For instance, in the case of the braided beam modelling, damage law and plasticity input parameters where obtained from uncut specimens since the beam is a closed section and has fibre continuity.

The following test program was therefore undertaken to quantify the difference between mechanical properties and failure for coupons having cut and uncut edges. A 40mm diameter braided preform with 24K STS tows manufactured by Eurocarbon [33], and the resin/hardener was LY3505/XB3403 from Huntsman Advanced Materials [66] was manufactured using the resin infusion process. The tubular braids were carefully flattened in order to maintain the fabric architecture prior to impregnation. Two types of specimen architecture were considered having ±30° and ±45° fibre angles. Figure 3.25 shows the flattening of the braids which were impregnated and, after curing, either cut, or left intact, to provide the two types of edge conditions.

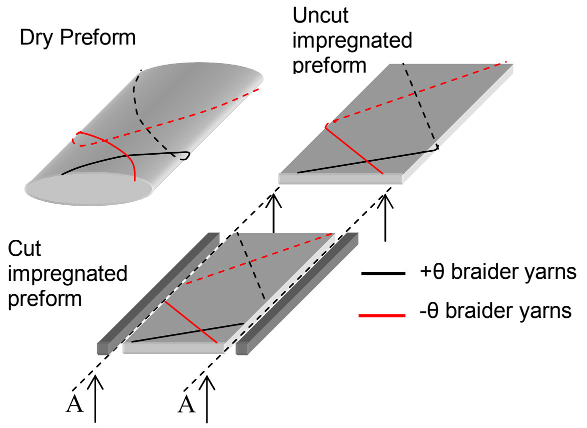

Figure 3.25: Preparation of the cut and uncut braid coupons [118].

For both the $[\pm30°]_{2S}$ glass and carbon braided composite the cut and uncut coupons had identical elastic properties; however, the uncut coupons showed significantly greater ultimate stress and strain to failure as shown in figure 3.26 and table 3.3. The observed failure modes are different for the two types of specimens. The loss of tow continuity in the cut specimen leads to a combination of tow pull-out and tow failure which initiate at the free edges; whereas, for the uncut specimen tow breakage initiates at the area of highest stress concentration adjacent to the tabs.

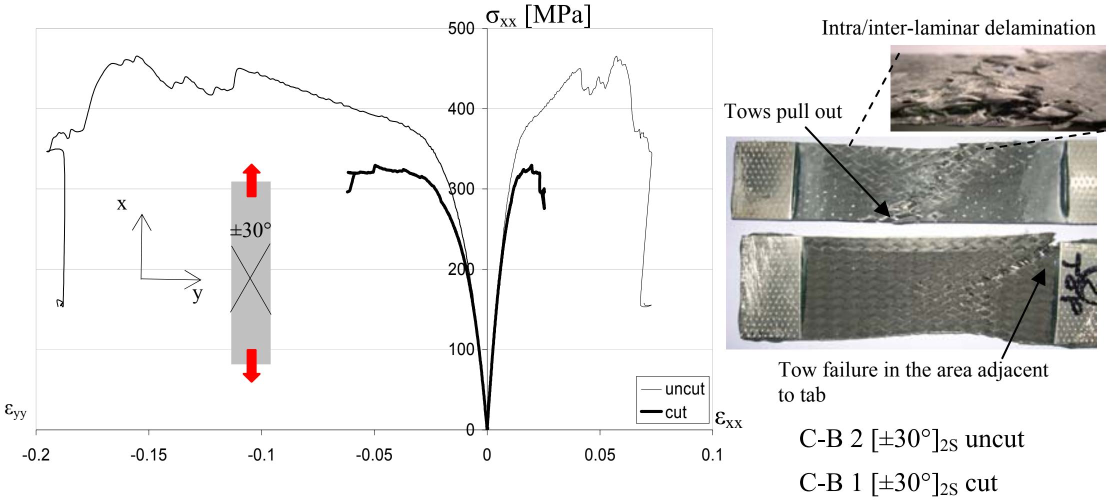

Figure 3.26: Comparison of results for the cut and uncut $[\pm30°]_{4S}$ carbon braided coupons.

specimens	Width [mm]	Thickness [mm]	E_{xx} [GPa]	ν_{xy}	σ_{UTS}[†] [MPa]	ε_{UTS}
Carbon						
C-B 1-uncut	45.50	1.95	38.461	1.227	465.29	0.0574
C-B 2- uncut	46.45	1.87	43.394	1.297	465.54	0.02478
C-B 3- uncut	46.92	1.87	41.412	1.293	429.26	0.0258
C-B 5-cut	36.06	1.90	38.400	1.359	329.24	0.0197
C-B 6-cut	37.02	1.89	40.231	1.124	319.42	0.0185
C-B 7-cut	36.53	1.88	41.245	1.213	332.56	0.0212
Glass						
G-B 1-uncut	48.58	1.72	23.680	0.652	428.75	0.0642
G-B 2- uncut	47.04	1.89	21.936	0.621	394.14	0.0538
G-B 3- uncut	47.5	1.85	21.752	0.608	359.38	0.0461
G-B 5-cut	41.72	1.85	20.548	0.632	288.71	0.0436
G-B 6-cut	40.93	1.90	21.678	0.624	275.67	0.0450
G-B 7-cut	42.21	1.88	20.934	0.617	281.35	0.0410

Table 3.3: Comparison of mechanical properties for the cut and uncut [±30°]$_{2S}$ carbon and glass braided coupon (50% mean Vf).

In the case of the [±45°]$_{2S}$ specimens a similar trend was observed to that shown in figure 3.26 except that the difference between cut and uncut strength was reduced [118]. This is due to the increased transfer of load by shear matrix mechanisms rather than fibre mechanisms; thus the anchorage effect of the fibres at the edges is less significant.

This brief study indicates that braid angle strongly influences the strength between ‘cut’ and ‘uncut’ braid reinforced coupons. It shows that failure in biaxial ‘open’ braids which are dominated by shear matrix failure and does not greatly affect the failure strength using the two edge conditions. Whereas for low angle braids the load transfer mechanisms are fibre dominated and the difference between ‘cut’ and ‘uncut’ edge condition is much greater. The width of the coupon tested can also be expected to influence these trends. It may be concluded that mechanical data obtained from cut coupons should be used with caution for the FE analysis of closed sectional members or large panels.

[†] The strength as failure was calculated using transverse strain ε_{yy} in order to take into account width reduction.

***NB**: for conciseness, the study on cut and uncut specimens is not fully presented in this section. Part dedicated to damage and plasticity laws is fully discussed in previous publication [118] (available in the Appendices chapter).*

3.3.3 Influence of the number of braided layers

A further variable that influences braid mechanical properties is the number of plies used in the test coupon as found, for example, in [93] for woven fabric laminates. Laminates having only a few plies tend to have distinct resin rich pockets between fabric tows as shown in figure 3.27.

Figure 3.27: Fabric architecture and potential resin rich areas for a single layer braid.

As additional plies are added these areas are displaced with tows from overlaid plies leading to greater material homogeneity. The effect on mechanical properties is investigated for four [±45°] braids having cut edges with 1, 2, 4 and 6 layers. Cyclic loading has been applied to determine the damage and hardening laws for each lay-up. Figure 3.28 shows that the number of plies does not appear to influence the damage law; however, it does have a significant effect on the hardening law, figure 3.28.

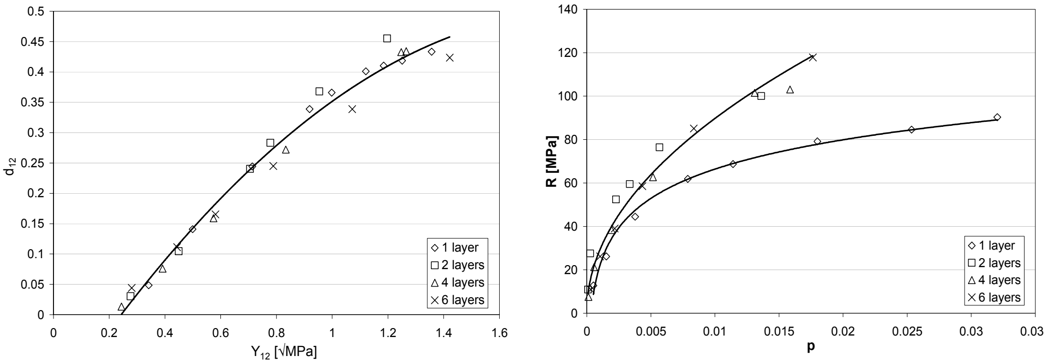

Figure 3.28: Damage and hardening laws for the different braid lay-ups.

Explanations related to damage and plasticity laws determination are presented in chapter 4.

The hardening law shows that a single ply exhibits significantly more deformation compared to the other lay-ups. This is probably due to the higher void content allowing greater freedom for fabric deformation. For laminates with two or more plies the plasticity law starts to become consistent. However, it must be noted that these observations were made on test measurements conducted to only about 3% strain[†] which was the limit of the strain gauges. It has also been observed that braids with low ply numbers are liable to fail at a slightly lower failure strain, probably due to inconsistencies in the fabric architecture.

***NB**: for conciseness, the study on the braid layer number effect is not fully presented in this section. Part dedicated to damage and plasticity laws is fully discussed in previous publication [118] (available in the Appendices chapter).*

3.3.4 Tensile loading in the fibre direction

Two sets of 10 braided carbon and glass specimens were cut from two panels with a 40% mean V_f using the 2-D biaxial braided preforms. The specimens tested were straight sided coupons according to ASTM D3039 requirements [9]. Aluminium chamfered tabs with a 45° taper, 35mm long and 1.5 mm thick were bonded to the ends of the gauge length in order to promote failure in the gauge section, giving an approximate gauge length of 110mm. The respective dimensions of the specimen are shown in figure 3.29.

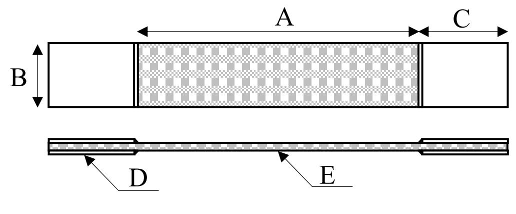

A: 110mm
B: 25mm
C: 35mm
D: 1.5mm
E: 3.0mm

Figure 3.29: Dimensions for $[0\text{-}90°]_{4S}$ tensile specimens.

Specimens were clamped at the tabbed-ends within a hydraulic testing machine and loaded to failure in stroke mode at a rate of 0.5mm/min. Failure was considered as the

---

[†] This study was conducted before the DIC technique was available.

point of first significant load drop. Tests have been carried out on carbon and glass braided composites and test results are presented and discussed in the following.

3.3.4.1 Results on [0-90°]$_{4S}$ carbon braided specimens

Generally, under tensile loading, a [0-90°]$_{4S}$ specimen exhibits a linear elastic behaviour to failure; in this case fibres in the 0°-direction mainly carry the load and the contribution of transverse fibres is negligible. For instance, a [0-90]$_{8S}$ IM9/2035 pre-impregnated woven twill fabric, 62% volume fraction, 6k tow size was tested under tensile loading showing an expected brittle elastic behaviour and failure perpendicular to the loading axis, as shown in figure 3.30.

The current carbon braided composite specimen of a larger tow size, 24k, and lower volume fraction (40%), also exhibited a linear behaviour, but only up to 0.60-0.65% longitudinal strain. After this threshold, a non-linear behaviour, up to 2.4% longitudinal failure strain was recorded, as shown in figure 3.30. It is worth noting that according to STS fibre properties (table 2.2), fibre failure should have occurred at 1.7% strain.

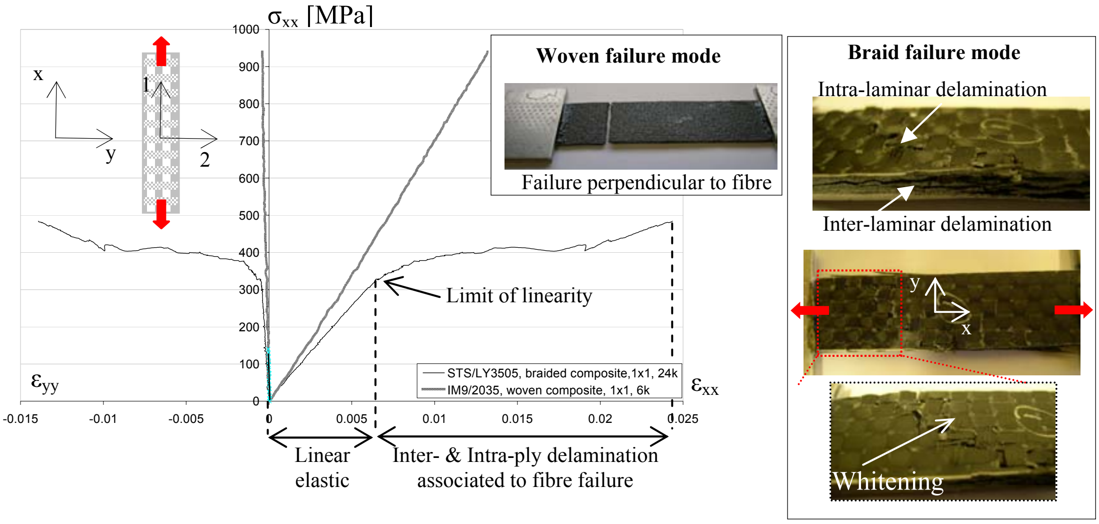

C-B 5 [0-90°]$_{4S}$ C-WF 1 [0-90°]$_{8S}$

Figure 3.30: Failure mode comparison between a [0-90°]$_{4S}$ STS/LY3505 carbon braided and woven fabric composites under tensile loading.

The braid failure mode was not fibre dominated as for the woven specimen, but it corresponds to a mixed mode between tow straightening and fibre failure. Indeed, until the limit of elasticity, the two materials behaved identically; however, beyond this point the braided specimen starts to damage and lose structural integrity. Visual inspection during testing, revealed whitening at each tow intersection which is a sign of tow/matrix debonding and matrix microcracking. Delamination between layers could also be observed, as shown in figure 3.30.

In comparison with the linear elastic failure of the woven fabric specimen, no delamination was observed. This failure mode discrepancy found for the braided specimen is not related to the matrix system mechanical properties as they are similar for both specimens, table 3.4.

Matrix systems	LY3505/XB3403	2035
Tensile modulus [GPa]	3.18-3.28	3.1
Tensile strength [MPa]	70-74	72

Table 3.4: Comparison between LY3505 and 2035 epoxy resins.

As visual inspection also revealed no macro-voids, and micro-analysis no apparent micro-voids, damaging was unlikely to be initiated from inherent specimen manufacturing defects.

The woven fabric has a compact fibre architecture and, consequently, also has a higher fibre volume fraction. These two factors most likely explain the fibre dominated linear elastic failure mode observed experimentally. For the heavy tow braid composite the large tow size and high degree of waviness creates resin rich pockets between tows and at tow intersections, thus reducing the fibre volume fraction to about 40%. The large resin pockets in the braided coupon undergo damage and plasticity as the tows straighten in the loading direction, leading to a large non-linear strain to failure; figure 3.31 schematically shows this failure mechanism and the corresponding plot of surface strain (ε_{xx}), where again the non-uniform distribution due to local damage is clearly visible.

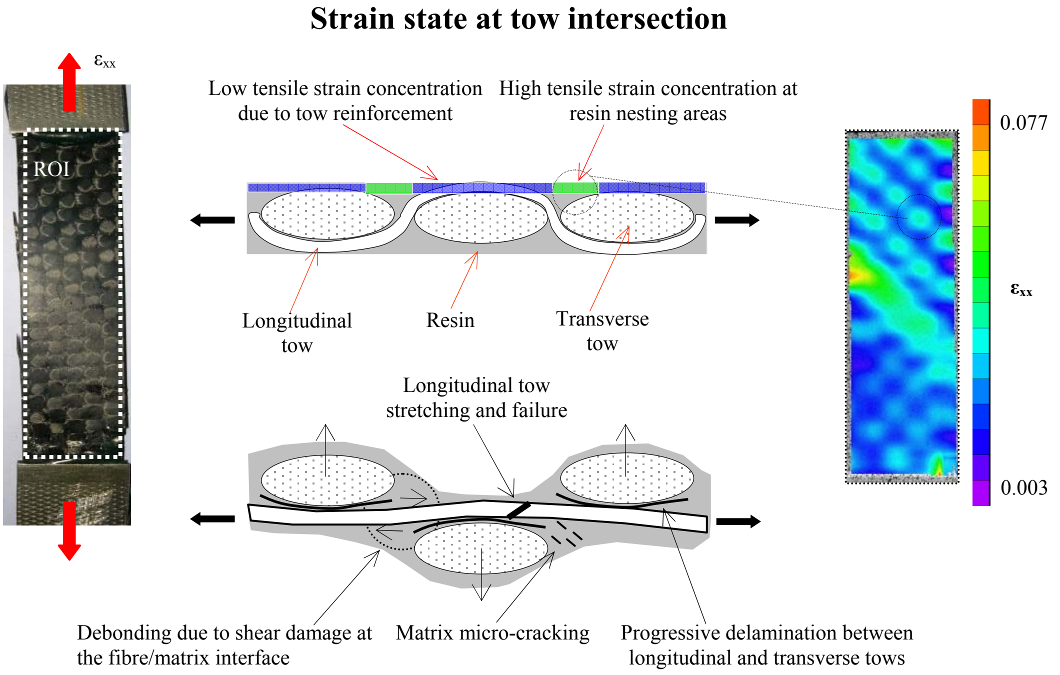

Figure 3.31: **Schematic of tow straightening mechanism observed in $[0\text{-}90°]_{4S}$ braid specimens under tensile loading.**

Associated with this failure, local separation between braid tows initiate and grow, leading to a global debonding (or delamination) between longitudinal and transverse tows and between distinct braid layers in the case of multilayered braids. This mechanism has been observed using the DIC technique, figure 3.32 with which intra-laminar delamination between tows can be monitored as the progressive appearance of peaks on the 3D plot of specimen surface displacements.

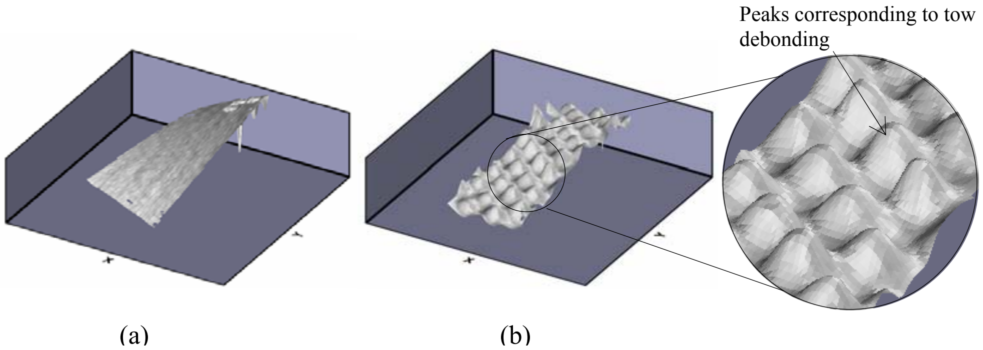

Figure 3.32: **Surface plot of a carbon braided composite (C-B 5 $[0\text{-}90°]_{4S}$), (a) reference state, (b) state after elastic limit.**

Progressive inter-laminar delamination was visually observed during testing, as shown in figure 3.30. However, this mechanism could not be quantified as it would have required non-destructive testing techniques. Table 3.4 summarises mechanical properties obtained from tensile tests on $[0\text{-}90°]_{4S}$ specimens.

specimens	Width [mm]	Thickness [mm]	E_{xx} [GPa]	ν_{xy}	σ_{UTS}[†] [MPa]	ε_{UTS}
C-B 1	26.53	2.96	50.630	0.052	495.15	0.016
C-B 2	26.03	2.93	49.390	0.055	490.13	0.018
C-B 3	26.93	2.96	49.433	0.053	520.32	0.021
C-B 4	25.85	2.88	49.342	0.05	514.05	0.0166
C-B 5	24.93	2.88	51.489	0.055	484.21	0.0201
C-B 6	24.91	2.87	52.459	0.054	486.15	0.0201
C-B 7	25.85	2.8	45.042	0.055	514.72	0.0170
C-B 8	26.17	3.01	51.037	0.055	512.43	0.0183
C-B 9	25.41	3.01	48.453	0.054	512.38	0.0210
C-B 10	26.01	2.92	50.977	0.057	508.15	0.0193
Mean	**25.86**	**2.92**	**49.825**	**0.054**	**503.76**	**0.0184**
STDEV	0.64	0.06	2.067	0.002	13.42	0.0018

Table 3.5: Mechanical characteristics for $[0\text{-}90°]_{4S}$ STS fibre carbon/LY3505 braided specimens (40% mean V_f) under monotonic tensile loading.

3.3.4.2 Results on $[0\text{-}90°]_{4S}$ glass braided specimens

Glass fibre unidirectional laminates loaded in the fibre direction exhibited similar linear elastic behaviour than unidirectional carbon laminates. In table 2.2, the comparison between E-glass and STS carbon fibres showed that intrinsically glass exhibits lower stiffness but larger deformation to failure (4.8% against 1.7%). However, test results obtained showed that carbon and glass braid specimens exhibited similar strain at failure. The glass specimen demonstrated a non-linear deformation as illustrated in figure 3.33, and the same mechanisms described previously for the carbon specimens also occurred. After the linear elastic domain, a combination of intra- and inter-ply delamination progressively damaged the specimen leading to fibre failure as shown in figure 3.33.

[†] The strength at failure was calculated assuming a constant cross-section size; this reasonable approximation was necessary due to the difficulty to measure thickness changes.

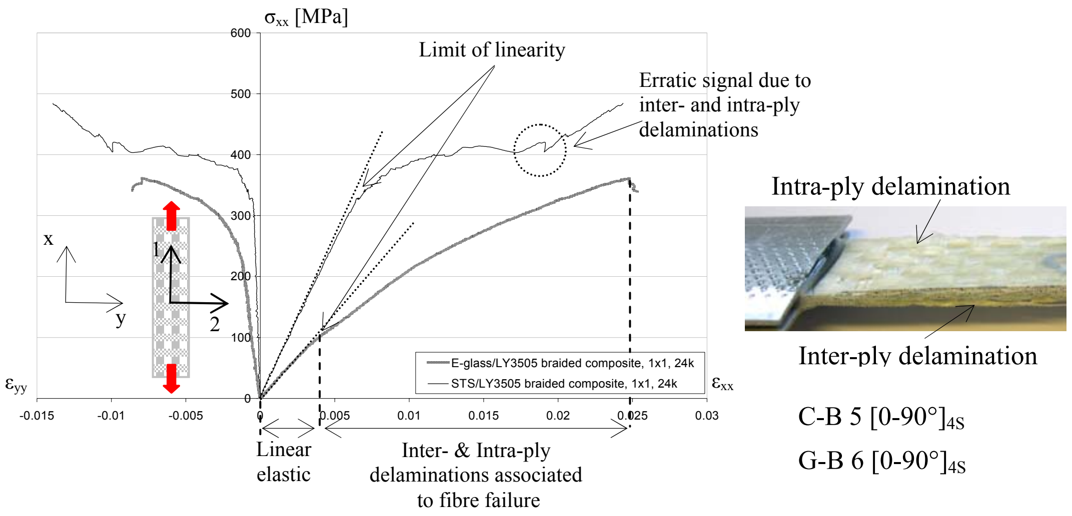

Figure 3.33: Comparison between [0-90°]$_{4S}$ E-glass and STS carbon braided specimens.

It is noteworthy that a ‘smoother’ curve has been found for the glass specimen compared to the erratic carbon behaviour, as shown in figure 3.33. Due to a lower stiffness and higher ultimate strain, glass fibre is relatively more ductile than carbon fibre which, combined with the matrix, it gives a more homogeneous specimen in terms of mechanical properties. Indeed, E-glass having closer mechanical properties to resin than STS carbon fibre leads to lower stress concentrations at the fibre/matrix interface and does not result in a major local failure, but in a more diffuse damage and progressive delamination.

The overall experimental results found for the material elastic and strength properties are presented in table 3.5.

specimens	Width [mm]	Thickness [mm]	E_{xx} [GPa]	ν_{xy}	σ_{UTS} [MPa]	ε_{UTS}
G-B 1	26.36	2.98	26.351	0.158	381.63	0.0280
G-B 2	25.85	3.02	25.991	0.154	387.82	0.0276
G-B 3	25.97	3.01	24.220	0.155	401.30	0.0311
G-B 4	25.87	3.01	28.416	0.146	373.36	0.0300
G-B 5	25.65	2.91	27.343	0.142	409.78	0.0272
G-B 6	24.90	2.89	27.530	0.180	360.98	0.0247
G-B 7	25.29	2.89	27.271	0.167	352.74	0.0248
G-B 8	25.17	3.02	27.234	0.145	382.21	0.0285
G-B 9	25.23	3.01	25.589	0.151	401.34	0.0319
G-B 10	25.04	2.92	26.678	0.149	389.23	0.0294
Mean	**25.53**	**2.96**	**26.662**	**0.1547**	**384.039**	**0.0283**
STDEV	0.47	0.05	1.185	0.0114	18.060	0.0024

Table 3.6: Mechanical characteristics for [0-90°]$_{4S}$ E-glass/LY3505 braided specimens under monotonic tensile loading.

3.3.5 Compressive loading in the fibre direction

3.3.5.1 Compression rig design for braided composites

The following testing programme has been conducted to determine in-plane compressive properties of glass and carbon braided composites. The compression specimens were cut out from the same panels as used for tensile specimens. The specimens tested were parallel sided coupons based on the ASTM standard D3410 [8] and were loaded quasi-statically at 0.5mm/min

A compression rig was specifically designed for this test, figure 3.34 (a), and is based on the IITRI (Illinois Institute of Technology Research Institute) rig originally dedicated to unidirectional composites testing. As compression test results using this test method are highly sensitive to specimen alignment, with respect to the longitudinal axis of loading, a specimen alignment rig was also designed, as shown in figure 3.34 (b), to ensure that specimens are mounted axially with respect to the wedges and loading direction.

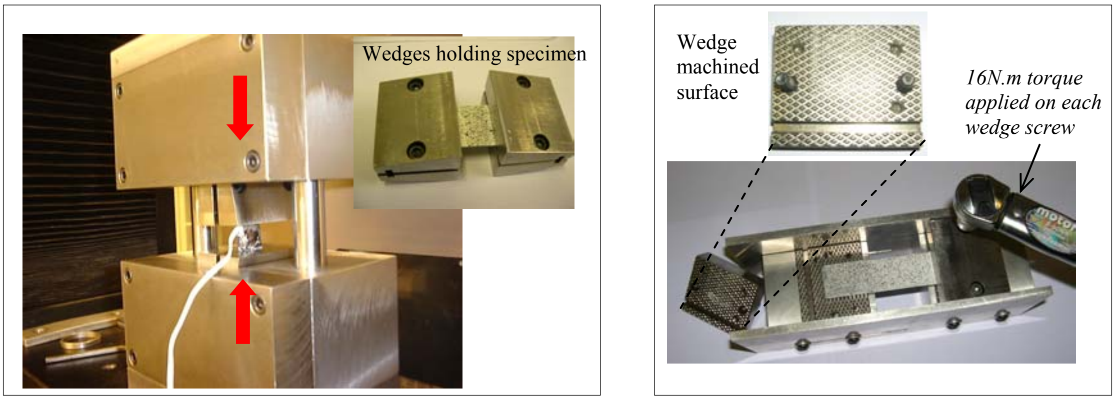

(a) Compression rig designed from the IITRI standard [8]

(b) Specimen alignment rig

Figure 3.34: Compression test and specimen alignment rigs.

3.3.5.2 Consideration on specimen dimensions

The original test was designed for a [0°] unidirectional composite specimen of 10mm width and 10-25mm gauge length. However, for textile composites, and particularly for the large tow size and large unit cell braids investigated, specimens having a wider width and longer gauge length are required. Indeed, as it has been previously stated the test region should comprise of at least three RUC [104] to ensure homogenous strain distribution within the specimen. In the [0-90°] configuration, the RUC size of braid specimen is 8mm and therefore specimens of a least 24mm width and gauge length should be used. Specimens were cut from the same panels as used for tensile specimens; these had a fixed thickness of 3mm. This thickness was used to determine the gauge length limit based on the Euler buckling criteria [105]. A conservative assumption of 'ideal pinned-ends' was used, as shown in figure 3.35.

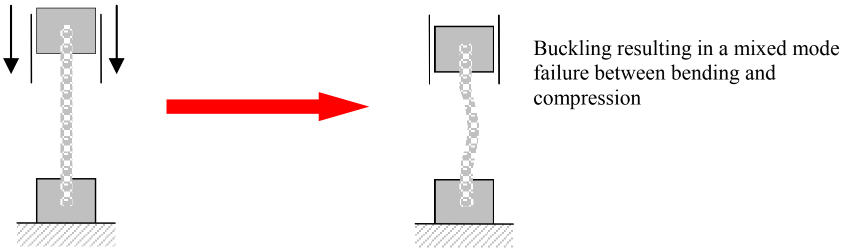

Figure 3.35: Euler buckling column for a rectangular beam [105].

The critical buckling length has been calculated using the simple Euler's formula for a pin ended beam,

$$P = \frac{\pi^2 E\, I_{Min}}{L^2}, \tag{3-6}$$

where the moment of inertia I for the beam cross section is,

$$I_{Min} = \frac{bh^3}{12}, \tag{3-7}$$

and b, h and L are the specimen width, thickness and unsupported gauge length respectively. As a safety factor, the modulus E and buckling load P have been conservatively chosen to be equal to the tensile modulus 50GPa and failure load 37500N measured from the tensile test. An unsupported length limit of 27mm has been obtained which does cover three unit cells. Practically, such a small and accurate gauge length is difficult to achieve if tabs are used; therefore, the gauge length could vary between 20 to 27 mm. For these tests aluminium chamfered tabs with 45° taper, 35mm long and 1.5 mm thick were bonded to the specimen to ensure load introduction. The specimen dimensions are presented in figure 3.36.

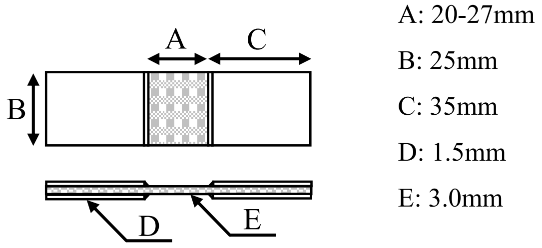

Figure 3.36: Dimensions for the $[0\text{-}90°]_{4S}$ compression specimens.

3.3.5.3 Results on $[0\text{-}90°]_{4S}$ carbon and glass braided specimens

Using the above specimen dimensions a first series of tests were conducted on both carbon and glass braided specimens using strain gauges bonded to each specimen face in order to monitor potential specimen buckling. Figure 3.37 shows a typical test in which both stress-strain curves obtained from surfaces A and B are monitored. These demonstrate a brittle linear elastic mode of failure. Even though the two curves are not identical, this plot indicates that both surfaces are under pure compression and no significant bending has occurred. The divergence is probably related to manufacturing defects; indeed, tow alignment on face A and B might have not been perfectly parallel.

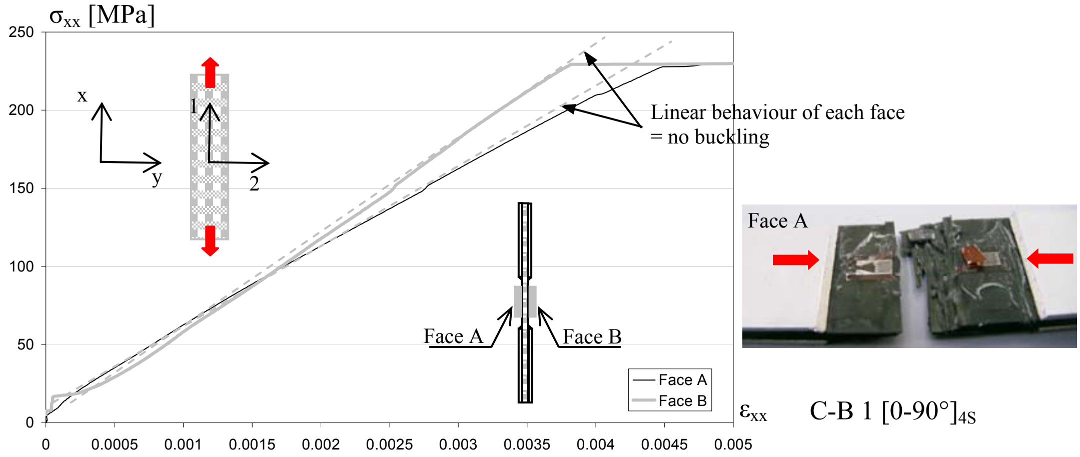

Figure 3.37: Buckling monitoring using strain gauges.

In later work, the digital image correlation technique was used in order to fully understand strain distribution in the specimen during loading. The ROI chosen covered the full specimen gauge area as shown in figure 3.38.

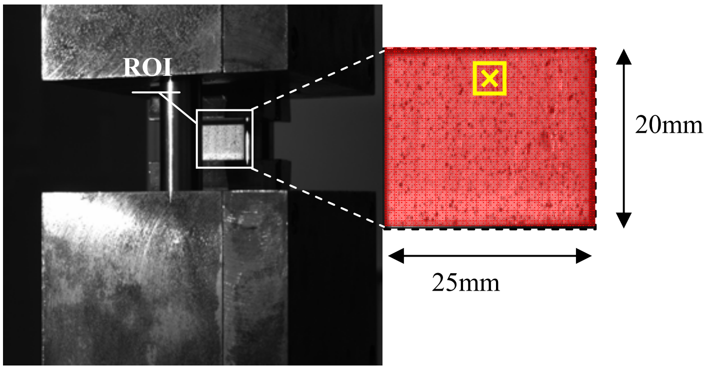

Figure 3.38: ROI used for strain measurement in compression tests.

Results from DIC analysis showed that out-of-plane displacements at the specimen surface were negligible, confirming the results found using strain gauges. Also, this indicates that wedges holding the specimen are well aligned and parallel, transmitting a pure planar compressive loading. Figure 3.39 presents the results for both carbon and glass specimens revealing expected linear elastic behaviour up to failure. Even though glass exhibits lower compressive stiffness and strength than carbon, it can withstand larger compressive strain. Also, average compressive stiffness found for each material was comparable to their tensile stiffness. This has helped to validate the test method for determining compressive properties.

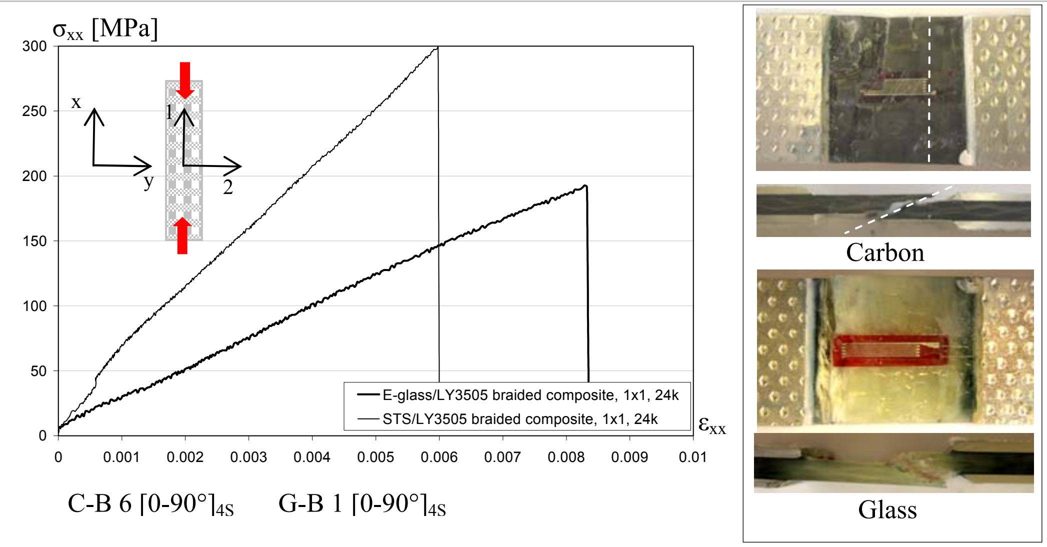

C-B 6 [0-90°]$_{4S}$ G-B 1 [0-90°]$_{4S}$

Figure 3.39: Comparison between carbon and glass [0-90°]$_{4S}$ specimens under monotonic compressive loading.

This test method seems appropriate for the elastic properties determination; however, relatively high standard deviations were found for ultimate stress and strain as shown in table 3.7 and 3.8.

specimens	Width [mm]	Thickness [mm]	E_{xx} [GPa]	σ_{UTS} [MPa]	ε_{UTS}
C-B 1	24.92	2.92	46.8	226.8	0.0047
C-B 2	25.08	3.15	48.29	210.1	0.0051
C-B 3	25.01	3.12	44.5	218.0	0.0046
C-B 4	25.07	3.13	44.3	272	0.0062
C-B 5	25.02	3.05	48.9	244.8	0.0054
C-B 6	25.08	2.92	45.7	295.3	0.0059
Mean	**25.03**	**3.04**	**46.4**	**244.5**	**0.0053**
STDEV	0.06	0.10	1.9	33.2	0.0006

Table 3.7: Mechanical characteristics for [0-90°]$_{4S}$ STS carbon/LY3505 braided specimen (40% mean V_f) under monotonic compressive loading.

specimens	Width [mm]	Thickness [mm]	E_{xx} [GPa]	σ_{UTS} [MPa]	ε_{UTS}
G-B 1	24.95	2.98	24.3	170.7	0.0072
G-B 2	25.06	3.00	23.1	148.7	0.0069
G-B 3	25.16	3.01	24.9	228.2	0.0099
G-B 4	25.03	2.94	26.8	180.1	0.0067
G-B 5	25.05	2.96	22.3	247.8	0.0119
G-B 6	25.13	3.02	27.0	212.3	0.0079
G-B 7	25.01	3.01	24.7	192.7	0.0082
Mean	**25.05**	**2.98**	**24.6**	**197.9**	**0.0084**
STDEV	0.07	0.03	1.9	37.6	0.0020

Table 3.8: Mechanical characteristics for $[0\text{-}90°]_{4S}$ E-glass/LY3505 braided specimen (40% mean V_f) under monotonic compressive loading.

3.3.5.4 Failure mode and strain distribution

The failure mode observed was a combination of shear and delamination. Shear failure appeared as kink bands and is a local shear instability in which a fibre tow rotate and rupture, causing almost total loss of axial strength for the tow. In addition, interlaminar delaminations occur between layers and intra-laminar delamination between tows within the same layer, as shown schematically in figure 3.40.

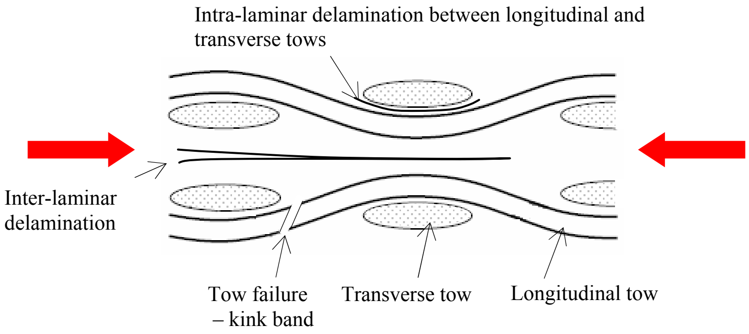

Figure 3.40: Illustration of delamination and shear failure occurring in $[0\text{-}90°]_{4S}$ specimen under compression loading (adaptation from [26]).

Furthermore, tests have revealed a wide scatter in failure location as shown in figure 3.41. This variability is attributed in part to the insufficient gauge length resulting in non-uniform compression strain fields.

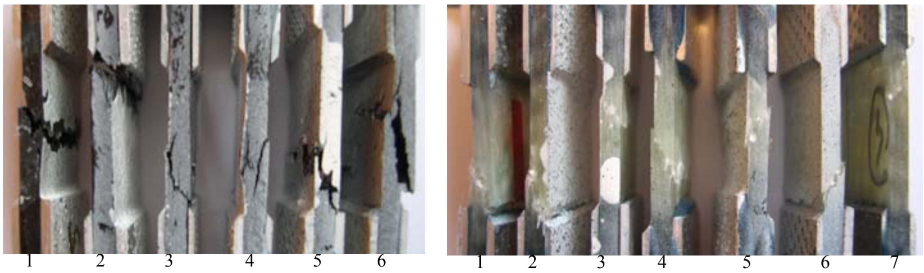

Figure 3.41: Failure locations in carbon and braid compression specimens.

A history of compressive longitudinal strain maps, figure 3.42, obtained from the previously presented carbon specimen (C-B 6 [0-90°]$_{4S}$), indicates a varying and non-uniform axial strain distribution ε_{xx} in the specimen gauge length.

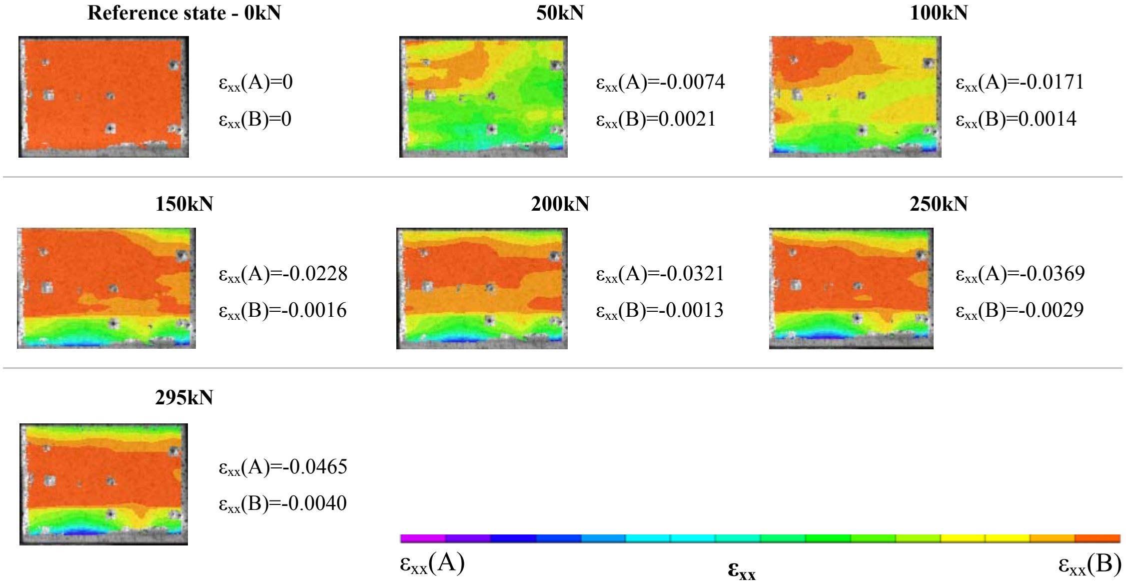

Figure 3.42: Strain distribution history in carbon and braid compression specimens.

These plots show that high compressive strain bands form at the edge of each grip; whereas, in the middle gauge length a more homogenous strain distribution is present. This localised effect induced by the grips is called the Saint-Venant end effects principle [59] and it dissipates, or smooths out, within the regions that are sufficiently removed from the loading location. As a general rule, the distance at which stress distribution is considered to be uniform is at least equal to the largest dimension of the loaded cross-section. However, in this particular case such a rule cannot be applied due to the previous buckling consideration necessitating a short gauge length; therefore, grips exert a non-negligible effect and affect greatly the specimen loading leading to premature damage in areas of high strain concentration. From this, failure can be expected to initiate prematurely in the vicinity of the grips.

The DIC technique could be used to improve the compression rigs for fabric and particularly, in this case, for large tow size fabric composites. In order to reduce the variability in the results, a larger ROI should be considered without exceeding the buckling length. The proposed test modification could be readily implemented in by increasing the length of the composite specimen. However, a radical modification of the test fixture would be required to enable to test a wide range of specimens. These considerations are proposed and detailed in Chapter 6 Overall Discussion.

3.3.6 Tensile cyclic shear loading

The aim of this test was to determine shear damage and plasticity law parameters, required for model calibration for both carbon and glass specimens. Two sets of 5 $[\pm45°]_{2S}$ carbon and glass specimens made from flattened cylindrical braid preforms of continuous fibre were tested under cyclic loading to measure shear modulus decrease for the damage law characterisation. Aluminium chamfered tabs with a 45° taper, 30mm long and 1.5mm thick were bonded to the ends of the gauge length in order to ensure good load introduction. Specimen gauge length and width were respectively 160mm and 67mm for both carbon and glass. The specimen dimensions are shown in figure 3.43.

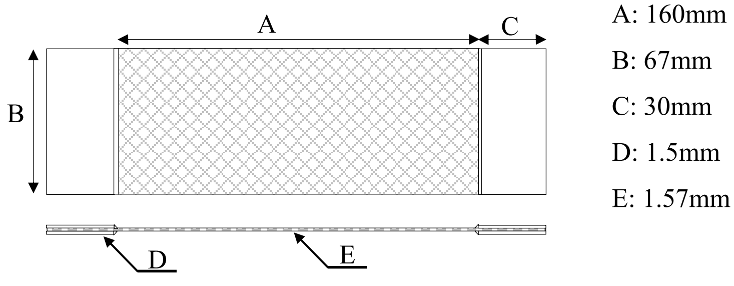

Figure 3.43: Dimensions for a $[\pm45°]_{2S}$ tensile specimen.

Specimens were clamped at the tabs-ends within the hydraulic machine and 5 to 6 tensile loading/unloading cycles at a 0.5mm/min velocity were applied to the specimen until complete failure. Failure was considered to occur when the specimen could no longer carry load.

3.3.6.1 Failure mechanism

For biaxial [±θ°] braids under tensile loading damage development has been shown to be due to matrix micro-cracking and plasticity associated with large fibre rotation [118]. Testing revealed that the fibre/matrix interface progressively debonds allowing tows to re-align; this scissor action continues until the tows reach a maximum interlocking angle leading to tow failure. This behaviour is illustrated in figure 3.44 (a) for a $[\pm45°]_{2S}$ carbon specimen. Significant fibre matrix debonding and tow re-alignment has occurred, leading to diffuse necking prior to final specimen failure. Delamination between plies was a further damage mechanism observed in multi-layered braid composites, figure 3.44 (b). This damage mode is due to the shearing deformation and is strongly coupled to the ply damage mechanisms. This failure leads to separation of the plies and reduces the ability of the laminate to sustain bending loads.

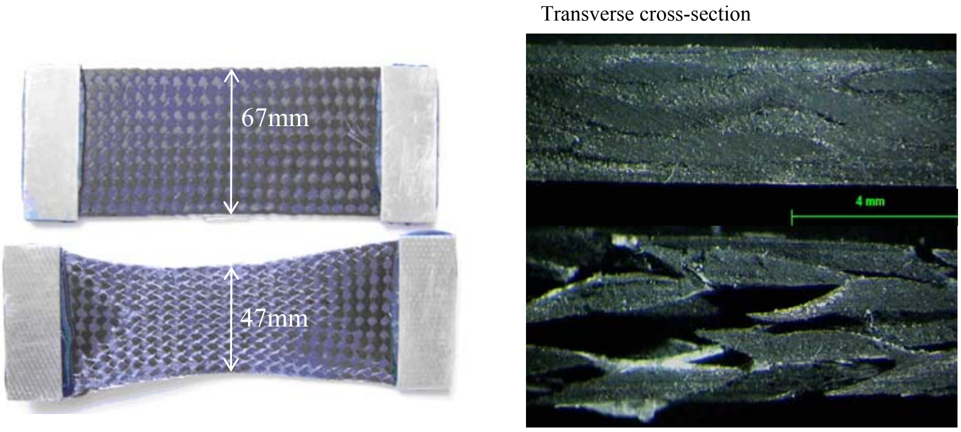

(a) (b)

Figure 3.44: Shear failure mechanism, (a) deformation and failure mechanism for a biaxial $[\pm45°]_{2S}$ carbon braid reinforced composite under tensile loading, (b) original and delaminated cross-section.

The damage growth at fibre/matrix interface was characterised using cyclic tensile testing on a $[\pm45°]_{2S}$ coupon; the damaged modulus at any instant is provided by the unloading modulus of the shear stress-strain curve. At each cycle the elastic and plastic strain components were available and used to determine the damage and plasticity laws respectively. At least 5-6 cycles were required to obtain a good evolution of damage and plasticity. Determination of damage and plasticity laws will be detailed in chapter 4 which is dedicated to numerical modelling of braided composites.

3.3.6.2 Hysteresis loops

The occurrence of hysteresis is a common feature for this type of cyclic loading in composite materials. Figure 3.45 shows the response under cyclic loading of the STS carbon braided composite studied and a 6014/T6 aluminium specimen. The aluminium exhibited elasto-plastic loading/unloading cycles, whereas the braided specimen featured significant hysteresis. This non-linear loading/unloading was generated by the frictional forces between fibre and matrix. In general, due to the presence of two phases (matrix/fibre) within composites, the overall material is heterogeneous which creates mechanical property discontinuities at the fibre/ matrix interface.

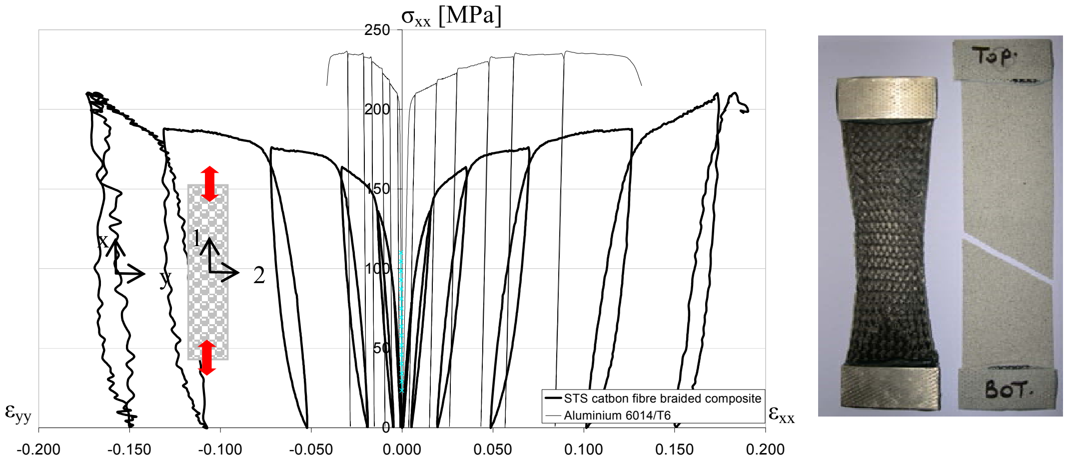

Figure 3.45: Shear cyclic loading for $[\pm 45°]_{2S}$ carbon braided and 6014/T6 aluminium specimens.

Also, despite lower strength and stiffness, the $[\pm 45°]_{2S}$ braided coupon demonstrates that large deformations are possible in the axial and transverse directions, as presented in table 3.9.

	width	thickness	E_{xx} [GPa]	ν_{xy}	σ_{xx} [Mpa]	ε_{xx} [MPa]
STS carbon braided	65.37	1.86	16.682	0.73	209	0.1840
Aluminium 6014/T6	66.44	1.57	61.158	0.348	233.66	0.1192

Table 3.9: Mechanical characteristics for a $[\pm 45°]_{2S}$ carbon braid specimen and an aluminium specimen under cyclic loading.

3.3.6.3 Fibre rotation – Scissoring effect

Due to fibre continuity braided composites have shown large deformation through scissoring mechanisms. The fibre/matrix interface progressively degrades which was monitored through surface whitening at tow cross-over points; this has allowed fibres to re-orientate in the loading direction. In order to integrate this mechanism into the damage model, it was important to quantify the fibre angle variation which could then be used in the damage model formulation.

Since no measurement technique was available to determine fibre rotation, numerical estimation through the generic trigonometric equation (3-6) was made on the basis of measured longitudinal and transverse strains, ε_{xx} and ε_{yy} respectively. This equation assumes that fibres are inextensible and rotate symmetrically toward the axis of loading,

$$\Delta\theta = Arc\tan\left(\frac{1+\varepsilon_{yy}}{1+\varepsilon_{xx}}\right). \tag{3-6}$$

Figure 3.46 shows the angle variation determined through equation (3-6) for carbon and glass braids with respect to the measured longitudinal strain ε_{xx}. The same angle variation was calculated for both carbon and glass specimens.

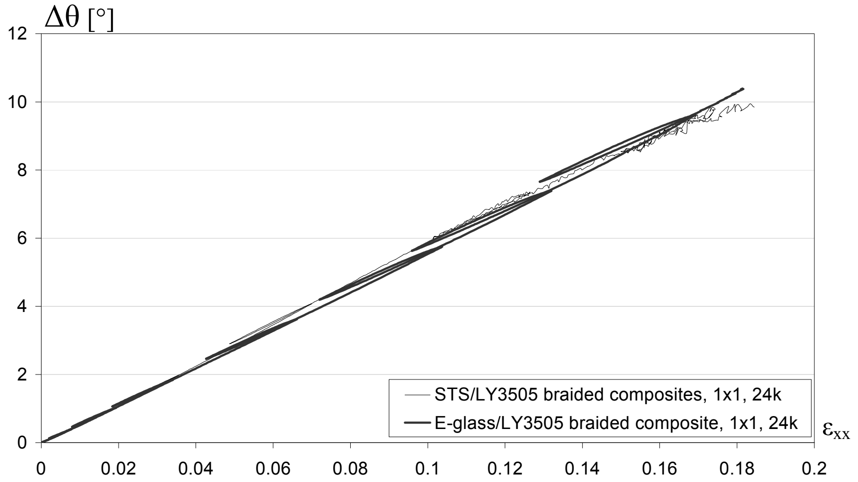

Figure 3.46: Braid angle variation comparison between two [±45°]$_{2S}$ carbon and glass braided composites.

In order to validate this method the final fibre angle was measured on the tested specimen and compared to the prediction. For the carbon specimen, an excellent correlation was found; indeed, the angle variation was measured between 45° to 30°, very close to calculated values as shown in figure 3.47. However, predictions for glass specimens were found to be in poor agreement with experimental results. In comparison with carbon specimens no necking was observed on the glass specimen, instead, a diffuse damage was noticed over the overall specimen surface as shown in figure 3.47. The final fibre angle measured on the specimen was only 39° which indicated lower fibre variation than carbon specimens. Such differences between experiment and prediction come from the limitation of equation (3-6) which assumes no fibre extension. In chapter 6 Overall discussion, an improved measurement method to fully obtain the true fibre angle variation is proposed.

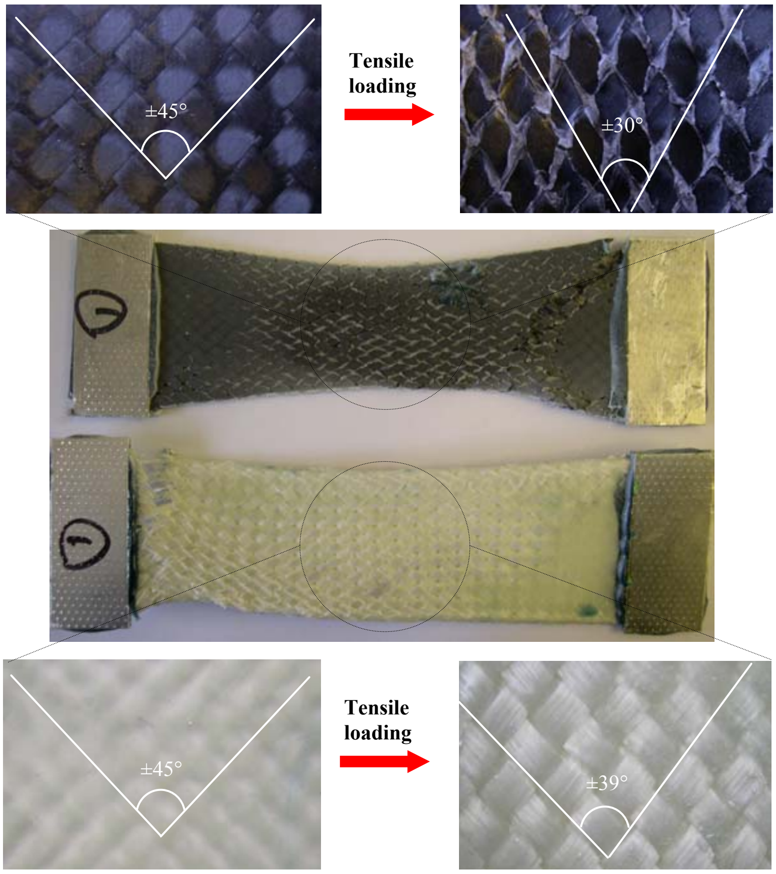

Figure 3.47: Braid angle variation comparison between two [±45°]$_{2S}$ carbon and glass braided specimens.

3.3.6.4 Results on [±45°]$_{2S}$ carbon and glass braided specimens

Figure 3.48 presents a comparison between [±45°]$_{2S}$ carbon and glass braid composites submitted to tensile cyclic loading. The ROI in which strains were measured was always located at the mid-length of the specimen where the main deformation occurred. Also, the ROI was chosen to be removed from specimen edges in order to avoid any edge effects. The carbon exhibited, as expected, higher strength than glass but, surprisingly, greater longitudinal strain ε_{xx} is obtained which is comparable to glass, as shown in figure 3.48.

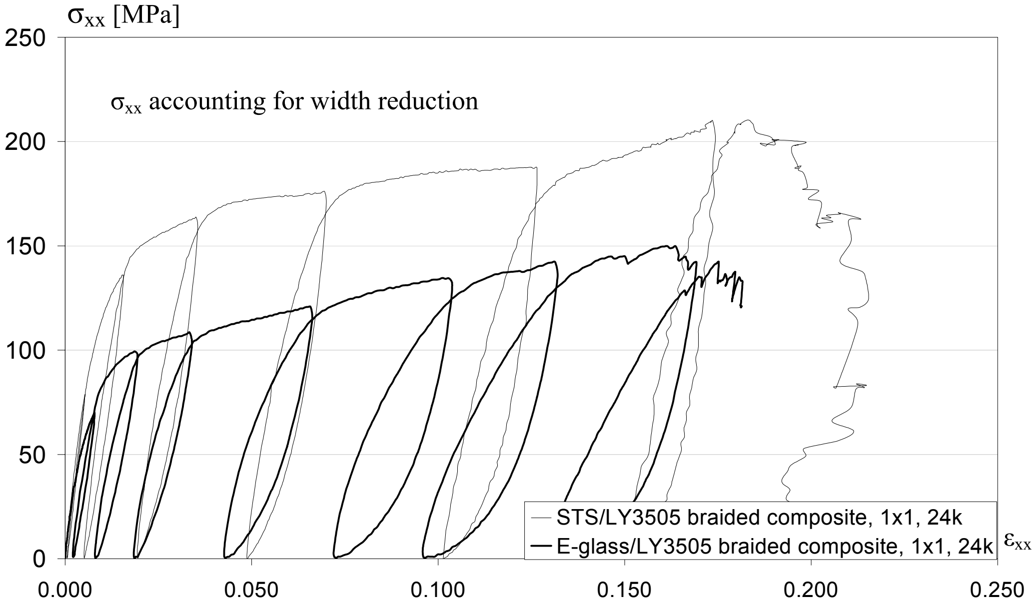

Figure 3.48: Cyclic test plot conducted on carbon and glass braided composites.

Failure mechanisms observed were substantially different between carbon and glass specimens, as shown in figure 3.49. As mentioned earlier, due to large fibre re-orientation in the mid-length of the carbon specimen, failure occurred by shearing between damaged and undamaged zones. Instead, for glass, due to greater glass fibre ductility a more diffused damage over the full specimen surface has led to a tow failure at the tabs.

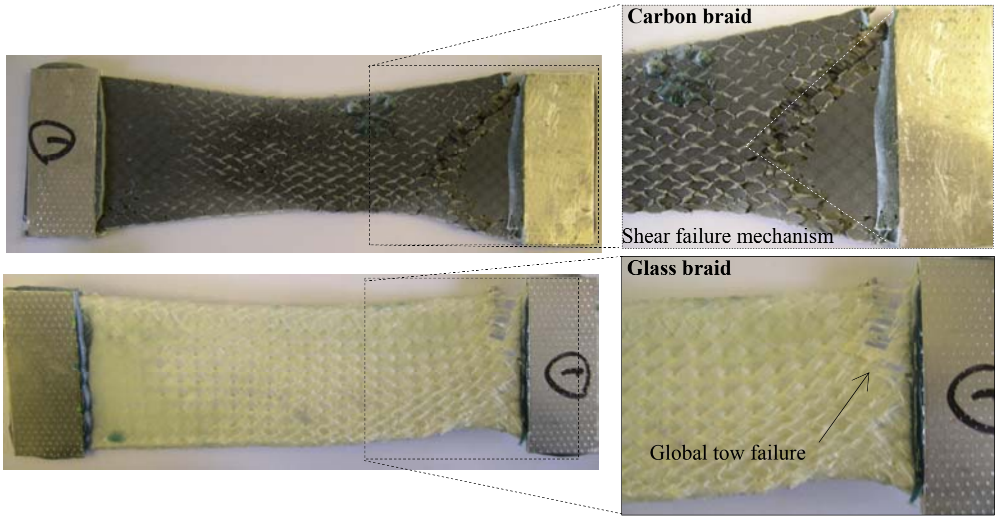

Figure 3.49: Comparison of failure modes for carbon and glass braided [±45°]$_{2S}$ composites.

The results found for both carbon and glass specimens are presented in tables 3.10 and 3.11. Only elastic properties E_{xx} and ν_{xy} used for model calibration are cited in these tables. In Chapter 4, calibration of an elementary ply will be conducted using these values.

specimens	Width [mm]	Thickness [mm]	E_{xx} [GPa]	ν_{xy}
C-B 1	67.21	1.57	16.450	0.72
C-B 2	67.13	1.58	16.623	0.78
C-B 3	67.45	1.51	16.814	0.8
C-B 4	67.51	1.49	16.310	0.74
C-B 5	67.12	1.58	16.430	0.73
Mean	**67.28**	**1.54**	**16.525**	**0.753**
STDEV	0.18	0.042	0.196	0.03

Table 3.10: Mechanical characteristics for [±45°]$_{2S}$ STS/LY3505 braided specimens under tensile cyclic loading.

specimens	Width [mm]	Thickness [mm]	E_{xx} [GPa]	ν_{xy}
G-B 1	66.3	1.50	16.120	0.431
G-B 2	67.50	1.52	15.84	0.42
G-B 3	66.45	1.49	16.32	0.621
G-B 4	67.23	1.54	15.93	0.56
G-B 5	67.65	1.53	16.562	0.54
Mean	**67.026**	**1.51**	**16.154**	**0.514**
STDEV	0.61	0.020	0.293	0.03

Table 3.11: Mechanical characteristics for [±45°]$_{2S}$ E-glass/LY3505 braided specimens under tensile cyclic loading.

3.3.7 Carbon and glass beams under four point bend loading

3.3.7.1 Experimental set-up presentation

Model validation has been conducted on coupons which have been used for material characterisation. In this section, it is proposed to go a step further and validate the model for a structural part such as a beam. The carbon and glass beams manufactured for this purpose have been tested under four point bending. The ASTM standard test method used to determine flexural properties of unreinforced and reinforced plastics material was used as a basis for this test [10].

The beams have a square cross-section and are supported on two rolls; loading is at two points by means of two impactors, as shown in figure 3.50 (a). The distance between the two loading impactors, or load span, was one third of the support pan, P, as shown in figure 3.50 (b). Optical DIC measuring was used and a coarse speckle pattern was sprayed on each beam since the cameras were located at approximately 2 meters from the ROI. Due to specimen surface access limitations (columns of the testing machine), only the region between the two impactors could be measured, as shown in figure 3.50 (c).

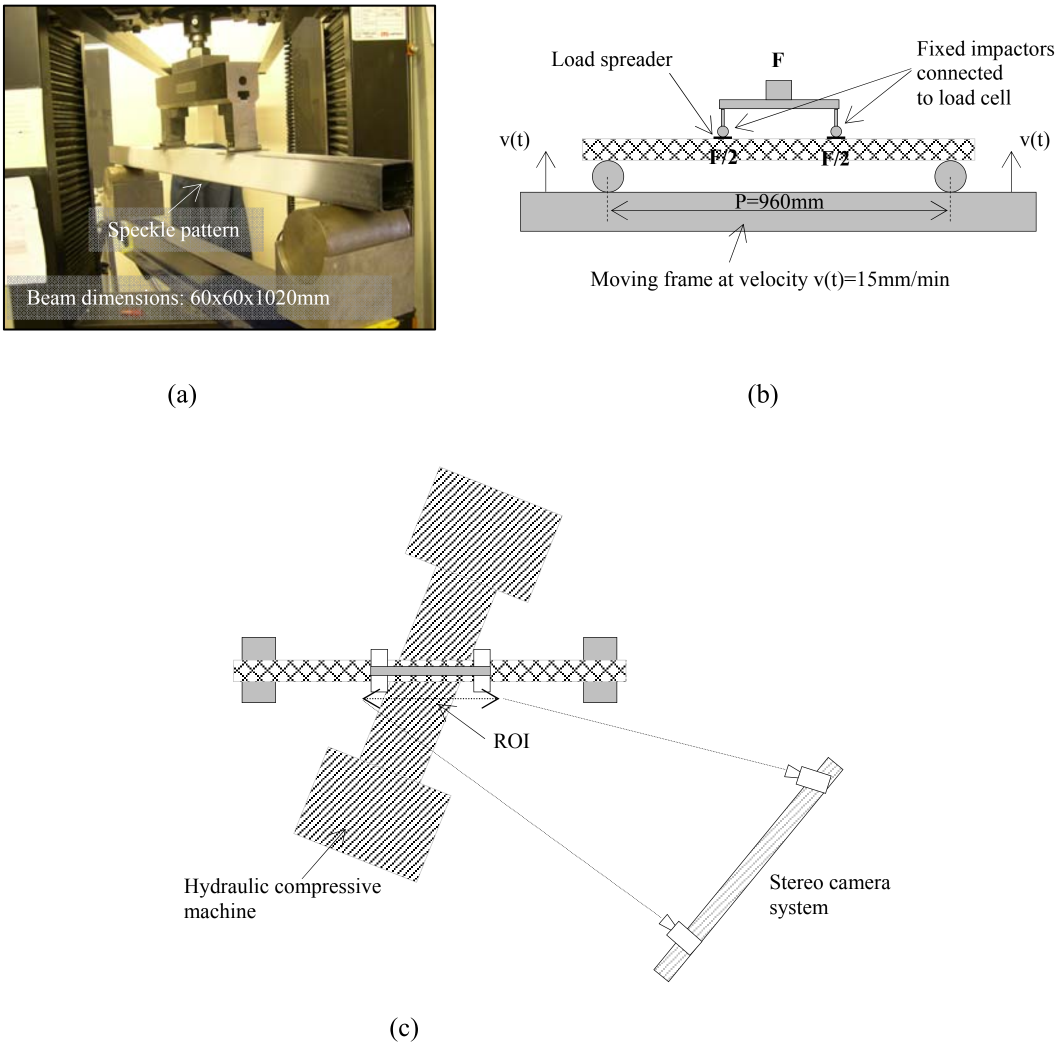

(a) (b)

(c)

Figure 3.50: Beam four point bending experimental set-up, (a) testing set-up, (b) schematic of the testing set up, and (c) stereo camera system positioning.

The beam was loaded at a stroke mode of 15mm/min to insure quasi-static loading and failure was considered to be at the first significant drop in load.

3.3.7.2 Test results on carbon and glass beams

The results presented in this section are the force versus displacement recorded by the tensile machine and strain results obtained from the DIC technique on four carbon and glass braided beams. Figure 3.51 shows a satisfying stiffness and strength consistency for the carbon beams; however, the two glass beams show a significant scatter which is attributed to the manufacturing problems described previously in section 3.1.4.2.

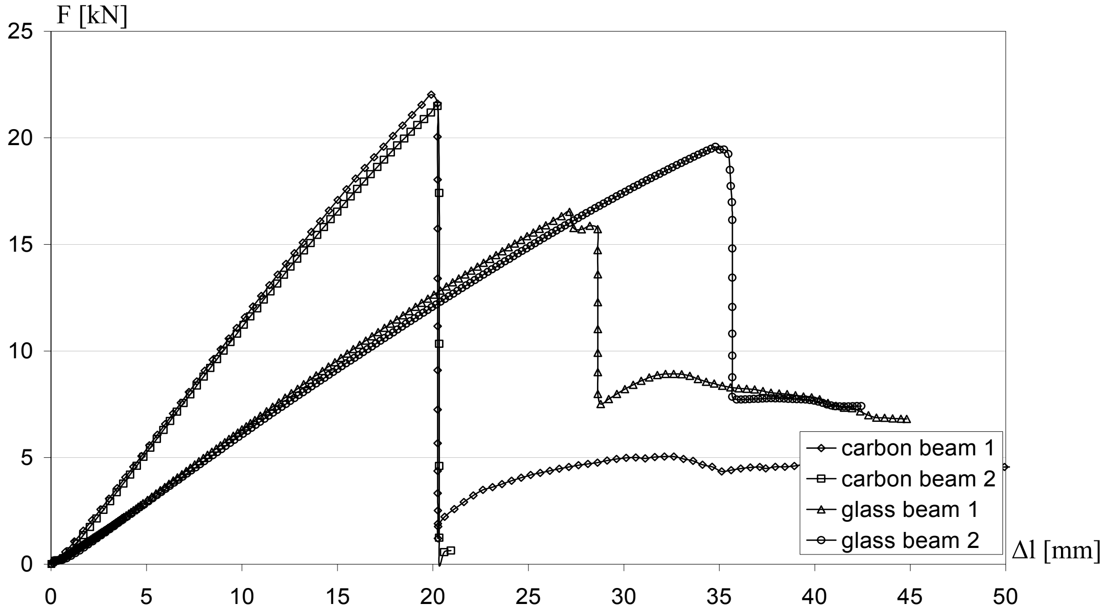

Figure 3.51: Force versus central deflection Δl curves for carbon and glass braided beams.

A compressive failure mode close to the impactors was observed for both the carbon and glass beams. The beam top surface, in contact with the impactors, failed by a combination of two modes: compressive shearing and bending which was clearly noticeable by the kink band running in the tows direction, as shown in figures 3.52 and 3.53. Under this particular loading condition, the top surface was more likely to fail before the bottom surface, since the compressive strain at failure for both carbon and glass fibres is significantly lower than the tensile strain to failure. Simultaneously, side wall failure by shearing was also observed in both cases, as shown in figures 3.52 and 3.53. It is noteworthy that the excess resin at the beam corners underwent significant cracking and small resin blocks were ejected at the time of beam failure.

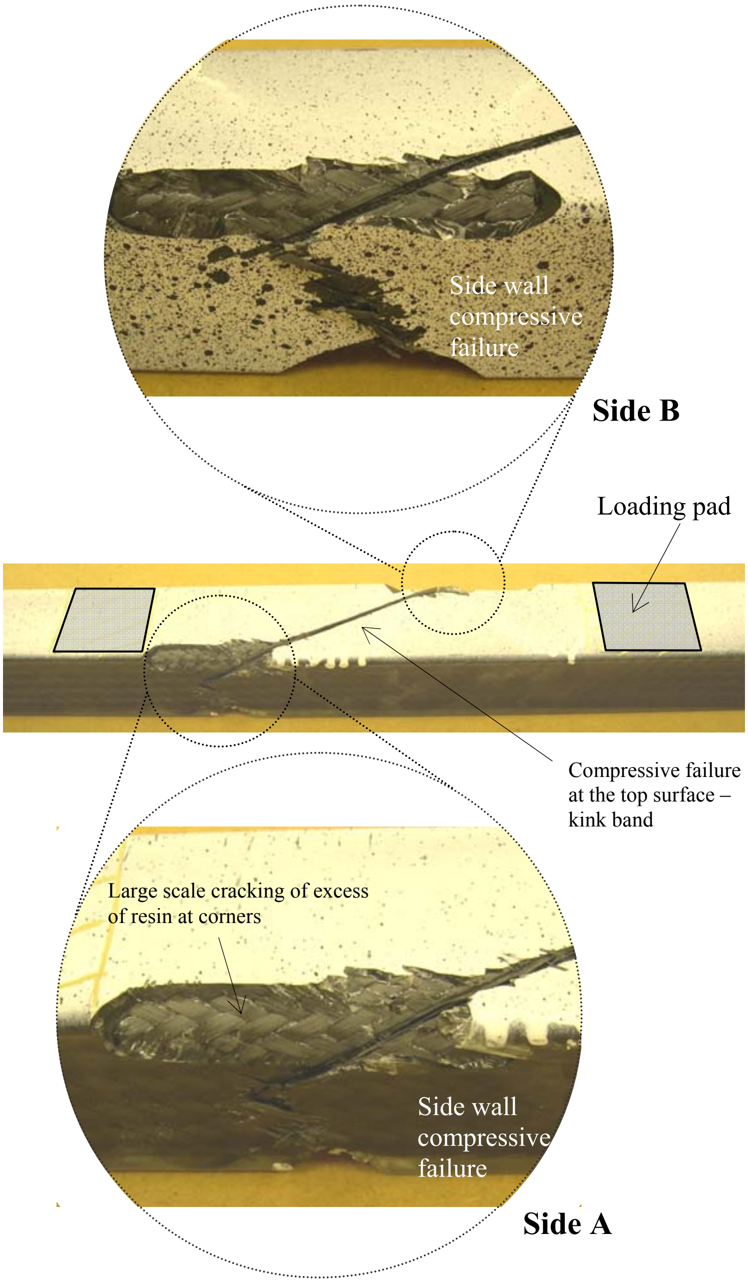

Figure 3.52: Failure mode for carbon braided beam 1.

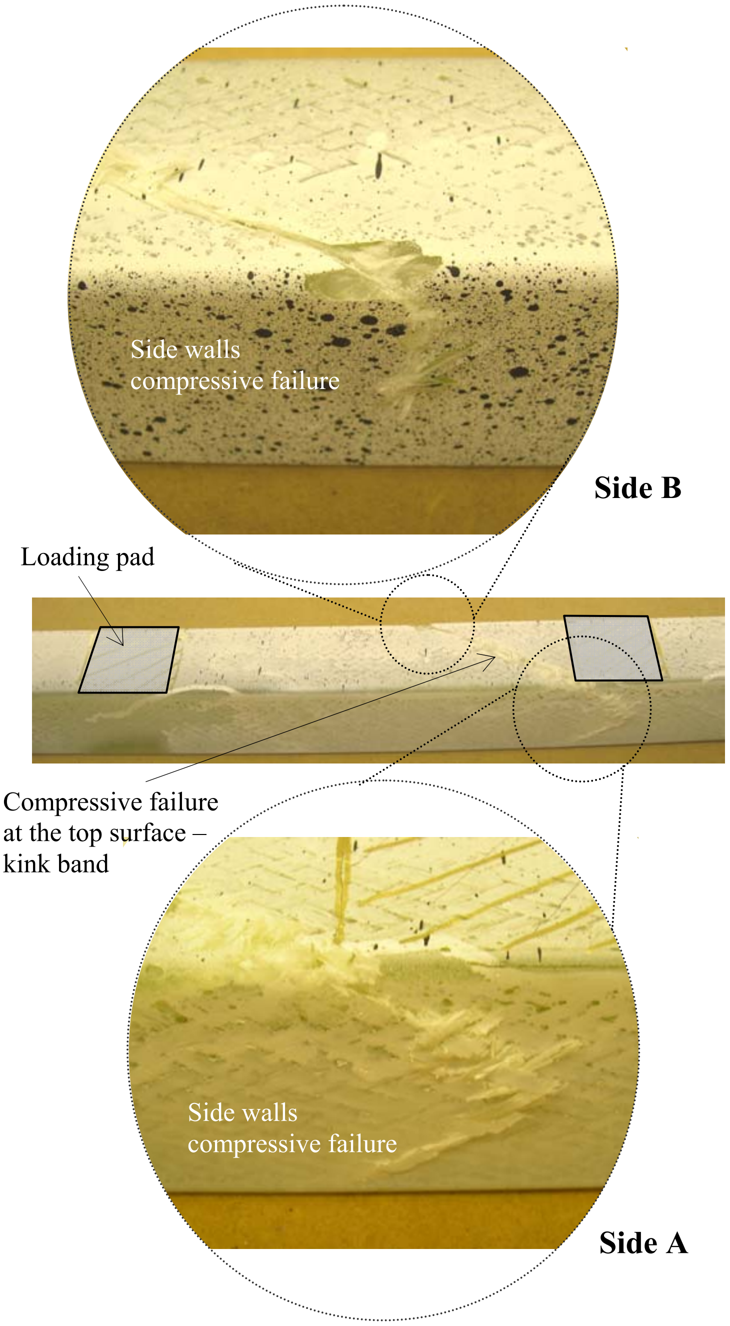

Figure 3.53: Failure mode for a glass braided beam 1.

Results obtained using the DIC technique revealed that the largest strain magnitudes in x and y direction were approximately 0.6% on the side walls. Figure 3.55, shows an example of strain plots obtained for the carbon beam 1 test. The first plot shows the distribution of strain in the x direction, ε_{xx} (axial axis of the beam), which confirms that beam side walls were submitted to a compressive strain loading at the top of the ROI and tensile loading at the bottom. The second plot presents the strain distribution in y direction, ε_{yy} (axis of loading), where tensile strain is measured at the top of the ROI and compressive strain at the bottom.

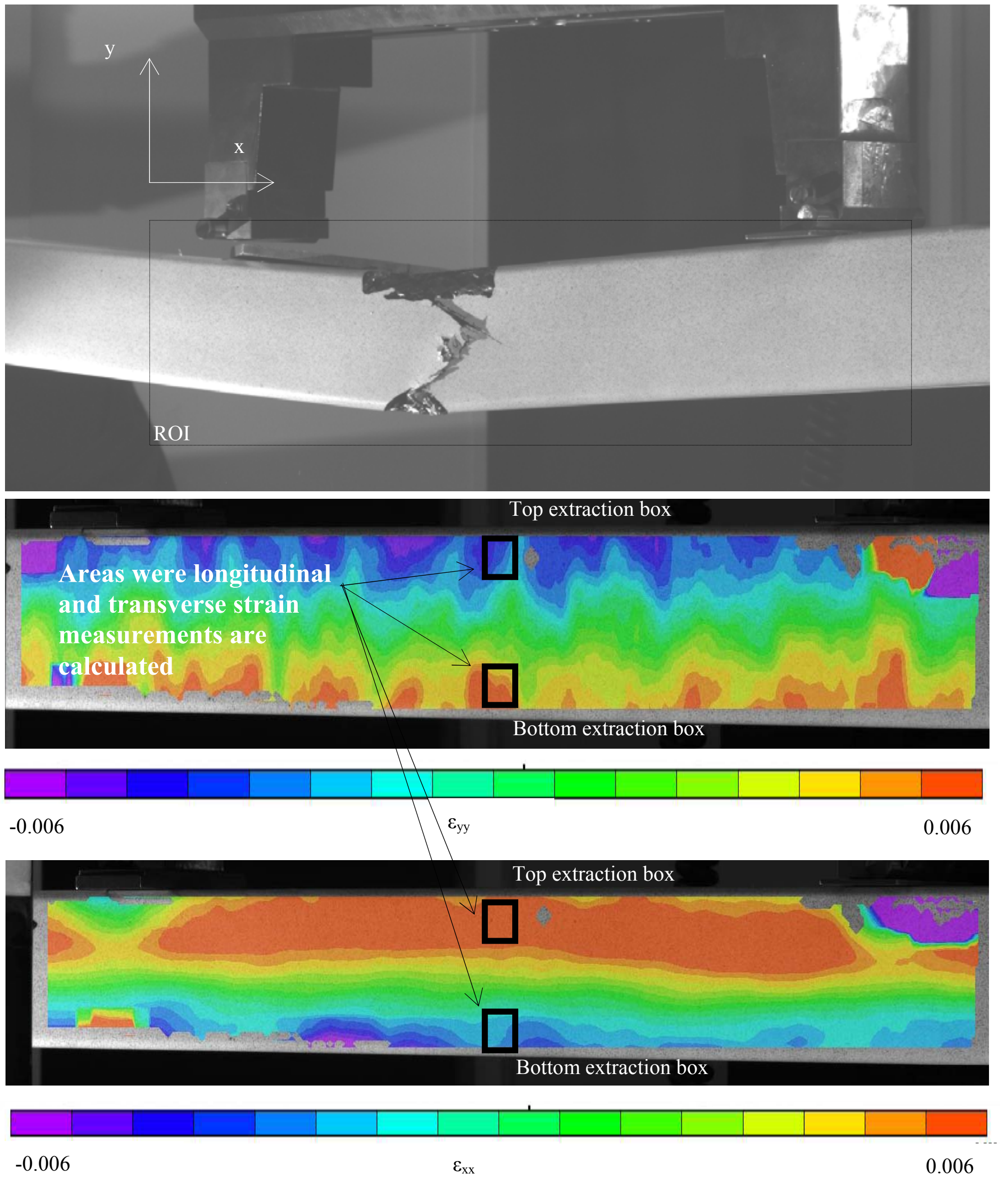

Figure 3.54: Longitudinal and transverse strain plots for the carbon beam 1.

Since main deformations occur in the centre of the ROI, it has been chosen to extract strain values ε_{xx}, ε_{yy} at the top and bottom of the ROI as shown in figure 3.54. Figure

3.55 shows that side wall strain magnitude for the carbon beam is only between -0.4% to 0.5% which reveals, and confirms, the linear elastic behaviour of the beam. Similar strain distributions and strain magnitudes were obtained for glass beams. This is readily explained by the low fibre angle (30°), which is very close to locking angle, and does not allow large fibre re-orientation. Assuming a larger braid angle, such as 45°, the beam should have had significantly more deflection and the force versus displacement measurement would have shown a non-linear curve.

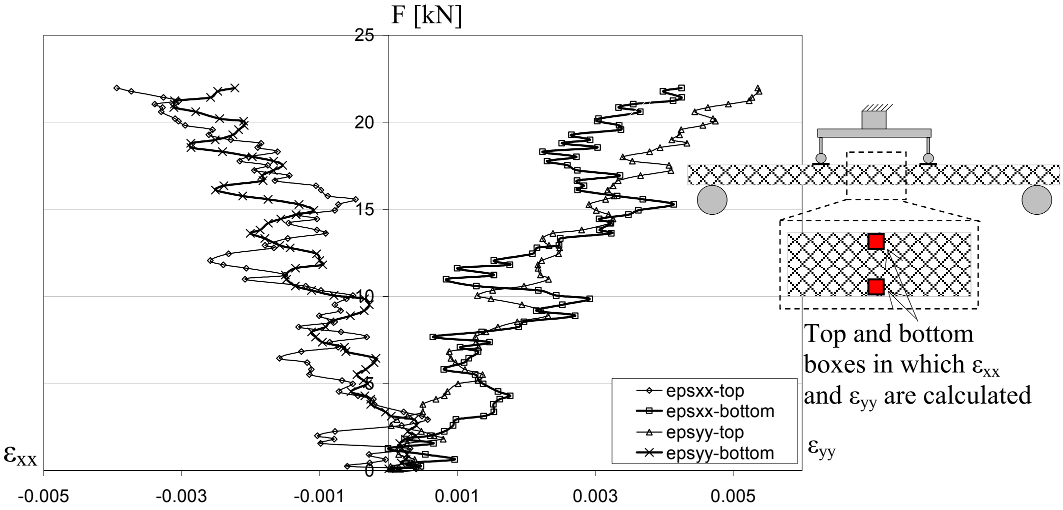

Figure 3.55: Force versus strain curve for the tested carbon beam 1.

3.4 Overview

An extensive test campaign has been conducted in this work for characterising the main failure modes of heavy tow braided composites. Conventional methods, such as strain gauges and laser extensometers, were found inappropriate to measure large deformations and strains in damaging composites, consequently an optical method has been developed and successfully used.

Particular braid characteristics, such as fibre continuity and layer effect were investigated showing a significant influence on material properties which concluded that these characteristics must be accounted for in damage model calibration. Furthermore, tensile testing in the fibre direction for $[0\text{-}90°]_{4S}$ braided specimens revealed a non-linear elasto-plastic behaviour caused by tow stretching mechanism induced by resin nesting at tow intersection. Compression loading in fibre direction showed also the limitation of the existing ASTM rig for large tow size fabrics in determining the stress and strain at failure. Fibre re-alignment in the loading direction was also observed for $[\pm 45°]_{2S}$ specimens under tensile loading. The fibre angle variation through loading history was numerically quantified for both carbon and glass braids which will be used in the modelling presented in the following chapter.

Finally, carbon and glass braided beams were tested under four point bending. A satisfying consistency was found in the test results. Failure mechanisms observed were similar for both materials which was characterised by a coupled shear compressive and bending failure of the beam top surface. These beam results will be used in chapter 5 to validate the damage model.

Chapter 4- Damage model theoretical developments

Micro-mechanical models based on the accurate representation of a RUC presented in section 2.4.1 allow the determination of the elastic properties of braided composites. Failure can also be predicted using existing models based on macro-mechanical strength theories, such as Tsai-Wu criterion, section 2.4.2.2. However, none of these models can predict the progressive damage and mixed modes of failure that can occur in braided composites under arbitrary loading conditions. For this, models based on damage mechanics appeared to be more suitable to predict the different damage mechanisms occurring in braided composite. Accordingly, the meso-scale damage model proposed by Ladevèze, initially developed for unidirectional composites, was chosen since damage parameters on fibre and matrix are available.

As mentioned in section 2.4.3, the Ladevèze model defines a unidirectional elementary ply's elastic, damage and plastic parameters calibrated through a defined exhaustive experimental test campaign. Since fibre angle in braids can vary accordingly to the chosen application, this model has also been found to offer flexibility in the modelling of braid layers. Indeed, a [±θ°] braid layer can be modelled as two respective plies at +θ° and – θ° angle, as shown in figure 4.1. For simplification, tow waviness was also assumed to be negligible in order to consider pseudo ideal straight fibres; each ply thickness was set equal to half of a braid layer thickness.

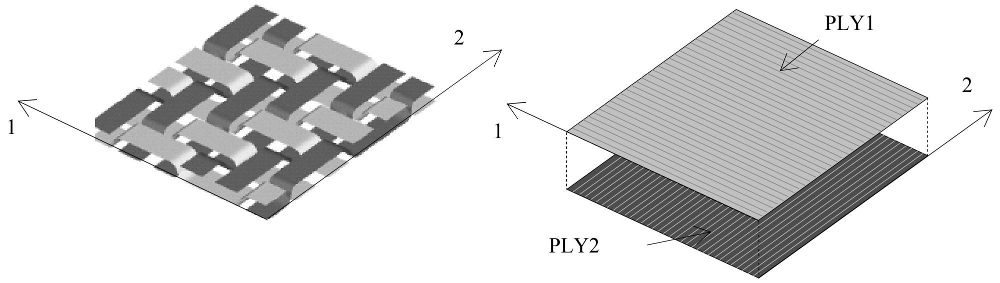

Figure 4.1: Modelling of a braid layer with unidirectional elementary plies.

The original calibration test campaign based on the loading of specific laminates, such as $[0°]_8$, $[\pm 45°]_{2S}$, $[\pm 67.5°]_{2S}$, $[+45°]_8$, allowing to determine elastic properties, damage and plasticity laws for a single elementary ply was found inappropriate for braids. A layer of 2D braided preform has two main directions, at $+\theta°$ and $-\theta°$ (biaxial case); therefore, testing on $[0°]_8$ and $[+45°]_8$ unidirectional laminates is not possible. In addition, due to the difficulty to obtain large braid angles with the investigated preform testing of a $[\pm 67.5°]_{2S}$ laminate also cannot be conducted. Since most of the tests required by the model were physically impractical, another approach was required to calibrate an 'equivalent braid unidirectional ply'.

In order to determine elastic properties for the elementary ply calibration, Classical Laminate Theory (CLT) for laminates was used and has given satisfying approximations. Also, as mentioned previously in the experimental testing campaign, both carbon and glass braided composites demonstrated large deformations through fibre re-orientation. In the standard Ladevèze damage formulation damage and plasticity laws are assumed to be independent of fibre angle variations which becomes a limitation for braid modelling that introduces inaccurate predictions. Hence CLT was again used to integrate fibre variation $\Delta\theta$ into the damage and hardening laws.

In this chapter, the Ladevèze damage model treating fibre damage (tensile/compressive loading) and matrix damage, and its implementation into the explicit FE code PAM-CRASH^{TM}, are presented. As mentioned previously, this model was found inappropriate for representing the effect of braided composite scissoring. Hence, modifications were required to accurately account for all braid failure features. The following enhancements are briefly described below and are discussed in further detail in this chapter.

- In order to determine elastic properties $\{E_{11}, E_{22}, \nu_{12}, G_{12}\}$ for an equivalent braid unidirectional ply a CLT based fitting method was adopted.

- As shown in section 3.3.4, carbon and glass braided composites under tension loaded in fibre direction are subjected to tow stretching leading to intra- and inter-ply delamination, resulting in non-linear stress-strain response; hence, a new modelling method has been integrated into the unidirectional ply to indirectly approximate delamination mechanisms.

- Since 2D biaxial braided coupons are always balanced, transverse damage was assumed to be negligible due to reinforcement of the orthogonal fibres and only shear damage was assumed to occur in the matrix.

- The initial experimental data analysis for model calibration does not account for fibre re-orientation and width reduction, which leads to an error when determining the shear stress-strain curve σ_{12} versus γ_{12}. Therefore, a new analysis method was introduced to integrate these two features in order to obtain more accurate predictions.

In addition, these models derived in the subsequent sections use the following basic assumptions,

- State of plane stress,
- One braid layer is equivalent to two unidirectional plies,
- Fibre waviness is accounted for in the ply calibration,
- Ply damage is independent of strain rate,
- Constant damage through ply thickness,
- No transverse damage
- Constant Poisson's ratio

4.1 Actual damage model implemented in PAM-CRASH^{TM}

The Ladevèze damage model is derived from the damaged strain energy, equation (2-8) defined in section 2.4.3.2, written in terms of ply local stresses; hence, all quantities are subsequently derived in terms of stresses. Therefore, this model formulation had to be rewritten in terms of strains in order to be implemented in the explicit FE code PAM-CRASH^{TM}. This implies that all damage relationships have had to be re-written in terms of strains, as presented in the following section.

4.1.1 Fibre damage treatment

4.1.1.1 Tensile fibre damage

Fibre damage evolution in a unidirectional laminate under tensile loading is treated, in PAM-CRASH^{TM}, as a linear function of longitudinal strain $d_{ft}=f(\varepsilon_{11})$. As shown in figure 4.2, the fibre damage remains equal to zero until the initial longitudinal fibre tensile damage threshold strain ε^{ft}_{i} is reached. Thereafter damage increases linearly until the ultimate fibre tensile damage threshold strain ε^{ft}_{u} is reached corresponding to the ultimate damage d^{ft}_{u}. Beyond this point damage increases asymptotically towards the value 1.0 which would correspond to complete failure.

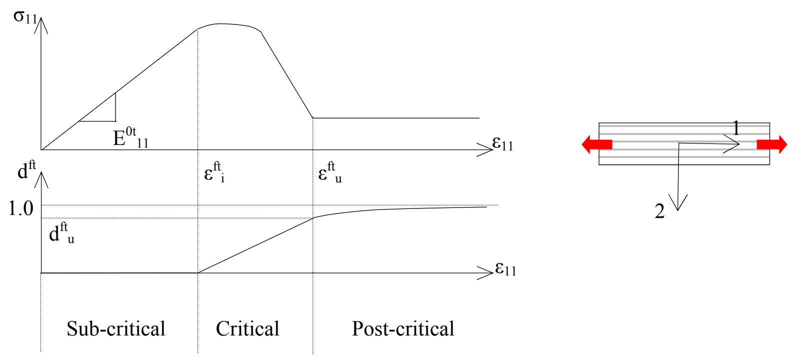

Figure 4.2: Tensile fibre damage treatment used in PAM-CRASH^{TM} (reproduced from [115]).

For the three damage regions identified, the damaged modulus can be calculated as follows,

$$\textit{Sub-critical} \qquad E_{11} = E_{11}^{0t} \ , \tag{4-1}$$

$$\textit{Critical} \qquad E_{11} = E_{11}^{0t}\left(1-d^{ft}\right) \text{ with } d^{ft} = d_{u}^{ft}\,\frac{\varepsilon_{11}-\varepsilon_{i}^{ft}}{\varepsilon_{u}^{ft}-\varepsilon_{i}^{ft}} \ ,$$

Post-critical $E_{11} = E_{11}^{0t}\left(1-d^{ft}\right)$ with $d^{ft} = 1-\left(1-d_u^{ft}\right)\dfrac{\varepsilon_{11}}{\varepsilon_u^{ft}}$.

This model can successfully predict failure for elastic behaviour such as the woven composites presented earlier in section 3.3.4.1. However, as discussed further in this section, it has been found unsuitable to predict the complex failure modes that occur in braided composites, such as tow straightening when loaded in the fibre direction.

4.1.1.2 Compressive fibre damage

Under compression loading, a similar damage treatment is used; however, due to fibre misalignment, or fibre micro-buckling, the stress-strain curve exhibits a slight non-linear trend when close to ultimate strength in the sub-critical domain, figure 4.3.

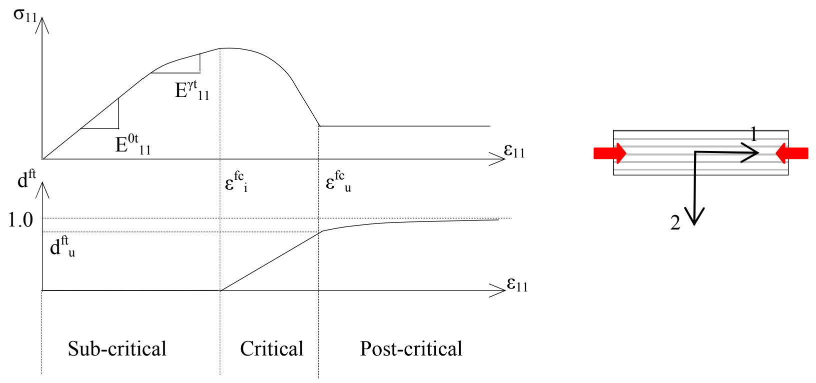

Figure 4.3: Compressive fibre damage treatment used in PAM-CRASH™ (reproduced from [115]).

In order to account for this non-linearity a corrective factor γ is introduced to model the decrease in compressive modulus, E^{0c}_{11} prior to damage,

$$\gamma = \frac{E_{11}^{0c} - E_{11}^{\gamma c}}{E_{11}^{\gamma c} E_{11}^{0c} \left|\varepsilon_{11}\right|}, \tag{4-2}$$

where $E^{\gamma c}_{11}$ is the secant modulus.

The stiffness and damage variation are then calculated as follows,

Sub-critical $E_{11}^{c} = E_{11}^{\gamma}$, (4-3)

Critical $E_{11}^{c} = E_{11}^{\gamma}\left(1-d^{fc}\right)$with $d^{fc} = d_u^{fc}\dfrac{\varepsilon_{11}-\varepsilon_i^{fc}}{\varepsilon_u^{fc}-\varepsilon_i^{ct}}$, *Post-critical* $E_{11}^{c} = E_{11}^{\gamma}\left(1-d^{fc}\right)$with $d^{fc} = 1-\left(1-d_{u}^{fc}\right)\frac{\varepsilon_{11}}{\varepsilon_{u}^{fc}}$.

4.1.2 Matrix damage treatment

4.1.2.1 Elastic damage model

As mentioned earlier, the model has been derived from its original thermodynamics form to obtain an explicit formulation required for its implementation in the explicit FE code PAM-CRASH^{TM} [121]. Instead of the compliance matrix [S], the stiffness matrix [C], has been used to provide the material internal variables to express transverse and shear stresses as functions of strains as follows,

$$\begin{aligned} \sigma_{22} &= C_{22}\left(\nu_{12}^{0}\varepsilon_{11}^{e}+\varepsilon_{22}^{e}\right), \\ \sigma_{12} &= 2C_{12}\varepsilon_{12}^{e}, \end{aligned} \tag{4-4}$$

with

$$\begin{aligned} &\textit{Tension} && C_{22} = C_{22}^{0}\left(1-d_{22}\right) = \frac{E_{22}^{0}}{1-\upsilon_{12}^{0}\upsilon_{21}^{0}}\left(1-d_{22}\right), \\ &\textit{Compression} && C_{22} = C_{22}^{0}, \\ & && C_{12} = G_{12}^{0}\left(1-d_{12}\right). \end{aligned} \tag{4-5}$$

The damaged material strain energy defined in equation (2-8) can be re-written as,

$$\begin{aligned} E_{D} &= \frac{1}{2}\underline{\underline{\sigma}}:\underline{\underline{\varepsilon}}^{e}, \\ &= \frac{1}{2}\begin{bmatrix} E_{11}^{0}\left(\varepsilon_{11}^{e}\right)^{2}+C_{22}^{0}\left(1-d_{22}\right)\left\langle\left(\nu_{12}^{0}\varepsilon_{11}^{e}+\varepsilon_{22}^{e}\right)^{2}\right\rangle_{+}+C_{22}^{0}\left\langle\left(\nu_{12}^{0}\varepsilon_{11}^{e}+\varepsilon_{22}^{e}\right)^{2}\right\rangle_{-} \\ +G_{12}^{0}\left(1-d_{12}\right)\left(2\varepsilon_{12}^{e}\right)^{2} \end{bmatrix}. \end{aligned} \tag{4-6}$$

The stress tensor is therefore calculated by derivation of equation (4-6),

$$\underline{\underline{\sigma}} = \left.\frac{\partial E_{D}}{\partial \underline{\underline{\varepsilon}}^{e}}\right|_{d_{22},\,d_{12}} \Rightarrow \begin{Bmatrix} \sigma_{11} \\ \sigma_{22} \\ \sigma_{12} \end{Bmatrix} = \left[C\right]\begin{Bmatrix} \varepsilon_{11} \\ \varepsilon_{22} \\ 2\varepsilon_{12} \end{Bmatrix}, \tag{4-7}$$

with

$$\left[C\right] = \begin{bmatrix} C_{11}^{0} & \nu_{12}^{0}C_{11}^{0} & 0 \\ \nu_{21}^{0}C_{11}^{0} & C_{22}^{0}\left(\left(1-d_{22}\right)\left\langle a\right\rangle_{+}+\left\langle a\right\rangle_{-}\right) & 0 \\ 0 & 0 & G_{12}^{0}\left(1-d_{12}\right) \end{bmatrix}, \tag{4-8}$$

and $\langle a \rangle_{\pm} = \dfrac{\langle \nu_{12}^{0} \varepsilon_{11}^{e} + \varepsilon_{22}^{e} \rangle_{\pm}}{\left| \nu_{12}^{0} \varepsilon_{11}^{e} + \varepsilon_{22}^{e} \right|}$.

In the same way, the thermodynamic forces Y_{22} and Y_{12} defined in equation (2-11) are re-written in terms of strains,

$$Y_{22} = -\left.\frac{\partial E_D}{\partial d_{22}}\right|_{\underline{\underline{\varepsilon}}^e\, d_{12}} = \frac{1}{2} C_{22}^{0} \left\langle \left(\nu_{12}^{0} \varepsilon_{11}^{e} + \varepsilon_{22}^{e} \right)^2 \right\rangle ,$$

$$Y_{12} = -\left.\frac{\partial E_D}{\partial d_{12}}\right|_{\underline{\underline{\varepsilon}}^e\, d_{22}} = \frac{1}{2} G_{12}^{0} \left(2\varepsilon_{12}^{e} \right)^2 . \tag{4-9}$$

These quantities are then linearly expressed in terms of the damage variables,

$$d_{22} = \frac{\langle Y_{12}(t) - Y_{220} \rangle_{+}}{Y_{22C}} \text{ if } d_{22}<d_{\max},\ Y_{22}<Y_{22R} \text{ and } Y_{12}<Y_{12R} ,$$

otherwise $d_{22} = d_{\max}$,

$$d_{12} = \frac{\langle Y_{12}(t) - Y_{120} \rangle_{+}}{Y_{12C}} \text{ if } d_{12}<d_{\max},\ Y_{22}<Y_{22R} \text{ and } Y_{12}<Y_{12R} , \tag{4-10}$$

otherwise $d_{12} = d_{\max}$,

where Y_{12C}, Y_{120}, Y_{22C}, Y_{220}, Y_{22R} and Y_{12R} are material constants.

4.1.2.2 Elastic damage model and plasticity coupling

The model also treats plasticity induced by matrix and fibre/matrix interface micro-cracking. The plasticity model formulation is expressed only in terms of transverse and shear stresses. In addition, isotropic hardening is assumed in order to simplify the formulation. As in the original model plasticity is coupled with elastic damage through effective stresses and strains (equation 2-15).

4.1.3 Elasto-plastic damage model implementation

4.1.3.1 Algorithm definition

A first version of this elastic damage model was available in PAM-CRASH$^{\text{TM}}$ v1996 which was followed by the PAM-CRASH$^{\text{TM}}$ v2000 version in which plasticity treatment was added. Figure 4.4 presents a flow chart of the algorithm used in the latest version of the code v2005. Total strains are assumed elastic for the first iteration which leads to the calculation of transverse/shear damages and local stresses in the elementary ply. If the plasticity criterion f_p is negative, or equal to zero, the solution of the problem corresponds to the previous iteration. Otherwise, a plasticity correction loop is introduced in which transverse/shear damage, local stresses and plasticity criterion are repeatedly updated in order to converge to a solution.

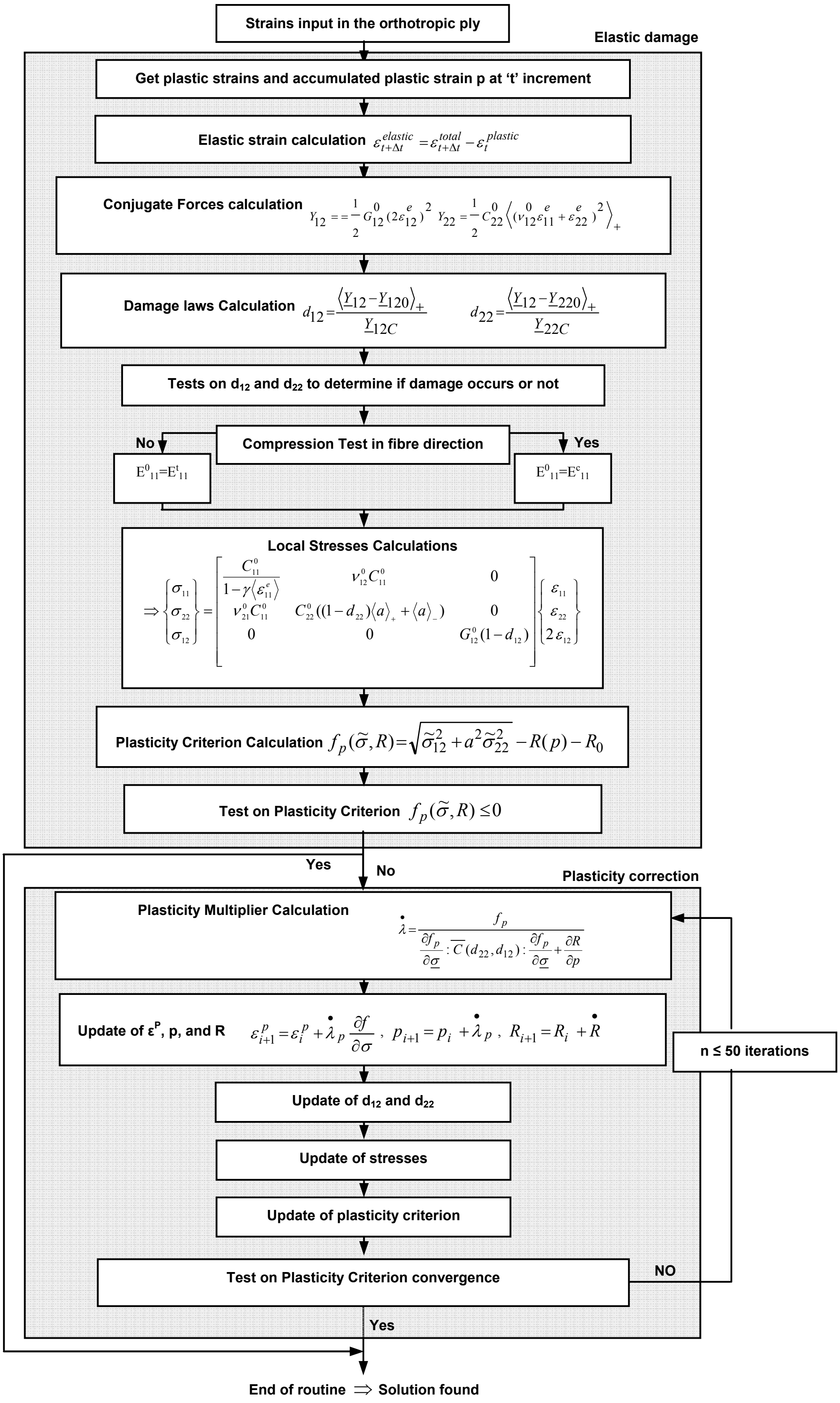

Figure 4.4: Coupled elastic damage and plasticity model implemented in PAM-CRASH^{TM} (translated from [121]).

4.2 Adaptation of the damage model to braided composites

4.2.1 Calibration of the elastic properties for an equivalent braid unidirectional ply

4.2.1.1 Ply calibration for ±45° braid specimens

The modelling approach adopted in this thesis states that a biaxial braided layer is modelled by two distinct unidirectional plies. Usually, monotonic tensile tests on [0°] and [90°] laminates are required to measure $\{E^t_{11}, \nu_{12}\}$ and E_{22} respectively; however, these tests are not practical for braids. The problem was, therefore, to find an alternative method to determine elastic properties for an equivalent elementary ply.

In principle the manufacture of equivalent unidirectional coupons having the same fibre/matrix system and volume fractions could have provided a good approximation of the elastic properties. However, these tests were not performed since equivalent unidirectional preforms could not be obtained for this work.

Another approach, based on CLT, was therefore applied. The test campaign conducted on the $[0\text{-}90°]_{4S}$ and $[\pm 45°]_{2S}$ laminates provided elastic properties, $\{E_{xx}, \nu_{xy}\}$, which were then used as a reference to tune the elastic properties $\{E^t_{11}, E^c_{11}, E_{22}$ and $\nu_{12}\}$ for a single unidirectional ply using CLT as shown in figure 4.5. The shear modulus was readily determined through the cyclic tensile test on a $[\pm 45°]_{2S}$ and used as a known constant in the fitting strategy. The determination of the 3 elastic constants $\{E_{11}, E_{22}, \nu_{12}\}$ was conducted using the CLT based software CADEC [14].

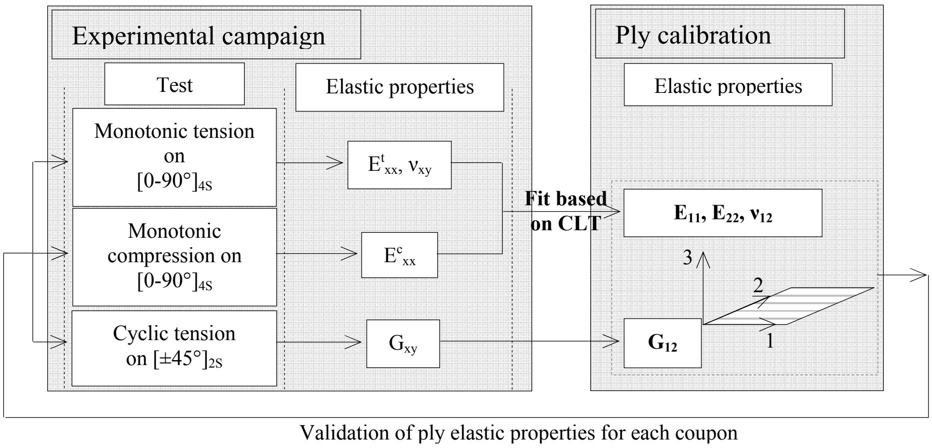

Figure 4.5: Flow chart illustrating the strategy used to determine the equivalent braid unidirectional ply elastic properties.

The rule of mixtures and Halpin-Tsai relationships, equations (4-11), were used to determine $\{E_{11}, E_{22}, \nu_{12}\}$. Generally, the rule of mixtures is known to underestimate the transverse modulus and therefore the Halpin-Tsai semi-empirical relationship is preferred,

$$(1)\, E_{11} = E^{fibre} V_f + E^{matrix}(1 - V_f),$$

$$(2)\; E_{22} = \frac{E_{22}^{f} E^{m}}{V_f E^{m} + V_m E_{22}^{f}},$$

$$(2')\; E_{22} = E^{matrix} \frac{1 + \xi_1 \eta_1 V_f}{1 - \eta_1 V_f},\ with\quad \eta_1 = \frac{E_{22}^{fibre} - E^{matrix}}{E_{22}^{fibre} + \xi_1 E^{matrix}}, \qquad (4\text{-}11)$$

$$(3)\, \nu_{12} = \nu^{fibre} V_f + \nu^{matrix}(1 - V_f),$$

where reinforcing factor ξ_1 is assumed to be 2.0 which supposes a fibre geometry of circular fibres in a packing geometry of a square array.

The experimentally determined 40% volume fraction, found in section 3.1.3.3 for the $[0\text{-}90°]_{4S}$ and $[\pm 45°]_{2S}$ laminates, and the fibre/matrix properties given in tables 2.2 and 3.1 respectively, were used in equations (4-11) to obtain the following equivalent ply elastic properties, table 4.1.

Material	E_{11} [GPa]	E_{22} [GPa]	ν_{12}
STS carbon	96.768	4.972 R M* 6.776 H-T**	0.33
E-glass	35.968	5.329 R M 8.743 H-T	0.298

*Rules of mixture **Halpin-Tsai

Table 4.1: Elastic properties prediction for equivalent STS carbon and E-glass unidirectional plies using CLT.

These values were used as inputs in the CADEC software to predict elastic properties $\{E_{xx},\nu_{xy}\}$ for the [0-90°]$_{4S}$ and [±45°]$_{2S}$ laminates. Tables 4.2 and 4.3 present the comparison between CLT prediction and experimental results found for both laminates. Predictions were conducted for values of E_{22}, determined using the rule of mixtures and the Halpin-Tsai relationships for comparison purposes.

Laminates	Laminate elastic properties	Preliminary inputs R M $\{E_{11}=96.768, E_{22}=4.972, \nu_{12}=0.33\}$	Preliminary inputs H-T $\{E_{11}=96.768, E_{22}=6.776, \nu_{12}=0.33\}$	Experimental values*
[0-90°]$_{4S}$	E_{xx} [GPa]	51.120	52.080	**49.825GPa**
	ν_{xy}	0.032	0.043	**0.054**
[±45°]$_{2S}$	E_{xx} [GPa]	16.450	16.560	**16.525**
	ν_{xy}	0.684	0.695	**0.753**

***average values obtained from tables 3.5 and 3.10.**

Table 4.2: Elastic properties prediction for [0-90°]$_{4S}$ and [±45°]$_{2S}$ STS/LY3505 laminates using Rule of Mixtures (RM) and Halpin-Tsai (HT) relationships.

Laminates	Laminate elastic properties	Preliminary inputs R M $\{E_{11}=35.968, E_{22}=5.329, \nu_{12}=0.298\}$	Preliminary inputs H-T $\{E_{11}=35.968, E_{22}=8.743, \nu_{12}=0.298\}$	Experimental values*
[0-90°]$_{4S}$	E_{xx} [GPa]	20.083	22.520	**26.662GPa**
	ν_{xy}	0.077	0.116	**0.154**
[±45°]$_{2S}$	E_{xx} [GPa]	13.370	13.81	**16.154**
	ν_{xy}	0.409	0.459	**0.514**

***average values obtained from table 3.6 and 3.11.**

Table 4.3: Elastic properties prediction for [0-90°]$_{4S}$ and [±45°]$_{2S}$ E-glass/LY3505 laminates using Rule of Mixtures (RM) and Halpin-Tsai (HT) relationships.

4.2.1.2 Ply calibration from ±30° braid angle specimens

Braid angle affects fibre compaction and hence, volume fraction. Consequently new elementary ply elastic properties have to be calculated for each fibre angle. A strategy, identical to that previously adopted, was used with 50% volume fraction determined through experimental measurements on $[\pm 30°]_{2S}$ coupons. Predicted elastic properties for an equivalent carbon and glass elementary ply are presented in table 4.4.

Material	**E_{11} [GPa]**	**E_{22} [GPa]**	**ν_{12}**
STS carbon	120.14	5.708 R M 8.077 H-T	0.325
E-glass	44.140	6.310 R M 11.21 H-T	0.285

Table 4.4: Elastic properties prediction for equivalent STS carbon and E-glass unidirectional plies using CLT.

These ply elastic properties have been validated successfully on the $[\pm 30°]_{2S}$ carbon and glass coupons as presented in tables 4.5 and 4.6.

Laminates	**Laminate elastic properties**	**Preliminary inputs R M {E_{11}=120.14, E_{22}=5.708, ν_{12}=0.325}**	**Preliminary inputs H-T {E_{11}=120.14, E_{22}=8.077, ν_{12}=0.325}**	**Experimental values***
$[\pm 30°]_{2S}$	E_{xx} [GPa]	42.230	43.250	**40.523GPa**
	ν_{xy}	1.419	1.337	**1.252**

***average values obtained from table 3.3**

Table 4.5: Elastic properties prediction for a $[\pm 30°]_{2S}$ STS/LY3505 laminate using Rule of Mixtures (RM) and Halpin-Tsai (HT) relationships.

Laminates	**Laminate elastic properties**	**Preliminary inputs R M {E_{11}=44.140, E_{22}=6.310, ν_{12}=0.285}**	**Preliminary inputs H-T {E_{11}=44.140, E_{22}=11.21, ν_{12}=0.285}**	**Experimental values***
$[\pm 30°]_{2S}$	E_{xx} [GPa]	25.000	25.000	**22.456GPa**
	ν_{xy}	0.676	0.648	**0.627**

***average values obtained from table 3.3**

Table 4.6: Elastic properties prediction for a $[\pm 30°]_{2S}$ E-glass/LY3505 laminate using Rule of Mixtures (RM) and Halpin-Tsai (HT) relationships.

4.2.2 Fibre damage treatment under tensile loading – Approximate treatment of delamination

As described in section 4.1.1.1, the model implemented in PAM-CRASH^{TM} always assumes an elastic failure for composite specimens under tensile loading in the fibre direction. Generally, only the elastic modulus E_{11} and limiting tensile strain ε^{t}_{111} are necessary in the model calibration since no critical, or post-critical domains, are present. For the braids investigated in this work the model is unsuitable since a highly non-linear stress-strain curve response has been measured. The heavy tow braided composites under tension exhibited significant tow stretching, leading to intra- and inter-ply delamination, which could be compared, effectively, to an 'elasto-plastic' material response.

In order to account for ply delamination, an interface element would have been necessary between each single ply using techniques proposed by Greve [49] [50] [51]. However, delamination characterisation and modelling of braided composites would have required a comprehensive experimental campaign, which was beyond the scope of this thesis. Therefore, inter-layer delamination damage has been integrated into the elementary unidirectional ply. The non-linearity was reproduced using the same approach as in the compressive damage model defined in the previous section. A corrective factor was initially introduced to account for stiffness loss in tension as follows [115],

$$\gamma = \frac{E_{11}^{0t} - E_{11}^{\gamma t}}{E_{11}^{\gamma t} E_{11}^{0t} \left|\varepsilon_{11}\right|}, \tag{4-12}$$

where $E^{\gamma t}_{11}$ is the tensile secant modulus at the failure strain. This approach has been used successfully for compression in the fibre direction, where small non-linearity caused by fibre buckling, was measured. However, this corrective factor could not be used for representing large non-linearity found for the tensile specimens.

In order to overcome this limitation, inter-ply delamination within a single elementary ply was modelled through tensile modulus degradation using a simple elastic modulus function depending on the longitudinal strain ε_{11} as follows,

$$E_{11}^{\gamma t} = f\left(\varepsilon_{11}\right), \tag{4-13}$$

where $E^{\gamma t}_{11}$ is the secant modulus in the fibre direction under tensile loading.

Figure 4.6 presents the evolution of the experimental longitudinal Young's modulus E_{11} with respect to longitudinal strain ε_{11} for two $[0\text{-}90°]_{4S}$ E-glass/LY3505 and STS/LY3505 specimens respectively, under tensile loading in the fibre direction. The polynomial functions, also shown in figure 4.6, were used to give the curve interpolation; these functions were then implemented within the shell element's FORTRAN routine.

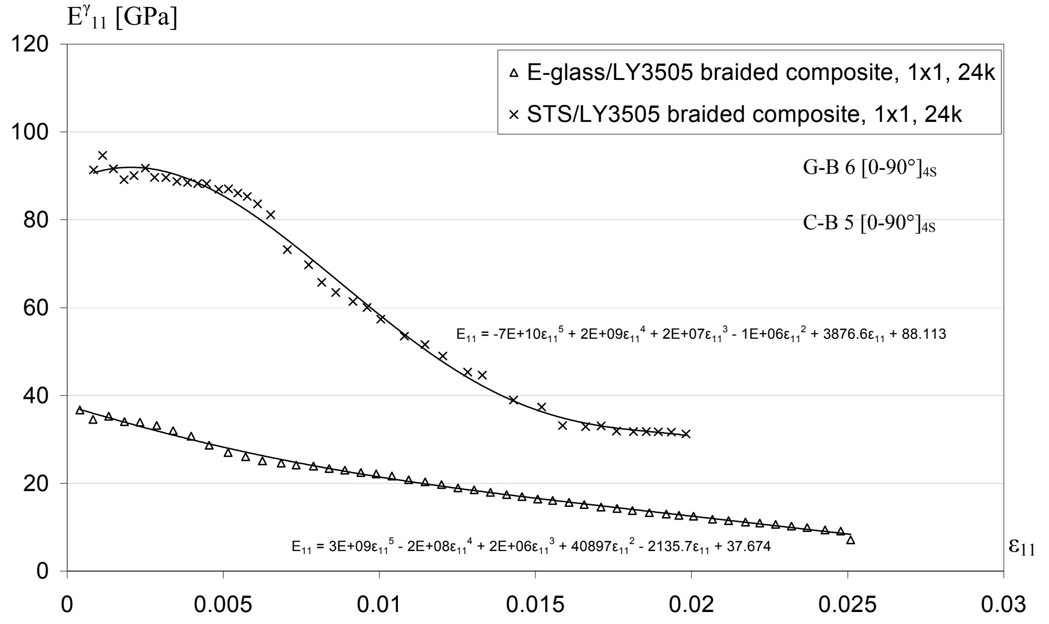

Figure 4.6: Polynomial interpolation of the secant modulus evolution.

For the damage parameters, the same initial and ultimate strains defined in the original model were used (tables 4.7 and 4.8 for carbon and glass respectively). Results presented in the next chapter showed that this technique is reasonably valid and that it could provide a more CPU efficient solution approach.

4.2.3 No transverse damage assumption ($d_{22}\approx0$)

As presented in the literature review chapter, the damage evolution related to the matrix in a unidirectional ply is monitored through two scalars parameters d_{22} and d_{12} which are, respectively, damage due to matrix micro-cracking parallel to the fibre direction and damage due to fibre/matrix interface debonding (shear). Transverse damage mainly occurs for unidirectional, or large fibre angle laminates (θ>45°). In this work, only balanced coupons with braid angles under 45° were studied. It was subsequently assumed that transverse damage could be neglected and that shear damage was the main damage mechanism. It will be shown, using comparisons with experimental results for coupons and beams, that this assumption is valid.

4.2.4 New procedure for σ_{12} versus ε_{12} curve determination

4.2.4.1 Inclusion of fibre rotation

The meso-scale damage model damage and plasticity laws were calibrated through cyclic tensile loading on $[\pm 45°]_{2S}$ laminates. The original unidirectional damage assumes a constant fibre angle throughout loading history. However, even experimental testing on a $[\pm 45°]_{8S}$ T300/913 unidirectional laminate, figure 4.7, has revealed fibre rotation such as those found in braided specimens. Fibre angle variation was not accounted for in the initial model due to measurement limitations of the strain gauges which can only measure strains up to 3%. This revealed a negligible fibre re-orientation of between 2 to 3 degrees, as shown in figure 4.7. However, the digital image correlation technique enabled full measurement of longitudinal strains, ε_{xx}, and transverse strains, ε_{yy}, required for plotting the shear stress strain curve, σ_{12} versus ε_{12}.

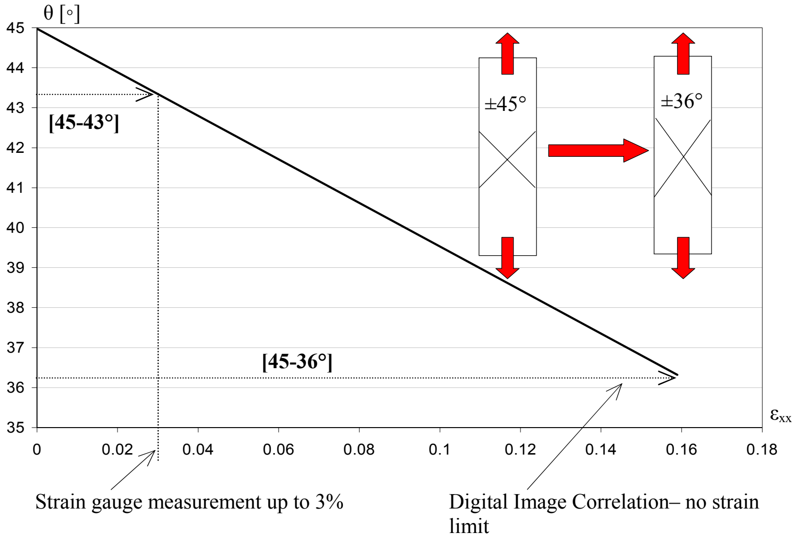

Strain gauge measurement up to 3%

Digital Image Correlation– no strain limit

Figure 4.7: Polynomial interpolation of the secant modulus evolution.

The shear stress-strain curve, σ_{12} versus ε_{12}, was determined using equation (4-14) and assuming a constant relationship between local and global quantities throughout the loading history,

$$
\begin{aligned}
&2\varepsilon_{12} = \left(\varepsilon_{xx} - \varepsilon_{yy}\right), \\
&\sigma_{12} = \frac{1}{2}\sigma_{xx},
\end{aligned}
\qquad (4\text{-}14)
$$

where suffices x and y stand for longitudinal and transverse directions respectively. However, this is only valid for small deformations, as shown above, where fibre rotations are negligible. In addition, the model states that the specimen has a constant cross-section meaning that axial stress σ_{xx} is calculated using a constant width and thickness.

Experimental results on braids showed that important fibre angle variations and width reductions occur, which significantly affect shear stress, σ_{12}, and shear strain, ε_{12}, calculations. In order to account for these two features equation (4-14) has had to be re-written. In the following, an attempt to enhance the formulation between local and global quantities and obtain more accurate material damage and plasticity laws is presented. It also appears that not only braids exhibit fibre rotation and cross-sectional reduction, but also unidirectional and woven fabric composites. Therefore, results found for these materials are also presented for comparison purposes.

The fibre angle variation, $\Delta\theta$, was numerically determined in the experimental chapter using equation (4-15) based on the axial and transverse strains variations, and assuming inextensible fibres,

$$\Delta\theta = Arc\tan\left[\left(\frac{1+\varepsilon_{yy}}{1+\varepsilon_{xx}}\right)\tan\theta_0\right]. \tag{4-15}$$

For each $\Delta\theta$ increment the principal strains ε_{11}, ε_{22}, and ε_{12} can be easily derived from the measured global strains ε_{xx}, ε_{yy} and ε_{xy} using,

$$\begin{aligned}\begin{Bmatrix}\varepsilon_{11}\\ \varepsilon_{22}\\ \gamma_{12}=2\varepsilon_{12}\end{Bmatrix} &= \left[T^{-1}\right]\begin{Bmatrix}\varepsilon_{xx}\\ \varepsilon_{yy}\\ 2\varepsilon_{xy}\end{Bmatrix},\\ &= \begin{bmatrix}\cos^2\theta & \sin^2\theta & \cos\theta\sin\theta\\ \sin^2\theta & \cos^2\theta & -\cos\theta\sin\theta\\ -2\cos\theta\sin\theta & 2\cos\theta\sin\theta & \cos^2\theta-\sin^2\theta\end{bmatrix}\begin{Bmatrix}\varepsilon_{xx}\\ \varepsilon_{yy}\\ 2\varepsilon_{xy}\end{Bmatrix}.\end{aligned} \tag{4-16}$$

In particular, the local shear strain ε_{12} is expressed as,

$$2\varepsilon_{12} = -2\cos\theta\sin\theta\ \varepsilon_{xx} + 2\cos\theta\sin\theta\ \varepsilon_{yy} + 2\left(\cos^2\theta-\sin^2\theta\right)\varepsilon_{xy}. \tag{4-17}$$

In order to derive the principle shear stress, σ_{12}, an approach based on CLT was used. This was initially proposed by Herakovich [58] for a unidirectional IM7-K3B graphite fibre/polyamide matrix composite exhibiting large fibre rotation. It allows the determination of principle stresses from the global axial stress accounting for fibre rotation and width reduction. The approach is first briefly explained and then used to plot the σ_{12} versus ε_{12} so that damage and plasticity laws may be calculated. The relationships between local and global quantities for a uniaxial tensile test can be written as,

$$\begin{cases} \sigma_{11} = S_1 \sigma_{xx} \\ \sigma_{22} = S_2 \sigma_{xx} \\ \sigma_{12} = S_3 \sigma_{xx}, \end{cases} \tag{4-18}$$

where S_1, S_2 and S_3 are functions of the fibre angle θ. The evolution of these 3 transformation variables S_1, S_2 and S_3 are plotted against θ for the STS carbon braid composite as shown in figure 4.8. The evolution of these 3 coefficients, according to θ, implies that,

- the transverse stress, σ_{22}, is either negligible or compressive,
- the axial stress, σ_{11}, increases since fibres re-orientate to align the axial direction,
- the shear stress, σ_{12}, decreases.

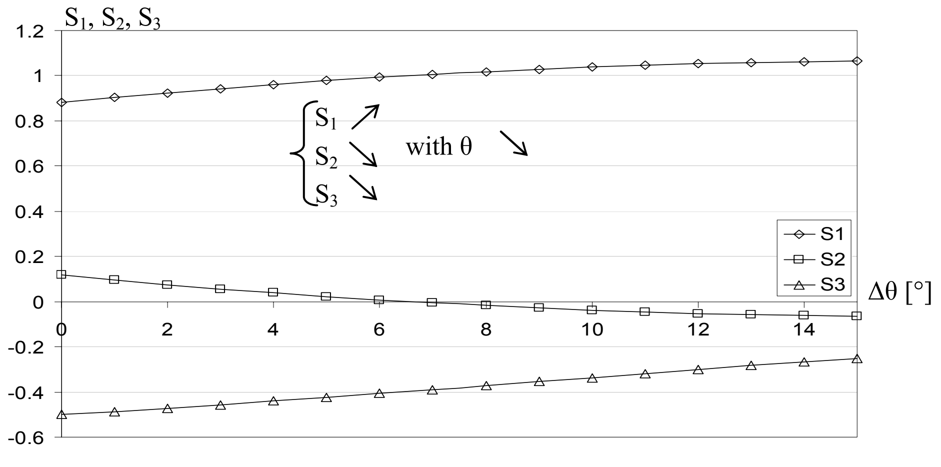

Figure 4.8: Evolution of the S1, S2 and S3 coefficients relative to decrease in fibre angle.

From the above figure it is clear that damage development within the laminate is a shear dominated event since transverse stresses are negligible, or compressive (micro-cracks closing), and damage associated with axial stresses σ_{11} does not occur until fibre failure.

The method to calculate the coefficients S_1, S_2, S_3 as a function of θ is based on the classical laminate approach. First, it is assumed that the fibre alignment process in the laminate is always balanced, meaning that for every ply at +θ orientation there is an identical ply with a –θ orientation. Therefore, for a [±θ°] laminate, the axial stress measured from tests can be expressed in terms of each ply as follows,

$$\sigma_{xx} = \frac{1}{2}\left(\sigma_{xx}^{+\theta} + \sigma_{xx}^{-\theta}\right). \tag{4-19}$$

The axial stress can also be expressed in terms of global strains using,

$$\begin{Bmatrix} \sigma_{xx} \\ 0 \\ 0 \end{Bmatrix} = \frac{1}{2}\left([T]_{+\theta}[C][T^{-1}]_{+\theta} + [T]_{-\theta}[C][T^{-1}]_{-\theta}\right)\begin{Bmatrix} \varepsilon_{xx} \\ \varepsilon_{yy} \\ 2\varepsilon_{xy} \end{Bmatrix},$$
$$\Rightarrow \begin{Bmatrix} \sigma_{xx} \\ 0 \\ 0 \end{Bmatrix} = \begin{bmatrix} \overline{C_{11}} & \overline{C_{12}} & 0 \\ \overline{C_{12}} & \overline{C_{22}} & 0 \\ 0 & 0 & \overline{C_{33}} \end{bmatrix}\begin{Bmatrix} \varepsilon_{xx} \\ \varepsilon_{yy} \\ 2\varepsilon_{xy} \end{Bmatrix} = \left[\overline{C}\right]\begin{Bmatrix} \varepsilon_{xx} \\ \varepsilon_{yy} \\ 2\varepsilon_{xy} \end{Bmatrix}, \tag{4-20}$$

where the stiffness matrix [C] is given by,

$$[C] = \begin{bmatrix} \dfrac{E_{11}}{1-\nu_{12}\nu_{21}} & \dfrac{\nu_{21}E_{11}}{1-\nu_{12}\nu_{21}} & 0 \\ \dfrac{\nu_{12}E_{22}}{1-\nu_{12}\nu_{21}} & \dfrac{E_{22}}{1-\nu_{12}\nu_{21}} & 0 \\ 0 & 0 & G_{12} \end{bmatrix}, \tag{4-21}$$

and the transformation matrices [T] and [T^{-1}] are given by,

$$[T] = \begin{bmatrix} \cos^2\theta & \sin^2\theta & -2\cos\theta\sin\theta \\ \sin^2\theta & \cos^2\theta & 2\cos\theta\sin\theta \\ \cos\theta\sin\theta & -\cos\theta\sin\theta & \cos^2\theta - \sin^2\theta \end{bmatrix},$$
$$[T^{-1}] = \begin{bmatrix} \cos^2\theta & \sin^2\theta & \cos\theta\sin\theta \\ \sin^2\theta & \cos^2\theta & -\cos\theta\sin\theta \\ -2\cos\theta\sin\theta & 2\cos\theta\sin\theta & \cos^2\theta - \sin^2\theta \end{bmatrix}. \tag{4-22}$$

Equation (4.20) is inverted to express global strains in terms of the axial stresses,

$$\begin{Bmatrix} \varepsilon_{xx} \\ \varepsilon_{yy} \\ 2\varepsilon_{xy} \end{Bmatrix} = \begin{bmatrix} \overline{C'_{11}} & \overline{C'_{12}} & 0 \\ \overline{C'_{12}} & \overline{C'_{22}} & 0 \\ 0 & 0 & \overline{C'_{33}} \end{bmatrix}\begin{Bmatrix} \sigma_{xx} \\ 0 \\ 0 \end{Bmatrix} = \left[\overline{C}\right]^{-1}\begin{Bmatrix} \sigma_{xx} \\ 0 \\ 0 \end{Bmatrix}. \tag{4-23}$$

The generalised Hooke's law gives the relationship between local stresses and strains for an elementary ply as follows,

$$\begin{Bmatrix} \sigma_{11} \\ \sigma_{22} \\ \sigma_{12} \end{Bmatrix} = [C] \begin{Bmatrix} \varepsilon_{11} \\ \varepsilon_{22} \\ 2\varepsilon_{12} \end{Bmatrix} . \tag{4-24}$$

The above relationship can be re-written using equations (4.16) and (4.23) to express local stresses in terms of the axial stress,

$$\begin{Bmatrix} \sigma_{11} \\ \sigma_{22} \\ \sigma_{12} \end{Bmatrix} = [C][T^{-1}][\overline{C}]^{-1} \begin{Bmatrix} \sigma_{xx} \\ 0 \\ 0 \end{Bmatrix} \Rightarrow \begin{Bmatrix} \sigma_{11} \\ \sigma_{22} \\ \sigma_{12} \end{Bmatrix} = \begin{bmatrix} S_{11} \\ S_{22} \\ S_{12} \end{bmatrix} \sigma_{xx} , \tag{4-25}$$

or,

$$\begin{aligned} \sigma_{11} &= S_{11}\sigma_{xx} = B\sigma_{xx} , \\ \sigma_{22} &= S_{22}\sigma_{xx} = (1-B)\sigma_{xx} , \\ \sigma_{12} &= S_{12}\sigma_{xx} = \frac{-1}{2\cos\theta\sin\theta}\left[B\left(1-2\cos^2\theta\right)+\cos^2\theta\right]\sigma_{xx} , \end{aligned} \tag{4-26}$$

with

$$B = \left[\frac{\cos^2\theta\left(2\cos^2\theta\ -1\right)+4\cos^2\theta\sin^2\theta\dfrac{G_{12}}{E_{22}}\left(\dfrac{E_{22}}{E_{11}}\nu_{12}+1\right)}{4\cos^2\theta\sin^2\theta\ \dfrac{G_{12}}{E_{22}}\left(\dfrac{E_{22}}{E_{11}}+2\dfrac{E_{22}}{E_{11}}\nu_{12}+1\right)+\left(2\cos^2\theta-1\right)\left(\cos^2\theta-\sin^2\theta\right)} \right] . \tag{4-26}$$

For a highly orthotropic material the ratio E_{22}/E_{11} tends to zero simplifying the calculation of the coefficient B,

$$B = \left[\frac{\cos^2\theta\left(2\cos^2\theta\ -1\right)+4\cos^2\theta\sin^2\theta\dfrac{G_{12}}{E_{22}}}{4\cos^2\theta\sin^2\theta\ \dfrac{G_{12}}{E_{22}}+\left(2\cos^2\theta-1\right)\left(\cos^2\theta-\sin^2\theta\right)} \right] . \tag{4-27}$$

In the following it is assumed that the ratio G_{12}/E_{22} remains constant throughout the loading history, even though G_{12} is varying due to damage. Equation (4.14) can now be re-written as follows,

$$\begin{aligned} \gamma_{12} &= 2\varepsilon_{12} = -2\cos\theta\sin\theta\ \varepsilon_{xx} + 2\cos\theta\sin\theta\ \varepsilon_{yy} + 2\left(\cos^2\theta-\sin^2\theta\right)\varepsilon_{xy} \\ \gamma_{12} &= 2\varepsilon_{12} \cong -2\cos\theta\sin\theta\ \varepsilon_{xx} + 2\cos\theta\sin\theta\ \varepsilon_{yy} \end{aligned} \tag{4-28}$$

$$\sigma_{12} = \frac{-1}{2\cos\theta\sin s\theta}\left[B\left(1-2\cos^2\theta\right)+\cos^2\theta\right]\sigma_{xx}$$

The contribution of the term $2(\cos^2\theta-\sin^2\theta)\varepsilon_{xy}$ was measured in experiment and found to be negligible; therefore, the principle shear strain, ε_{12}, may be readily expressed in terms of ε_{xx} and ε_{yy}.

4.2.4.2 Inclusion of width reduction and treatment of necking

In order to account for reduction of cross-sectional dimensions the axial stress, σ_{xx}, depends on the transverse strain, ε_{yy}, as follows,

$$\sigma_{xx} = \frac{F}{w(1-\varepsilon_{yy})t}, \qquad (4\text{-}29)$$

where F, w, and t are axial force, specimen width and thickness respectively.

4.2.4.3 Original and new σ_{12} versus ε_{12} curves comparison

In this work, not only braided composites have been investigated, but also unidirectional and woven fabric composites were briefly studied in order to determine if fibre re-orientation was common to these materials and to assist validation of the work. Figure 4.9 shows the σ_{12} versus ε_{12} curves for braided, unidirectional and woven fabric composites using either equation (4-14), or (4-28). The elastic properties required to calibrate equation (4-28) are presented on each respective graph.

For all materials an expected reduction in the magnitude of the shear stress, σ_{12}, has been found when fibre rotation and width reduction are included in the model. It is to be noted that the same modelling approach as defined above for braided composites, based on an equivalent unidirectional ply, was adopted for the woven fabric laminate.

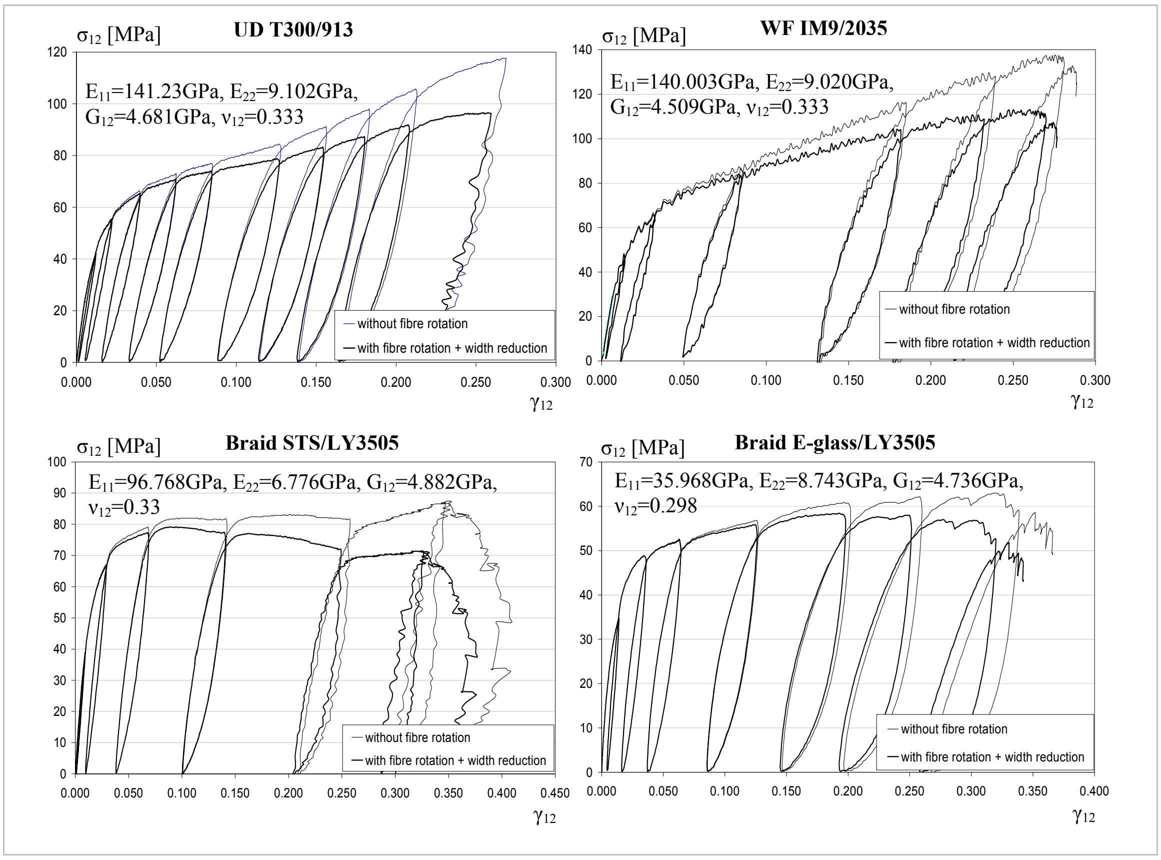

Figure 4.9: **Stress-strain curves, σ_{12} versus ε_{12}, with, or without, fibre rotation and necking considerations.**

4.2.5 Shear damage and plasticity laws

4.2.5.1 Non-linear damage law – $d_{12}=g(Y_{12})$

Figure 4.10 shows the stress-strain curve obtained from a cyclic test carried out on a $[\pm 45°]_{2S}$ STS carbon fibre braided specimen. As mentioned earlier the shear damage variable d_{12} is determined from loss of stiffness from the cyclic tensile testing of a $[\pm 45°]_{2S}$ laminate coupon. The shear modulus G^{i}_{12} for each cycle is calculated from the elastic strains γ^{ie}_{12} and the respective shear stress σ^{i}_{12}. In addition, in order to monitor the evolution of plasticity, plastic strains γ^{ip}_{12} are extracted for each cycle. At least 5-6 cycles are required to obtain a good evolution of damage and plasticity. The data analysis process to obtain material laws manually is relatively time consuming and consequently a Matlab^{TM} program [101] was developed to automatically calculate damage and plasticity laws from the coupon force and strain measurements.

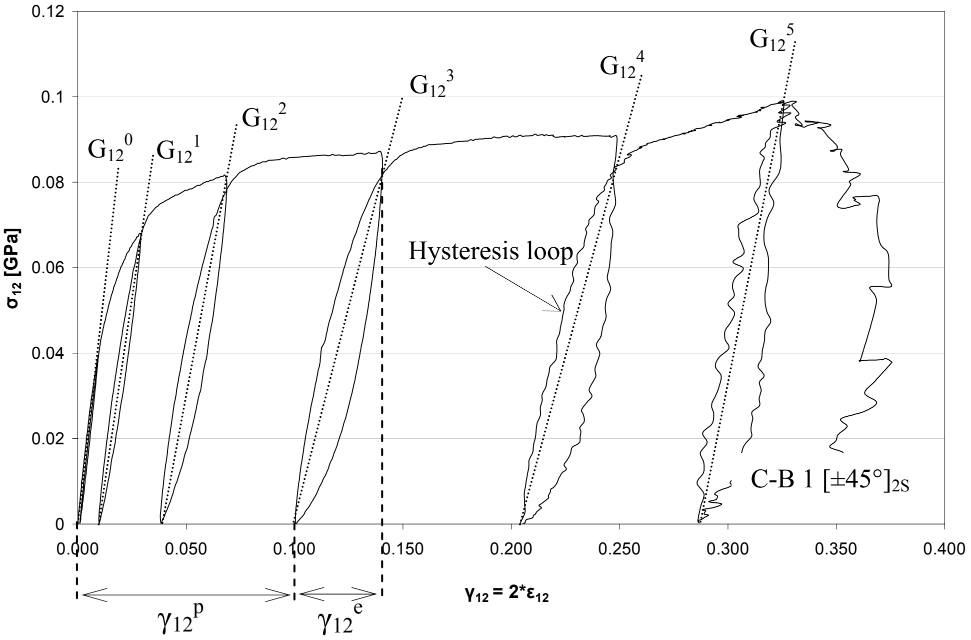

Figure 4.10: Cyclic tensile test on a [±45°]$_{2S}$ STS/LY3505 braided specimen.

From equation (2-10), the shear damage d^i_{12} at each cycle is,

$$d_{12} = 1 - \frac{G^i_{12}}{G^0_{12}} \tag{4-30}$$

where G^i_{12} is the damaged modulus and G^0_{12} is the initial undamaged value. For convenient implementation of the damage model in the explicit FE code PAM-CRASH^{TM} it is necessary to define the law in terms of strains and not stresses. Therefore, the conjugate force Y^i_{12} defined in equation (2-11), has to be re-written in terms of elastic strains γ^{ie}_{12} as follows,

$$\underline{Y}^i_{12} = \sqrt{\frac{1}{2} G^0_{12} \left(\gamma^{ie}_{12}\right)^2}\,. \tag{4-31}$$

The damage evolution curve d_{12} versus Y_{12} is then plotted using (Y^i_{12}, d^i_{12}) points that are calculated for each cycle. Figure 4.11 presents the damage curve determined for the four materials defined in the previous section, with and without treatment of fibre rotation and width reduction. Results show that fibre rotation and width reduction do not greatly affect the damage behaviour up to a certain threshold angle. However, beyond this point it is shown that inclusion of these effects becomes increasingly important, especially to avoid the questionable decrease in damage near to ultimate failure.

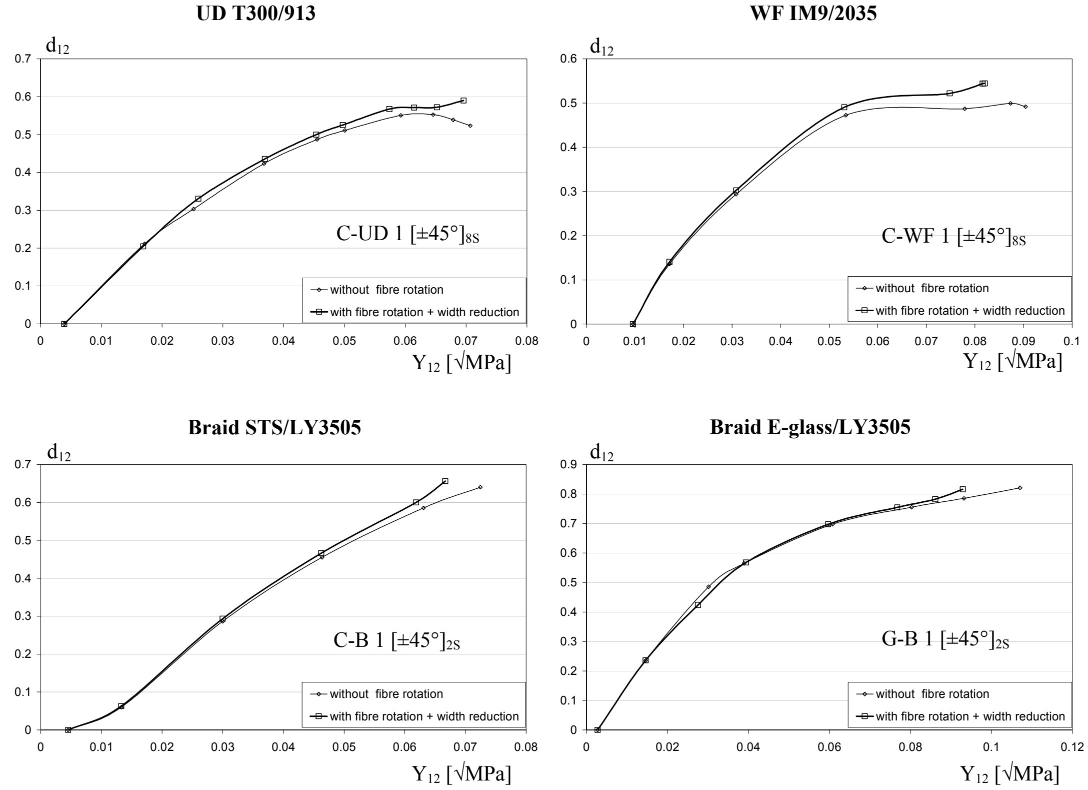
UD T300/913

WF IM9/2035

Braid STS/LY3505

Braid E-glass/LY3505

Figure 4.11: Damage laws for UD, WF, glass and carbon braided composites.

The damage law originally relates linearly conjugate shear forces Y_{12} to shear damage d_{12}, as shown in equation (4-10). This approximation was used successfully for experimental results having limited shear strain to failure (<3%). Figure 4.11 shows, however, that this interpolation is suitable only for the very beginning of the curve and becomes quickly inaccurate for large shear strains that occur particularly in the case of the braided composites investigated. Therefore, a polynomial function was introduced to represent damage evolution more accurately. Figure 4.12 shows the experimental damage law obtained from cyclic test and its polynomial fit for an E-glass braided specimens.

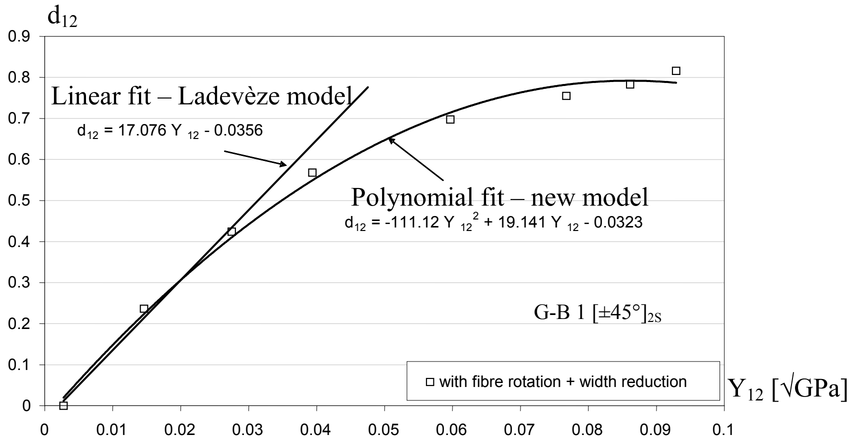

Figure 4.12: Damage laws for a E-glass/LY3505 braided composites.

The damage laws found for carbon and glass braided coupons were interpolated using a generic polynomial function of the form,

$$d_{12} = a_n Y_{12}^n + ... + a_1 Y_{12} + a_0 \tag{4-32}$$

where a_n, …, a_1 and a_0 are material constants. Results found for calibration of this polynomial function are presented in tables 4.7 and 4.8 for carbon and glass braided coupons respectively (section 4.3).

4.2.5.2 Plasticity/Hardening law

Parameters for the plasticity law are derived from the evolution of plastic strains at each cycle. The plasticity hardening function $R(p)$ and respective accumulated plastic strain p are derived from the following equations (4-33) and (4-34),

$$R(p) - R_0 = \frac{\sigma_{12}}{1 - d_{12}}, \tag{4-33}$$

$$p = \int_0^{\varepsilon_{12}^p} 2(1 - d_{12})\, d\varepsilon_{12}^p, \tag{4-34}$$

where R_0 is the initial threshold effective stress for initiation of plastic strains. The evolution of the hardening function *R(p)* is interpolated using the following power law function,

$$R(p) = \beta p^{\alpha}, \tag{4-35}$$

where material constants β and α are hardening coefficients to be obtained from cyclic testing. The hardening laws for the materials introduced in the previous section are presented in figure 4.13 which compares curves accounting or not for fibre rotation.

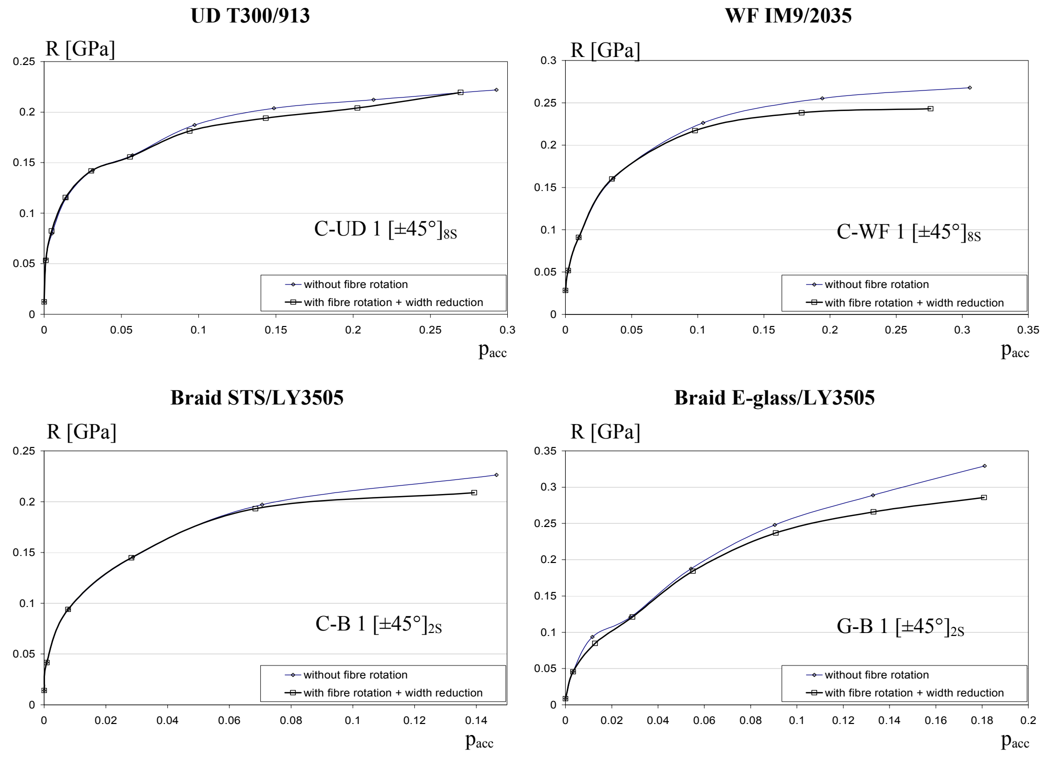

Figure 4.13: Plasticity laws for a UD, woven fabric, carbon and glass braided composites.

The above figures demonstrate that taking fibre re-orientation and width reduction into account does influence the plasticity law by reducing the magnitude of R(p) and lowering the accumulated plastic strains p. The material constants β and α from the power law that are used to interpolate the hardening experimental curve are given in tables 4.7 and 4.8 for carbon and glass braided coupons respectively (section 4.3).

4.2.5.3 Damage and plasticity laws updated in terms of braid angle

As demonstrated previously in section 4.2.1.1, a decrease in braid angle affects the elastic properties together with the damage and plasticity laws. Indeed, the previous damage law obtained for the [±45°] coupon could not be used to represent damage evolution in the [±30°]$_{2S}$ coupon, since damage and plasticity both initiate later in the loading history. Therefore, assuming an equivalent damage trend (polynomial), the damage initiation value, Y_{120}, and the plasticity initiation value, R_0, must be determined.

The shear stress-strain curve, σ_{12} versus ε_{12}, obtained from the tensile shear test is therefore plotted accounting for fibre rotation and width reduction using equation (4.28), as is shown in figures 4.14 and 4.15. It is noteworthy that using a 30° fibre angle affects the relationships between global and local quantities; for instance the coefficients S_1, S_2, and S_3 must be re-derived. Elastic properties used for the calculation of coefficient S3 are presented in tables 4.9 and 4.10 for carbon and glass braids respectively (section 4.3).

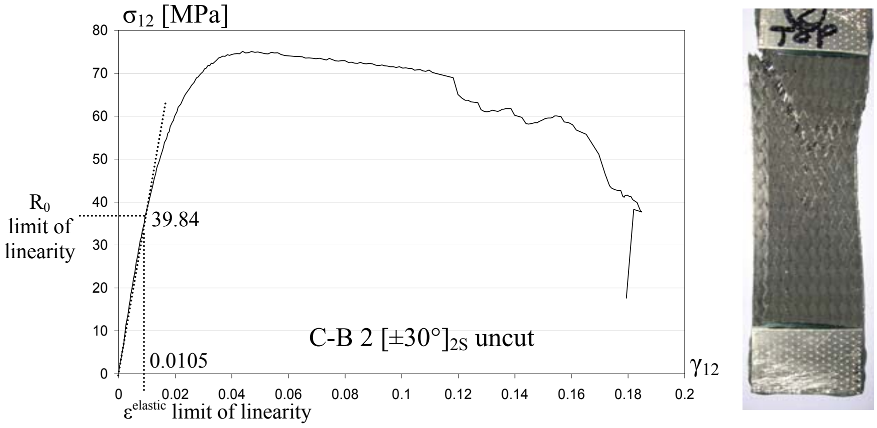

Figure 4.14: σ_{12} versus ε_{12} curve for a [±30°]$_{2S}$ STS/LY3505 carbon braided composite specimen including fibre rotation and width reduction.

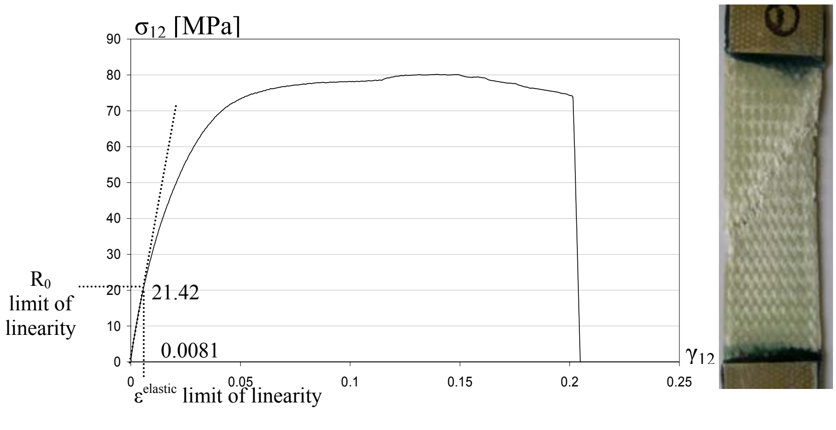

Figure 4.15: σ_{12} versus ε_{12} curve for a [±30°]$_{2S}$ E-glass/LY3505 braided composite specimen including fibre rotation and width reduction.

The elastic strain threshold allows the calculation of Y_{120} using equation (4.31). Assuming a similar damage trend, the curve has to be shifted in order to delay damage initiation, as shown in figures 4.16 and 4.17 for carbon and glass fibre respectively.

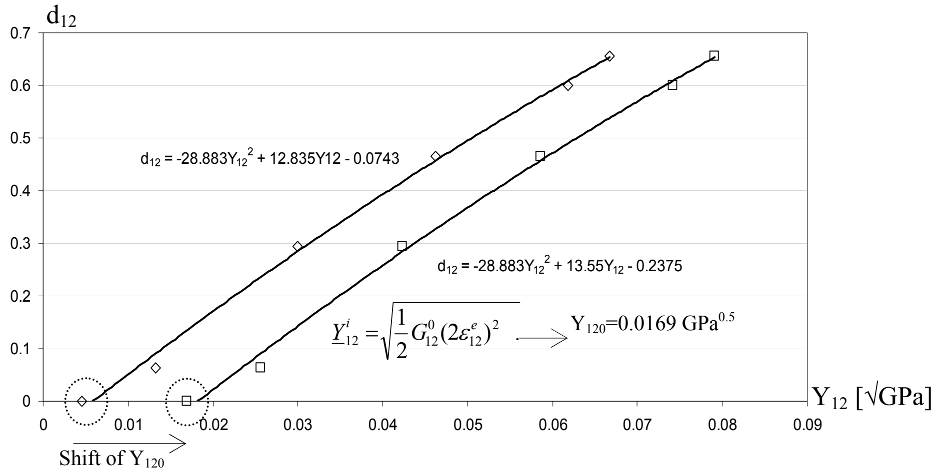

Figure 4.16: Damage law shift for a [±30°]$_{2S}$ STS/LY3505 carbon braided coupon.

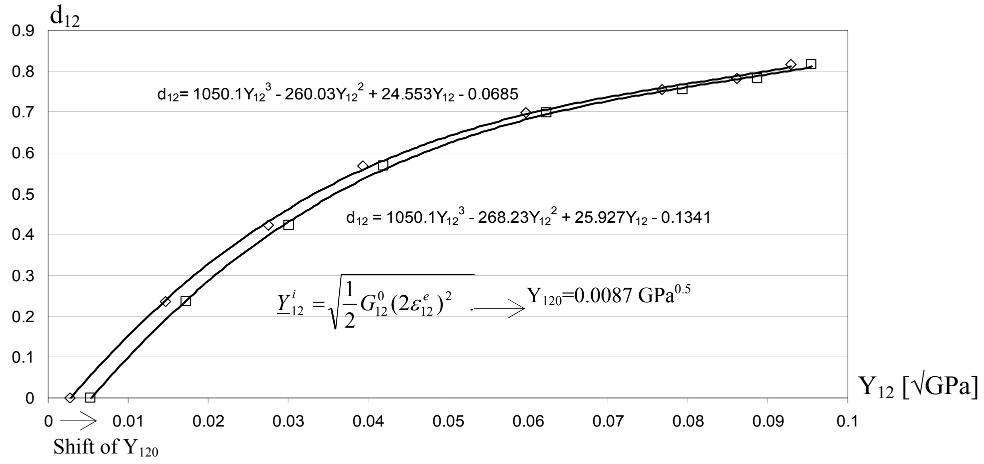

Figure 4.17: Damage law shift for a [±30°]$_{2S}$ E-glass/LY3505 braided coupon.

Therefore, new material input data for the PAM-CRASH^{TM} model has to be defined in the case of 30° fibre angle. Results on damage and plasticity laws interpolation through polynomial and power functions for carbon and glass braided coupons are summarised in tables 4.9 and 4.10 respectively (section 4.3).

As previously mentioned, the braid angle varies accordingly to the application. Therefore the previous damage delaying strategy could be used for various fibre angles in order to determine the respective damage and plasticity laws. In Chapter 6 – Overall discussion, an alternative method based on cyclic testing of different fibre angles is proposed in order to estimate the damage and plasticity laws variation accordingly to braid angle.

4.3 Overview

A new modelling approach has been proposed in this chapter to enable prediction of progressive damage and failure in carbon and glass braided composites. A [±θ°] braided layer is represented using two distinct unidirectional plies, super-imposed at +θ° and -θ°. The Ladevèze damage model for a unidirectional ply and implemented in the explicit FE code PAM-CRASH^{TM} is used as a basis to model failure mechanisms in braided composites.

The calibration to determine elastic properties of an 'equivalent braided unidirectional ply' was conducted using a standard CLT approach. However, due to fibre re-orientation, or so-called 'scissoring', during loading, the original Ladevèze model, which is based on the assumption of a constant fibre angle, had to be modified. An alternative σ_{12} versus ε_{12} formulation accounting for fibre angle variation was derived from CLT which gives an improved representation of shear damage and hardening laws for the investigated carbon and glass braided composites.

It has also been shown that for various braid angles, ±45° or ±30°, the volume fraction V_f changes and, therefore, elastic properties, damage evolution and plasticity laws of the 'equivalent braid unidirectional ply' are affected. The results obtained for the different equivalent braid unidirectional plies are presented in tables 4.7, 4.8, 4.9, and 4.10. This data will be used in the next chapter to validate, through coupons and beams simulations, the new formulation of the Ladevèze damage model adapted to braided composites. It should be noted that the curve fitting software IGOR [132] has been used for damage and plasticity laws interpolations since this was found to give greater accuracy than the built-in fitting tool available in Microsoft Excel.

The necessary steps to calibrate an equivalent braid unidirectional ply are summarised in the flow chart presented in figure 4.18.

Elastic properties							
	$E_{11}^{t0}=E_{11}^{c0}$ [GPA]	ν_{12}^{0}	E_{22}^{0} [GPa]	G_{12}^{0} [GPa]	G_{23}^{0} [GPa]		
	96.768	0.33	6.776	4.882	4.882		
Fibre damage parameters							
	Tension			**Compression**			
	ε_{11l}^{t}	ε_{11u}^{t}	d_{11u}^{t}	γ	ε_{11l}^{c}	ε_{11u}^{c}	d_{11u}^{c}
	0.0184	0.0185	1.0	0.1	0.0064	0.0065	1.0
Shear damage law $d_{12}=a_1Y_{12}^2+a_2Y_{12}+a_3$							
	a_1	a_2	a_3	Y_{Rmax} [√GPa]	d_{max}		
	-28.883	12.835	-0.0743	0.0766	1.0		
Plasticity law $R(p)=\beta p^{\alpha}$							
	β [GPa]	α	R_0 [GPa]				
	0.3883	0.2873	0.0171				

Table 4.7: Ply data input for an 'equivalent braid unidirectional ply' derived from a ±45° STS/LY3505 carbon braided composite.

Elastic properties							
	$E_{11}^{t0}=E_{11}^{c0}$ [GPA]	ν_{12}^{0}	E_{22}^{0} [GPa]	G_{12}^{0} [GPa]	G_{23}^{0} [GPa]		
	35.968	0.298	8.743	4.736	4.736		
Fibre damage parameters							
	Tension			**Compression**			
	ε_{11l}^{t}	ε_{11u}^{t}	d_{11u}^{t}	γ	ε_{11l}^{c}	ε_{11u}^{c}	d_{11u}^{c}
	0.0283	0.0283	1	0.09	0.0083	0.00831	1
Shear damage law $d_{12}=a_1Y_{12}^3+a_2Y_{12}^2+a_3Y_{12}+a_4$							
a_1	a_2	a_3	a_4	Y_{Rmax} [√GPa]	d_{max}		
1050.1	-260.03	24.553	-0.0685	0.0929	1		
Plasticity law $R(p)=\beta p^{\alpha}$							
	β [GPa]	α	R_0 [GPa]				
	0.6490	0.4506	0.0067				

Table 4.8: Ply data input for an 'equivalent braid unidirectional ply' derived from a ±45° E-glass/LY3505 braided composite.

Elastic properties							
	$E_{11}^{t0}=E_{11}^{c0}$ [GPA]	ν_{12}^{0}	E_{22}^{0} [GPa]	G_{12}^{0} [GPa]	G_{23}^{0} [GPa]		
	120.140	0.325	8.077	5.200	5.200		
Fibre damage parameters							
	Tension			**Compression**			
	ε_{11l}^{t}	ε_{11u}^{t}	d_{11u}^{t}	γ	ε_{11l}^{c}	ε_{11u}^{c}	d_{11u}^{c}
	0.0184	0.0185	1.0	0.1	0.0064	0.0065	1.0
Shear damage law $d_{12}=a_1Y_{12}^2+a_2Y_{12}+a_3$							
	a_1	a_2	a_3	Y_{Rmax} [√GPa]	d_{max}		
	-28.883	13.55	-0.2375	0.0790	1.0		
Plasticity law $R(p)=\beta p^{\alpha}$							
	β [GPa]	α	R_0 [GPa]				
	0.3883	0.2873	0.0398				

Table 4.9: Ply data input for an 'equivalent braid unidirectional ply' derived from a ±30° STS/LY3505 carbon braided composite.

Elastic properties							
	$E_{11}^{t0}=E_{11}^{c0}$ [GPA]	ν_{12}^{0}	E_{22}^{0} [GPa]	G_{12}^{0} [GPa]	G_{23}^{0} [GPa]		
	44.140	0.285	11.210	5.100	5.100		
Fibre damage parameters							
	Tension			**Compression**			
	ε_{11l}^{t}	ε_{11u}^{t}	d_{11u}^{t}	γ	ε_{11l}^{c}	ε_{11u}^{c}	d_{11u}^{c}
	0.0283	0.0284	1	0.09	0.0083	0.00831	1
Shear damage law $d_{12}=a_1Y_{12}^3+a_2Y_{12}^2+a_3\,Y_{12}+a_4$							
a_1	a_2	a_3	a_4	Y_{Rmax} [√GPa]	d_{max}		
1050.1	-268.23	25.92	-0.1341	0.0955	1		
Plasticity law $R(p)=\beta p^{\alpha}$							
	β [GPa]	α	R_0 [GPa]				
	0.6490	0.4506	0.0214				

Table 4.10: Ply data input for an 'equivalent braid unidirectional ply' derived from a ±30° E-glass/LY3505 braided composite.

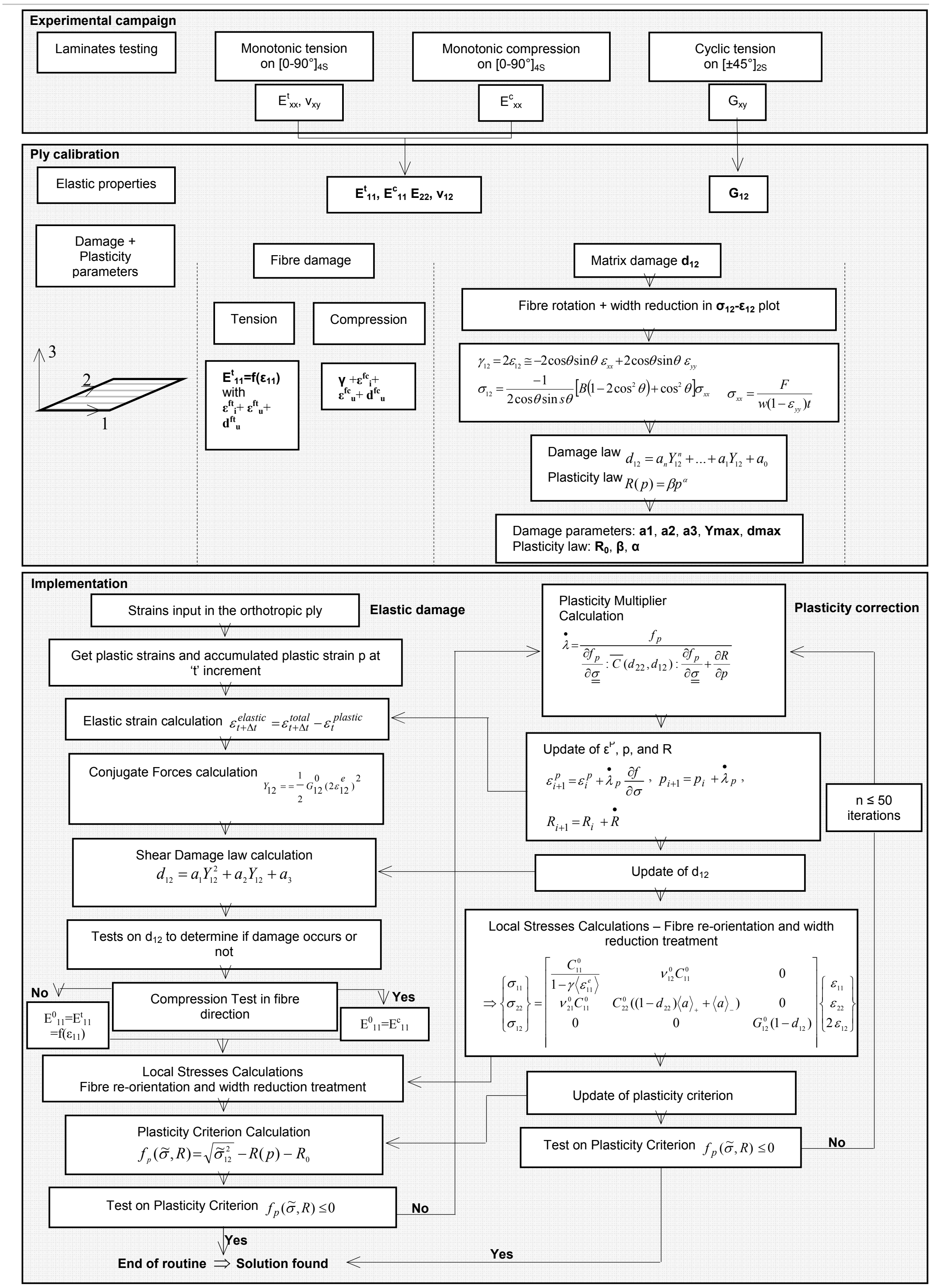

Figure 4.18: Flow chart illustrating the strategy used for characterisation of carbon and glass braided composites.

Chapter 5- Damage model validation

In the chapter 3, the different failure mechanisms encountered in 2D braided composites were investigated through an extensive experimental testing campaign. In chapter 4, the meso-mechanical damage model proposed by Ladevèze for unidirectional composites was used as a basis to develop a new model for braided composites that accounts for fibre rotations and width reductions observed experimentally. This new model formulation led to the characterisation of damage and plasticity laws for both carbon and glass braided composites. Non-linear damage evolution was found for carbon and glass specimens, and also for unidirectional and woven fabric composites; accordingly, new polynomial interpolation functions were implemented in the explicit FE code PAM-CRASH^{TM} [115] for these material types.

In this chapter, the model will be validated by correlating coupons and beams experimental results with simulations. The new damage law was implemented into the multi-layered PAM-CRASH^{TM} shell element (MAT 131) presented in section 2.5.2.1; elastic, damage and plasticity parameters where input in the related ply data card (ITYP1). In the following, preliminary simulations conducted on a single shell element are presented. Hence, simulations of the different experimental coupons were investigated and closely compared to experimental results. Finally, the manufactured carbon and glass beams subjected to four point loading were also simulated. Results obtained from simulations are presented and compared to experimental tests.

5.1 Single shell element and coupon definition

5.1.1 Multilayered shell element (Mat 131) and unidirectional composite global ply model (ITYP=1)

In the following, the multilayered shell element, material type 131, in PAM-CRASH^{TM}, has been used to model braided composites. The elastic properties, damage and plasticity law parameters obtained from calibration with tests results and presented in the tables 4.7, 4.8, 4.9 and 4.10 are used as ply input data for failure analysis of carbon and glass braid materials.

The orthotropy coordinate system, figure 5.1, was defined such that the first axis (1) of orthotropy coincides with the fibre longitudinal axis x of the test piece. The second axis of orthotropy (2) coincides with the transverse axis y of the test piece.

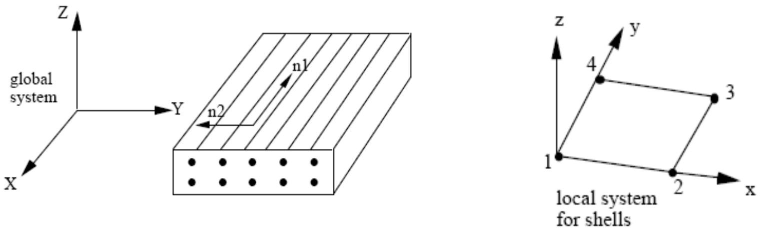

Figure 5.1: Orthotropy definition [115].

5.1.2 Single shell element validation

The model has been first checked, and validated, using only a single shell element for which plane stress and constant damage through the thickness were assumed. The orthotropy system adopted was identical to that defined above. The boundary and loading conditions applied on the four nodes of the element are defined as shown in figure 5.2. These load the element in the x direction and allow the element to deform freely in the transverse direction.

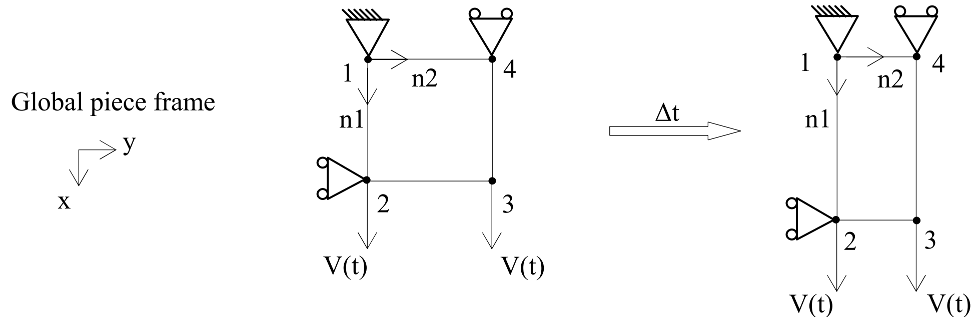

Figure 5.2: Validation using a single shell element.

The velocity function applied to nodes 2 and 3 loads the specimen progressively using a preliminary 'ramp', figure 5.3, to avoid abrupt loading of the element; thereafter, the speed is held constant at 0.01mm/ms. This insures quasi-static loading of the element.

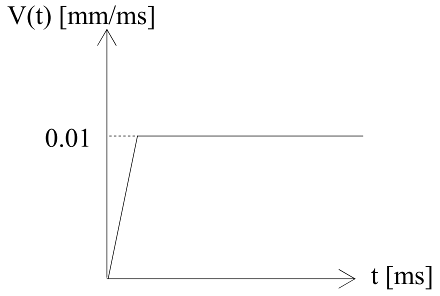

Figure 5.3: Velocity function applied to the shell element.

The 'equivalent braid unidirectional ply' defined in the previous chapter was used to represent each coupon stacking sequence tested. Ply directions were input with respect of the first direction of orthotropy, for instance the $[\pm45°]_{2S}$ braided coupon had plies at +45° and -45°, stacked symmetrically, as shown in figure 5.4.

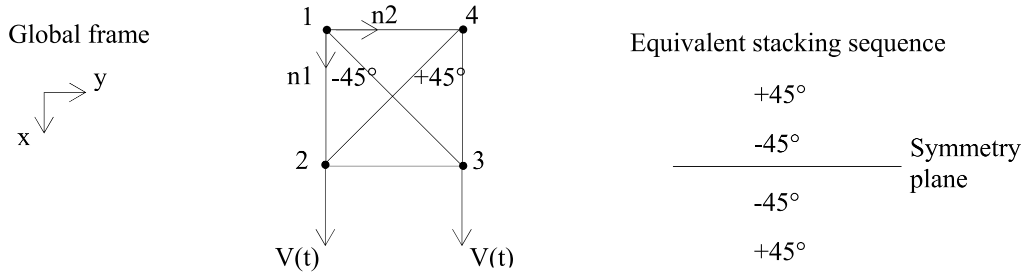

Figure 5.4: Plies stacking sequence for a $[\pm45°]_{2S}$ coupon.

The shell element formulation implemented in PAM-CRASH^{TM}, also allows determining the fibre angle variation using the respective rotation of the element diagonals. Therefore, for each angle increment the code gives the updated local stresses and strains in the element. The relationships used for these calculations are based on an identical approach to CLT as mentioned in the previous chapter, with using $\{S_1, S_2, S_3\}$ as transformation coefficients [115].

5.1.3 Mesh for coupon validation

The validated shell element was then used as a basis to mesh the entire coupon. The boundary and loading conditions imposed were identical to the experiment, being clamped at one end and moving at the other end with a constant velocity, as shown in figure 5.5. For each experimental coupon a fine mesh has been created; for instance, the $[\pm45°]_{2S}$ coupon of 157*67*1.57 mm dimensions uses 532 elements having an initial ply angle of ±45°.

Output from the simulation is compared with experimental results for longitudinal stress versus strain, σ_{xx} versus ε_{xx}. The longitudinal stress has been calculated from the reaction force divided by the variable cross sectional area. The longitudinal and transverse strains were readily calculated using the relative displacement of points {A, B} and {C, D} respectively. The ply orientation was identical for all elements and was input according to the braid angle of the coupon simulated.

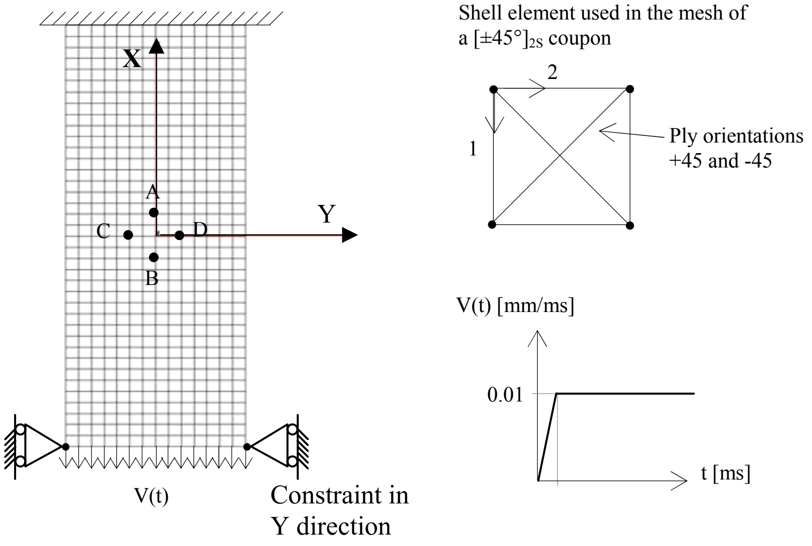

Figure 5.5: FE model for a $[\pm45°]_{2S}$ braided coupon.

5.2 Simulations results

In the next section, simulations of the different experimental tests conducted in chapter 3 are presented and compared to experimental results. The ply data cards used for the simulations were chosen according to the tests. Table 1 presents the ply data card used for each simulation.

Simulation	**Carbon**	**Glass**
Tension on [0-90°]$_{4S}$	Table 4.7	Table 4.8
Compression on [0-90°]$_{4S}$	Table 4.7	Table 4.8
Cyclic tension on [±45°]$_{2S}$	Table 4.7	Table 4.8
Tension on [±30°]$_{2S}$	Table 4.9	Table 4.10
Four point bending on square cross-section beam	Table 4.9	Table 4.10

Table 5.1: Ply data cards used in the simulations.

5.2.1 Model validation for fibre damage and delamination treatment

5.2.1.1 Monotonic tension on a [0-90°]$_{4S}$ laminate

In chapter 4, it has been shown that the original fibre damage model implemented in PAM-CRASH^{TM} enabled only to predict linear elastic ply failure without the effect of delamination, as shown in figure 5.6. By accounting for ply delamination through a ply stiffness function, $E_{11}=f(\varepsilon_{11})$, the new improved model showed a better correlation with experiment for both carbon and glass braids, for the single shell element and coupon, figures 5.6 and 5.7. The new model allowed accurate prediction of the non-linear response of carbon and glass [0-90°]$_{4S}$ laminates in which intra-ply damage and inter-ply delamination mechanisms occur. In addition, the failure location predicted at the grips correlated well with experimental results, as shown in figures 5.6 and 5.7.

It should be noted that further calibration of the strain limit ε^{tl}_{11} was required when using a coupon. Indeed, the initial strain limit value, 1.84%, found for carbon (2.83% for glass) had to be increased to 5.57% (5.87% for glass) in order to obtain good agreement with experiment. Elements located at the edges of the fixed grips have stringent boundary conditions, compared to elements at the coupon mid-length, hence they are likely to fail first.

Although a good agreement for the longitudinal behaviour was found, it appears that transverse deformation does not give a good prediction of transverse strain at failure. Normally, not only the Young modulus, E_{11}, should be degraded by damage and delamination but, also, Poisson's ratio should be treated as a damage variable. However, the implementation of a Poisson's ratio that varies with damage could not be achieved since it would have required considerable modification to several routines which were not available.

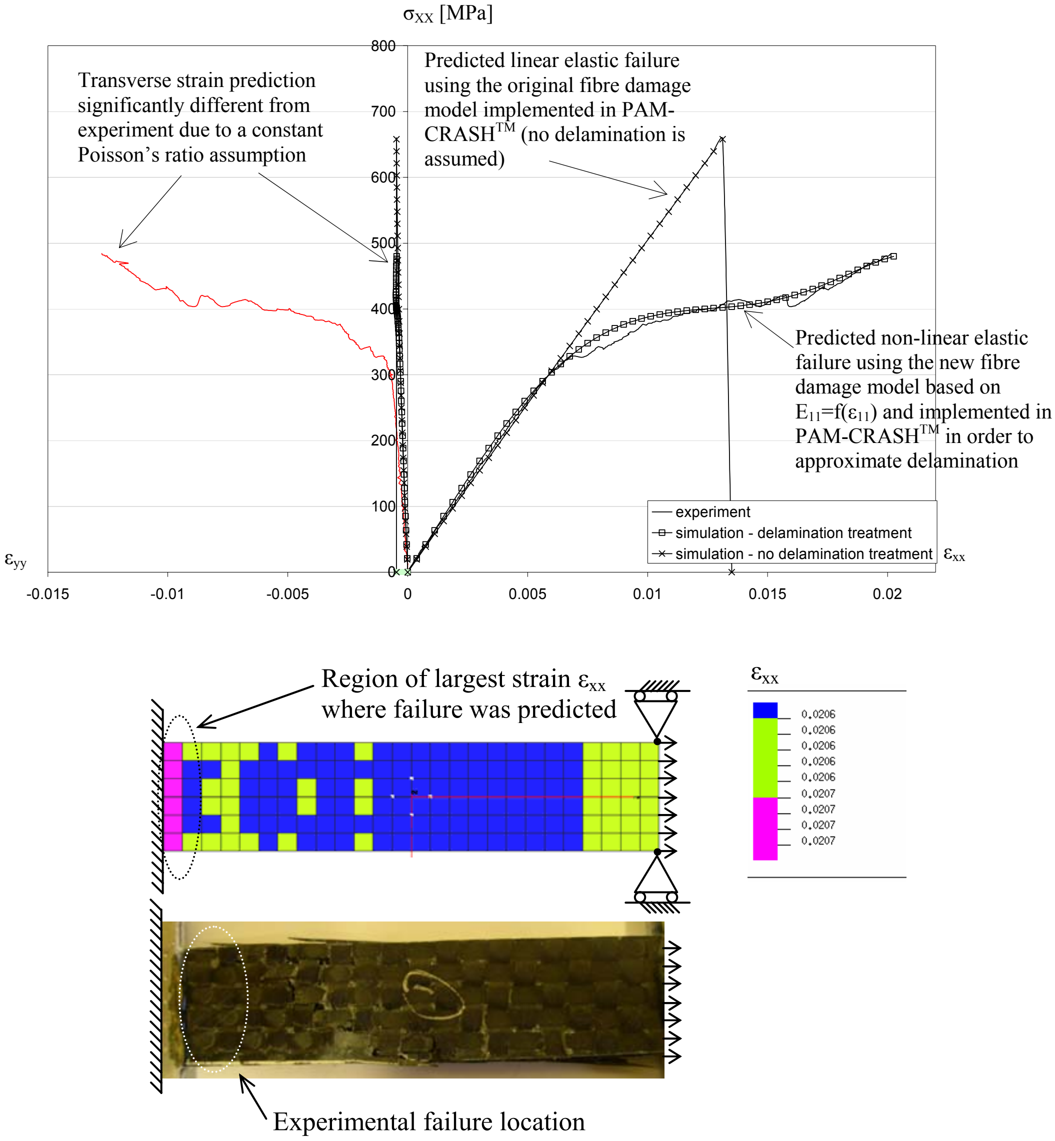

Figure 5.6: Failure prediction for a $[0\text{-}90°]_{4S}$ STS carbon braided specimen.

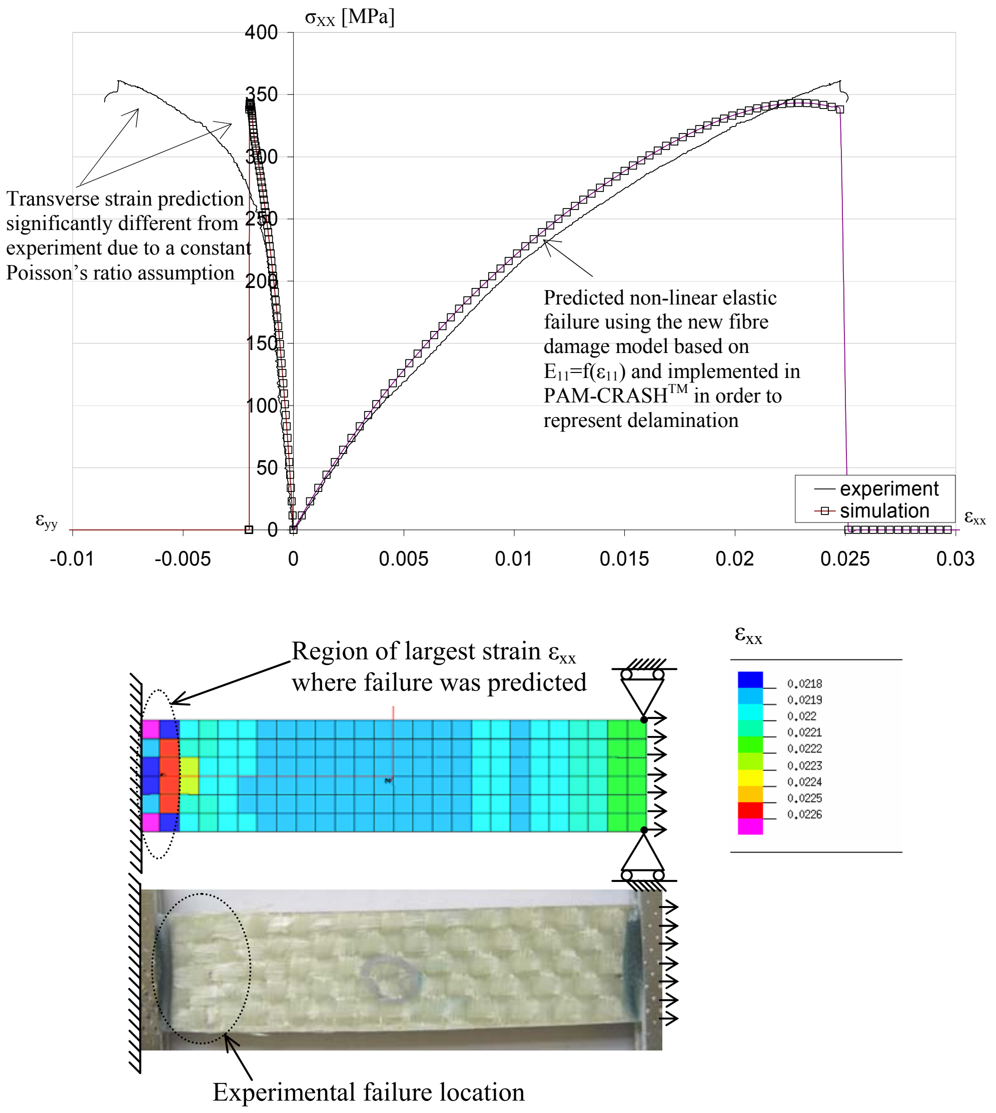

Figure 5.7: Failure prediction for a $[0\text{-}90]_{4S}$ E-glass braided specimen.

5.2.1.2 Monotonic compression on a $[0\text{-}90°]_{4S}$ laminate

The same single element used for tensile loading was also used for compression loading by reversing the direction of the applied velocity curve. The prediction found for a single element correlated perfectly with experimental results for both glass and carbon, as shown in figures 5.8 and 5.9. This validation was also conducted for coupons, figures 5.8 and 5.9. Results found for stress-strain curve were identical to those identified for the single element. The strain distribution within the coupon centre was homogenous as found experimentally. Failure occurred when elements exceed the strain limit ε^{c}_{11l}, or the strain at which the fibres fail by pure compression. Strain plots revealed that corner elements were likely to fail first, since they showed largest strain for carbon and glass coupons, as shown in figure 5.8 and 5.9 respectively.

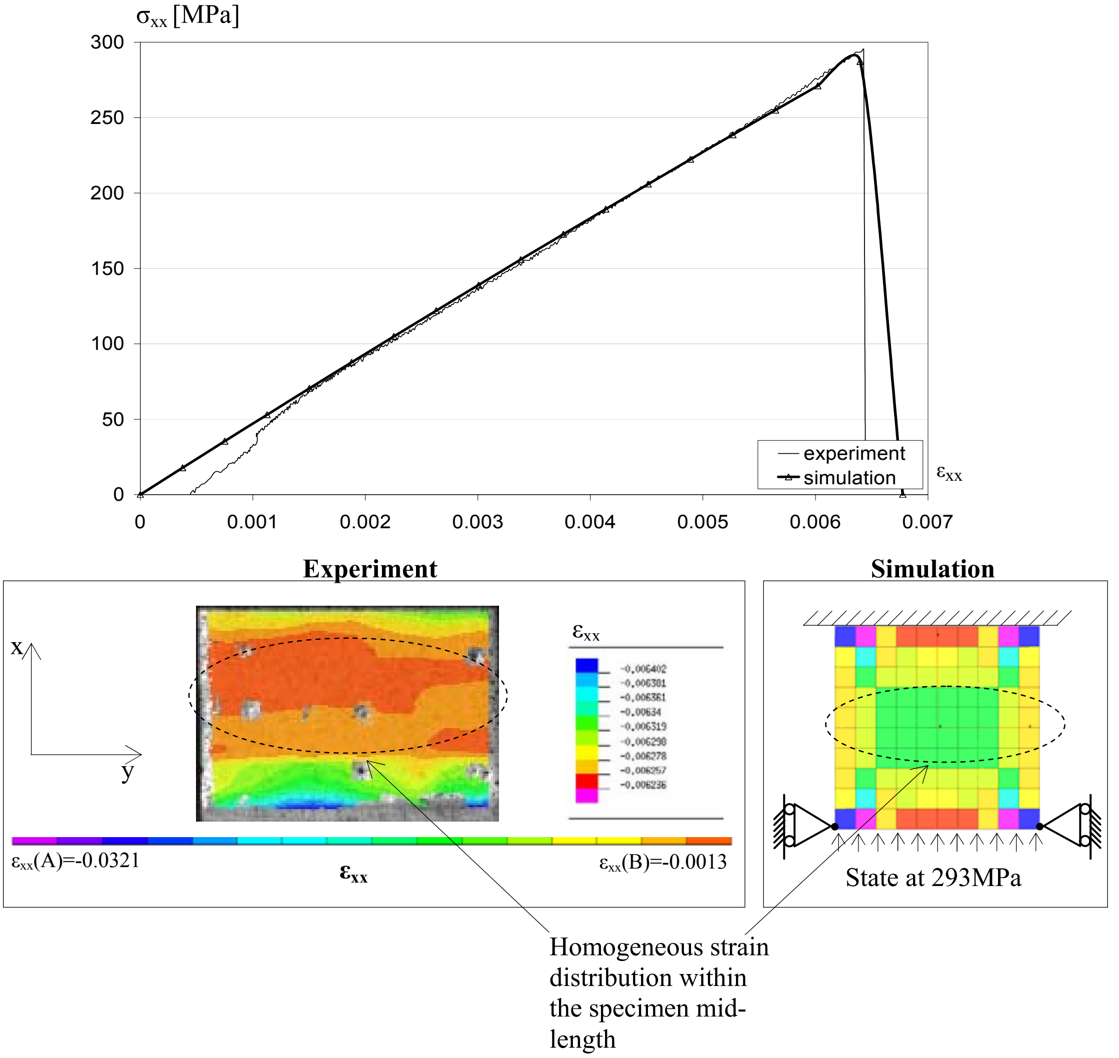

Figure 5.8: Prediction of the longitudinal strain distribution for a $[0\text{-}90]_{4S}$ STS carbon braided specimen under compression loading.

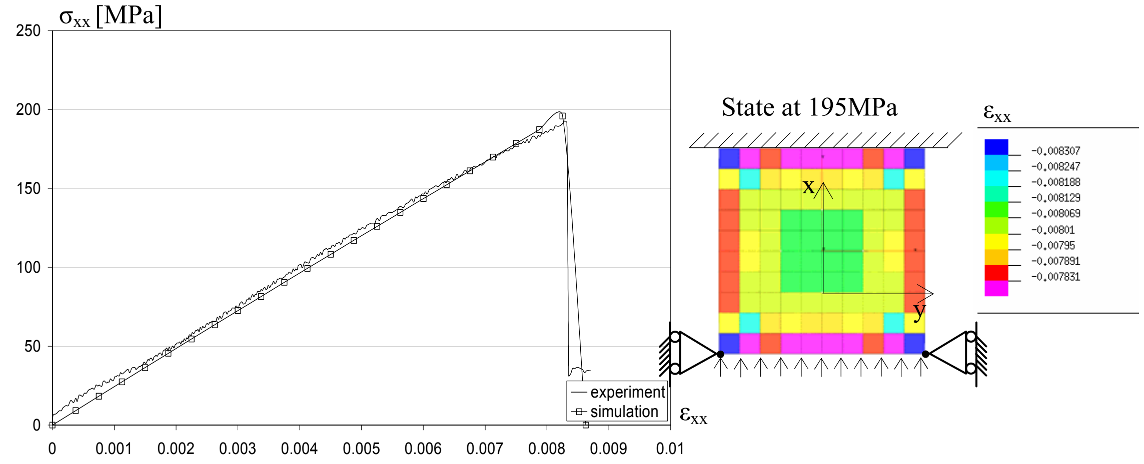

Figure 5.9: **Prediction of the longitudinal strain distribution for a $[0\text{-}90]_{4S}$ E-glass braided specimen under compression loading.**

5.2.2 Model validation for matrix damage treatment

The new model presented in the previous chapter for braided composites assumed no transverse damage and that matrix is mainly damaged through shear. Therefore, the FORTRAN routine, in which damages are calculated, was modified to allow only shear damage d_{12}. Respective polynomial damage laws found for both carbon and glass braided coupons were also implemented to the routine allowing to compile appropriate PAM-CRASH^{TM} executables for the investigated materials.

5.2.2.1 Tensile loading on a $[\pm 45°]_{2S}$ carbon braided coupon

The PAM-CRASH^{TM} shell element formulation, as previously mentioned, enables the prediction of fibre angle variation throughout loading history. The calculation of angle variation $\Delta\theta$ is based on trigonometric relationships similar to the one used experimentally. Prediction results on the $[\pm 45°]_{2S}$ carbon braided specimen showed a good correlation with experiment when using a single shell element, as shown in figure 5.10.

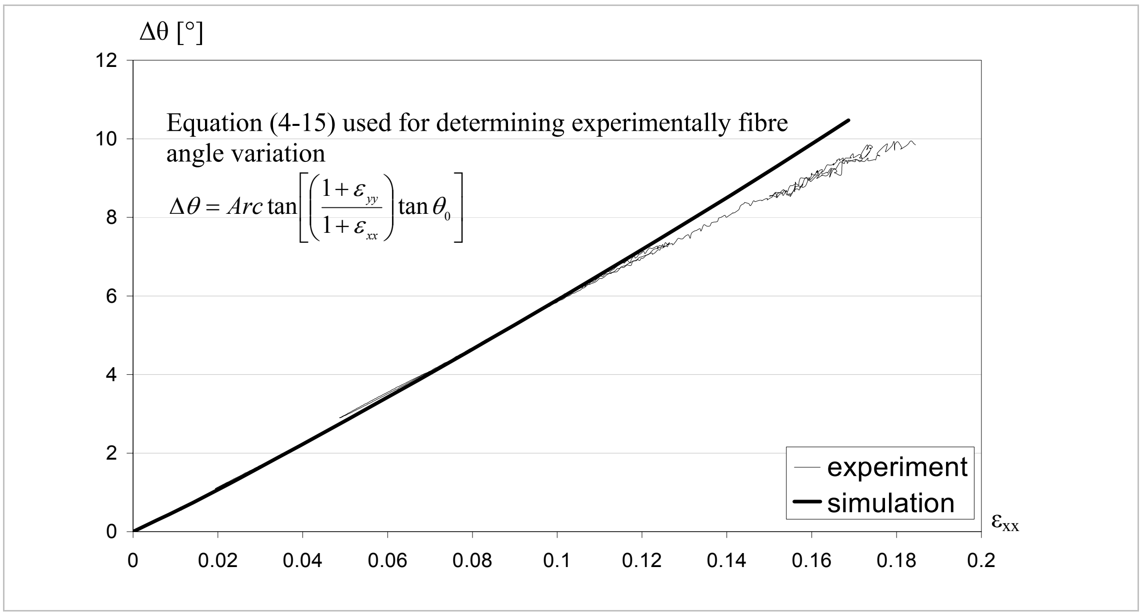

Figure 5.10: Δθ versus ε_{xx} curve using a single shell element for a $[\pm 45°]_{2S}$ STS/LY3505 braided composite.

The prediction using a single shell element also showed identical variations of the shear and axial stresses observed in experiment. Figure 5.11 shows the expected decrease in shear stress magnitude due to fibre realignment in the loading direction. The model gave an excellent correlation and also predicted accurately shear failure.

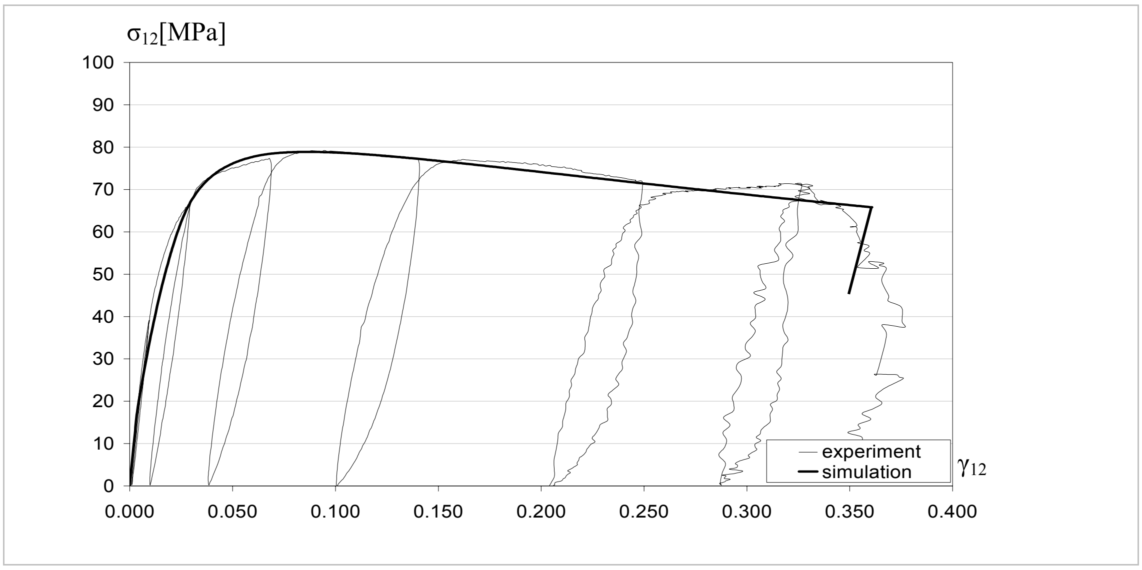

Figure 5.11: σ_{12} versus γ_{12} curve and failure prediction using a single shell element for a $[\pm 45°]_{2S}$ carbon braid.

Figure 5.12 presents the expected increase in longitudinal stress σ_{xx} observed experimentally for the $[\pm 45°]_{2S}$ carbon braid; furthermore, predicted failure was found to be in excellent correlation with experimental results.

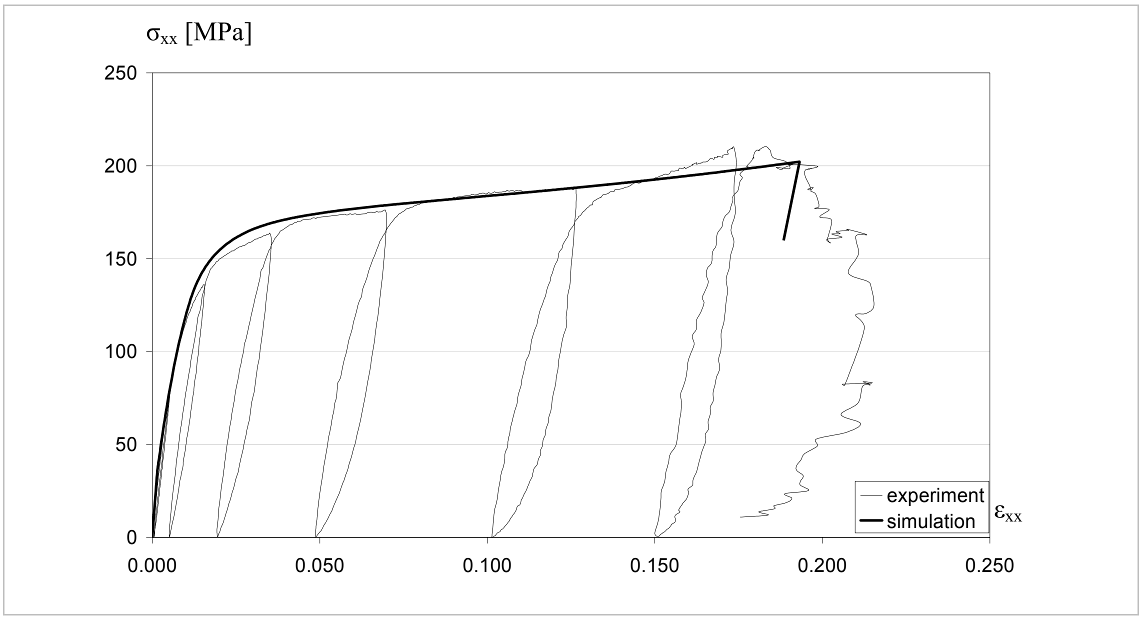

Figure 5.12: **σ_{xx} versus ε_{xx} curve and failure prediction using a single shell element for a $[\pm 45]_{2S}$ carbon braid.**

The single shell element was then used to mesh a $[\pm 45°]_{2S}$ coupon. Three different meshes were used to observe how mesh quality affect damage distribution and failure predictions. As expected, the finest mesh gave, for the carbon specimen, excellent correlation predicting accurately fibre re-orientation and reduction in cross-sectional area as shown in figure 5.13. Plots shows that shear damage, d_{12}, was concentrated at the specimen mid-length as observed in experiment; in addition, failure was correctly predicted to occur at the same location as observed in the experimental coupons.

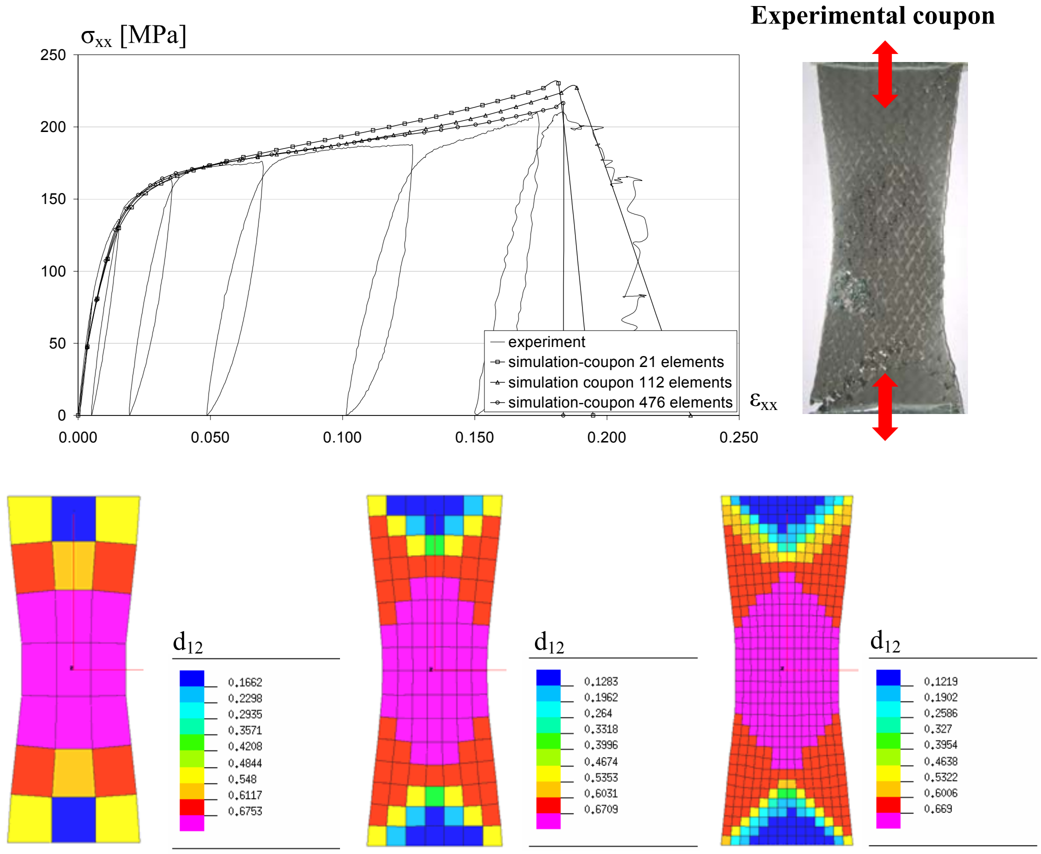

Figure 5.13: **Prediction of the σ_{xx}-ε_{xx} curve for a $[\pm 45°]_{2S}$ STS carbon braid.**

5.2.2.2 Tensile loading on a $[\pm 45°]_{2S}$ glass braided coupon

Fibre angle variation and shear stress versus shear strain, σ_{12} versus γ_{12}, predictions obtained with a single shell element for the glass braided composite specimen also gave good correlation with experimental results, as shown in figures 5.14 and 5.15 for $\Delta\theta$ versus ε_{xx} and σ_{12} versus γ_{12} respectively.

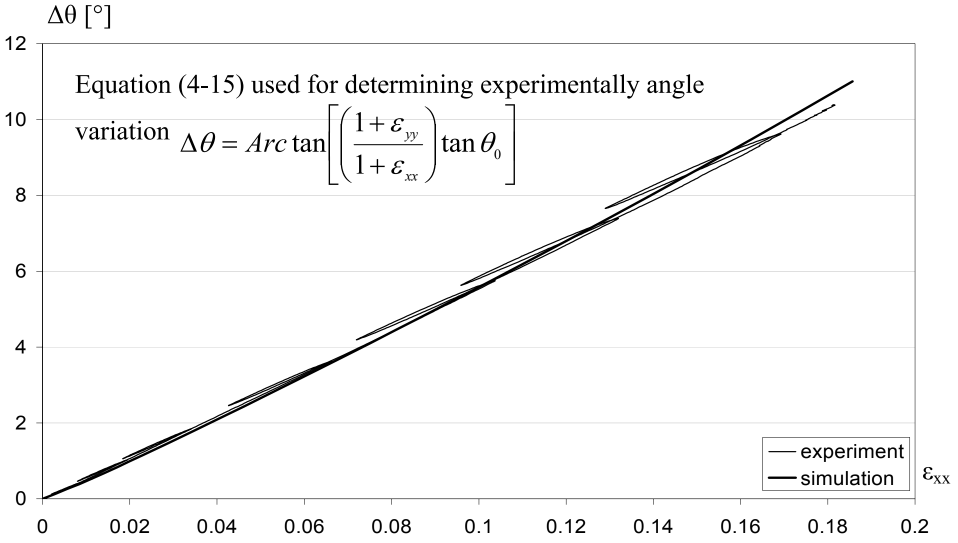

Figure 5.14: Δθ versus ε_{xx} curve prediction using a single shell element for a $[\pm 45]_{2S}$ glass braid.

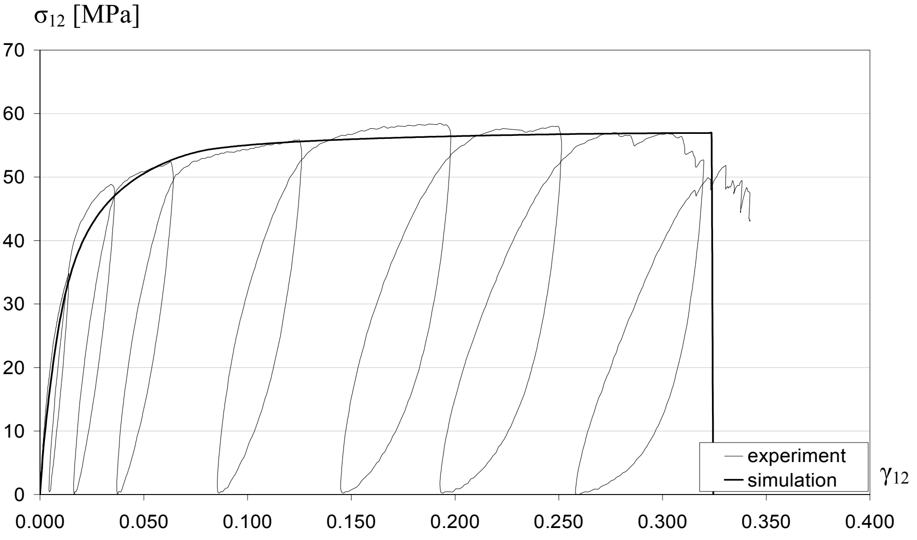

Figure 5.15: σ_{12} versus γ_{12} curve prediction using a single shell element for a $[\pm 45]_{2S}$ glass braid.

Prediction of the longitudinal stress-strain curve, σ_{xx} versus ε_{xx}, revealed that the model overestimated the longitudinal stress magnitude leading to a higher stress at failure, as shown in figure 5.16.

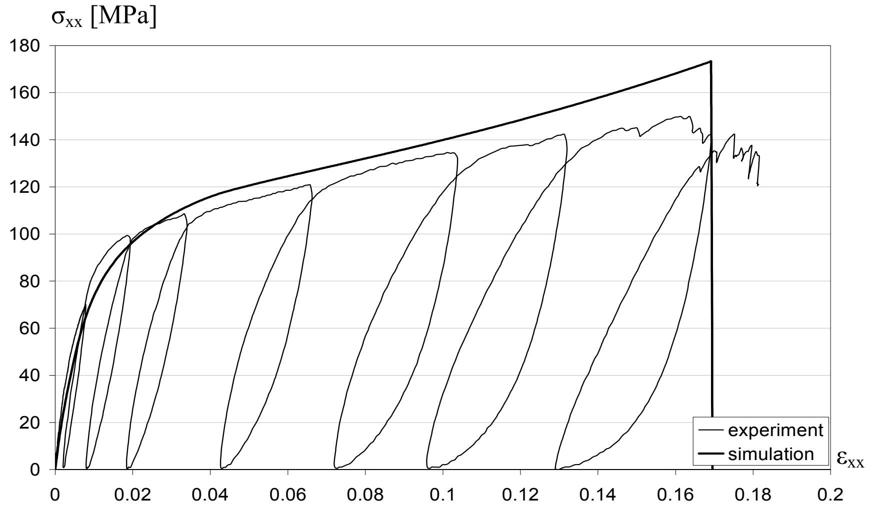

Figure 5.16: σ_{xx} versus ε_{xx} curve prediction using a single shell element for $[\pm 45]_{2S}$ glass braid.

The same three meshes presented previously for mesh sensitivity analysis were used to simulate glass braided specimens. Results were also found to be slightly inconsistent with experimental results for the σ_{xx} versus ε_{xx} curves. Even though, the two coarse meshes gave satisfying longitudinal strength prediction, they both simulated localised necking in the specimen mid-length contradicting experimental results.

From section 3.3.6.3, the tests on glass specimens revealed that shear damage was diffused over the full specimen length and that necking was observed at the lower end where tows are constraint by the grips, as shown in figure 5.17. Results from the finest mesh showed a premature failure due to damage localisation at the corner elements.

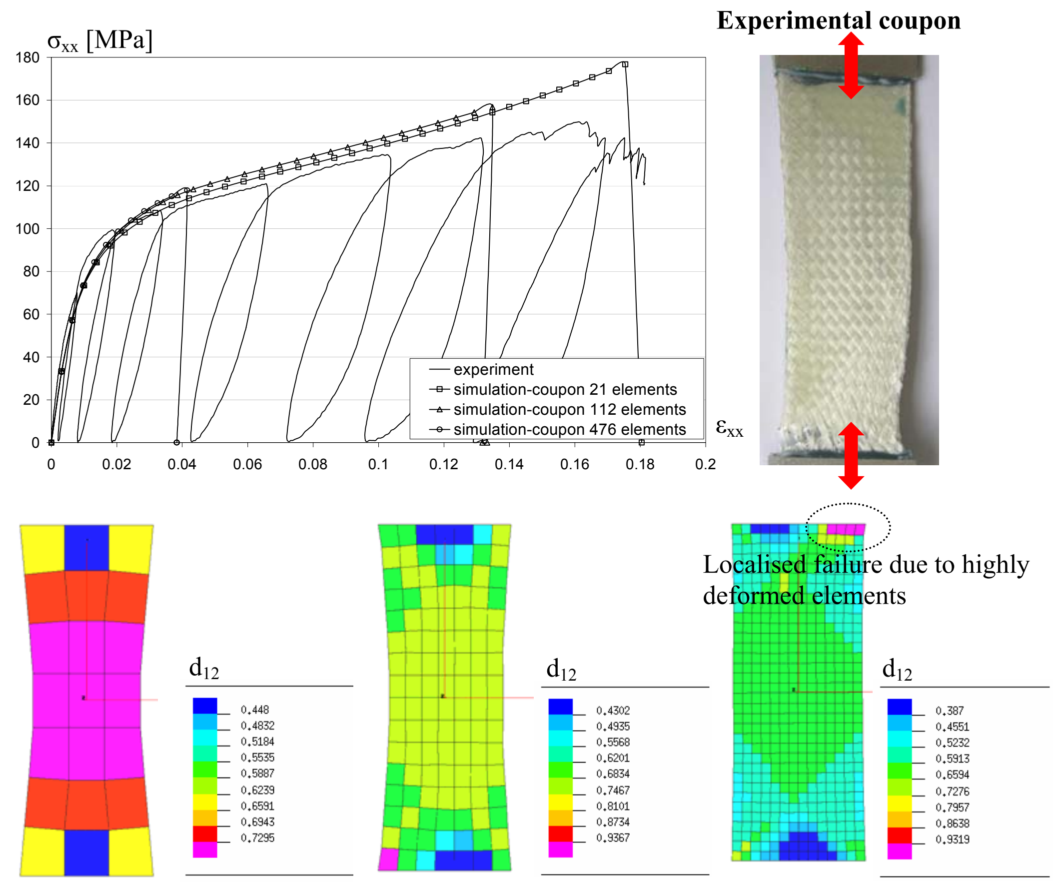

Figure 5.17: **Prediction of the σ_{xx}-ε_{xx} curve for a $[\pm 45°]_{2S}$ E-glass braid.**

The discrepancy between experiment and simulation found for the σ_{xx} versus ε_{xx} curve was induced by the method adopted in the experiment to determine fibre angle variation. As mentioned in chapter 3, the formula used to compute angle variation for glass is based on the trigonometric relationship between longitudinal and transverse strains and is found inaccurate for extensible fibres. Therefore, the new model, in which fibre rotation is integrated, has been inaccurately calibrated for glass since experimental fibre angle variation is lower than the one calculated with equation (4.-15). Damage and plasticity laws used to calibrate the ‘equivalent glass braid unidirectional ply’ are subsequently inappropriate.

As mentioned previously, the ply damage formulation implemented in the PAM-CRASH^{TM} code is identical to the new model proposed; meaning that fibre rotation is taken into account in the element stress-strain calculation. Therefore, it is always expected to obtain good correlation for angle variation and shear stress vs. shear strain prediction, since they are derived in the same way. However, for the σ_{xx} versus ε_{xx} curve prediction the model predicts larger fibre re-orientation and subsequently higher axial stresses.

5.2.3 Model validation for a ±30° braid laminate

5.2.3.1 Tensile loading on a $[\pm30°]_{2S}$ carbon braid laminate

Results found for $[\pm30°]_{2S}$ STS carbon specimen were in good agreement with experiment for both the single shell element and entire mesh coupon study, as shown in figure 5.18. The predicted σ_{xx} versus ε_{xx} curve, using a single element, revealed that damage initiated at the same time in the loading history as in the experiment; however, the strength was over-predicted, as shown in figure 5.18. Prediction using a fine mesh showed an earlier damage initiation; theoretically the results should be the same as for a single element; this is mainly due to the element size chosen.

The total damage distribution within the simulated coupon appeared to be concentrated at the mid-length where maximum fibre scissoring occurs. In addition, the model predicts the correct width reduction measured during test.

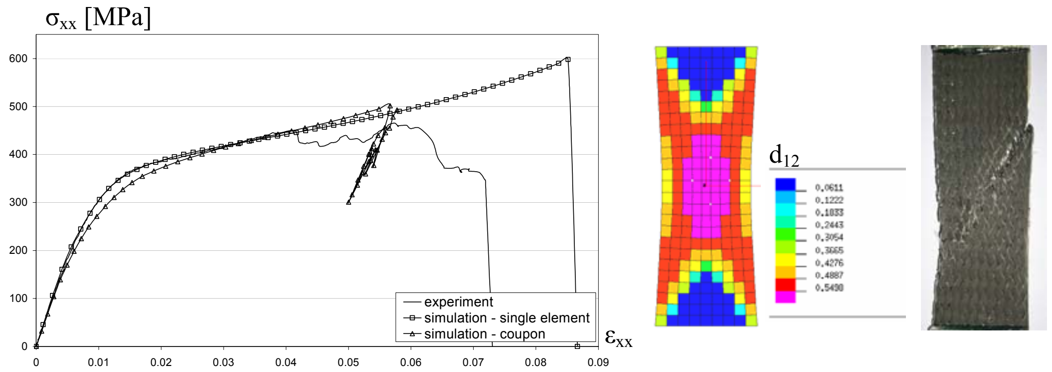

Figure 5.18: Simulation results for a $[\pm30°]_{2S}$ STS carbon braid.

5.2.3.2 Tensile loading on a $[\pm30°]_{2S}$ glass braided laminate

Results for glass using a single element were also found to over-estimate the axial strength due to fibre re-orientation and gave much larger failure stresses than observed experimentally, figure 5.19. The coupon exhibited identical behaviour as in the single element case; however, failure occurred earlier due to corner elements premature failure.

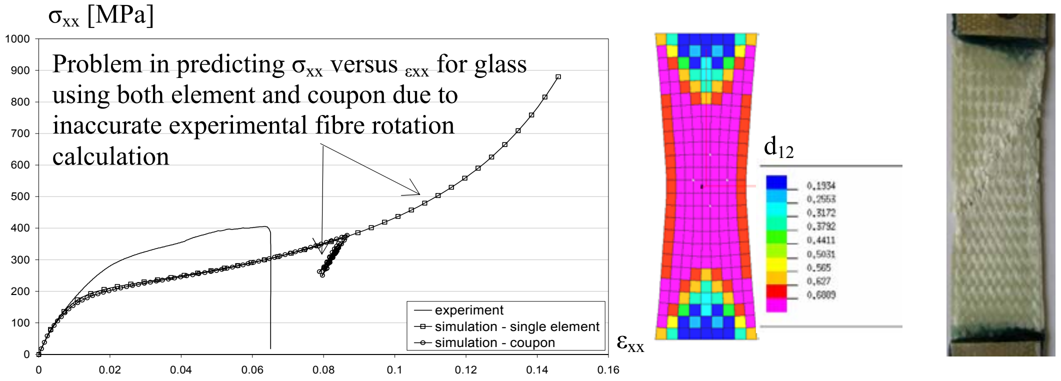

Figure 5.19: Simulation results for a $[\pm 30°]_{2S}$ E-glass braid.

5.2.4 Validation using a square cross-section beam

5.2.4.1 Modelling strategy

In order to validate the model for a more complex loading case than the previous coupons, glass and carbon braided beams were manufactured and tested under four point bending and compared with simulation results. A 0.01mm/ms velocity was used to simulate the quasi-static loading with an initial ramp in order to progressively load the part. A relatively coarse mesh using 15*15mm square elements was used and is presented in figure 5.20. The cross sectional area of the beam was identical to experiment; however, the resin rich areas at the corners, discussed in section 3.1.4.2, were not considered to influence the beam strength and therefore only the braid contour was modelled, as shown in figure 5.20.

The average fibre angle measured at the beam surface was approximately 30°; therefore, the mechanical and failure data used in the simulations were the same as for $[\pm 30°]_{2S}$ specimens. The layup was 8 plies, stacked symmetrically at ±30° fibre angle. A 4mm overall thickness was input in the multilayered shell element, corresponding to the thickness of 4 braided layers.

In order to model the contact between both load spreaders and the beam, a symmetric node-to-segment contact with edge treatment (PAM-CRASH™ contact Type 33) sliding interface was chosen. This allowed the contact force under each load spreader to be obtained. To model the contact interface between support rollers and the beam, a self impacting contact with edge treatment sliding interface (PAM-CRASH™ contact Type 36) was used. The material data cards used for load spreaders and supports were based on a linear elastic isotropic thin shell continuous material (PAM-CRASH™ material MAT 101) calibrated with standard steel mechanical properties.

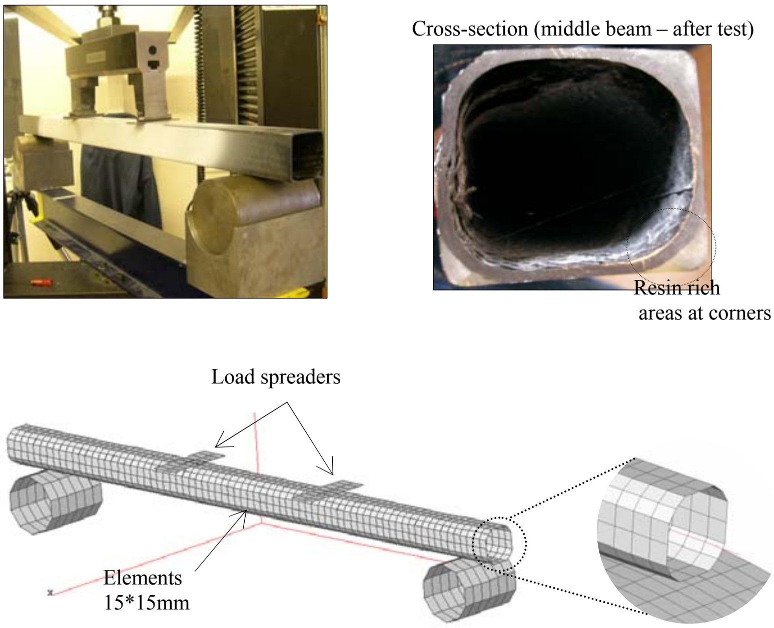

Figure 5.20: Modelling validation with a square cross-section beam.

5.2.4.2 Simulations results for the carbon/glass braided beams

Results found for both carbon and glass beams were in excellent agreement with experiment in terms of stiffness, as shown in figures 5.21 and 5.22. Although force at failure for the carbon beam correlated well with experiment, the glass beam results using ply data card from $[\pm 30°]_{2S}$ coupons showed a premature failure, as shown in figure 5.22. This was the consequence of an inaccurate damage and plasticity laws parameters as explained in last section. Therefore, damage law values were re-calibrated to delay damage initiation and obtain a better fit, as shown in figure 5.22. The predicted failure mode found in both cases did not correlate well with experimental results; shell elements located under the load spreaders failed by bending for both the carbon and glass beams, figures 5.21 and 5.22 respectively. However, the predicted post failure behaviour is similar to experiment since the beam still can carry the loading as shown in figures 5.21 and 5.22.

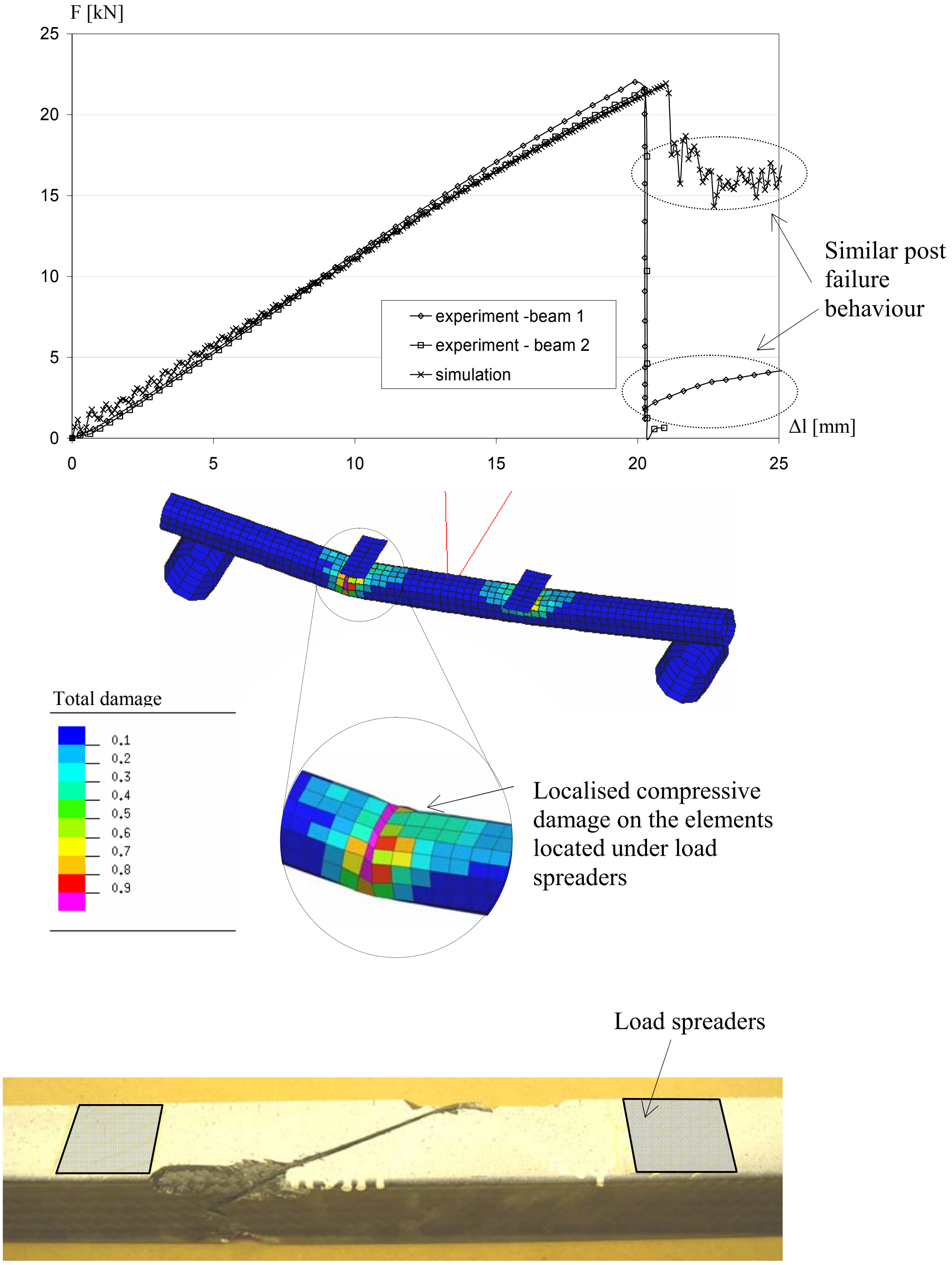

Figure 5.21: Comparison between experimental results and prediction for a carbon beam.

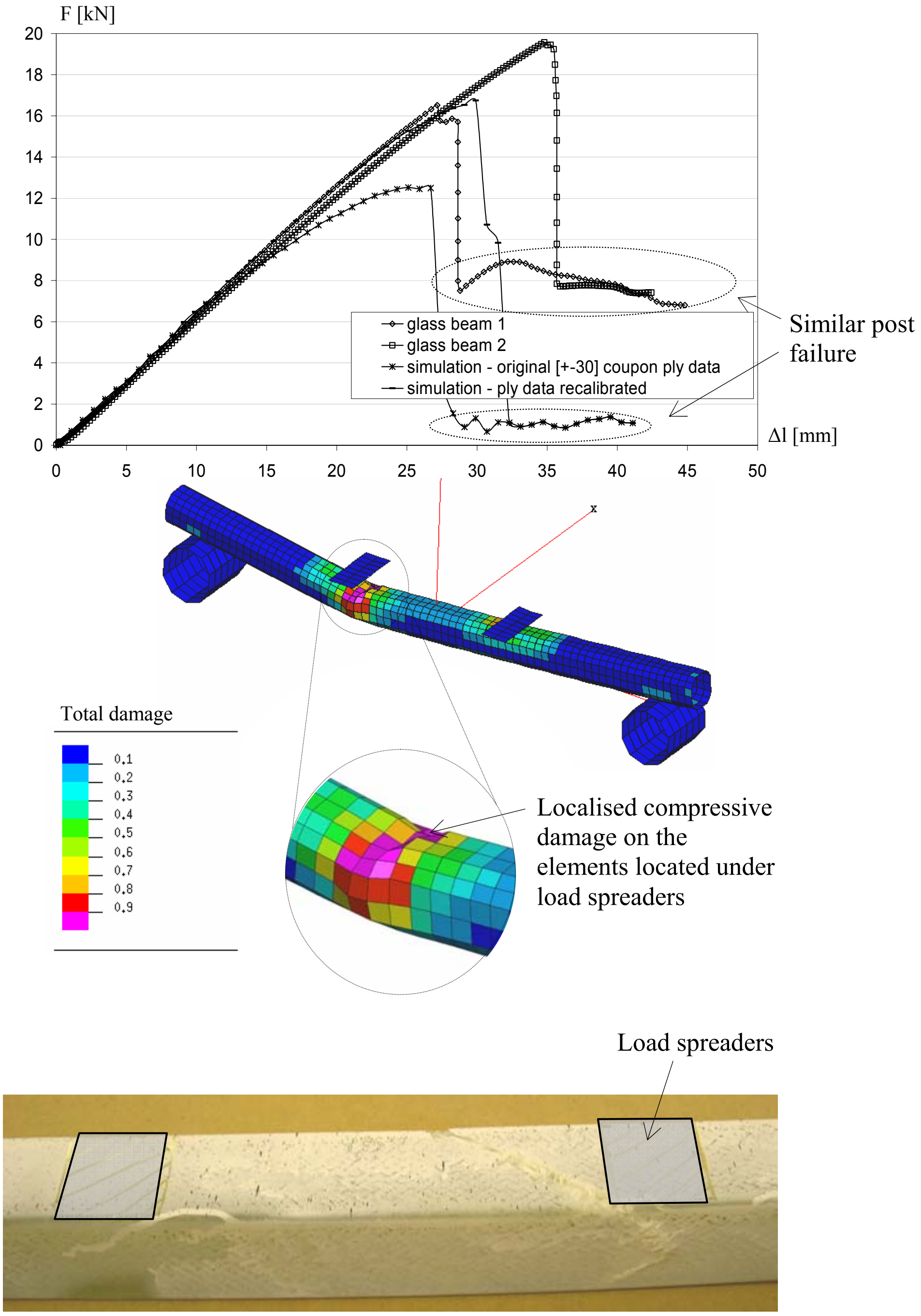

Similar post failure

Localised compressive damage on the elements located under load spreaders

Load spreaders

Figure 5.22: Comparison between experimental results and prediction for a glass beam.

5.3 Overview

Simulations using single shell element, coupons and beams have been conducted in order to validate the new damage model proposed for braids in this chapter. Results found for the tensile test on [0-90°]$_{4S}$ carbon and glass coupons showed that the new fibre elastic damage model formulation, using a modulus degradation function ($E_{11}=f(\varepsilon_{11})$), allows accurate prediction and can approximate successfully the delamination mechanism. Also, simulation results for compression simulations on $[0-90°]_{4S}$ carbon and glass coupons were in close agreement with experiment.

The new model also assumes shear matrix damage through the damage variable d_{12} as main damage mechanism occurring in braided composites. Results presented previously for a $[\pm45°]_{2S}$ carbon braided specimen revealed an excellent correlation with experimental results; however, for the glass specimen the axial strength prediction was higher due to inaccurate damage and plasticity parameters. This was a consequence of inaccurate fibre angle variation measurements. The discrepancy between simulation and experiment are found to be even more important for the $[\pm30°]_{2S}$ glass coupon; indeed, the predicted damage was found to initiate earlier leading to premature failure.

Four point bending tests on braided beams were carried out and results presented in chapter 3. Simulations of these beams using the new failure model were conducted in this chapter. Results using a relatively coarse mesh showed encouraging correlation for both stiffness and strength prediction. However, the predicted failure mode was very localised and corresponded to element failure under the load spreaders. The compressive shear failure mechanism found experimentally could not be matched showing a limitation of the model.

Chapter 6- Overall discussion

In this work, heavy tows carbon and glass braided fabric reinforced composites were investigated. The resin infusion process was used to manufacture braided coupons and beams which were ultimately tested under different loading conditions. Experimental tests on coupons revealed different failure modes exhibited by these two types of fabric composites; instead of an expected linear elastic failure for a specimen loaded under tension in the fibre direction, it has been observed a more complex failure mode combining tow straightening and fibre failure. Under compression loading in the fibre direction, it was also observed that strain measurements for the ROI were not representative of the overall material since the relative ROI size to RUC size were too close. Tensile tests on $[\pm 45°]_{2S}$ specimens also revealed fibre re-orientation toward the axis of loading leading to large axial strains ε_{xx}.

These different failure characteristics were modelled by using and adapting the existing Ladevèze damage model implemented in the explicit FE code PAM-CRASH^{TM}. The modelling approach chosen was based on an 'equivalent braid unidirectional ply' used to reproduce a specific braided composite lay-up. This model has required a new formulation to treat non-linearity induced by tow straightening when loaded in the fibre direction and fibre angle variation for shear loading. The model validation presented earlier for coupons and beams showed encouraging correlation with experimental results. However, it presents limitations; indeed, a further and more detailed validation exercise should be conducted.

In this chapter, a detailed discussion on manufacture, testing and modelling issues mentioned in the previous chapters is presented.

6.1 Manufacturing quality issues

The manufacturing of flat panels and square cross-section beams conducted in this work using the resin infusion technique revealed different problems affecting the quality of the finished parts. First, in order to obtain the required fibre angle, preforms were handled to obtain the closest approximation. An approximate 2° standard deviation on the braid angle has been measured which, consequently, has influenced characterisation of mechanical properties such as modulus and damage law. In addition, as mentioned earlier, voids formation at tow intersections was frequently observed on panels manufactured.

Resin infusion of heavy tow braided composites was also found to be non-consistent. Due to low mechanical pressure applied to the preform, and the high waviness of the braid it is easy to create, at each tow intersection, a free volume in which either matrix or air bubbles can nest. Theoretically, by mechanically applying a higher pressure to the preform increased fibre compaction should be possible thus reducing these free volumes and lowering void content; a higher volume fraction should be then obtained.

The manufacture of the cross-section beams also revealed resin rich corners which is a limitation in the chosen manufacturing route. The pressure applied by the vacuum was not homogenous and controlled which resulted in large resin content areas. For this particular case, more appropriate tooling would have been necessary to obtain better net shape. A close rubber bladder, acting as a mandrel, could have been used in order to apply a progressive and homogenous pressure onto the preform.

Test results on the different coupons tested were consistent since they were extracted from regions where good impregnation and low void content were achieved. Even though this work did not aim initially to optimise the mechanical properties of the part produced, this could be expected for future work to manufacture panel using more appropriate manufacturing routes, such as RTM.

6.2 Braided composites testing issues

6.2.1 Considerations on the testing method

This work showed the potential of non-contact measurement techniques for monitoring damage under large deformations. It also offers the possibility to determine the strain field over the full specimen during the complete loading history and select the appropriate ROI. However, a common limitation of these methods for both the ‘markers tracking’ and DIC techniques was a poor measurement definition when the surface underwent too much degradation so that dot recognition could not be properly achieved. The result in this case was a noisy signal and erratic stress versus strain curves.

6.2.2 Results on the [0-90°]$_{4S}$ braided specimens under tensile loading

Experimental results found that using the DIC technique were encouraging and allowed monitoring axial strain up to complete specimen failure. However, the axial strain limit ε_{11l}^{t} used in the equivalent braid unidirectional ply calibration does not represent accurately the ply failure strain. It has been observed that interlaminar delamination occurred during loading history; meaning that strain in each ply, beyond elasticity, are not equal to the strain measured at the surface of the specimen which only reflects the coupon surface strain.

In order to minimise the measurement error, another camera system should be set on the other specimen surface, and strains map for both surface compared. Therefore, the strain limit use in the equivalent unidirectional braid ply should be the average between these two measurements. Unfortunately, due to equipment limitation such measurement could not be achieved.

6.2.3 Results on the [0-90°]$_{4S}$ braided specimens under compressive loading

In section 3.3.5.4, results revealed that specimen clamping conditions affect the strain distribution within the gauge length of compression specimens; leaving only a 10mm region of uniform strain distribution centred at the specimen mid-length. However, according to previous considerations on the ROI size, at least three unit cells should be considered to obtain valid mechanical parameters. In this case, a 10mm ROI size represents only 1 unit cell which explains the discrepancy found for the axial strain at failure for both carbon and glass braided composites. In addition, the large tow size (4mm) relative to the specimen width (25mm), gauge length (20mm) and thickness (3mm) has a non-negligible structural effect, and in case of misalignment, the stress distribution in the ROI is greatly influence. This could explain the large standard deviation found for the strength property.

Ultimately, the actual compressive method used in this work for determining mechanical properties of braided composites only allows providing reliable elastic properties; since, as damage occurs the loading in the specimen changes and becomes non-uniform. Specimen defects, such as tow misalignment, affect greatly the force at failure and failure locations. In order to obtain more reliable strength properties, test should be conducted on larger specimens, in which defects would not have such impact.

The increase of specimen dimensions would give a more representative strain measurement; however, this implies to re-consider the buckling issues. Thickness is the first parameter which could be increased due to its cubic exponent in the moment of inertia formula. But, to fulfil plane stress condition, the thickness should be 10%, or less, of the shortest in-plane dimension. The actual rig allows a maximum of 35mm specimen width; the thickness cannot, therefore, exceed 3.5mm. According to the Euler's formula this represents a 40mm gauge length specimen. Hence, a larger ROI comprising three unit cells could be used and improved consistency in strength results should be found. Nevertheless, there are limits in reducing specimen dimensions to avoid buckling; for instance, problems of short gauge length would arise for low longitudinal compressive modulus, such as $[\pm 45°]_{2S}$ specimens.

The testing rig should, therefore, be improved to enable testing various specimens independently of their geometry, lay-up and fibre/matrix types. Consequently ongoing work to enhance this test standard has recently been conducted aiming to add an anti-buckling apparatus to allow increased size of the test area. A first attempt consists of applying two local supports, such as screws, on each specimen face as shown in figure

6.1 (a). This solution has been designed and preliminary tests on 50mm gauge length specimens have given promising results [23]. The main drawback of this method lays in data analysis; indeed the zone of interest is hidden in some areas by rods and screws reducing the size of the measurement zone. In order to obtain a full area, plates support can be placed at the specimen sides allowing specimen translation only in one direction as shown in figure 6.1 (b).

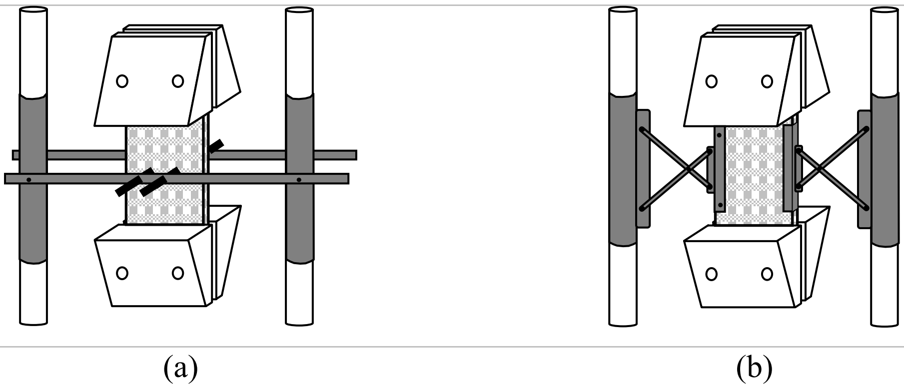

Figure 6.1: Compressive rig enhancement, (a) solution being investigated, (b) future solution.

6.2.4 Results on the $[\pm45°]_{4S}$ braided specimens under cyclic tensile loading

Model prediction results obtained for carbon braids were found to be in good agreement with experiment both for standard flat coupons and square beams; however, simulation results found for glass coupons exhibited premature failure. Experimental results showed that $[\pm45°]_{2S}$ glass coupons exhibit shear deformation on the overall surface; whereas, for carbon coupons shear deformation was localised in the mid-length leading to necking as shown in figure 6.2.

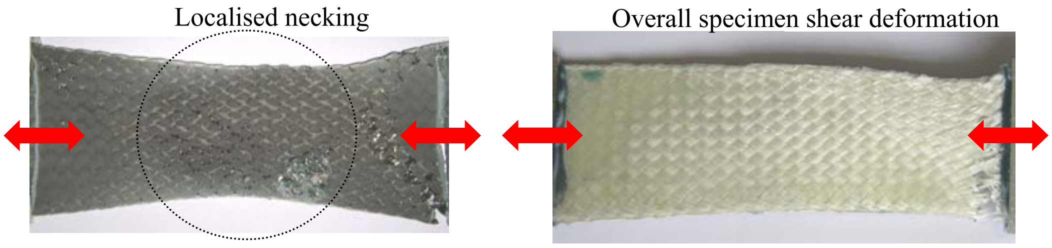

Figure 6.2: Deformation within the $[\pm45°]_{2S}$ carbon and glass specimens.

The discrepancy between simulation and experimental results was found to be associated to inaccurate fibre angle variation calculations for the glass specimens. The formula using longitudinal, ε_{xx}, and transverse strain, ε_{yy}, used to quantify fibre rotation assumed inextensible fibres; however, glass fibre exhibits a two to three fold increase in strain at failure compared to STS carbon fibre meaning that the assumption based on inextensible fibre is no longer valid. As a result the angle values used in the model calibration lead to inaccurate predictions.

From experiment, fibre angle measurement at failure for glass was lower than carbon and, paradoxically, the axial strain measured was almost identical. This means that the shear mechanism, corresponding to fibre realignment, is coupled to fibre extension. Glass fibre could be considered as a spring of constant stiffness, E, deforming elastically in the axial direction. Figure 6.3 shows schematically the coupled shear-stretching difference between carbon and glass fibres.

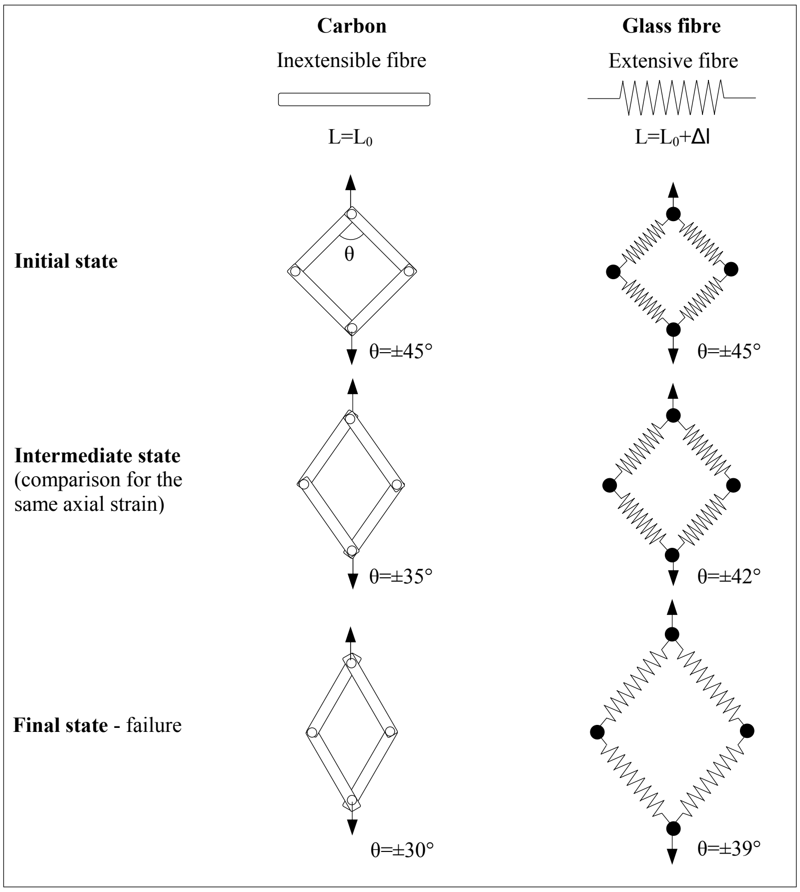

Figure 6.3: Difference between extensive and inextensible fibre during scissoring.

Since fibre angle variation cannot be determined numerically for glass braided specimens, direct experimental measurement appears to be the only alternative. Due to project time-scale consideration, measurement of the angle variation during loading history for glass coupon has not been conducted. However, an experimental method based on the markers tracking technique, presented earlier, could be used for accurately determining fibre rotation.

This would consist of painting 2 makers on each tow, as shown in figure 6.4. For each picture taken the angle between the lines passing through the two markers could be derived. The true fibre angle could then be used as input in the equations necessary to plot σ_{12} versus ε_{12}.

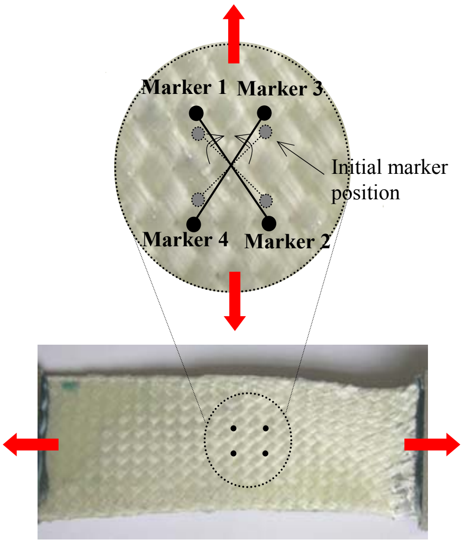

Figure 6.4: Markers tracking technique applied for measuring angle variation.

6.3 Braided composites modelling issues

The modelling approach based on an ‘equivalent braid unidirectional ply’ used in this work showed satisfying correlation between prediction and experimental results. However, it still has limitations since, for instance, delamination mechanisms and tow waviness are not properly accounted for. The following section describes proposals to help overcome the different model limitations and gives an eventual enhancement to the model.

6.3.1 Elastic properties calibration for an equivalent braid unidirectional ply

In order to determine the elastic properties for an equivalent braid unidirectional ply, CLT theory was used. Fibre/matrix properties and volume fraction were required as input in the law of mixtures. These laws assume straight and undamaged fibres neglecting the important fibre waviness encountered in braids and also fibre damage due to braiding process; the elastic properties are therefore overestimated.

Micro-mechanical modelling of the RUC would offer more reliable prediction to the elastic properties. The complete RUC comprising longitudinal and transverse tows could be first calibrated to fit experimental elastic values. Transverse tows could then be removed to obtain a unidirectional RUC and elastic properties could be derived.

6.3.2 Delamination treatment in $[0\text{-}90°]_{4S}$ specimen under tensile loading

Test on $[0\text{-}90°]_{4S}$ specimens loaded under tension in the fibre direction revealed an unexpected failure mechanism. Instead of linear elastic failure as found in most unidirectional laminates, tow straightening and subsequent delamination were observed, leading to a large non-linearity for both carbon and glass braids. The approach proposed to model this mechanism is based on a degrading elastic modulus through the function $E_{11}=f(\varepsilon_{11})$. Simulated results obtained using this technique are in good agreement with experiment; however, this assumes that the specimen deforms only elastically.

Tow straightening is the result of shearing mechanisms at the interface between tow and matrix which implies plasticity. Even though the previous elastic damage model mentioned earlier does account for this failure mechanism, it remains only a mathematic fitting. A more sophisticated approach would consist of determining the damage law and plasticity laws using the same cyclic tests conducted for the $[\pm 45°]_{2S}$ specimen. Figure 6.5 shows a cyclic test conducted on a $[0\text{-}90°]_{4S}$ glass braided specimen.

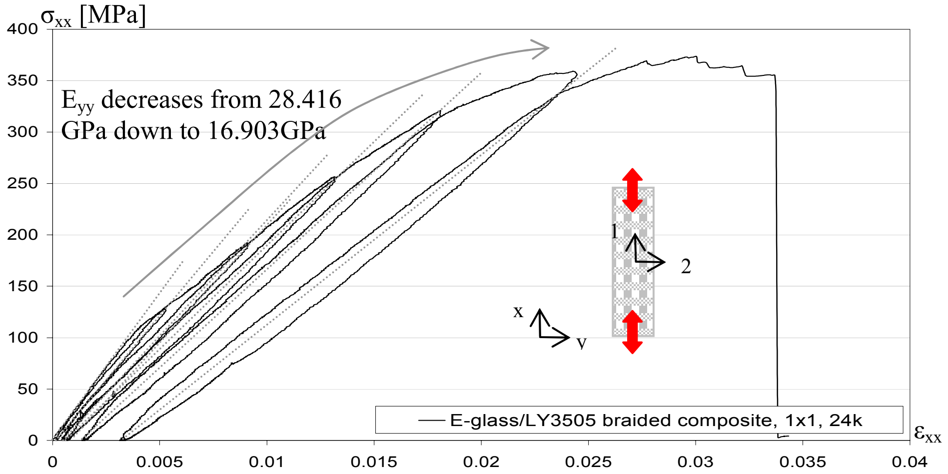

Figure 6.5: Cyclic test on a [0-90°]$_{2S}$ E-glass/LY3505 braided coupon.

Similar to procedure used for shear testing, elastic and plastic strains could be extracted and an equivalent elasto-plastic damage model could be introduced such as,

$$d_{xx} = 1 - \frac{E^i_{xx}}{E^0_{xx}}, \tag{6-1}$$

where d_{xx} and E^i_{xx} are the longitudinal damage and Young's modulus for each cycle respectively. And the associated conjugate force is written such as,

$$Y_{xx} = \sqrt{E^0_{xx} \times \varepsilon^e_{xx}}\,. \tag{6-2}$$

Plasticity law could also be derived in the same way,

$$p = \int_0^{\varepsilon^p_{xx}} (1 - d_{xx}) d\varepsilon^p_{xx}, \tag{6-3}$$

$$R(p) = \frac{\sigma_{xx}}{1 - d_{xx}}\,.$$

These lead to the damage and plasticity laws for the [0-90°]$_{4S}$ glass specimen as shown in figure 6.6.

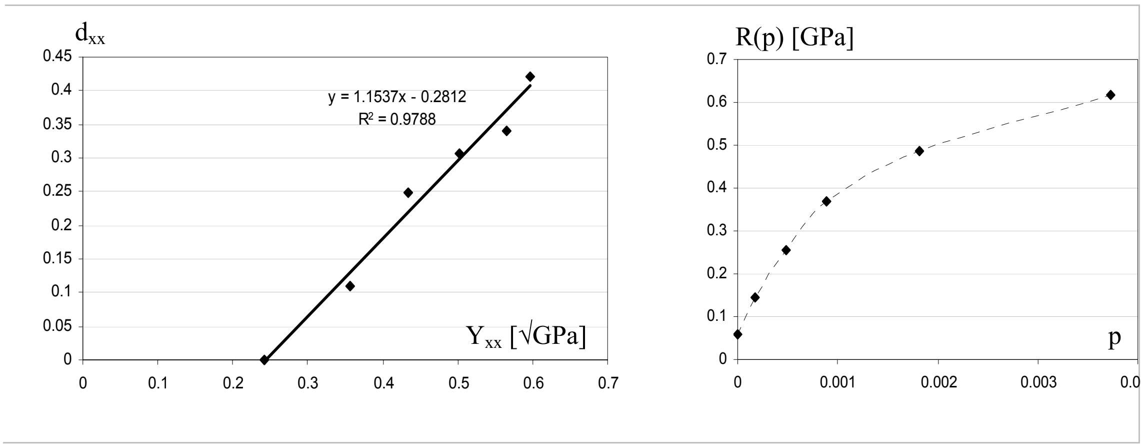

Figure 6.6: Damage and plasticity laws for a [0-90°]$_{2S}$ E-glass/LY3505 braided coupon.

This model would therefore allow representation of intra-ply damage; however, delamination between layers would still not be accounted for. These two mechanisms are narrowly linked and also are dependent on the architecture of the fabric. A test campaign on Mode I and II would be required to determine delamination parameters for this specimen and results could be used as input in the existing delamination interface element available in PAM-CRASH^{TM}.

6.3.3 Modelling of fibre rotation

6.3.3.1 Limitation for shear stresses σ_{12} determination

The fibre angle variation monitored throughout loading history on the [±45°]$_{2S}$ specimens was integrated in the Ladevèze damage model. Local quantities σ_{12} and ε_{12} were calculated for each angle variation increment $\Delta\theta$ by using standard CLT. Simulation results on coupons showed an excellent correlation with experimental results; however, the method presented to calculate the S_3 coefficient is based on an inaccurate assumption.

As previously presented, the shear stress σ_{12} is calculated using

$$\sigma_{12} = S_{12}\sigma_{xx} = \frac{-1}{2\cos\theta\sin s\theta}\left[B\left(1-2\cos^2\theta\right)+\cos^2\theta\right]\sigma_{xx}, \qquad (6\text{-}4)$$

with

$$B = \left[\frac{\cos^2\theta\left(2\cos^2\theta - 1\right) + 4\cos^2\theta\sin^2\theta\,\frac{G_{12}}{E_{22}}\left(\frac{E_{22}}{E_{11}}\nu_{12} + 1\right)}{4\cos^2\theta\sin^2\theta\,\frac{G_{12}}{E_{22}}\left(\frac{E_{22}}{E_{11}} + 2\frac{E_{22}}{E_{11}}\nu_{12} + 1\right) + \left(2\cos^2\theta - 1\right)\left(\cos^2\theta - \sin^2\theta\right)} \right]. \qquad (6\text{-}5)$$

The elastic properties of the unidirectional ply {E_{11}, E_{22}, ν_{12}, G_{12}} were assumed to be undamaged. However, E_{22}, ν_{12}, and G_{12} are likely to be damaged due to matrix micro-cracking and fibre/matrix interface debonding. This approximation, used in the calculation of B, cannot be estimated as it would require knowing the individual damage laws acting on transverse and shear moduli. Nevertheless, this limitation did not seem to greatly affect the accuracy for the σ_{xx} versus ε_{xx} prediction for both carbon and glass specimens.

6.3.3.2 Damage/plasticity laws and braid angle

In section 4.2.5.2, a method to determine damage and plasticity laws was proposed for $[\pm 30°]_{2S}$ specimens. Identical trend lines were assumed for both laws and they were shifted for delaying damage initiation. This approach gave good results for the carbon braid specimens; however for glass specimens a poor prediction was found. Since braided composite exhibit a wide range of braid angle, a characterisation of damage and plasticity laws for various braid angles should be conducted throughout cyclic testing. This would enable to quantify the braid angle effect on damage and plasticity laws.

Chapter 7- Conclusions and future work

The different contributions to knowledge of this work can be summarised as follows.

Contributions to the manufacturing of braided composites

1 The manufacture of carbon and glass braided beams using an alternative manufacturing route, based on resin infusion, was achieved.

2 Different component quality issues encountered in the manufacture of heavy tow braided composites with resin infusion process have been described, characterised and solutions proposed.

Contributions to the mechanical characterisation of braided composites

1 Classical measurement methods such as strain gauges, or extensometers, were unable to measure large strains combined with surface degradation observed in the investigated braided composites. Consequently, the work has proposed a method based on 'markers tracking' to optically measure longitudinal and transverse strains required for material characterisation.

2 The Digital Image Correlation (DIC) technique has been successfully applied and has allowed the complete strain field measurement to be made and used to derive damage evolution in the braided specimens. Also, it was used to characterise fully the different failure mechanisms.

3 The fibre continuity and overbraiding effects on the damage/plasticity laws and failure modes have been investigated.

4 Tensile testing in the fibre direction on $[0\text{-}90°]_{4S}$ coupons revealed an unexpected and relatively large strain to failure for heavy tow braids due to significant tow stretching. A non-linear behaviour for both carbon and glass braids was observed and successfully measured.

5 Compression testing on $[0\text{-}90°]_{4S}$ coupons showed consistent results for elastic properties; however, the scatter in stress and strain at failure values measured for the compression specimens has revealed limitations of the current compressive rig for braided composites.

6 Tensile cyclic testing on $[\pm 45°]_{2S}$ coupons has revealed fibre re-orientation in the axis of loading caused by shear damaging of the fibre/matrix interface. The angle variation calculated using axial and transverse strains was found to be inadequate for glass and an alternative method has been proposed for direct and more accurate measurements.

Contributions to the mechanical modelling of braided composites

1 A modelling approach based on the superposition of 'equivalent braid unidirectional plies' has been successfully used to represent the different braided layers in a laminate.

2 The characterisation of elastic properties for the 'equivalent unidirectional ply' was conducted using CLT and validated with experiment.

3 Tow straightening and delamination mechanisms observed in the $[0\text{-}90°]_{4S}$ coupons under tensile loading led to the modification of an existing Ladevèze damage model implemented in PAM-CRASH^{TM} in order to account for these non-linear behaviours.

4 Fibre re-orientation, or scissoring, has also been integrated into the model when plotting the σ_{12} versus ε_{12} curve. This was conducted using CLT for $[\pm\theta°]$ laminates.

5 A successful validation of the new damage model using single element coupons and beams have been presented. Indeed, correlation with experimental results is satisfying and encouraging; however, further material characterisation of carbon and glass should be conducted to appreciate the effect of braid angle on damage and plasticity laws.

The different directions of work which could be undertaken for future research are summarised below:

1. The model could now be used in structural parts since it has been validated for beams. This modelling approach offers flexibility in choosing the adequate braid angle. For instance, the bumper beam presented in figure 7.1 exhibits different fibre angles according to the location. Therefore, this could be modelled by readily varying the ply angle value in the shell element definition.

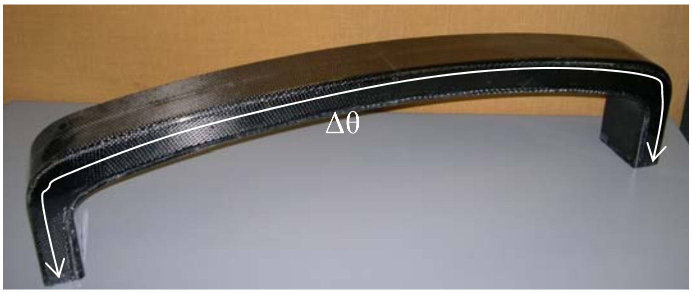

Figure 7.1: Example of a bumper beam with varying braid angle.

2. In order to minimise void content and insufficient impregnation, an additional mechanical pressure should be applied to obtain higher fibre compaction. This would help to lower the tow waviness and reduce the nesting of air bubbles, or resin concentrations, at tow intersections.
3. The manufactured beams have revealed resin rich corners and, as a consequence, much lower volume fraction in these regions. In order to obtain higher and homogenous fibre compaction a bladder should be used instead of a vacuum bag. This would result in more consistent cross sectional areas and fibre/void content distribution.
4. A large scatter for experimental compressive strength has been found which has been explained by the presence of non-uniform loading conditions. New work has been conducted to re-design the compression rig for fabric reinforced composites. The DIC technique should be used accordingly to estimate how the specimen size and clamping conditions affect failure.
5. The limitation in determining the angle variation during fibre scissoring could lead to the development of a new marker tracking technique.

6 RUC model development using the FE method should be conducted to determine more accurate elastic properties for equivalent unidirectional ply calibration for braid reinforced composites.

7 Experimental observations have shown that specimens generally underwent intra-ply damage strongly coupled with inter-ply delamination. Since this latter failure mechanism has not been considered in this work; an extensive testing campaign should be conducted to characterise delamination modes I and II for different specimen lay-ups, such as [0-90°], [±45°], [±40°], [±35°], [±30°], in order to establish relationships between fracture toughness and braid angle. These test results could then be used as input data to the existing delamination interface element available in PAM-CRASH^{TM}. In addition, an experimental characterisation of the damage and plasticity laws throughout tensile cyclic testing on the previous laminates should be conducted.

8 An improved model based on an elasto-plastic damage model coupled with the delamination model should be developed to account for the tow straightening mechanism observed in the $[0\text{-}90°]_{4S}$ specimens under tensile loading. Indeed, the non-linear elastic failure model introduced in this work should account for plasticity and damage. This could be a further development in the explicit FE code PAM-CRASH^{TM}.

Chapter 8- References

[1] Afendi M., Banks W. M., Kirkwood D. Bubble free resin for infusion process. Composites: Part A, 36, 739-746, 2005.

[2] Allix O., Ladevèze P. Interlaminar interface modelling for the prediction of laminates delamination. Composite structures, 22, 235-242, 1992.

[3] Allix O., Ladevèze P., Corigliano A. Damage analysis of interlaminar fracture specimens. Composite structures, 31, 61-74, 1995.

[4] Ambur D. R., Jaunky N., Hilburger M. W. Progressive failure studies of stiffened panels subjected to shear loading. Composite Structures, 65, 129-142, 2004.

[5] Anderson T. Fracture mechanics - fundamental and applications. CRC press, 1995.

[6] Antonucci V. et al. Resin flow monitoring in resin film infusion process. Journal of materials processing technology143-144, 687-692, 2003.

[7] ASM Handbook. Composites, volume 21, The materials information Society.

[8] ASTM. Standard test method for compressive properties of polymer matrix composite materials with unsupported gauge section by shear loading. D3410/D3410M, 1995.

[9] ASTM. Standard test method for tensile properties of polymer matrix composite materials. D 3039', 1995.

[10] ASTM. Standard test method for flexural properties of unreinforced and reinforced plastics and electrical insulating materials by four-point bendin. D6272, 1998.

[11] ASTM. Standard test method for in-plane shear response of polymer matrix composite materials by tensile test of a ±45° laminate. D 3518/D D3518M, 1994.

[12] Aubard X., Cluzel C., Guitard L., Ladevèze P. Damage modelling at two scales for 4D carbon/carbon composites. Computers and Structures 78, 83-91. 2000.

[13] Aubard X., Cluzel C., Guitard L., Ladevèze P. Modelling of the mechanical behaviour of 4D carbon/carbon composite materials. Composites science and technology, 58, 701-708, 1998.

[14] E. Barbero. CADEC, Computer Aided Design Environment for Composites software. West Virginia University, www.mae.wvu.edu/~barbero/cadec.html.

[15] Beard S. Energy absorption of braided composite tubes. PhD thesis, Standford University, 2001.

[16] Beardmore P., Jonhson C.F. The potential for composites in structural automotive applications. Composite science and technology, 26. 251-281, 1986.

[17] Brooks R. and Pharaoh M. Crashworthy automotive structures using thermoplastic composites. The Coventry automobile division of the IMechE automotive composites, Warwick University IMC, Coventry.

[18] Carruthers J., Kettle A., and Robinson A. Energy absorption capability and crashworthiness of composite material structures: A review. Applied Mechanics Reviews, 51(10), 635-649. 98.

[19] Chang C. Y., Hourng L. W. Study on void formation in resin transfer moulding. Polymer Engineering and Science, 38(5), 809-818, 1998.

[20] Chiu C., Tsai K., and Huang W. Effects of braiding parameters on energy absorption capability of triaxially braided composite tubes. Journal of Composite Material 32(21), 1964-1983. 98.

[21] Chou T. W. Microstructural design of fiber composites. Cambridge, Solid state, Science series, 1992.

[22] Chretien N. Numerical constitutive models of woven and braided textile structural composites. Master thesis, Virginia Polytechnic Institute and State University, 2002.

[23] M. Colin de Verdiere. Dynamic behaviour of composites under impact loading. Nine month review, Cranfield University, January 2006.

[24] Correlated Solution, Inc. P.O. Box 4840West Columbia, SC 29171 – USA. http://www.correlatedsolutions.com.

[25] Cox B. N., Carter W. C., Fleck N. A. A binary model of textile composites- I. Formulation. Acta Metallurgica et Materialia, Vol 42, n10, 3463-3479, 1994.

[26] Cox B., Flanagan G. Handbook of analytical methods for textile composites. NASA contractor report 4750, 1997.

[27] D'Amato E. Finite element modelling of textile composites. Composite structures, 54, 467-475, 2001.

[28] Daniel I. M., Ishai O. Engineering mechanics of composite materials. Oxford university press, 1994.

[29] Davila C. G., Camanho P. P. Physically based failure criteria for transverse matrix cracking. 9th Portuguese conference on fracture, 2004.

[30] Davila C. G., Camanho P. P. Failure criteria for FRP laminates in plane stress. NASA/TM-2003-212663, 2003.

[31] De Blic A. Performance car crash energy management structures, MSc individual thesis, Cranfield University, 2003.

[32] De Saint Joseph G. Composite 2D: Modélisation mécanique et identification de la couche élémentaire. Université de Pierre et Mari Curie - Paris 6, 1985.

[33] Eurocarbon, www.eurocarbon.com, 2004.

[34] Falzon, P. and Herszberg I. Mechanical performance of 2-D braided carbon/epoxy composites. Composites science and technology, 58, 253-265, 1998.

[35] Farley G. L. Energy absorption of composite materials. Journal of composite materials, 17, 267-279, 1983.

[36] Fedro M. and Willden K. Characterization and manufacture of braided composites for large commercial aircraft structures. Proceedings of the second NASA Advanced Composites Technology Conference, NASA CP 3154, 387-429, 1992.

[37] FISITA. Mercedes-Benz SLR McLaren – Technology for the 21st-Century. Autotechnology magazine, www.fisita.com, may 2003.

[38] Fouinneteau M. Mechanical testing of non-crimp CF and twill woven laminate - Part 2: In plane testing. Cranfield, 2002

[39] Fouinneteau M. Nine month: Failure and Impact modelling of braid reinforced composites. Cranfield University, 2003.

[40] Foye R. L. Finite element analysis of the stiffness of fabric reinforced composites. NASA Contract report 189597, 1992.

[41] Fujita A, Maekawa Z., Hamada H, Yokoama A. Mechanical behaviour and fracture mechanism in flat braided composites. Part 1: Braided flat bar. Journal of reinforced plastics and composites, 11, 600-617, 1992.

[42] Fujita A, Maekawa Z., Hamada H. Tensile properties of carbon fiber triaxial woven fabric composites. Journal of composites materials, 27 (15), 1428-1442, 1993.

[43] Gall. K. and Lake M. Development of a shockless thermally actuated release nut using elastic memory composite material. American Institute of Aeronautics and Astronautics. 44th Structures, Structural Dynamics, and Materials Conference -1582, April 2003.

[44] Gao F., Boniface L., Ogin S., Smith P., and Greaves R. Damage accumulation in woven-fabric CFRP laminates under tensile loading: Part 1: Observations and damage accumulation. Composites Science and Technology 59, 123-136, 1999.

[45] Gao F., Boniface L., Ogin S., Smith P., and Greaves R. Damage accumulation in woven-fabric CFRP laminates under tensile loading: Part 2: Modelling the effect of damage on macro-mechanical properties. Composites Science and Technology 59, 137-145, 1999.

[46] Gasser A., Ladevèze P., Poss M. Damage mechanisms of a woven SiC/SiC composite: modelling and identification. Composites science and technology, 56, 779-784, 1996.

[47] Ghoirse S. R. Effect of voids content on the mechanical properties of carbon-epoxy laminates. SAMPE Q, 24 (2) 54-59, 1993.

[48] Gowayed A., Pastore C., Howarth C. Modification and application of a unit cell continuum model to predict the elastic properties of textile composites. Composites: Part A, 27 A, 149-155, 1996.

[49] Greve L. The numerical prediction of composite crashworthiness. Nine month review, Cranfield University, 2003.

[50] Greve L. Damage and failure modelling of carbon/epoxy non-crimp fabric composites. PhD thesis, Cranfield University, 2005.

[51] Greve L., A. K. Pickett. Delamination testing and modelling for composite crash simulation. Composites science and technology, 66(6), 816-826, 2006.

[52] Greve L., A. K. Pickett. Modelling damage and failure in carbon/epoxy non-crimp fabric composites including effects of fabric pre-shear. Composites Part A, article in press, 2006.

[53] Hamidi Y. K. et al. Formation of microscopic voids in resin transfer moulded composites. Journal of Engineering Materials and Technology, 126 (4), 420-426, 2004.

[54] Harper B. D., Staab G. H., Chen R. S. A note on the effect of voids upon the hygral and mechanical properties of AS4/3502 Graphite/Epoxy. Journal of composite materials, 21 (3), 280-289, 1987.

[55] Hart D. C. Development of a progressive failure finite element analysis for a braided composite fuselage frame. Master Thesis, Faculty of the Virginia Polytechnic Institute and State University, 2002.

[56] Harte A. and Fleck N. On the mechanics of braided composites in tension. European Journal of Mechanics A/Solids, 19, 259-275, 2000.

[57] Harte A., Fleck N., and Ashby M. Energy absorption of foam-filled circular tubes with braided composite walls. European Journal of .Mechanics A/Solids, 19, 31-50, 2000.

[58] Herakovich C., Schroedter R., Gasser Alain, and Guitard L. Damage evolution in $[\pm 45]_S$ laminates with fiber rotation. Composites Science and Technology, 60, 2781-2789, 2000.

[59] Hibbeler R. C. Mechanics of materials. International edition, fifth edition, 2003.

[60] Hinton M., Kaddour A., and Soden P. A comparison of the predictive capabilities of current failure theories for composites laminates, judged experimental evidence. Composites Science and Technology 62(12-13), 1725-1797, 2002.

[61] Hochard C., Aubourg P., and Charles J. Modelling of the mechanical behaviour of woven fabric CFRP laminates up to failure. Composites Science and Technology 61, 221-230, 2000.

[62] Huang Z. Modelling and characterization of bending strength of braided fabric reinforced laminates. Journal of composite materials, 36, 2537-2566, 2002.

[63] Huang Z. The mechanical properties of composites reinforced with woven and braided fabrics. Composites science and technology, 60 (4) 479-498, 2000.

[64] Hull D. A unified approach to progressive crushing of fibre-reinforced composites tubes. Composites Science and Technology 40, 377-421, 1991.

[65] Hull D., Clyne T. W. An introduction to composite Materials, second edition, Cambridge University press, 1996.

[66] Huntsman Advanced Materials, www.huntsman.com, 2004.

[67] Ishikawa T., Chou T. W., Elastic behavior of woven hybrid composites. Journal of composite materials, 16, 2-19, 1982.

[68] Ishikawa T., Chou T. W., In-plane thermal expansion and thermal bending coefficients of fabric composites. Journal of composite materials, 17, 92-104, 1983.

[69] Ishikawa T., Chou T. W., Nonlinear elastic behaviour of woven fabric composites. Journal of composite materials, 17, 399-413, 1983.

[70] Johnson A. and Simon J. Modelling fabric reinforced composites under impact loads. EUROMECH 400. Impact and damage tolerance modelling of composite materials and structures.

[71] Johnson A.F., Pickett A., and Rozycki P. Computational methods for predicting impact damage in composite structures. Composites Science and Technology 61, 2183-2192, 2001.

[72] Judd N. C. W., Wright W. W. Voids and their effects on the mechanical properties of composites- an appraisal. SAMPE Journal, 14-10, 1978.

[73] Kachanov L. M. Time of the rupture process creep conditions. Izv. Akad Nauk SSR Otd Tekh., 8:26-31, 1958.

[74] Kaddour A. S., Hinton M. J., Soden P. D. A comparison of the predictive capabilities of current failure theories for composite laminates: additional contributions. Composite science and technology, 64, 449-476, 2004.

[75] Kalidindi S. R., Abusafieh A. Longitudinal and transverse moduli and strength of low angle 3-D braided composites. Journal of composite materials, 30 (8), 1996.

[76] Kang M. K., Lee W., Hahn H. T. Formation of microvoids during resin-transfer moulding process. Composites Science and Technology, 60 (123-13), 2427-2434, 2000.

[77] Karbhari V., Falzon P., and Herszberg I. Energy absorption characteristics of hybrid braided composites tubes. Journal of Composite Materials 31 (12), 1165-1186, 1997.

[78] Karbhari V. and Haller J. Rate and architecture effects on progressive crush braided tubes. Composite Structures 43, 93-108, 1998.

[79] Karbhari V., Haller J., Falzon P., and Herszberg I. Post-impact crush of hybrid braided composite tubes. International Journal of Impact Engineering 22, 419-433, 1999.

[80] Kaw A. K. Mechanics of composite materials. CRC press, 1997.

[81] Kelkar A., Tate J., Whitcomb J., and Tang X. Performance evaluation and modelling of braided composites. American Institute of Aeronautics and Astronautics. 44th Structures, Structural Dynamics, and Materials Conference. 1475, April 2003.

[82] Kim Y., Cho Y., Im K., and Yang I. A study on the collapse characteristics of stacking sequences using CFRP composite tubes. International Journal of Vehicle Design 30, 146-154, 2002.

[83] Ko F. K. From textile to geotextiles. Seminar in honour of professor Robert Koerner, September 2004.

[84] Ladevèze P., Allix O., Deu J., and Leveque D. A mesomodel for localisation and damage computation in laminates. Computer Methods in applied mechanics and engineering 183, 105-122, 2000.

[85] Ladevèze P., Gasser A., Allix O. Damage mechanisms modelling for ceramic composites. Journal of engineering material and technology, 116, 331-336, 1994.

[86] Ladevèze P., Guitard L., Champaney L., and Aubard X. Debond modeling for multidirectional composites. Computer methods in applied mechanics and engineering 185, 109-122, 2000.

[87] Ladevèze P. and Le Dantec E. Damage modelling of the elementary ply for laminated composites. Composites Science and Technology, 43, 257-267, 1992.

[88] Ladevèze P. and Lubineau G. An enhanced mesomodel for laminates based on micromechanics. Composites Science and Technology, 62, 533-541, 2002.

[89] Ladevèze P. and Lubineau G. On a damage mesomodel for laminates: micromechanics basis and improvement. Mechanics of Materials, 35, 763-775, 2003.

[90] Lecompte D., Smits A. Quality assessment of speckle patterns for digital image correlation. Optics and lasers in engineering. To be published.

[91] Lemaître J., Chaboche J. L. Mechanics of solids materials. Cambridge university press, 1990.

[92] Lemire T., Onodera H. J. Carbon fiber, what's in the wind? Presentation, february, Albuquerque, 2004.

[93] Le page B. H., Guild F. J., OginS. L., Smith P. A. Finite element simulation of woven fabric composites. Composites Part, 35,861-872, 2004.

[94] LIMESS Gmbh. www.limess.com.

[95] Lomov S. V., Barbursky M., Stoilova T., Verpoest I., Akkerman R., Loendersloot R., Thije R. H. W. Carbon composites based on multiaxial multiply stitched preforms. Part 3: biaxial tension, picture frame and compression tests of the preforms. Composites: part A. Article in press, 2005.

[96] Lubineau G., Ladevèze P., Violeau D. Durability of CFRP laminates under thermomechanical loading: a micro-meso damage model. To be published, 2005.

[97] Lundström S. et al. Influence from process parameters on void formation in the Resin Transfer Moulding. Polymer Composites, 15 (1), 1994.

[98] Macander A., Crane R., and Camponeshi E. Fabrication and mechanical properties of multidimensionally (X-D) braided composite materials. 7th Conference in Composite Materials: Testing and Design , 422-443, 1984.

[99] Matthews F. L., Rawlings R. D. Composite materials: engineering and science. CRC press, Woodhead publishing Limited, 1999.

[100] www.matweb.com, 2004.

[101] Matworks inc. Matlab. version 6.5.0.1, 2002.

[102] McGlockton M. A., Cox B.N., McMeeking R. M. A binary model of textile composites: III high failure strain and work of fracture in 3D weaves. Journal of the mechanics and physics solids, 51, 1573-1600, 2003.

[103] Mehran E., Razvan A., Reifsnider K. L. Characterisation of composite material's dynamic response using load/stroke frequency response measurement. Composite materials – Fatigue and fracture. 4th volume, Stinchcomb/Ashbaugh, 1993.

[104] Minguet, P.J., Fedro, M.K., and Gunther, C.K. Test methods for textile composites NASA CR 4609, 1994.

[105] Muller J. Formulaire de mecanique generale. Imprimerie F. Paillart, Abbeville, 16eme edition, 1977.

[106] Naik N. and Kuchibhotla R. Analytical study of strength and failure behaviour of plain weave fabric composites made of twisted yarns. Composites: Part A, 33, 697-708. 2002.

[107] Naik R. A., Analysis of woven and braid reinforced composites, NASA Contract Report-194930, 1994.

[108] Naik R. Failure analysis of woven and braided fabric reinforced composites. Journal of Composite Materials 29, 17, 2334-2363, 1995.

[109] Naik R., Ifju P., Masters J. Effect of fibre architecture parameters on deformation fields and elastic moduli of 2-D braided composites. Journal of composite materials, 28 (7), 657-681, 1994.

[110] National Instruments Vision Assistant v7.0, www.ni.com.

[111] National Instruments Labview v7.1, www.ni.com.

[112] Ng S., Tse P., and Lau K. Numerical and experimental determination of in-plane elastic properties of 2x2 twill weave fabric composites. Composites Part B 29B, 735-744, 1998.

[113] Oliver P., Cottu J.P., Ferret B. Effects of cure cycle pressure and voids on some mechanical properties of carbon/epoxy laminates. Composites, 26, 7, 509-515, 1995.

[114] Ortiz M. and Simo J. An analysis of a new class of integration algorithms for elasto-plastic constitutive relations. International Journal for Numerical methods in Engineering 23, 353-366, 1986.

[115] PAM-CRASH^{TM}. ESI Software Engineering Systems International, 99, rue des Solets, SILIC 112 94513 Rungis cedex France, 2002.

[116] Patel N., James Lee L. Modelling of void formation and removal in liquid composite moulding. Part II: Model development and implementation. Polymer Composites, 17(10), 1996.

[117] Pickett A. Review of finite element simulation methods applied to manufacturing and failure prediction in composites structures. Applied Composite Materials 9, 43-58. 2002.

[118] Pickett A. K., Fouinneteau M. R. C. Material characterisation and calibration of a meso- mechanical damage model for braid reinforced composites. Composites A, 37, 368-377, 2006.

[119] Pihno S. T., Davila C. G., Camanho P. P., Iannucci L., Robinson P. Failure models and criteria for FRP under in-plane or three dimensional stress states including shear non-linearity. NASA /TM-2005-213530, 2005.

[120] Rabotnov Y. U. Creep rupture. In: Proceedings XII International congress on applied mechanics, Stanford, Berlin, 1968.

[121] Rozycki P. Contribution au developement de lois de comportement pour materiaux composites soumis a l'impact. Universite de Valenciennes et du Hainaut-Cambresis, 2000.

[122] Rudd C. D. Liquid moulding technologies. SAE international, Woodhead publishing limited, 1997.

[123] Schmueser D. W., Wickliffe L. E. Impact energy absorption of continuous fibre composite tubes. Journal of engineering materials and technology, 109, 72-77, 1987.

[124] Shojaei A. et al. Modelling and simulation approaches in the resin transfer mouldings process: A review. Polymer Composites, 24 (4), 2003.

[125] Soden P. D., Hinton M. J., KaddourA. S. A comparison of the predictive capabilities of current failure theories for composites laminates. Composites science and technology, 58, 1225-1254, 1998.

[126] Siron O., Pailhes J., and Lamon J. Modelling of the stress/strain behaviour of a carbon/carbon composite with 2.5 dimensional fibre architecture under tensile and shear loads at room temperature. Composites Scienceand Technology 59, 1-12, 1999.

[127] Swanson S. and Smith L. Comparison of the biaxal strength properties of braided and laminated carbon fiber composites. Composite: Part B 27B, 71-77. 1996.

[128] Tabiei A. and Jiang Y. Woven fabric composite material model with material nonlinearity for nonlinear finite element simulation. International Journal of Solids and Structures, 36, 2757-2771, 1999.

[129] Tang G., Yan Y., Chen X., Zhang J., Xu B., and Feng Z. Dynamic damage and fracture mechanism of three-dimensional braided carbon fiber/epoxy resin composites. Materials and Design, 22, 21-25, 2001.

[130] Tang J-M., Lee W. I., Springer G. S., Effects of cure pressure on resin flow, voids, and mechanical properties. Journal of composite materials, 21 (5) 421-440, 1987.

[131] Tang X., Whitcomb J., Goyal D., and Kelkar A. Effect of braid angle and waviness ratio on effective moduli of 2x2 biaxial braided composites. American Institute of Aeronautics and Astronautics. 44th Structures, Structural Dynamics, and Materials Conference- 1877, April 2003.

[132] Wavemetrics, inc. Igor –Pro software. Oregon USA, www.wavemerics.com.

[133] Whitcomb J. D. Iterative global/local finite element analysis. Computers and structures, vol 40, n4, 1027-1031, 1991.

[134] Whitcomb J. D., Woo K., Application of iterative global/local finite element analysis, part I: linear analysis. Communications in numerical methods in engineering, 9, 745-756, 1993.

[135] Whitcomb J. D., Woo K., Application of iterative global/local finite element analysis, part II: geometrical non-linear analysis. Communications in numerical methods in engineering, 9, 757-766, 1993.

[136] Woo K., Whitcomb J. D., Global/local finite element analysis for textile composites. Journal of Composite Materials, 28 (14), 1305-1321, 1994.

[137] Woo K., Whitcomb J.D. A post-processor approach for stress analysis of woven textile composites. Composites science and technology, 60, 693-704, 2000.

[138] Woo K., Whitcomb J.D. Macro finite element using subdomain integration. Communications in numerical methods in engineering, 9, 937-949, 1993.

[139] Woo K., Whitcomb J.D. Three-dimensional failure analysis of plain weave textile composites using global/local finite element method. Journal of composite materials, 30, 984-1003, 1996.

[140] Wood J. R., Bader M. G. Void control for Polymer-Matrix composites (1): Theoretical and experimental methods for determining the growth and collapse of gas bubbles. Composites Manufacturing, 5 (3), 1994.

[141] Xu J., Cox B. N., McGlockton M. A., Carter W. C., A binary model of textile composite-II. The elastic regime. Acta metallurgica et materialia, 43 (9), 3511-3524, 1995.

[142] Yan Y. and Van Hoa S. Energy model for prediction of mechanical behaviour of 2-D triaxially braided composites, Part1: model development. Journal of Composite Materials, 36, 963-981. 2002.

[143] Yan Y. and Van Hoa S. Energy model for prediction of mechanical behaviour of 2-D triaxially braided composites, Part1: parameters analysis. Journal of Composite Materials 36, 1233-1253. 2002.

Chapter 9- Appendices

Four publications relative to this work are presented in the following chapter.

Appendice 1	Paper published in Composites Part A.
Appendice 2	Extended abstract from Comptest 2004 proceedings.
Appendice 3	Extended abstract from Comptest 2006 proceedings.
Appendice 4	Accepted paper for BSSM 2006, published in Applied Mechanics and Materials.